NEAR FIELD MIXING OF NEGATIVELY BUOYANT JETS

by *Cameron John Oliver*

A thesis submitted in partial fulfilment of the requirements for the degree of Doctor of Philosophy in Civil Engineering

30 January 2012

Supervisors: Dr. Mark J. Davidson and Dr. Roger I. Nokes

University of Canterbury
Department of Civil and Natural Resources Engineering
Christchurch, New Zealand

Abstract

Negatively buoyant jets are turbulent flows that are frequently employed by the desalination industry to disperse reject brines into oceanic environments. Although such brines are characterised by elevated concentrations of the same elemental components as the discharge environment contains, there is significant potential for marine ecosystem damage if this waste is not diluted properly. Numerous workers have analysed the dilution and spatial characteristics of negatively buoyant jets, but published data demonstrates notable inconsistencies. An important reason for these discrepancies is the variety of bottom-boundary conditions employed. This complicates comparison with predictions by integral models typically employed for discharge design, as these generally have not been developed with consideration to boundary interaction. In the present study, negatively buoyant jet experimental data is collected where bottom boundary distances are sufficiently large to avoid boundary influence at the point where the discharge returns to its source height (the return point).

Near-field centreline dilution data is measured under still ambient conditions, for the source inclinations of 15–75°. Considerable attention is paid to experimental data quality, and all relevant issues are mitigated where possible. In order to ensure the boundary has no influence, source heights in this study range between $2.33\, d\, F_0$ and $8.07\, d\, F_0$. A variety of time-averaged and temporal statistics are calculated, and these statistics are compared with published experimental data and predictions by integral models. Normalised trajectory and dilution data from the source through to the return point collapses well at each inclination. The attention to signal quality and the self-consistency of derived experimental results in this study suggest a high level of accuracy, and large distances to the bottom boundary ensure that results are not confused by boundary interaction. Data for dilution rate at the return point supports the use of higher source inclinations (60° and 75°) to maximise dilution capability.

A new 'forced jet' model is developed that incorporates the concept of a reducing buoyancy flux as the flow rises to maximum height. While this model is not applicable above source inclinations of 60°, predictions at other inclinations are reasonable. Dilution predictions are notably improved when compared to those from existing integral models. Finally, CFD simulations of negatively buoyant jets are conducted using the k-ε turbulence model. Despite the sophistication of this model, the quality of spatial and dilution bulk flow predictions at the centreline maximum height are no better than those obtained from the forced jet model or analytical solutions of Kikkert *et al.* (2007).

Acknowledgements

Thanks must first go to my supervisor, Dr. Mark Davidson. Your constant support and encouragement both in times of success and in times of frustration or poor progress has been truly appreciated. Thanks for the many discussions we had regarding physical problems, experimental problems, or whatever else I was doing at the time. Thanks for doing so much to try get the MEDRC project off the ground, even if it was unsuccessful in the end.

Thanks to Dr. Roger Nokes for editing text and for providing valuable second opinions on a variety of technical topics. To my office-mates—Claire, Adam, Sarah and numerous others—thanks for keeping me sane and for the great conversations we had. Thanks to Ian for being the always-helpful 'first port of call' regarding most of the laboratory-related questions I had during my time. Alan you were the "let's do it" man, always quick to help in many things. And thanks to Kevin for being the ideas man; the one who built almost every bit of kit I used—including my experimental tank! I pray that one day you will come to know true Hope that can never let you down.

Thanks to Mum and Dad for your constant encouragement and support. I can't thank you enough for your financial support too. Thanks to Camille, Cristelle and Chad for being such neat siblings. And James too—you rock. I have an amazing family.

And finally, a very special mention must go to my lovely wife, Lydia (my fiancée prior to submission). Thanks for your encouragement, your comfort, your reassurances and for all the yummy nibbles that helped me get through! Thanks for being such an incredible person and a faithful servant of God. Thanks as well for allowing me to spend the time I needed to on my PhD. I know it was hard for both of us.

This PhD would never have been possible without the millions who have come before me. The new work I have contributed is small compared to all of the technology I have used to carry it out, and to the scientific discoveries made by others that I have relied upon.

It seems that almost as a rule, we are utterly oblivious to the complexity and wonder of what goes on around us every day. Thus the greatest thanks rightly go to the maker of everything that this thesis investigates: God.

Soli Deo Gloria—to God alone be the glory.

"Behold, these are but the outskirts of his ways,
and how small a whisper do we hear of him!
But the thunder of his power who can understand?"

Job 26:14, ESV

Contents

Chapter 1

Introduction

"We never know the worth of water till the well is dry"
Thomas Fuller (1732, p. 237)

1.1 Water Scarcity

The earth holds a staggering amount of water. Gleick (2000) estimates the total to be 1,386,000,000 km^3, which if divided equally between the world's 6.9 billion people (Haub, 2010, est.), would leave over 200 billion litres of water per person. And this water is a completely 'renewable' resource: as it is used, it is recirculated and purified by the earth's natural water cycle; albeit over varying timescales.

Yet simultaneously, there are millions around the world for whom water is a scarce resource. Some must travel long distances each day to collect just enough to survive; others have enough for survival but not enough to service their desired lifestyle or income source. More than 1.2 billion people—equivalent to a fifth of the world's population—live in areas of physical water scarcity: areas where water resources development is approaching or has exceeded sustainable limits (CA, 2007). Invariably it is the rural populations that are hardest hit. Worldwide, only 27% of rural dwellers had water piped into their homes or onto their premises in 2006 (UN, 2009).

There are a myriad of factors that contribute to such problems. For one, water reservoirs are not evenly spread around the globe. Some areas have a natural abundance of water, while other areas, such as deserts, have a natural scarcity of water. But the most significant reason is that a large majority of water on the earth is unusable by humans due to the form in which it is found.

Table 1.1 outlines the quantities of water found in various stocks. Considering the subtotals, we may make two particular observations. Firstly, the volume of freshwater that is underground or frozen is much larger than all other stocks of freshwater. Secondly, the volume of saltwater dwarfs the total of freshwater. The former is problematic because underground water requires expensive drilling to access, and frozen water requires large amounts of energy to melt. The latter

is even more problematic, because saltwater tastes foul, does little to relieve thirst, and is toxic for most irrigation purposes. Thus what is the most abundant source of water is for the most part rendered useless in the alleviation of water scarcity.

Table 1.1: Volume of water on earth, from Gleick (2000).

	Volume (1000 km^3)	**Proportion of total**
Oceans	1,338,000	96.54
Saline and brackish groundwater	12,870	0.93
Saltwater lakes	85	0.006
Total saltwater stocks	***1,350,955***	***97.48***
Glaciers and permanent snow cover	24,064	1.74
Fresh groundwater	10,530	0.76
Ground ice and permafrost	300	0.022
Total frozen and underground freshwater stocks	***34,894***	***2.52***
Freshwater lakes	91	0.007
Soil moisture	16.5	0.001
Atmospheric water vapour	12.9	0.001
Marshes and wetlands	11.5	0.001
Rivers	2.12	0.0002
Incorporated in biota	1.12	0.0001
Total freshwater stocks not frozen or underground	***135***	***0.010***
Total water on Earth	***1,385,984***	***100.0***

1.2 Desalination

While saltwater is of little direct use to humans, it is in fact possible to remove salt from water in order to generate fresh water. This process, in its many forms, is generically referred to as 'desalination'. In fact, desalination is an entirely natural process. As the sun heats the ocean and causes surface water to evaporate, it is fresh water that rises. This salt-less vapour condenses in the sky and later falls back to the earth as rain; an integral part of the earth's water cycle. Aristotle (c. 350 BC) is the earliest known person to have noted this process—now referred to as 'distillation'. He writes:

> "Salt water when it turns into vapour becomes sweet, and the vapour does not form salt water when it condenses again. This I know by experiment."

The major factor that historically inhibited the wide-scale adoption of distillation in coastal settlements around the world is its energy requirements. In order to distill significant proportions of a feed supply, it must be heated to boiling temperature—or at least near to this temperature. Given that ocean temperatures are rarely higher than 40°C, and at coastal altitudes boiling temperature is approximately 100°C, this is a difficult goal to achieve for any large volume of water.

Desalination became feasible to incorporate into municipal water supplies with the development of plants based on 'multi-stage flash'. This technology takes advantage of the fact that water evaporates at lower temperatures as the surrounding pressure decreases. Input water is heated and injected into a series of vessels under progressively decreasing pressures; where upon each injection a proportion of the water evaporates ('flashes' to steam). In such a way, a significant percentage of the supplied salt-water can be evaporated with a relatively limited supply of heat. It is important to note however that with increasing recovery ratios comes quickly increasing production costs. In practice, a relatively low proportion of intake seawater is recovered; the rest is disposed of in some manner. Note that with brines of lower salinities than seawater, higher recovery ratios can be obtained.

Multi-stage flash (MSF) desalination plants gained a strong foothold in the Middle East region during the 1970s (Morris, 1993). Because of their ability to utilise waste thermal energy, MSF plants have often been collocated with power plants. Approximately 50% of desalination plants today are located in the Middle East and North Africa (Gleick *et al.*, 2006), where natural water supplies are limited and population growth has been large.

A newer technology, and one which is more energy efficient, is that of Reverse Osmosis (RO). As the name implies, Reverse Osmosis involves forcing water to flow through semipermeable membranes in the opposite direction to that in which it would flow naturally—*i.e.*, forcing it to flow from the salt-water side into the fresh-water side. This is achieved by the application of a pressure greater than the natural osmotic pressure. While osmotic pressure is linear with the solution salinity (Amiji & Sandmann, 2002), salinity grows rapidly with recovery rate (Baker, 2004, p. 216):

$$\frac{C_b}{C_0} = \frac{1}{1-R} \tag{1.1}$$

where C_0 is the initial concentration of salt, C_b is the concentration of salt in the (reject) brine, and R is the recovery rate as a fraction. Thus, like MSF, with increasing recovery ratios comes quickly increasing costs. RO plants typically achieve higher recovery rates than MSF plants, but rarely operate above 45% for seawater desalination (Greenlee *et al.*, 2009, p. 2331).

Reverse Osmosis of saline water was first investigated in the mid-1950s by researchers at UCLA (Glater, 1998). The first commercial seawater-RO unit was installed in late 1974, on the island of Bermuda (Andrews & Laker, 2001). As improvements were made in membrane technologies, energy requirements dropped and RO quickly became a popular option.

As of 30 June 2008, the total contracted capacity of desalination plants around the world stood at 62.8 million m^3 per day (IDA, 2009). MSF and RO plants together account for approximately 82% of this capacity (Gleick *et al.*, 2006). Production costs have dropped to as low as \$0.48 per m^3 (Allison, 2006).

Desalination technologies are particularly appealing to those countries for whom security of water supply is a major issue. Numerous countries share water sources (such as aquifers or rivers)

with neighbouring states, leaving themselves vulnerable to manipulation in the event that political relations become sour. Singapore for example imports a large proportion of its water from Malaysia, and as a result has been left open to manipulation on matters such as railways, airspace and trade (Stratfor, 1999). Other areas are beginning to see increased variability in climate patterns, particularly with more frequent extremes such as floods and droughts. Desalination plants provide a water supply that is largely immune to such pressures; a reliable portion of municipal water portfolios.

Nevertheless, few cities around the world can afford to operate entirely from desalinated water sources. Seawater desalination is significantly more expensive than treatment of most fresh surface or aquifer water: residents even in the wealthy city of Melbourne, Australia have protested against installation of a plant to supply a relatively modest part of their needs (see for example Devine, 2008). Although brackish water desalination can be comparable in cost to traditional water treatment techniques (Martínez Beltrán & Koo-Oshima, 2006, p. 29), not many areas have the luxury (or as some may see it, the curse) of large brackish water sources. In addition, while many have spoken glowingly of how the sea could be the answer to all the world's water woes, often it is the poorest communities around the world who are in the most desperate need—and thus least able to afford such technology.

Martínez Beltrán & Koo-Oshima (2006) discussed the use of desalination in agricultural applications, and concluded that although it may have some role in achieving food security, it is generally very cost-ineffective for such purposes.

This of course does not mean that desalination cannot have a place in carefully planned municipal water portfolios. As a secure and potentially unlimited supply, it is a valuable complement to traditional supplies such as those from rivers, reservoirs and aquifers, as well as wastewater recycling systems and localised (*e.g.* rooftop) collection systems. It is important however that research into understanding and reducing the cost of desalination continues in haste, as there is much benefit to be gained from a truly widespread adoption of the technology.

1.3 Environmental Effects of Desalination

Financial cost is by no means the only cost of desalination plants. Numerous potential environmental impacts exist; many of which are project- and site-specific. The direct impacts are largely associated with the intake and outfall systems used to withdraw input water and dispose of reject brine. However, there are important indirect environmental effects also.

1.3.1 Direct impacts

1.3.1.1 Intake

Whether the feed brine is of seawater origin or of surface water origin, in the majority of cases inlet structures must be screened to keep debris and aquatic life from entering. Morton *et al.* (1996)

notes that the mesh on these screens is typically in the order of 5 mm, which, while preventing the intake of large fish and invertebrates, poses a significant threat to phytoplankton, zooplankton and ichthyoplankton. Any such entrained organisms will be subject to chlorination, pressure changes, and/or temperature changes; making it very unlikely that they will survive. Larger marine life can be sucked up against the screens (impinged), leading to physical damage or stress. In addition, because plankton are an important part of the marine food chain, the entire ecological community may be adversely affected, with a reduction of population numbers or even localised species extinction. The seriousness of this threat should not be underestimated. Pankratz (2004) states, "recent analyses have noted that marine life impingement and entrainment associated with intake designs…may represent the most significant direct adverse environmental impact of seawater desalination."

Ideally intake screens should be very fine, and placed at such a distance from the intake structures themselves that velocities across the screens are only slightly greater than ambient velocities. Unfortunately, such screens would also be very difficult—if not impossible—to keep clean. Current cleaning systems for medium to large desalination intakes are either air-backwash based or mechanical-raking based (Gille, 2003), both of which would be notably harder to use on large fine screens. An alternative intake method is to use underground beach-wells. However, beach-wells are generally only suitable for small or medium sized plants (Lattemann & Höpner, 2008).

1.3.1.2 Outfall

It would not be unreasonable to assume at first that the waste water generated from desalination processes would be of no particular environmental concern. If this water contains only elevated concentrations of the same components as the input water, and if it is being ejected into the same environment from which it was extracted, one might expect that no serious problems could be caused. Certainly these discharges are not carrying the same bacteria or nutrient loads that discharges from municipal waste-water treatment plants carry.

Unfortunately, the reality is that discharges from desalination plants have potential to cause a myriad of problems. Firstly and most importantly, even relatively small changes in salt concentrations can affect the health of many marine organisms. This can be inferred simply by considering the process of osmosis: if a cell that originally had the same concentration of salt as the surrounding is subjected to an increased surrounding salt concentration level, the net flow across the cell's membrane will be from the cell out into its surroundings. That is, the cell will (tend to) shrivel. Nonetheless, natural variations in ocean salinity do exist, especially with depth (Karleskint *et al.*, 2009, p. 85); indicating marine life does have some tolerance to salinity changes.

Numerous workers have listed the potential effects of elevated salinity levels (Baalousha, 2006; Einav & Lokiec, 2003; Höpner & Windelberg, 1996, *etc.*), but comparatively little has been done to collect empirical data for the response of marine flora and fauna. This problem is exacerbated by the incredible diversity of habitats and species present among the different locations where

desalination plants are situated around the world.

Sáanchez-Lizaso *et al.* (2008) reported on a multi-part study of *Posidonia oceanica* (L.) Delile, an endemic seagrass of the Mediterranean Sea that was found in the locality of a proposed desalination plant in Spain. This study incorporated laboratory work where *P. oceanica* shoots were placed in tanks of various salinities for 15 days at a time (Fernández-Torquemada & Sáanchez-Lizaso (2005) describes this in detail). With respect to a control (environment-replicating) salinity of 38.0 psu[1], plant mortalities were statistically significant above 39.1 psu. When a sea urchin species and a mysid species were placed in the tanks also, an increase in mortality rates was detected at 41 psu. An accompanying field study, where $1m^2$ plots were treated *in situ* with discharge water from a pilot desalination plant, found increased plant mortality at 0.71 psu and 1.52 psu above background salinity levels. The authors recommended that the brine from the proposed plant not exceed 38.5 psu for more than 25% of all observations, and not exceed 40 psu for more than 5% of all observations.

Fernández-Torquemada *et al.* (2005) studied a *P. oceanica* meadow soon after a sea-water Reverse Osmosis (SWRO) plant began discharging in the area, and found that while the brine discharge did not produce regression of the meadow, it did affect plant vitality.

Tomasko *et al.* (2000) diverted the discharge plume from a SWRO plant onto a (previously unaffected) healthy and productive *Thalassia testudinum* seagrass meadow and studied various community parameters with respect to time of exposure and measured salinity levels. Plume salinity was around 57–65 ppt, yet no information was provided on how this plume was discharged (surface, seabed, *etc.*). A weak but statistically significant relationship was found between exposure salinity level and macroalgal biomass; probably due to filter backwashing or storm-water runoff from the desalination plant complex which had been flushed out with the discharge. No relationship was found between temporal changes in seagrass shoot density, areal blade biomass or areal blade productivity and the degree of brine exposure.

Raventos *et al.* (2006) carried out visual marine species censuses 12 times before and 12 times after a desalination plant in Blanes, Spain had begun operating, and found no statistically significant variations attributable to the brine. They comment that the failure to record any change may be because of the rapid dilution undergone by the brine diffuser and the natural high variability characteristic of such environments.

The above workers have focused exclusively on the effect of brine salinity on marine environments, and do not come to a common consensus on the extent to which these environments are affected. This is in large part due to the (aforementioned) diversity of habitats that were studied. However, salinity is not the only problematic property of desalination discharges. Brines from MSF plants are typically hotter than the body of water to which they are returned. Dissolved oxygen levels in desalination brines can be lower than that in the ambient seawater (Lattemann & Höpner, 2008), and, importantly, brines typically carry significant loads of added chemicals. These chemicals are employed in desalination processes to control bio-fouling, scaling and

[1] Practical Salinity Units; simply a value on the Practical Salinity Scale (PSS)

foaming, to remove suspended solids, and to clean various components of the plant. In addition, heavy metals may also be present due to corrosion of heat exchangers and such like. Numerous workers list these chemicals (Lattemann & Höpner, 2008; Sadhwani *et al.*, 2005; Meerganz von Medeazza, 2005; Morton *et al.*, 1996; Winters *et al.*, 1979, *etc.*), but it is unclear exactly how marine environments are affected by individual chemicals or a combination of chemicals typical of that used in a desalination plant. Reduction of chemical usage and/or ensuring rapid dilution is the only practical recommendation available, provided of course there is no bio-accumulation.

Exact characteristics and constituents of discharges from a given desalination plant will depend on the desalination technology used, the quality of the intake water, and the chemicals used for pretreatment (*e.g.* Hashmin & Hajjaj, 2005). Because of this dependence, proper environmental impact assessments should be carried out when planning each new discharge, on a per-project basis. Lattemann & Höpner (2008) make a valuable point that, while technical options exist to mitigate environmental impacts, "equally or even more important than the technical options, however, is the selection of a proper site for a desalination project."

1.3.2 Indirect impacts

1.3.2.1 Greenhouse gases

The proportionally high energy demand of desalination has been discussed in section 1.2. For Multi-Stage Flash (MSF) plants, this demand is primarily in the form of heat. In some circumstances, MSF plants may be co-located with another industrial plant which can supply waste heat; thus reducing the amount of heating that must be done on site. For Reverse Osmosis (RO) plants, the energy demand is primarily in the form of pressure. Here, a variety of systems can be utilised to recover the energy held in the pressurised waste stream (Greenlee *et al.*, 2009). Despite the energy efficiencies that may be achieved, invariably when a sizable desalination plant is built in a district, the electricity demand imposed on the local grid is significant. The Kwinana Seawater Desalination Plant, a RO plant built to supply approximately 17% of Perth's water needs, was expected to consume 185 GWh/year of electricity; approximately equivalent to the energy consumption of 30,000 households (Crisp, 2008).

If this energy load is taken by fossil fuel generation facilities, desalination plants can be responsible for large greenhouse gas emissions. In many parts of the world, this is certainly the case (Meerganz von Medeazza, 2005). Greenhouse gas emissions are linked to global warming, which in turn is predicted to decrease water availability and increase drought frequency in mid-latitudes and semi-arid low latitudes (Parry *et al.*, 2007). Additionally, Meerganz von Medeazza (2005) points out that the use of fossil fuels effectively shifts the problems from one scarce resource (water) to another scarce resource (non-renewable energy).

Various renewable energy sources do exist. Solar thermal energy, solar photo-voltaic, wind power, biomass, geothermal energy and oceanic energy can all be used to power desalination plants (García-Rodríguez, 2003), each with various advantages and disadvantages. In Australia,

wind power is proving a popular option, with a 272 GWhr/year wind farm built to power the Kwinana desalination plant (Crisp, 2008), and a wind farm planned for a desalination plant being built in Kurnell, Sydney (Sydney Water, 2007). Yet the disadvantage with most renewable energy sources is that they are subject to fluctuations in generating capacity, while desalination plants are designed to be continuous and steady state (Meerganz von Medeazza, 2005). Invariably generating facilities built to supply desalination plants are fed through the regional electricity grid, so when they are not producing enough power other facilities such as coal-fired plants are utilised to cover the deficit.

1.3.2.2 Creating demand

Counter-intuitively, the building of desalination plants in an area can ultimately result in an *increased* water demand. While the root cause is sociological, the result can be a multiplicity of environmental stresses across an entire district's water supply and disposal portfolio.

Meerganz von Medeazza (2005) points out that when water supplies to a region are increased, water-squandering habits are inadvertently both satisfied and encouraged. Citing Naredo (2003), he comments that the principal imbalance between water availability and its consumption originate not from population increases, weather changes and such like; but from the importation of activities into zones without any consideration of their capability to host such actions. Thus, supplying water to a desert-type region to satisfy the needs of these activities only allows those activities to flourish and regional water needs to rise even further. If these future demands are in turn met by desalination, the environmental risks outlined in this section may occur. In fact, any method chosen to satisfy that demand will have at least some associated environmental effects.

The phenomenon of 'supply creating demand' is not confined to water. Mill (1808, pg. 135), in explaining a concept in economics known as Say's Law, states that "the production of commodities creates, and is the one and universal cause which creates a market for the commodities produced." While the universality of this principal in the field of economics is questioned (Mankiw, 2002, pp. 238-255), it has been well regarded. In the field of transportation, Litman (2001) explains that road improvements that reduce commuter travel costs (including time) tend to attract traffic from other routes, times and modes; encouraging increased and more frequent usage. Conversely, traffic congestion causes people to defer non-urgent trips, reroute, choose alternative transportation modes if possible, and even forgo avoidable trips. The analogy with water is a close one: water shortages are likely to cause people to defer or avoid un-necessary water usage, and seek out activities that are less water-intensive.

1.3.3 Moving forward

It is impossible for public infrastructure to be built without having any type of environmental effect; without changing the environment in some way. At times these changes are small and insignificant, but at other times the changes may have large repercussions for future human

generations, or for the survival of certain species. It would not be too extreme to hold that desalination has the potential to fall into the latter category. However, it would also be wrong to dismiss the technology completely because of this potential. Rather, those involved in planning and designing must proceed with a measure of caution.

In deciding whether to build a plant, desalination as a technology should be properly evaluated in the context of alternative options, not only upon its own merit. All available water sources should be considered, including non-conventional "sources" such as water recycling and leak reduction. The opportunity for demand reduction should also be investigated.

Likewise, when designing intake or outfall structures, as much information as possible should be gathered about the surrounding marine environment, and steps should be taken to mitigate or minimise potential environmental impacts wherever possible.

Desalination holds great potential to be a key part of many municipal water systems around the globe. Water scarcity is predicted to worsen across many parts of the world in the foreseeable future. UN Water (2007) for example projects that 1.8 billion people will be living in areas with absolute water scarcity by 2025, and two thirds of the world population could be subject to water stress. Already numerous aquifers are over-extracted and have a limited useful lifespan. While demand management can be a powerful tool in some areas, population growth will always reduce its effectiveness and necessitate eventual supply expansion.

Nevertheless, a paucity of firm empirical data in many important areas is evident. In particular, little is understood regarding the mixing of reject desalination brines and their ecological impact. The current study will focus on collecting quality data on the dilution rate of waste brines in the region close to where they are emitted. While not contributing directly to understanding how this brine affects marine biota, confidence in prediction of the near-field mixing rate is crucial for the informed design of outfall structures that minimise environmental risk, while not unnecessarily increasing construction costs.

1.4 Brine Disposal

Numerous options exist for the disposal of brine originating from desalination plants. Truesdall *et al.* (1995) surveyed US membrane plants in 1992, and found that the following disposal methods were being used:

- Publicly owned sewage treatment works
- Evaporation ponds
- Irrigation and other land application methods
- Deep-well injection
- Disposal into surface waterways and lakes
- Disposal into ocean

For desalination plants located near the ocean, the most common and the least expensive disposal method is ocean discharge (Del Bene *et al.*, 1994). There are countless ways that this can be performed; the simplest of these being gravity-driven open channel flows. Due to increased concern for environmental protection and human health, open channel flows are now largely frowned upon. By far the preferred method is disposal via submerged diffuser: that is, disposal from undersea nozzles that create *turbulent buoyant jet* flow at their source. It is with these flows that the interest of this present study lies. Section 1.4.1 will describe turbulent buoyant jets generally, and in Section 1.5 the particular scope of this work will be oulined.

1.4.1 Turbulent Jets and Plumes

Turbulent jets and plumes are rapidly spreading and mixing flows that can begin at a single point-source; usually a circular pipe opening (orifice). While the terms "jet" and "plume" both hold a spectrum of technical meanings, here *jet* refers specifically to a flow generated by a continuous source of momentum, or more specifically, a flow that is dominated by its initial momentum flux. Likewise, here the term *plume* refers to a flow generated by a continuous source of buoyancy, or generally a buoyancy-dominated flow. A *buoyant jet* is an initial-momentum dominated flow (a jet) that has a non-zero density difference between it and the surrounding ambient fluid, and thus at some distance becomes buoyancy-dominated (a plume).

Turbulence is an unsteady flow type that is characterised by significant irregularity, diffusivity, vorticity and dissipation (Tennekes & Lumley, 1972). Because of its vorticial (*i.e.* rotational) nature, it is often described as being made up of *eddies*. These eddies exist at many different scales, but are difficult to identify or follow due to the randomness of turbulent motions. Turbulence occurs at high Reynolds number; a unitless quantity representing the ratio of inertial forces to viscous forces:

$$Re = \frac{UL}{\nu} \tag{1.2}$$

where U is a velocity scale, L is a length scale, and ν is the kinematic viscosity of the fluid. Here U is U_0, the velocity at the exit, and L is d, the diameter of the orifice.

Statistical methods are used extensively to describe turbulent flows. While turbulence dictates that the flow is unsteady and chaotic, distinct averages may be discerned as functions of space and time (Hinze, 1975, p. 2). That is, turbulence can simultaneously be described as being *orderly* in the mean.

Time-averaged turbulent jet and plume behaviour has been found to remain unchanged where the bulk driving conditions remain the same; from one completely independent experiment to another. For this present study, the decomposition of any parameter into its time-average and fluctuating components will be denoted as $p = \overline{p} + p'$; where p is the parameter in question.

Turbulent jets and plumes are ubiquitous; formed in countless ways both in liquids (*e.g.*

water) and gases (*e.g.* the atmosphere). Research on these structures is similarly extensive. A variety of factors may influence the behaviour of turbulent jets and plumes in field applications, including currents that move the ambient fluid into which the discharge is emitted, stratification of this ambient fluid, and boundary interactions. In many cases, these effects cause a transition into flow regimes that are distinct from those of the jet and the plume. Lee & Chu (2003), Wood *et al.* (1993), Jirka (2004) and others have summarised a broad range of such regimes.

In order to make experimental data applicable to full-scale industrial discharges, data must invariably be scaled upon dimensionless parameters. In the case of a buoyant jet in a stationary, unstratified ambient, the relevant dimensionless parameter is the initial densimetric Froude number. This parameter is defined as:

$$F_0 = \frac{U_0}{\sqrt{\hat{g}_0 d}} \tag{1.3}$$

where $\hat{g}_0$ is *reduced gravity*[2] at the nozzle. $\hat{g}$ is defined as $g\frac{\Delta\rho_0}{\rho_a}$ where g is acceleration due to gravity, ρ_a is density of the ambient fluid and $\Delta\rho_0$ is the density difference between source and ambient fluids.

Time-averaged velocity and concentration cross-sectional profiles for both pure jets and pure plumes have been shown to be Gaussian in form. However, velocity and concentration profile widths differ to some extent. This difference is denoted by the factor λ, which has been found to change between jet and plume regions (Wang & Law, 2002). Thus we define

$$\frac{u}{u_{\text{℄}}} = e^{-r^2/b^2}, \quad \frac{\hat{g}}{\hat{g}_{\text{℄}}} = e^{-r^2/(\lambda b)^2} = e^{-r^2/b_c^2} \tag{1.4}$$

where b is a measure of velocity-profile width or 'spread'; $b_c = \lambda b$ is the equivalent concentration-profile width; r is radial distance; u is time-averaged velocity; $\hat{g}$ is time-averaged reduced gravity (which can function as the time-averaged tracer C). Subscript ℄ denotes centreline values. Wang & Law (2002) found the velocity spread rate with respect to path, $\frac{db}{ds}$ (where s is path length) to be 0.106 for a pure jet and 0.105 for a pure plume. Note that these values are different for different definitions of 'spread'.

Despite the extent of turbulent jet and plume research, most research has focused on neutrally- or positively-buoyant discharges; that is, discharges that are the same or 'lighter' than the surrounding fluid. Common applications of positively buoyant flows include hot exhaust from chimneys and municipal waste (essentially fresh-water) discharged into the ocean (salt-water).

Of those that have studied *negatively*-buoyant discharges—the type of discharge generated by desalination brine waste—many have focused on the vertical-fountain scenario. In this configuration, fluid exiting the source rises due to its initial momentum flux, but then falls back on top of

[2] In other literature, reduced gravity is denoted as g'. Here the $'$ symbol is reserved for fluctuating components.

itself as the buoyancy-generated momentum flux becomes dominant. As with all turbulent jets or plumes, the rising central 'core' of flow expands by entraining the surrounding fluid. However, because the surrounding fluid is now the fluid that is falling down from the top, this entrainment process becomes much less effective at dilution. In addition, as turbulence is stochastic and the falling fluid never falls in a perfectly symmetrical manner, a vertical fountain is a highly dynamic system.

While some workers have measured the dilution rate of vertical fountains (*e.g.* James *et al.*, 1983), a large number have been concerned with their rise height (*e.g.* Turner, 1966; Cresswell & Szczepura, 1993; Pantzlaff & Lueptow, 1999; Kaye & Hunt, 2006, to name a few). Zeitoun *et al.* (1970) was the first to make a detailed study into *inclined* dense jets; that is, negatively-buoyant jets that are discharged at a non-vertical (and non-horizontal) angle. By their analysis, the few previous studies on dense jets had been confined to the case of vertical fountains. Their statement that vertical fountains are "exceedingly difficult to treat mathematically in any rational manner" still holds true today.

Usual design practice for submerged discharges dictates that a certain minimum dilution must be achieved under worst-case conditions. Although dense fountains are effective at mixing in the presence of a cross-current (see for example, Gungor & Roberts, 2009; Holly & Grace, 1972), if the range of possible ambient velocities includes the zero—or stagnant—case then they are a poor choice when compared to inclined discharges. Roberts & Toms (1987) state this clearly, saying:

> "...when the ambient fluid is stagnant the [vertical dense] jet falls back on itself resulting in considerably impaired dilution. This does not occur with an inclined jet, which has the additional advantage of a horizontal momentum component, which aids in clearing the wastefield from the discharge site."

As a rule, dilution rates in all turbulent jets and plumes increase as ambient velocities increase. Thus even with inclined discharges, it is the still ambient ($U_a = 0$) that is of greatest concern (Roberts & Toms, 1987). Similarly, it is the region nearest the source that is of particular interest. The rapid timescales in this region dictate that physical mixing is dominant, rather than any biological or chemical processes. Conditions at the end of the initial mixing region are critical for providing the inputs into models of far-field processes such as gravity-driven currents moving along the ocean floor (see for example, Purnama & Al-Barwani, 2006; Shao & Law, 2009). Thus it is essential that the location and conditions at the point of return to the ocean floor are predicted accurately. Nevertheless, as boundary interaction itself influences this "return-point" location and dilution behaviour, predictions must be specific to the particular boundary location in question.

Of important consideration with respect to desalination-generated discharges is the cause of their density difference. As already mentioned, discharges from MSF plants are typically characterised by elevated temperatures as well as elevated salinities. Because the molecular diffusivities

of these two components are significantly different (that of heat being approximately 80 times that of salt; Taylor & Veronis, 1996), there is potential for such a flow to bifurcate—that is, to split into two distinct parts. Such systems are commonly known as *double diffusive*. The importance of this variation in diffusivity in the context of laminar plumes has been discussed by McDougall (1983); Turner (1995, 2003) and others. Its relevance to fully turbulent discharges from desalination plants has been investigated in part by Law *et al.* (2004). Of the three sets of submerged jet experiments they carried out, two sets were fully turbulent at the source. Temperature and salinity were varied, but always such that the net initial buoyancy was zero. In all cases, the jets were observed to plunge downwards. This behaviour is inconsistent with that expected of a neutrally buoyant discharge and is indicative of potential modelling and design difficulties for such mixed-component flows. Nevertheless, because of the declining popularity of MSF and similar heat-based processes, this is a less pressing issue. Where mixing salt and heat streams from separate sources is a possibility, Roberts & Toms (1988) recommends keeping them separate in order to more reliably predict their behaviour.

It is important to note that while negatively buoyant jets find their primary commercial application in desalination plants, there are many other practical applications also. These include (Ferrari & Querzoli, 2010),

- oil or gas-drilling facilities and mineral salt industries, e.g. from leaching of mineral salts domes
- gypsum or acidic wastes from fertilizer factories
- dense effluents from wastewater treatment plants
- replenishing of cold salt water at the bottom of solar ponds
- improvement of water quality by forced mixing in reservoirs
- small lakes and harbours
- forced heating or cooling of large structures such as aircraft hangars, buildings or rooms
- replenishment of magma chambers in the Earth's crust
- the evolution of volcanic eruption columns
- exit snow from snowploughs
- vehicle exhausts from diesel engines
- accidental leaks of hazardous gases.

1.5 Scope of present study

The current work will focus on the *near-field dilution* behaviour of *single-component inclined negatively buoyant discharges*, under *still ambient conditions*. An emphasis will be placed on collecting

high-quality data regarding concentration and spatial extent, where the bottom boundary distances are sufficiently large to avoid any complicating boundary influence where the discharge returns to the source height.

Being orderly in nature, time-averaged dilutions from a negatively buoyant flow are expected to fall around a consistent "path". Although the area occupied by the flow at a particular instant may be extremely unpredictable, in the time-averaged field there will invariably be at least one line—or ridge—of peak concentration (*i.e.* minimum dilution) running through the flow. Unless otherwise noted, in this study the terms "centreline" and "trajectory" will refer to the location of this ridge of peak concentration, with the underlying assumption that cross-sectional concentration profiles have only one peak. This *a priori* assumption is based upon research on positively buoyant jets, where, under stagnant ambient conditions, researchers have found cross-sections of both concentration and velocity to be Gaussian in nature. It is worth noting that in turbulent buoyant jets this ridge of peak concentration is generally collocated with the ridge of maximum velocity magnitude.

Figure 1.1 provides a configuration plot, depicting important parameters that will be discussed in the following chapters. These parameters are:

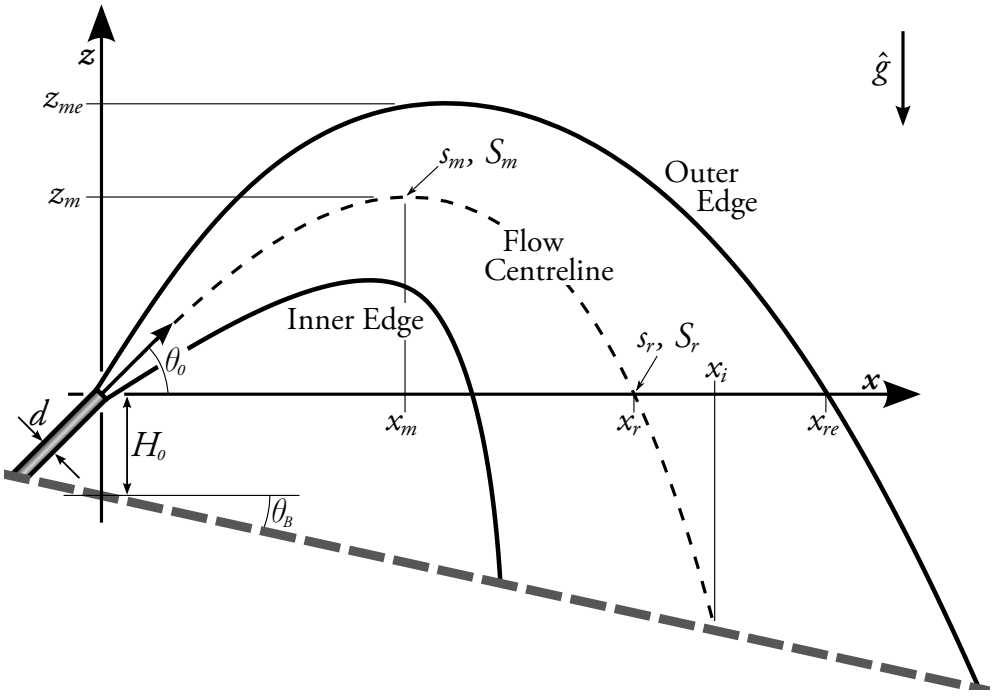

Figure 1.1: Configuration and notation plot for an inclined negatively-buoyant jet. Vertical and horizontal coordinates are both measured from the discharge nozzle

- z_m, the *maximum centreline height*, and x_m, the horizontal distance from the source this point
- z_{me}, the *maximum edge height*
- x_r, the horizontal distance to the centreline at the source height; termed the *return point*

- x_{re}, the horizontal distance to the outer edge of the flow at the source height
- x_i, the horizontal distance to the *impact point*; that is, the location where the centreline impacts a bottom boundary. This boundary may be real (such as a seabed) or nominal (existing only to denote an imaginary plane).
- s_m and S_m, the path length and dilution at the maximum centreline height $[x_m, z_m]$
- s_r and S_r, the path length and dilution at the return point $[x_r, 0]$
- θ_0, the source inclination
- H_0 and θ_B, the riser height and bottom boundary slope, respectively

Flow 'edge' is defined as the edge of the tracer concentration field. Concentration—referring strictly to concentration *anomaly*—will be denoted in this study as C, and dilution S as $\frac{C_0}{C}$; where C_0 is the concentration at the source. Dilution should not be confused with path length, denoted by the lower case s. Note that the return point is distinct from the impact point if H_0 or θ_B are non-zero.

In Chapter 2, the current literature on negatively buoyant jets will be reviewed, and in Chapter 3, integral modelling of these flows will be discussed. Chapters 4 & 5 will outline the experimental work performed on negatively buoyant jets with source inclinations of 15–75°, while Chapter 6 will outline computer simulations performed for source inclinations of 15–60°. Where quotations have been given in this document from other authors, notation has been modified to be consistent with the notation presented above.

Chapter 2

Literature Review

"The heart of the discerning acquires knowledge; the ears of the wise seek it out."
Proverbs 18:15, NIV

In designing buoyant discharges, practitioners must be satisfied that their solution is capable of attaining some desired and/or regulated dilution rate within a specific distance from the source. Rarely is it feasible or desirable to perform laboratory-scale experiments to test the complete set of possible configurations before the construction of each discharge. Instead, models derived with respect to prior scaled laboratory experiments are employed, and an iterative procedure adopted in order to ascertain which set of parameters corresponds to the global (system-wide) optimum. Consequently, the primary goal of an experimentalist is the provision of quality data to test and calibrate such models.

Modelling approaches applied to turbulent jets generally fall into the categories of integral models and Computational Fluid Dynamics (CFD) simulations. These will be properly described in Section 2.2. The effectiveness of each model can only be assessed to the accuracy of experimental data that is available for calibration.

All modelling approaches can provide time-averaged predictions. As described in Section 1.4.1, this is only meaningful because turbulence can be described as "orderly", and averages remain the same if bulk driving conditions remain the same. Thus the occurrence of specific events will be statistically distributed, and therefore accounted for by an average carried out over a sufficiently long period of time. It is widely accepted that averaged flow behaviour provides a solid basis for engineering design of such outfalls.

This chapter will discuss past research on inclined negatively buoyant jets; constrained to that which concerns the same conditions as those outlined in Section 1.5 for the current research. The primary focus will be experimental results, but modelling approaches will also be summarised. First however, it is helpful to define precisely what is meant by the term "negatively-buoyant".

In common usage, the word "buoyant" is used to describe an object floating on a liquid. By extension, "buoyant" also describes objects that are fully submersed but are lighter than the

surrounding fluid they have displaced, and thus have a natural tendency to rise. It must be noted that fluids themselves, if lighter than the surrounding fluid, may come under the category of buoyant objects.

Traditionally, the phrase "negatively buoyant" has been used to refer to the inverse of this scenario: that is, to objects (including fluids) that are heavier than their surroundings, and thus have a natural tendency to fall. These objects may be thrust upwards with some initial momentum, but will always fall back down again, because the net buoyancy force is acting downwards.

In this context however, such a definition of "negatively buoyant" has the potential to be misleading. This is because most, if not all, laboratory work on [positively-] buoyant jets is in fact carried out with dense jets that are discharged from near the surface of the experimental tank. In other words, the source and ambient densities are swapped and the experiment is performed upside down. Such an approach is desirable due to the much smaller volume of saltwater required, and is possible because of the *Boussinesq approximation*. This approximation states that for flows where the density difference ($\frac{\Delta\rho}{\rho}$) is small, the only important way that the respective densities of the fluids enters the problem is via the reduced gravity ($\hat{g}$; denoted also in Figure 1.1)—which is advantageous because reduced gravity only undergoes a sign change when the densities of the two fluids are swapped[1]. That is, for dense jet modelling to be made applicable to positively buoyant jets, only the sign of the vertical axis need change.

Yet this does not necessarily mean the "inclined negatively buoyant" discharges used for desalination-plant outfalls will act in exactly the same way as the ubiquitous positively buoyant jets used for municipal wastewater discharge; albeit with a somewhat more curved trajectory. Following Kikkert *et al.* (2007) and Lindberg (1994), the phrase "negatively buoyant jets" is defined here to refer to jets where the buoyancy force acts in the opposite direction to the vertical component of the initial momentum flux. This has two consequences. Firstly, the majority of experiments performed for positively buoyant jets are not directly applicable to this study, including those performed with horizontal buoyant jets. Secondly, where the Boussinesq approximation is still applicable, negatively buoyant jet experiments may in fact be performed using fluid discharged downwards that is lighter than the surrounding fluid; as for example was performed by Pantokratoras (1999) with heated water jets.

2.1 Experimental Data

A wide variety of techniques have been used to measure characteristics of fluid flows (see for example, Smits & Lim, 2000). Traditionally, much research work has revolved around taking still photographs and point measurements. Photographs provide valuable quantitative information regarding spatial extent, and qualitative information regarding dilutions. Typically these are of

[1] Boussinesq (1903) postulated that for two fluids where the density difference is small, "the variations of density can be ignored except were they are multiplied by the acceleration of gravity in equation of motion for the vertical component of the velocity vector."

dyed fluids, but refractive index differences can also be exploited to produce *shadowgraphs* which emphasise areas of high tracer gradients. Point measurements, although requiring the insertion of probes or suction pipes into the flow (and thus altering flow patterns to some extent), provide accurate dilution information. Conductivity probes, calculating salinity levels by changes in electrical conductance, have been the most widely-used under this category.

Such techniques are still in use today, but much more popular are those approaches afforded by modern technology which allow non-intrusive measurements of concentration and velocity. Invariably these involve the use of digital video cameras. Predominant in this category are Light Attenuation (LA), Laser-Induced Fluorescence (LIF), Particle Image Velocimetry (PIV) and Particle Tracking Velocimetry (PTV). These are described below.

Light Attenuation When light passes through a dye that is sensitive to that particular electromagnetic wavelength, it is attenuated. That is, its intensity is reduced. LA takes advantage of this to determine the *integrated concentration* of the dye (and hence the flow) between a fixed light bank and the camera. By 'integrated' it is meant that the concentration detected at a given camera pixel is the integration of the concentrations between the light bank and the camera along the path travelled by the incident light rays. As such, it is distinct from point or planar concentration measurements.

Laser Induced Fluorescence Described in detail in Section 4.1, LIF involves using lasers to excite fluorescent particles in the fluid, which in turn emit light that can be recorded by a camera. Emission intensity can then be related to concentration. LIF in the context of Fluid Mechanics usually refers to *planar* LIF: that is, experiments where the laser light has been changed into a thin sheet of light that cuts through the experimental tank at some location. In such a manner, concentrations from the flow can be determined across any desired cut-plane.

Particle Image Velocimetry & Particle Tracking Velocimetry By mixing small particles into the experimental fluid that are of very similar density to that fluid, velocity patterns can be observed visually. Side-lighting these particles along a narrow plane, such that they reflect light towards the observer, can provide an accurate two-dimensional view of the flow velocity field[2]. PIV and PTV both use video sequences of such seeded flows, and endeavour to algorithmically determine the velocity field. Experimental systems and procedures are virtually identical between each technique: the difference lies in the algorithms used to calculate the velocities. PIV is based on cross-correlation of segments of the raster intensity field between successive frames. PTV, however, involves identifying individual particles in each frame and matching these particles between frames.

[2]Note that minimising particle size minimises the effect of their own inertia. However they must still be visible.

2.1.1 Visual observations and point measurements

Bosanquet *et al.* (1961) were possibly the first to conduct experiments on negatively-buoyant jets. They used diluted magnetite slurry as their source fluid—a material which provided both colour and density increase—and presented results for horizontal and 45° inclined negatively buoyant jets. Instantaneous photographs of these jets were presented; however due to the intense concentration of slurry only their outlines are discernible. In most cases a starting-jet is evident. An integral model for predicting the trajectory of such jets is presented, which the authors state is also applicable in determining the trajectory of "a light fluid rising within a heavier one". Because the slurry was too uniformly dark to visually determine locations of peak concentration, the centreline was calculated as the mean of the upper and lower boundary coordinates. Heating the slurry and taking vertical distributions of temperature with a fine-wire thermocouple indicated that "the concentration axis was in fact near to the axis of symmetry". Model results matched horizontal dense jet trajectories with reasonable accuracy, but performed much more poorly for 45° negatively buoyant jets.

Zeitoun *et al.* (1970) studied 30°, 45° and 60° inclined jets. Trajectories were determined by adding Rhodamine B to the jet fluid, and time-averaging sets of five photographs. They found that although the non-dimensionalised maximum edge height varied with angle of inclination, the non-dimensionalised return-point edge location was approximately the same. Plotting the product of these two parameters, their maximum was found to be at an angle of 63°. They therefore came to the conclusion that "the 60° angle nozzles will produce a maximum path and therefore maximum dilution of the effluent under the same conditions of initial flow." While direct measurements of concentration—and thus dilution—were carried out by extracting point samples and measuring their density, this was found to be difficult due to natural flow variability and uncertainty regarding the exact location of the jet axis.

Roberts & Toms (1987) measured dilutions and trajectories of 60° inclined jets. Rhodamine B was added to the jet fluid, and concentrations were determined by fluorometer measurements of vacuum-extracted samples from a vertically-arranged rack of sampling tubes ($0.8\,d$ internal diameter, with minimum spacing of $2.3\,d$). These tubes were positioned at the visually-identified locations of maximum edge height and impact point. Sets of three photographs were taken of each experiment, and edge height calculated as the average "height to top of visible dye plume". Non-dimensional edge height and impact dilution results for experiments at sufficiently large F_0 compared well with data from Zeitoun *et al.* (1970). However, normalised minimum dilution at maximum centreline height was measured to be approximately 68% of the value measured by Zeitoun *et al.*. Expressing concern with the experimental technique employed by Zeitoun *et al.*, the authors suggested their value(s) were more accurate.

Roberts & Toms note that at low F_0 numbers ($F_0 < 20$ and $F_0 < 25$ respectively), experimental coefficients for maximum edge height and dilution at maximum centreline height were slightly higher than those experiments at high F_0 numbers. They conclude that the effect of

source volume flux—and thus F_0—can be neglected only when dilution rates are greater than 10; as per arguments presented by Fischer *et al.* (1979). Of potential concern is that their experiments were conducted with the relatively large density difference of 10%. It is unclear whether the Boussinesq approximation remains accurate near the source at such density differences.

Lane-Serff *et al.* (1993) conducted negatively-buoyant jet experiments in order to determine the accuracy of a buoyant-jet model they developed. Shadowgraph images were used to calculate the jet maximum edge height, and vertical concentration profiles were measured with conductivity probes. An example shadowgraph image is displayed, reproduced here in Figure 2.1, of which the authors make the following comment:

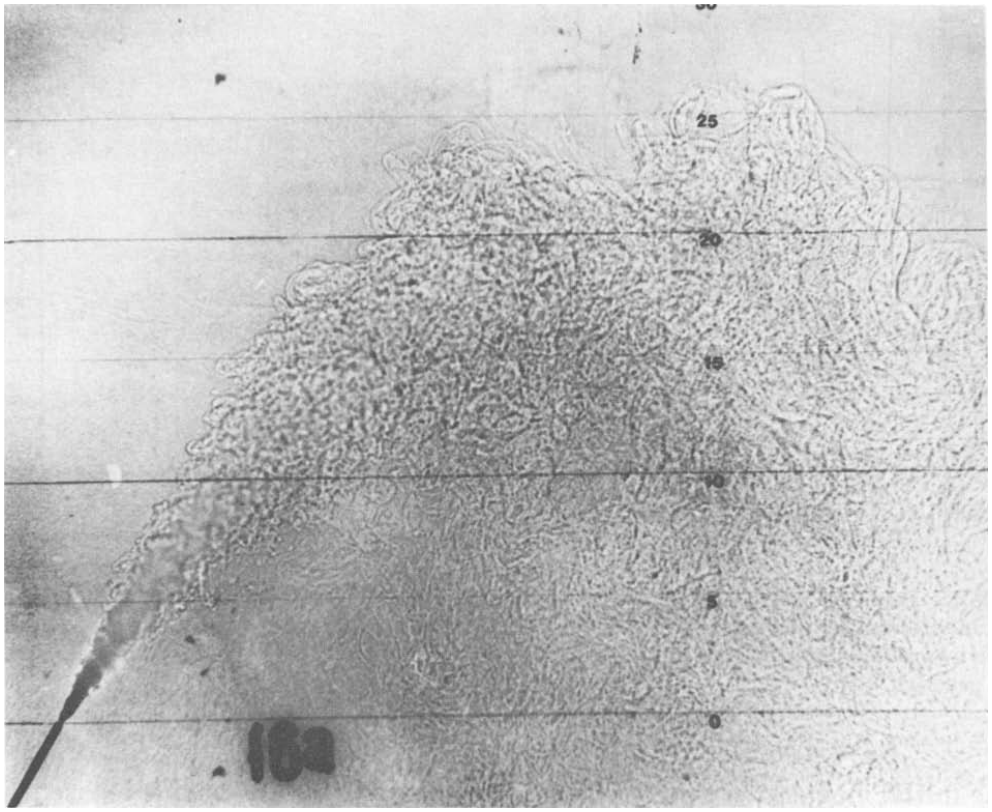

Figure 2.1: Figure 16 from Lane-Serff *et al.* (1993). Shadowgraph of negatively buoyant jet at 60° source inclination

> "Close to the source the plume is symmetrical but a pronounced asymmetry develops downstream. The upper side of the plume remains sharp and well defined while the lower side is diffuse and has no distinct edge even in an instantaneous picture as shown in the shadowgraph. This asymmetry results from the opposite effects of the buoyancy force on the two sides of the plume. On the upper side, buoyancy forces create a stabilising stratification which tends to inhibit entrainment of the environmental fluid. On the lower side the buoyancy forces produce a convectively unstable configuration and there is enhanced mixing between the plume and the environment. Detrainment of plume fluid is observed on the lower side, a feature which is not observed in vertical plumes."

The 'asymmetries' evident in this image are evident also in the vertical concentration profiles plotted. Although fairly coarse, their shapes are distinctly non-Gaussian from approximately the maximum centreline height location onwards. Trajectory and concentration decay data correlated poorly with model predictions, but maximum edge height data agreed well within the bounds of its experimental error. No direct discussion is made regarding the influence of the observed asymmetries on model results. Nevertheless, the authors note that "below the plume axis the dense fluid is mixing much more vigorously with the surrounding fluid as a result of the gravitational instability". Thus it may be logically deduced that modelling approaches that do not attempt to address this asymmetry (of which this model was one) will perform badly.

Lindberg (1994) conducted shadowgraph experiments at 30°, 45°, 60° and 90° inclinations, measuring edge-height and horizontal distance to this location. The temporal variability in all length scales was found to increase with higher inclinations, and the author stated this to be a result of the interaction of the jet/plume with the fluid falling back around the rising fluid. Lindberg noted that one of the most striking flow features was "the almost immediate descent of the low momentum interfacial fluid which exited from the nozzle."

Roberts *et al.* (1997) examined the impact-point and bottom layer dilution of 60° discharges using conductivity probes. Because the tank floor (and thus the impact point) was only 8.1 d below the source, it could be assumed that return point dilution measurements would not be significantly different. However, this is questionable due to the interaction of the jet with the tank floor and the surrounding bottom layer.

LIF images were recorded in addition to the conductivity measurements, and whilst care was taken to calibrate images carefully, obstructions and reflections close to the lower boundary prevented the desired dilution measurements from being derived in a reliable manner. An instantaneous LIF image is presented, along with a time-averaged image. Both images show evidence of asymmetry, though this is not commented upon. The authors present maximum edge height data but do not describe how it was calculated. One can only assume the LIF images were used in some manner for this purpose.

Doneker & Jirka (1999) discussed the possibility that the limited tank dimensions in the Roberts *et al.* (1997) experiments could have caused lateral boundary interaction. The response given by the authors (Roberts *et al.*, 1999) argues that the false floor placed in the channel circumvented this problem; although conceding that all laboratory experiments are influenced in some way by the experimental configurations. The response also made clear that the maximum edge height quoted included the height of the riser pipe.

More recently, Bloomfield & Kerr (2002) used the shadowgraph technique to measure maximum edge heights for negatively buoyant jets with inclinations between 30° and 90°. Their exact method for determining these heights—and the length of time over which values were averaged—was not discussed; however they state that their measurements were accurate to within 4–6%. 33 experiments were conducted at varying source inclinations but unknown F_0. Non-dimensional results showed the maximum edge height to be highest at approximately 80°. At

this point the edge height was 20% larger than that of a vertical fountain. Of some concern is the size of the tank used for these experiments: in some images the downward-falling fluid can be seen impacting the side boundary before the return point is reached, thus altering the flow trajectory somewhat. Such flow restriction may have affected the edge height also.

It is informative to point out that unless otherwise defined, "edge height" in the context of this document refers only to the final, or fully-established, edge height. Bloomfield & Kerr (2002) looked in detail at the initial edge height achieved as the discharge was started, and compared these initial edge heights with the corresponding "final" edge heights. This is of little use to the practitioner designing discharges from a desalination plant, for two reasons. Firstly, achieving such initial edge heights requires the almost-instantaneous opening of valves, so as to immediately achieve full source velocity. Near instantaneous valve openings are neither desirable or achievable in practice, and indeed achieving them in the laboratory is not trivial. Secondly, it is the long-term behaviour that dictates the effectiveness or not of a discharge. Although larger edge heights often correspond closely with larger dilution rates, such brief improvements would not help the ongoing mixing of waste from a continuously-running plant.

Papakonstantis *et al.* (2011b) reported concentration measurements on 45°, 60° and 75° negatively buoyant jets made with a microscale conductivity probe. Measurements at each discrete location were averaged for 40 s. Vertical and transverse profiles were recorded at the predicted and/or visually observed location of maximum centreline height (x_m). Non-dimensionalised vertical profiles, although displaying substantial scatter, were shown to be Gaussian on the outer boundary. On the inner boundary, profiles were "much flatter"; deviating significantly from the corresponding Gaussian distributions. Concentration turbulent intensity (defined as the root mean square of concentration fluctuations, RMS(C')) profiles were plotted for the same locations, and showed similar asymmetry. With respect to the ratio of RMS(C') to time-averaged concentration at the centreline, the authors note that as far as turbulent characteristics are concerned, the flow resembles a plume at maximum height. The ratio of the height of maximum RMS(C') to the maximum centreline height (z_m) was found to be almost constant, with an average value of 1.17 (equivalent to 0.75 b_c, where b_c is the concentration spread, defined in Section 4.5.4.1).

Transverse concentration profiles were found to be Gaussian on both sides (and thus symmetrical). The non-dimensional fitted width in this direction (b_{cy}) was found to be very similar to the fitted width on the outer side of the vertical concentration profiles. Such a result indicates that the outer side of the flow at maximum height is circular and not unequally distorted. Nevertheless, the authors caution that the number of experiments they performed in the transverse direction was limited.

Papakonstantis *et al.* found non-dimensional dilution rates at the maximum centreline height to be "almost the same for all angles". The corresponding data at the return point show considerable scatter, but are also similar in magnitude.

2.1.2 Optical techniques

Fischer *et al.* (1979) briefly touched upon negatively buoyant jets; presenting an instantaneous LA image which clearly shows asymmetric tracer distribution—reproduced here in Figure 2.2. A large "gap" may also be seen in one part of the primary flow, where concentrations are significantly lower than in locations before and after. However, a thick layer of discharge fluid has been allowed to build up along the bottom of their experimental tank, and this may have directly affected flow behaviour. Fischer *et al.* comment that "insufficient data exists to specify the dependence [of terminal rise height] on the jet angle". They present the relationship

$$z_{me}/(d\,F_0) \sim \left(\frac{\pi}{4}\right)^{1/4} (\sin\theta)^{3/4} \tag{2.1}$$

as a "reasonable estimate" of terminal rise height based upon "a few tests".

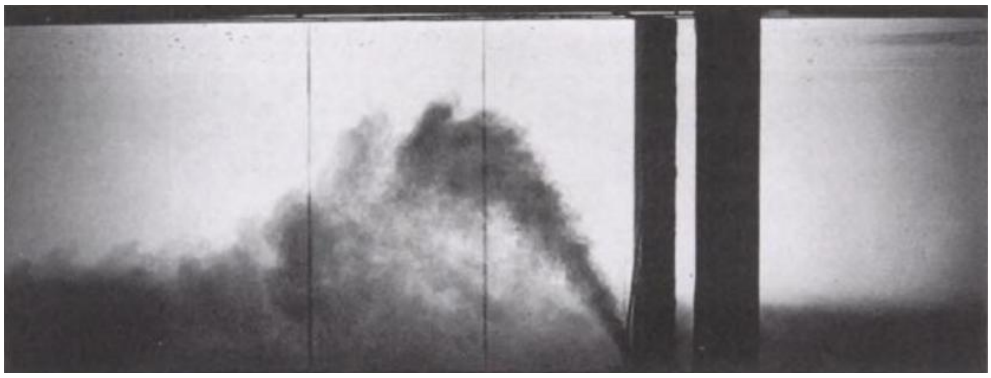

Figure 2.2: Figure 9.12 from Fischer *et al.* (1979). Negatively buoyant jet at 60°source inclination

Ferrari & Querzoli (2004, 2010) performed LIF experiments on initially-laminar negatively buoyant jets emitted from a sharp-edged hole in a transverse pipe, at angles from 45° to 90°, in 5° steps. The authors remark that a "sudden widening" of the flow occurs near the orifice, as Kelvin-Helmholtz billows "grow and drag external fluid into the jet, increasing mixing and dilution." This statement is confirmed by visual inspection of concentration images they present such as those reproduced here in Figure 2.3, and indicates that their discharges were not fully turbulent at the source; contrary to standard practice. Ferrari & Querzoli (2010) explain asymmetries that they observe on the inner side as the local unstable stratification tending to "transform the growing [Kelvin-Helmholtz] waves [into] plumes propagating downwards at the lower boundary."

A set of trajectories are plotted, and it is noted that the trajectory of the highest F_0 discharge ($F_0 = 30.8$) was less symmetric than the others. Ferrari & Querzoli found that the maximum height the centreline reached was at approximately 80°, confirming the observation made by Bloomfield & Kerr (2002). While rise height does not necessarily correlate with dilution rates, this was the basis for Zeitoun *et al.*'s determination of maximum trajectory length and expected maximum dilution. Hence these results bring into question the accuracy of the 60° inclination "best practice" assumption.

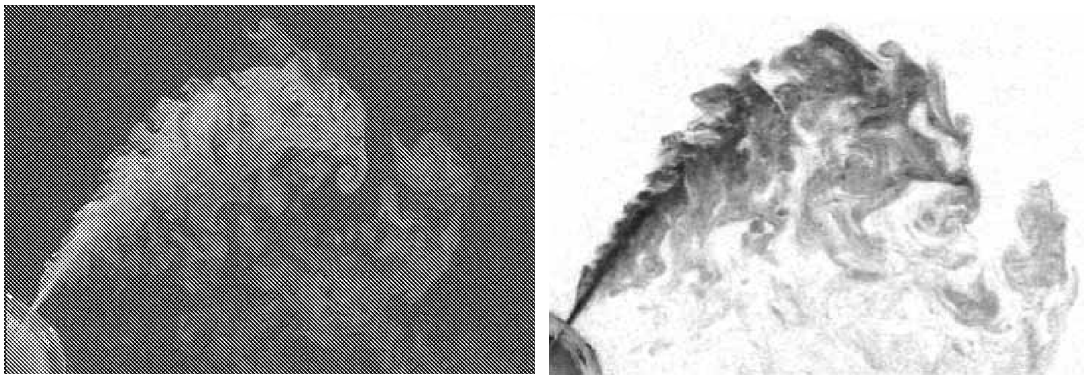

(**a**) Figure 3 from Ferrari & Querzoli (2004) (**b**) Figure 1a from Ferrari & Querzoli (2010)

Figure 2.3: Instantaneous images of the concentration field for a negatively buoyant jet with inclination of 55° and $F_0 = 14.8$.

Cipollina *et al.* (2005) used a simple form of LA to examine in detail the trajectory of 30, 45 and 60° discharges, focusing on the 45° case. Maximum centreline location (x_m and z_m), maximum edge height (z_{me}) and return point location (x_r) were assessed using time-averages of 30 frames recorded at 1 Hz. They correctly note that in order for the discharge trajectory to be parabolic (and thus symmetrical about the vertical axis), the return point distance must be twice the horizontal distance to the maximum centreline height. Their tabulated data proves they are correct in pointing out that this is not the case for a negatively buoyant jet. They comment that the trajectory on the rising side of the flow was found to be almost straight, whereas "after reaching their maximum they fall down rapidly" due to the effect of a "negative buoyancy flux" that the authors do not explain. Indeed, the instantaneous and time-averaged images plotted of a 45° negatively buoyant jet suggest the same flow asymmetry as observed by Lane-Serff *et al.* (1993), Ferrari & Querzoli (2010) and others.

Kikkert *et al.* (2007) measured both dilutions and trajectories of negatively buoyant jets with inclinations between 0° and 75°, using LA supplemented with LIF. LA images were fully calibrated, but LIF images were only calibrated spatially and thus could not provide quantitative dilution information. Images obtained using the LA system were typically recorded for a period of 1 minute at 24 Hz, and begun only after flow had visibly stabilised. In discussing the assumption of Gaussian-distributed cross-sectional profiles used in their analytical model, they state:

> "The inner edge of the jet is inherently unstable and buoyancy-driven instabilities in this region generate a significant vertical flux of material out of the buoyant jet as it moves in a predominantly horizontal direction. This flux appears to destroy the typical entrained flows one would expect to see near the edge of a jet, but in turn creates additional mixing in this region, and hence, additional dilution of the dye tracer."

While their analytical model predicted the centreline and outer edge of the flow with reasonable accuracy, the inner edge was poorly matched. Experimental concentration profiles that are

presented—recorded using both LA and LIF—show distinct asymmetries. Kikkert *et al.* observe that these mean concentration profile distortions appear to increase with distance up until the maximum height is reached, and almost stay constant in size beyond this. Nevertheless, on the outer edge of the flow, these profiles collapse satisfactorily onto a single Gaussian curve; leading the authors to remark that this side is "apparently unaffected by the gravitationally stable nature of the fluid in this area".

Kikkert *et al.* plot both trajectory and dilution data against that from other workers. In all cases their experimental trajectory coefficients match well with other experimental data, and their corresponding model predictions lie between the scatter of these data. However, model predictions for minimum spatially-integrated dilutions were approximately 18% less than measured values at maximum centreline height and 34% less at the return point. Comparisons at maximum centreline height with integrated dilutions calculated by the commercial modelling packages CorJet (Jirka, 2004) and VISJET (Lee *et al.*, 2000) fared worse still, and showed a dependence on inclination angle that was not evident in the data.

Yet, while providing valuable insight into the behaviour of negatively buoyant discharges, this experimental investigation was limited by the relatively simple technique (Light Attenuation) employed to measure dilution data. This technique provided concentration data that was integrated over the flow cross-section and therefore it was not possible to accurately determine peak centreline values. They note that "point dilution estimates from the present experimental study should be treated with some caution, because more detailed cross-sectional information is required to make an accurate transformation [between integrated and minimum values of dilution]".

Papakonstantis *et al.* (2011a), the companion paper to Papakonstantis *et al.* (2011b) and Papakonstantis *et al.* (2007), determined trajectory coefficients for 45°, 60°, 75°, 80°, 85° and 90° negatively buoyant jets ($7.5 \leq F_0 \leq 59.2$) by (it appears) visually examining uncalibrated LA images. Their spatial resolution was low (2.5 mm/pixel) and measurements were averaged only over "several" frames per experiment. Nevertheless, all results were in agreement with those of at least one other worker.

With respect to experiments performed at 85°, Papakonstantis *et al.* comment that "…around and beyond the region of the terminal height of rise, chunks separate from the flow and descend almost vertically to the bottom." Because of this, they found that beyond the maximum edge height, "the visual determination of the lower boundary is practically impossible".

Lai (2010) carried out LIF experiments in both longitudinal and transverse planes through negatively buoyant jets inclined at 15–60°. Transverse cutplanes were made at the maximum edge height location, and showed distinct elongations on the lower side. Nevertheless, the author noted that "the upper half of a dense jet is circular and symmetrical with respect to the vertical axis": a result that agreed with the findings of Papakonstantis *et al.* (2011b).

Lai recorded LIF images for 60 seconds on longitudinal planes and 90 seconds on transverse

planes. Geometrical properties were found to have an additional dependence on initial Froude number below approximately $F_0 = 25$–30. Likewise, normalised minimum dilutions were found to increase at low F_0 (*i.e.* $F_0 < 15$ and $F_0 < 20$ at maximum centreline height and impact point respectively). At maximum centreline height, normalised dilution for $F_0 > 15$ was found to peak at source inclinations of 52°, and decrease towards 60°. Between 30° and 45° average normalised dilution showed little variation. However, per-experiment dilution values at maximum centreline height, presented in Table 5.4 of Lai (2010), correlated poorly with initial Froude number. The reasons for this are not clear.

Lai also carried out a small number of (longitudinal) PIV experiments at 60°. Centreline velocity decay was found to be jet-like up until maximum centreline height, and faster than jet-like decay thereafter. This suggested that the rate of ambient entrainment was unaffected by buoyancy-induced instabilities in the region prior to maximum centreline height.

Also relevant to the current study is the work of Shao & Law (2010). They performed simultaneous LIF and PIV measurements on discharges inclined at 30° and 45°, using cameras fitted with different optical filters facing opposite sides of their experimental tank. Due to a small recording area (90 mm-square) a traverse system was used to move the camera across the extent of the flow, with 60 s recordings made in each location. After filming in two successive locations the experimental tank was re-filled. The source dye concentration was increased before recording portions of the jet further from the source, in order to increase the dynamic range.

The riser heights (H_0) chosen for these experiments were between $0.05\,dF_0$ and $0.47\,dF_0$; such that some experiments were expected to have boundary effects but that others were to be "well above the lower boundary". They state,

> For 45°, the [geometrical and mixing] coefficients are found to be similar for all tests, whereas for 30° a distinction can be identified for tests with H_0/L_M values below and above 0.15. Hence a major outcome from this exercise is that H_0/L_M is revealed to be the deciding factor for the determination of boundary influence."

where L_M is equal to $\left(\frac{\pi}{4}\right)^{1/4} dF_0$.

Nevertheless, the bottom layer thickness extending from a negatively buoyant jet was measured by Roberts *et al.* (1997) to be $0.7\,dF_0$ (at 60° source inclination) and Lai (2010) to be $0.4\,dF_0$ (for 15–60° inclinations), so there is concern that for all Shao & Law experiments return point behaviour may have been impacted in some way by the developing layer.

Shao & Law defined the centreline of the flow to be the streamline (in the averaged velocity field) starting from the centre of the nozzle; a distinctly unconventional approach, but one that was afforded by the velocity field available. Yet this approach was problematic in deriving return point locations, as in some flows the 'centreline' had already been deflected significantly before returning to the source height. Consequently, return point location and dilution data were obtained by finding the point of minimum dilution on the horizontal line at source height.

2.1.3 Field studies

Studies of the dilution achieved—and spatial area occupied—by discharges from installed desalination plants are complex, time-consuming and expensive. In addition, their results can be hard to interpret, since many factors that are controlled within the laboratory environment can be both spatially and temporally variable. Ocean currents are the primary variable in this regard; however temperature, stratification and plume or layer re-entrainment can all be significant. As a result, such studies are rare.

Near-field dilution rates from 60° inclined negatively buoyant jets discharging waste from the Perth Seawater Desalination Plant were studied by Marti *et al.* (2010). This plant operated at a nominal 40% recovery rate, and on the three field-sampling days the discharge density was 1.57%, 2.41% and 2.34% above the ambient density.

Conductivity-Temperature-Depth (CTD) profiling was conducted in conjunction with routine plant maintenance so that one-third and two-third flowrate regimes could be tested along with full (or normal) flowrate. Depth and dilution of the bottom layer were calculated directly from vertical salinity profiles, while concentrated profiling near each diffuser source allowed the estimation of impact-point dilution. Flow trajectory data could not be accurately determined using these CTD drop-probes, and as such were considered to be of secondary importance.

Marti *et al.* compared their dilution and bottom-layer-thickness results to the scaling arguments given by Roberts *et al.* (1997). They found that for $F_0 = 23.8$, while the thickness of the layer was underestimated the plume dilution was as-predicted. However, for $F_0 < 20$, dilution rates and layer thickness were significantly greater than predicted by extrapolation of the Roberts *et al.* results, indicating "some effect of source volume flux".

The only other similar field study found was that of Randall (1981). Randall used CTD probes to plot vertical salinity profiles and isohaline contours for the area surrounding a *vertical* discharge. The maximum vertical extent was found to be 2.3% greater than predicted by the equations of Tong & Stolzenbach (1979) on the first day of near-field measurements (with $U_0/U_a = 22.5$), and 16.4% less than predicted on the second day (with $U_0/U_a = 68.0$). The thickness of the bottom layer was not discussed; however they comment that "the vertical extent of the plume was confined to the lower third of the water column".

2.1.4 Data summary

Parameters such as maximum edge height (z_{me}) and return-point dilution ($\frac{C_0}{C_{m,or}}$) have been shown to be accurately described by dimensionless coefficients that hold true provided the flow is fully turbulent. For example, maximum edge height was given by Zeitoun *et al.* (1970) to be $\frac{z_{me}}{d \cdot F_0} = 2.04$ for a negatively-buoyant jet inclined at 60° from the horizontal. Thus, a designer need only to substitute in the desired values for F_0 and d to find the corresponding absolute edge height (z_{me}) at that inclination.

Tables 2.1–2.5 list the experimental geometric and dilution coefficients given in the works surveyed in Section 2.1 for 15°, 30°, 45°, 60° and 75° inclined negatively buoyant jets. Where impact point coefficients were presented, these have been assumed to be equivalent to return point coefficients. Also given are equivalent coefficients derived from predictions by the models CorJet and VISJET, and by the analytical model developed in Kikkert *et al.* (2007). Section 5.4 will plot these results against those of the present study and discuss the extent of coefficient variability.

Table 2.6 (found on page 38) summarises key experimental conditions from the aforementioned workers, such as recording times and boundary proximity. Few authors explicitly stated boundary proximity in appropriate non-dimensional terms, and therefore these data have generally been calculated from information provided in each respective article. Only three authors for which boundary proximity is known (Lai, 2010; Marti *et al.*, 2010; Papakonstantis *et al.*, 2011b) collected data at source heights greater than the bottom layer thickness measured by Roberts *et al.* (1997). Boundary proximities vary widely, and no standard distance has been employed. No author has rigorously investigated and characterised the effect of bottom-boundary interaction, and thus it is difficult to compare the experimental coefficients given in Tables 2.1–2.5 with certainty. This highlights the need for a "base case" experimental dataset in which the source height is sufficiently large to avoid boundary interaction effects at the return point.

2.2 Modelling

As mentioned at the beginning of this chapter, there are two major categories of models employed by researchers to predict the behaviour of negatively buoyant jets. These are described below.

2.2.1 Integral models

Integral models are sets of simultaneous equations for bulk parameters of the flow—dilution, spread rate, velocity and such like—that are solved for the entire trajectory of the flow. These equations attempt to replicate in some manner the physical behaviour of buoyant jets.

In the average, cross-sectional profiles of velocity and dilution in turbulent flows do not have abrupt edges. Rather, recorded values tend gradually to zero. Typically such cross-sections can be characterised by Gaussian distributions, which in theory never reach zero anywhere. Thus in order to more easily represent turbulent buoyant jets mathematically, uniform values of density, velocity and concentration may be assumed across each cross-section: a technique referred to as *top-hat* modelling. The radial width of these cross-sections is then chosen such that momentum and volume fluxes are matched with those of the equivalent Gaussian distributions. True Gaussian distributions can be back-calculated after the model solution has been obtained, using appropriate conversion factors (see Section 3.3.1). Whether top-hat modelling is used or Gaussian relationships used directly, numerical solutions are typically employed for such models,

Table 2.1: 15° empirical coefficients

	$x_m/(d\,F_0)$	$z_m/(d\,F_0)$	$z_{me}/(d\,F_0)$	S_m/F_0	$x_r/(d\,F_0)$	S_r/F_0	$x_{re}/(d\,F_0)$
Lane-Serff *et al.* (1993)			0.57 ± 0.08				
Nemlioglu & Roberts (2006)			0.68		2.4	1.4	
Kikkert *et al.* (2007) LA data	1.30	0.22	0.57		2.30		
Kikkert *et al.* (2007) LIF data	1.50	0.26	0.60		2.59		
Lai (2010)				0.27 ± 0.01		0.42 ± 0.03	
VISJET (data from Lai, 2010)	1.19	0.21		0.24		0.44	
CorJet (data from Jirka, 2008)	1.18	0.20	0.52	0.21	1.90	0.39	
Kikkert *et al.* (2007) Analytical Model	1.28	0.23	0.54	0.25	2.41		

Table 2.2: 30° empirical coefficients

	$x_m/(d\,F_0)$	$z_m/(d\,F_0)$	$z_{me}/(d\,F_0)$	S_m/F_0	$x_r/(d\,F_0)$	S_r/F_0	$x_{re}/(d\,F_0)$
Zeitoun *et al.* (1970)			1.15	0.36			3.48
Lane-Serff *et al.* (1993)			1.10 ± 0.11				
Lindberg (1994)	2.39 ± 0.32		1.27 ± 0.17				
Bloomfield & Kerr (2002)			1.19				
Otranto (2004)			1.01				4.35
Cipollina *et al.* (2005)	1.95	0.79	1.08		3.03		
Nemlioglu & Roberts (2006)			1.4		3.3	1.9	
Kikkert *et al.* (2007) LA data	1.79	0.60	1.06		3.17		
Kikkert *et al.* (2007) LIF data	1.86	0.69	1.20				
Shao & Law (2010) $0.10 \leq H_0/L_M \leq 0.15$	1.70	0.66	1.05	0.62	2.88	1.18	
Shao & Law (2010) $H_0/L_M > 0.15$	1.54			0.66	3.00	1.45	
Lai (2010)	1.94	0.65	0.95	0.40 ± 0.01	3.17		
VISJET (data from Lai, 2010)	1.51	0.56		0.31		0.65	
CorJet (data from Jirka, 2008)	1.48	0.56	0.95	0.27	2.53	0.56	
Kikkert *et al.* (2007) Analytical Model	1.72	0.63	1.07	0.34	2.96	0.68	

Table 2.3: 45° empirical coefficients

	$x_m/(d\,F_0)$	$z_m/(d\,F_0)$	$z_{me}/(d\,F_0)$	S_m/F_0	$x_r/(d\,F_0)$	S_r/F_0	$x_{re}/(d\,F_0)$
Bosanquet *et al.* (1961)	2.68	1.67					
Zeitoun *et al.* (1970)			1.43	0.42			3.33
Lane-Serff *et al.* (1993)			1.77 ± 0.20				
Lindberg (1994)	1.86 ± 0.25		1.57 ± 0.21				
Bloomfield & Kerr (2002)			1.76				
Ferrari & Querzoli (2004)		1.22			3.23		
Otranto (2004)			1.54				3.76
Cipollina *et al.* (2005)	1.8	1.17	1.61		2.82		
Nemlioglu & Roberts (2006)			2.0		3.2	1.7	
Kikkert *et al.* (2007) LA data	1.86	1.09	1.71		3.31		
Kikkert *et al.* (2007) LIF data	2.01	1.21	1.78				
Papakonstantis *et al.* (2007)			1.45				
Papakonstantis *et al.* (2011a)	2.03 ± 0.13		1.58 ± 0.03				3.78 ± 0.16
Papakonstantis *et al.* (2011b)		1.17		0.52 ± 0.05	3.16	1.55 ± 0.14	
Shao & Law (2010) $H_0/L_M \geq 0.05$	1.69	1.14	1.47	0.46	2.83	1.26	
Lai (2010)	2.08	1.18	1.57	0.45 ± 0.05	3.32	1.09 ± 0.05	
VISJET (data from Lai, 2010)	1.58	1.00		0.32		0.78	
CorJet (data from Jirka, 2008)	1.51	0.99	1.48	0.28	2.62	0.65	
Kikkert *et al.* (2007) Analytical Model	1.89	1.14	1.66	0.41	3.05	0.96	

Table 2.4: 60° empirical coefficients

	$x_m/(d\,F_0)$	$z_m/(d\,F_0)$	$z_{me}/(d\,F_0)$	S_m/F_0	$x_r/(d\,F_0)$	S_r/F_0	$x_{re}/(d\,F_0)$
Zeitoun *et al.* (1970)			2.04	0.56			3.28
Roberts & Toms (1987)			2.08 for $F_0 > 20$	0.38 for $F_0 > 25$		1.03 for $F_0 > 12$	
Lane-Serff *et al.* (1993)			2.33 ± 0.34				
Lindberg (1994)	1.82 ± 0.24		2.16 ± 0.29				
Roberts *et al.* (1997)			2.2[a]		2.4	$1.6 \pm 12\%$	
Bloomfield & Kerr (2002)			2.32[b]				
Ferrari & Querzoli (2004)		1.68			2.78		
Otranto (2004)			2.07				3.51
Cipollina *et al.* (2005)	1.42	1.77	2.32		2.25		
Nemlioglu & Roberts (2006)			2.85		3.25	1.7	
Kikkert *et al.* (2007) LA data	1.66	1.60	2.28		2.78		
Kikkert *et al.* (2007) LIF data	1.80	1.76	2.45				
Papakonstantis *et al.* (2007)			1.99				
Papakonstantis *et al.* (2011a)	1.83 ± 0.08		2.14 ± 0.04				3.57 ± 0.10
Papakonstantis *et al.* (2011b)		1.68		0.56 ± 0.05	2.75	1.68 ± 0.10	
Marti *et al.* (2010)						1.72[c]	
Lai (2010)	1.76	1.62	2.06	0.44 ± 0.05	2.81	1.06 ± 0.03	
VISJET (data from Lai, 2010)	1.34	1.43		0.29		0.82	
CorJet (data from Jirka, 2008)	1.24	1.38	1.93	0.27	2.23	0.69	
Kikkert *et al.* (2007) Analytical Model	1.8	1.7	2.27	0.45	2.72	1.27	

[a] Includes riser height
[b] 62° source inclination
[c] Minimum of three recorded impact dilutions

Table 2.5: 75° empirical coefficients

	$x_m/(d\,F_0)$	$z_m/(d\,F_0)$	$z_{me}/(d\,F_0)$	S_m/F_0	$x_r/(d\,F_0)$	S_r/F_0	$x_{re}/(d\,F_0)$
Lane-Serff *et al.* (1993)			2.82 ± 0.53				
Bloomfield & Kerr (2002)			2.59				
Ferrari & Querzoli (2004)		1.91			1.66		
Nemlioglu & Roberts (2006)			3.0		1.9	1.8	
Kikkert *et al.* (2007) LA data	1.01	1.90	2.57				
Papakonstantis *et al.* (2007)			2.32				
Papakonstantis *et al.* (2011a)	1.15 ± 0.05		2.48 ± 0.07				2.42 ± 0.18
Papakonstantis *et al.* (2011b)		1.93		0.51 ± 0.02	1.80	1.67 ± 0.15	
VISJET (data from Lai, 2010)				0.23			
CorJet (data from Jirka, 2008)	0.73	1.65	2.19	0.25	1.29	0.69	
Kikkert *et al.* (2007) Analytical Model	1.36	2.23	2.84	0.48	1.88	1.57	

providing the flexibility of being able to implement location-dependant adjustments.

While integral models do not and cannot capture all of the physical detail in these flows, they are valuable because of their simplicity and calculation speed. On modern computers solutions may be obtained almost instantly. *Analytical solutions* are a sub-category of integral models where the solutions are kept simple enough to be integrated directly. Such solutions allow quick and accurate investigation of results for a wide range of input parameters. For instance, analytical solutions were developed by Kikkert *et al.* (2007) to model negatively-buoyant jets.

A number of generic integral models are available as commercial software packages. Foremost among these are CorJet (Jirka, 2004) and VISJET (Lee *et al.*, 2000), which are applicable to a wide variety of turbulent jets and plumes, and are calibrated against extensive sets of experimental data.

To date, integral models applied to negatively-buoyant jets have all made the assumptions of flow axisymmetry and self-similarity in their development. These assumptions have been shown to be good assumptions in the context of positively-buoyant jets. The only notable exception is the axially-asymmetric vortex-pair structure formed in strongly-advected buoyant flows; however as these flows remain self-similar, top-hat models must only employ differing conversion factors to make effective predictions. Yet, the works surveyed in Section 2.1 provide overwhelming evidence that negatively-buoyant flows are substantially *asymmetric* along their trajectory axis, and *do not* remain self-similar. Indeed, it is not clear what mathematical distribution inner-side profiles follow, if any.

Jirka (2008) compared CorJet predictions for negatively buoyant jets at various inclinations on a flat seabed to experimental results from Zeitoun *et al.* (1970); Roberts & Toms (1987); Roberts *et al.* (1997); Zhang & Baddour (1998) and Cipollina *et al.* (2005). After deducing that CorJet appeared to be "reasonably validated with available experimental data sources", this model was applied to the entire range of discharge angles ($0 \leq \theta_0 \leq 90$), with a range of bottom slopes ($0 \leq \theta_B \leq 30$). Trajectory and impact-point dilution plots were presented, and Jirka concluded that discharge angles (θ_0) in the range of 30–45° appeared preferable as a *de facto* design recommendation. Nevertheless, Jirka notes:

> "Given the paucity of reliable experimental data (notably dilution measurements) for the entire negatively buoyant jet including sloping bottom interaction, the above recommendations are considered preliminary. To further corroborate them, a vigorous program of experimental studies using modern field-resolving techniques, such as LIF and particle image velocimetry (PIV), supported by detailed computational fluid mechanics (CFD) modelling, is called for in several laboratories. This appears crucial in view of ongoing design and siting activities for numerous new desalination plants all around the globe."

While integral models have typically predicted geometric properties with reasonable accuracy, dilution rates have been more problematic. Indeed, difficulties associated with employing

models developed for positively buoyant discharges to predict the behaviour of negatively buoyant discharges were noted more than thirty-five years ago by Anderson *et al.* (1973), in studying inclined negatively buoyant jets in a crossflow. Anderson *et al.* found that the "drag coefficient" (C_d) used to model positively buoyant jets had to be made zero in order to satisfactorily model negatively buoyant jets.

Although it may not be necessary to abandon the (incorrect) assumptions of self-similarity and axisymmetric mean profiles—particularly in the top-hat formulation stage—it is essential that models are developed in such a manner that recognises the physical processes within negatively buoyant jets are significantly different to those in positively buoyant jets. Comprehensive validation with reliable experimental data is a crucial part of such a process.

2.2.2 CFD simulations

A much more fundamental approach to modelling turbulent jets is to numerically model—or solve—the Navier–Stokes equations. These are continuous equations describing the motion of any Newtonian fluid in three dimensions, which can be discretised onto regular or irregular grids so as to be suitable for computational evaluation. For most applications the Navier-Stokes equations must be approximated by way of some collection of assumptions in order to be economically feasible to solve in the desired timeframe. Generally this involves employing *turbulence models* to represent the effect of small-length-scale turbulence on larger-scale, directly simulated, turbulence (Large Eddy Simulation; LES) or to estimate the Reynolds stress tensor in time-averaged formulations of the Navier Stokes equations. The latter category, termed RANS (Reynolds Averaged Navier Stokes) models, includes the k-ε turbulence model; arguably the most common of turbulence models. Even such steady-state solutions provide significantly more detail than integral modelling approaches.

CFD simulations of vertical fountains have been performed by various authors (Wada *et al.*, 1977; Brzoska *et al.*, 2000, *etc.*). Petersen & Larsen (1998) performed vertical fountain simulations with a non-stagnant ambient.

Vafeiadou *et al.* (2005) carried out CFD simulations of negatively-buoyant jets inclined between 45° and 90°. The Shear Stress Transport (SST) turbulence model was adopted, which under such circumstances was essentially a k-ε turbulence model. They employed the commercial software package *ANSYS CFX* with a mesh of 160–400,000 elements, and their results were compared with experimental data from Bloomfield & Kerr (2002) and Roberts *et al.* (1997). Based on the limited data available they concluded that their numerical results were mostly in agreement with laboratory experiments, and that this agreement supports the use of such models to predict the behaviour of inclined negatively buoyant discharges.

Seil & Zhang (2010) modelled single- and multi-port inclined discharges in the near field and in their transition to bottom layer flows using SST and Renormalization Group (RNG) turbulence models. They employed the *ANSYS FLUENT* commercial software package. Predictions

for dilution rates on the seabed created by a single-port discharge were compared against the experimental results of Roberts *et al.* (1997) and Nemlioglu & Roberts (2006), and were found to be conservative in the range $0 \leq x/(d\,F_0) \leq 7$. Qualitative concentration contour images were presented for two multi-port configurations. While quantitative data for these simulations were not presented, the authors comment that, "impact dilutions from the individual jets were in both cases found to be less than for the equivalent single plume."

2.3 Context

This chapter has outlined a significant body of research that has been made on the behaviour of negatively buoyant jets. These studies have provided valuable data and discussed important features of this flow. However, many inconsistencies can be seen in the collected dilution and spatial relationship data (Tables 2.1–2.5). These are particularly apparent in data of minimum dilution at the return point, S_r/F_0, which is simultaneously the most important parameter for field diffuser design. For instance, the return-point dilution given by Nemlioglu & Roberts (2006) for a 15° source inclination was over 200% greater than that given by Lai (2010). Although the popular integral models VISJET and CorJet predict return point dilution for the same inclination to be similar to the value given by Lai (2010), they predict lower dilutions than all other published experimental data at greater inclinations.

The present study aims to conduct a rigorous experimental programme to collect reliable laboratory data on the centre-plane concentration of the negatively buoyant jet, where bottom-boundary distances are sufficiently large to avoid boundary interaction effects at the return point. A non-intrusive technique will be used (LIF), which will enable full two-dimensional field recordings. Long data collection periods will be emphasised. In addition, a new integral model will be developed which attempts to more closely emulate the physical flow conditions of this jet. The focus will be kept intentionally narrow (no boundary interaction, no moving ambients, no experimental velocity data, *etc.*) with the goal of collecting a trustworthy dataset of these basic and fundamental conditions, upon which other broader research can be built.

Table 2.6: Experimental conditions

Worker(s)	Experimental technique	Inclinations	Froude numbers	Recording times	Boundary proximity
Bloomfield & Kerr (2002)	Shadowgraphs	30–90°	Unknown	Unknown	Unknown but their Figure 2d shows significant boundary interaction for a 80° discharge, and thus boundary interaction at other angles is highly likely.
Bosanquet *et al.* (1961)	LA; trajectory only	45°	32.8	Instantaneous images presented (their Figure 6) are starting plumes and it appears trajectories were recorded using similar images	Unknown
Cipollina *et al.* (2005)	LA; trajectory only	30°, 45° and 60°	14–216	30 seconds	Not stated but instantaneous image presented (their Figure 1c) shows clear boundary interaction around source height
Ferrari & Querzoli (2004)	LIF	45–90° in 5° steps	8.0, 14.8, 23.8 and 30.8	Unknown	Unknown but boundary interaction expected because of experimental configuration.
Kikkert *et al.* (2007)	LA and LIF	LA: 15°, 30°, 45°, 47°, 60° and 75°; LIF: ten inclinations in 5–65.5° range	LA: 27.3–66.0; LIF: 39.5–78.7	"Typically sampled for a period of 1 min"	"The sources were located above the tank floor, so the layer of dense fluid that formed in this area during the experiment did not interfere with the flow of interest." (no other information available)

Table 2.6: Experimental conditions (continued)

Worker(s)	Experimental technique	Inclinations	Froude numbers	Recording times	Boundary proximity
Lai (2010)	LIF, PIV	15°, 30°, 38°, 45°, 52°, 60° and 90°	10.9–41.1	60 seconds	$H_0/(d\,F_0) = 0.24$–0.92
Lane-Serff *et al.* (1993)	Shadowgraphs and conductivity probes	15°, 30°, 45°, 60° and 75°	Unknown	Unknown	"[Tank] dimensions were large compared with typical length scales of the flow and so this configuration approximates an infinite, unstratified environment at rest." (no other information provided)
Lindberg (1994)	Shadowgraphs	30°, 45°, 60° and 90°	8.5–120	Unknown but limited	"The water jet was mounted 10cm above the bottom of the tank". Source diameter not stated.
Marti *et al.* (2010)	CTD profiling	60°	8.5, 15.4 and 23.8	N/A	$H_0/(d\,F_0) = 0.32$–0.90
Nemlioglu & Roberts (2006)	LIF	15°, 30°, 45°, 60°, 75° and 90°	21.2–24.1 (one experiment per angle)	Unknown	Not stated but instantaneous and time-averaged images clearly show boundary interaction and formation of bottom layer
Otranto (2004)	Conductivity probe	30°, 45° and 60°	25–50	Unknown	Unknown but boundary interaction expected because of experimental configuration.
Papakonstantis *et al.* (2007)	LA; trajectory only	45°, 60°, 75° and 90°	24.3–53.9	Unknown but their Figure 4 indicates approximately 45 seconds	$H_0/(d\,F_0) = 0.03$–0.07

Table 2.6: Experimental conditions (continued)

Worker(s)	Experimental technique	Inclinations	Froude numbers	Recording times	Boundary proximity
Papakonstantis *et al.* (2011a)	LA; trajectory only	45°, 60°, 75°, 80°, 85° and 90°	7.5–59.2	"Several frames extracted from the video recordings" used to determine spatial coefficients	$H_0/(d\,F_0)$ within range of 0.017–0.22
Papakonstantis *et al.* (2011b)	Conductivity probe	45°, 60° and 75°	18–50	40 seconds "in most cases"	$H_0/(d\,F_0)$ within range of 0.37–1.39
Roberts *et al.* (1997)	LIF and conductivity probe	60°	18.7–35.7	34 seconds	$H_0/(d\,F_0) = 0.30$–0.44
Roberts & Toms (1987)	Fluorometer measurement of vacuum-extracted samples	60°	12.2–26.0	1–2 minutes	$H_0/(d\,F_0) = 0.04$–0.08
Shao & Law (2010)	LIF and PIV	30° and 45°	7.4–32.2	60 seconds	$H_0/(d\,F_0) = 0.05$–0.47
Zeitoun *et al.* (1970)	LA for trajectory measurements; sample extraction for concentration measurements	30°, 45° and 60°	8–57	Five photographs over 10 seconds to determine trajectory	Unknown but boundary interaction expected because of experimental configuration.
Present study	LIF	15°, 30°, 45°, 60°, 70° and 75°	14.9–106.4	100–688 seconds	$H_0/(d\,F_0) = 2.33$–8.07

Chapter 3

Integral Modelling

*"*Mathema'ticks. n. f. *That ſcience which contemplates whatever is capable of being numbered or meaſured; and it is either pure or mixt: pure conſiders abſtracted quantity, without any relation to matter; mixt is interwoven with phyſical conſiderations"*
Johnson (1766)

Integral modelling of turbulent buoyant jets involves, at a minimum, conservation of three properties: volume, mass and momentum. For some arbitrary control volume CV (of volume V) with its surface CS (of area A), we may write

$$\int_{CS} (\vec{u} \cdot \vec{n}) dA = 0 \tag{3.1}$$

$$\frac{\partial}{\partial t}\left[\int_{CV} \rho dV\right] + \int_{CS} \rho(\vec{u} \cdot \vec{n}) dA = 0 \tag{3.2}$$

$$\sum \vec{F} = \int_{CS} \vec{u}\rho(\vec{u} \cdot \vec{n}) dA + \frac{\partial}{\partial t}\left[\int_{CV} \rho \vec{u} dV\right] \tag{3.3}$$

where $\vec{n}$ is the unit vector, ρ is density, $\vec{F}$ is the force vector, and t is time.

If total mass in the control volume under question does not vary with time, the first term in Equation 3.2 vanishes.

Section 1.4.1 discussed the fact that time-averaged cross-sectional velocity and concentration profiles of turbulent jets and plumes are Gaussian in form. While axisymmetric jets and plumes represent two limiting scenarios of turbulent flow generated from a nozzle, other intermediate and limiting flow types may also develop; particularly when the ambient velocity U_a is non-zero. Some of these flow types are not Gaussian in the mean. Top-hat modelling (introduced in Section 2.2.1) has the inherent advantage that governing equations need not change between flow types; instead only the conversions applied to obtain distribution-specific values must be unique.

As discussed in Section 2.1, experiments have suggested that (at least) the outer edge of the

negatively buoyant jet tracer field is Gaussian in the mean. Kikkert (2006) and Lai (2010) found the concentration spread rate ($\frac{db_c}{ds}$) on this outer edge to be constant for 15–45° jets. Kikkert (2006) found this value to be 0.127, while Lai (2010) found it to be 0.123.

All integral modelling must incorporate some representation of flow spreading in order to make proper closure to the governing equations. In some cases this is done by direct specification of the spreading rate $\frac{db}{ds}$, but historically the most common method has been by application of the "entrainment hypothesis" proposed by Morton *et al.* (1956). These researchers made the assumption that "the rate of entrainment at the edge of the plume or cloud is proportional to some characteristic velocity at that height"; such that (in Gaussian terms)

$$\frac{dQ}{ds} = 2\pi b u_{\text{℄}} \alpha \tag{3.4}$$

The parameter α is known as the entrainment coefficient, and was found by Fischer *et al.* (1979) and List (1982) to be equal to 0.0535 for a pure jet and 0.0833 for a pure plume. In a buoyant jet, α follows some transition between these two limiting values.

In the following sections, two prominent integral models used for negatively buoyant jets will be presented and discussed. Both models are based on the entrainment hypothesis. Subsequently a new model will be developed to more accurately take into account the unique behaviour of this flow.

All models will be presented in dimensionless forms, allowing clear identification of governing parameters (such as the initial densimetric Froude number, F_0) and eliminating unnecessary scale-dependence. Variables will be non-dimensionalised using the appropriate initial values for length (d), velocity (U_0), buoyancy ($\hat{g}_0$), volume flux (Q_0), momentum flux (M_0) and buoyancy flux (B_0). These non-dimensional variables will be denoted by a subscript star ($\star$). For clarity, variables will be also be denoted with a subscript g if the corresponding dimensional value is a characteristic of the Gaussian distribution (centreline value, *etc.*), or a subscript T if the variable is a top-hat variable.

3.1 Jirka (2004)

Jirka (2004) presents the fundamental equations used in the modelling software package 'CorJet'. These equations are suitable for buoyant jets with three-dimensional trajectories, issuing into an unbounded, stagnant or moving ambient, with uniform or stable stratification. We will assume here that ambient velocity U_a and ambient density distribution $\frac{d\rho_a}{dz}$ are both zero. Additionally, the horizontal angle σ is set to zero.

The equations for axial momentum flux M and total volume flux Q defined by Jirka are non-dimensionalised as

$$M_\star = 2u_{g\star}^2 b_{g\star}^2, \quad Q_\star = 4u_{g\star} b_{g\star}^2 \tag{3.5}$$

Dimensionless horizontal and vertical momentum fluxes are $M_{H\star} = M_\star \cos\theta$ and $M_{V\star} = M_\star \sin\theta$.

The conservation equations given in section 3.3 of Jirka (2004) for change in volume flux, momentum flux and buoyancy flux with respect to path length, and change in trajectory with respect to path length are simplified and non-dimensionalised as follows:

$$\frac{dQ_\star}{ds_\star} = 8 b_{g\star} u_{g\star} \alpha \tag{3.6}$$

$$\frac{dM_{V\star}}{ds_\star} = \frac{-4}{F_0^2} \lambda^2 b_{g\star}^2 \hat{g}_{g\star} \tag{3.7}$$

$$\frac{dM_{H\star}}{ds_\star} = 0 \tag{3.8}$$

$$\frac{dB_\star}{ds_\star} = 0 \tag{3.9}$$

$$\frac{dx_\star}{ds_\star} = \cos\theta, \quad \frac{dz_\star}{ds_\star} = \sin\theta \tag{3.10}$$

where λ is a constant, equal to 1.20. Reduced gravity $\hat{g}_{g\star}$ is defined as

$$\hat{g}_{g\star} = \frac{B_\star}{Q_{scalar\star}} \tag{3.11}$$

where $Q_{scalar\star} = Q_\star \frac{\lambda^2}{1+\lambda^2}$.

The entrainment coefficient, α, is defined in Equation (20) of Jirka (2004) as

$$\alpha = \alpha_1 + \alpha_2 \frac{\sin(-\theta)}{F_{Lg\star}^2 F_0^2} \tag{3.12}$$

The constants α_1 and α_2 are equal to 0.055 and 0.6 respectively. The local Froude number, $F_{Lg\star}$, is

$$F_{Lg\star} = \frac{u_{g\star}}{\sqrt{\hat{g}_{g\star} b_{g\star}}} \tag{3.13}$$

It can be shown that in the plume region ($\theta = -90°$), $F_{Lg\star}$ tends to

$$\frac{F_{\ell p}}{F_0} = \frac{\sqrt{\frac{\frac{5}{4}\lambda^2 - \alpha_2}{\alpha_1}}}{F_0} \approx \frac{4.67}{F_0} \tag{3.14}$$

denoted as $F_{Lp,g\star}$. Hence, in the pure plume region $\alpha = \alpha_1 + \frac{\alpha_2}{F_{\ell p}^2} = 0.0825$. In the jet region, $F_{Lg\star}$ is large, so that $\alpha \approx \alpha_1 = 0.055$. Of course, when θ is zero, α is always equal to α_1.

It is interesting to note that the ratio of entrainment coefficients $\alpha_{plume}/\alpha_{jet}$ is 1.5, which is

lower than the 5/3 derived theoretically in Wood *et al.* (1993) using the assumption of a constant spreading rate ($\frac{db_{g\star}}{ds_\star}$). Analysis of the spreading rates generated in jet and plume regions of the current model supports this difference. Even so, the current α_{jet} and α_{plume} coefficients are similar to those derived by other researchers (such as Fischer *et al.* (1979) and List (1982) who found $\alpha_{jet} = 0.0535$ and $\alpha_{plume} = 0.0833$).

Jirka discusses the fact that for a vertical fountain $\alpha \leq \alpha_1$, because $\sin(-\theta) = -1$ in the region before reversal. He states that this is because "work is being done against gravity", and cites two previous models which employ the same assumption. Nevertheless, in this section the local Froude number also tends to zero ($\lim_{z \to z_m} F_{Lg\star} = 0$), simply because $u_{g\star}$ tends to zero. Thus, the limit at the reversal point is $\alpha = -\infty$. In other words, the flow *detrains* all of its fluid, and Q goes to zero. Essentially, the flow disappears.

In order to avoid such a model collapse, Jirka applies a linear transition to α between the points $(F_{Lg\star}^2 F_0^2)/\sin\theta = F_{\ell p}^2$ and $(F_{Lg\star}^2 F_0^2)/\sin\theta = -F_{\ell p}^2$ (corresponding to $\alpha = 0.0825$ and $\alpha = 0.0275$ respectively), as shown in Figure 3.1. By not allowing α to become negative, $\frac{dQ_\star}{ds_\star}$ is also not allowed to become negative. This can be seen by substituting Equation 3.5 into Equation 3.6,

$$\frac{dQ_\star}{ds_\star} = \sqrt{32 M_\star}\,\alpha \tag{3.15}$$

and considering that for a fountain, total momentum ($M_\star$) is zero at the reversal point and positive everywhere else.

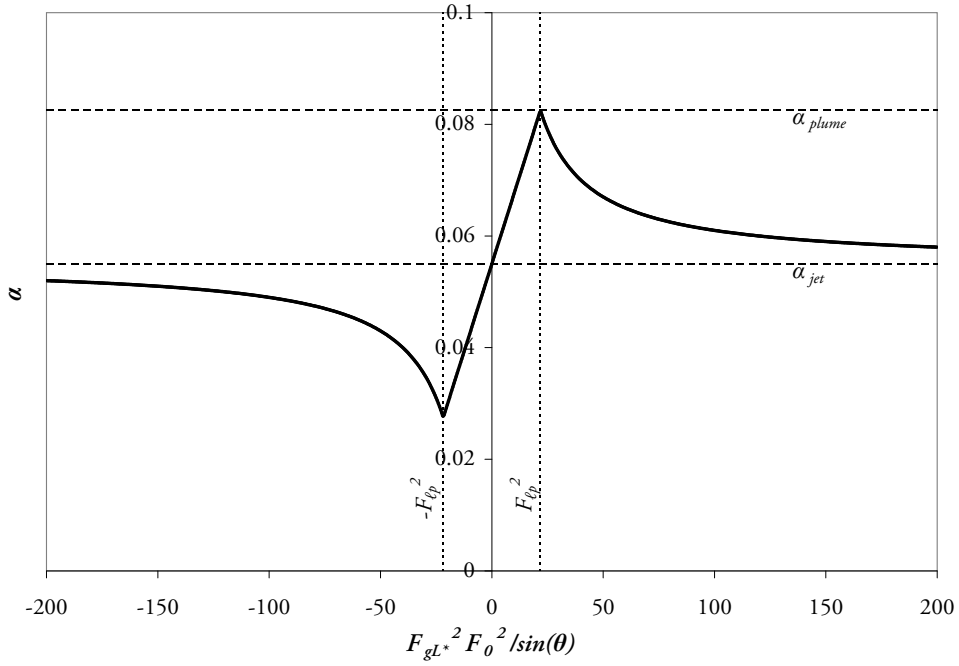

Figure 3.1: Entrainment coefficient used in Jirka (2004), and as defined in Equation 3.16

Therefore the complete equation for entrainment rate becomes

$$\alpha = \begin{cases} \left(\alpha_1 + \alpha_2 \frac{\sin(-\theta)}{F_{Lg\star}^2 F_0^2}\right) & \text{if} \quad |(F_{Lg\star}^2 F_0^2)/\sin\theta| \geq F_{\ell p}^2 \\ \frac{F_{Lg\star}^2 F_0^2}{\sin(-\theta)} \cdot \frac{\alpha_2}{F_{\ell p}^4} + \alpha_1 & \text{if} \quad F_{\ell p}^2 \leq (F_{Lg\star}^2 F_0^2)/\sin\theta \leq F_{\ell p}^2 \end{cases} \tag{3.16}$$

Initial values for the model are $x_\star = L_{e\star}\cos\theta_0$, $z_\star = L_{e\star}\sin\theta_0$, $M_{V\star} = \sin\theta_0$), $M_{H\star} = \cos\theta_0$, $Q_\star = \sqrt{2}$ and $B_\star = 1$; where $L_{e\star} = 5\left(1 - e^{-2F_0/F_{\ell p}}\right)$.

Because $B_\star = 1$ everywhere (see Equation 3.9), $\hat{g}_{g\star}$ can be redefined as

$$\hat{g}_{g\star} = \frac{1+\lambda^2}{Q_\star \lambda^2} \tag{3.17}$$

It is helpful to note that Jirka defines also a tracer volume flux parameter, Q_c. Under the same assumptions as given above, this parameter renders an equation for tracer concentration, $c_{g\star}$, equal to that given for $\hat{g}_{g\star}$ in Equation 3.17.

3.1.1 Discussion

3.1.1.1 Model verification

The above integral model was coded in Python and numerically integrated with the SciPy odeint library. Solutions were checked against the pure jet, pure plume and horizontal buoyant jet results plotted in Figures 4–7 & 11-12 of Jirka (2004), and in all cases were found to match accurately. Jirka (2008) presented trajectory and dilution coefficients for CorJet specific to negatively buoyant jets, and comparisons with these results are shown in Figures 3.2 and 3.3 respectively. The present implementation matches closely for z_m, x_m and x_r, although the latter two show small discrepancies at low source inclinations. This may be due to differences in the numerical integration system, or otherwise due to additional adjustments made in the CorJet software that have not been clearly explained in Jirka (2004).

Of more concern is the z_{me} coefficient, which is similar in magnitude for the inclination range shown (15–75°), but becomes increasingly different as θ_0 tends to 90°. In the present implementation, for large source inclinations the flow width (b) increases rapidly near the point of maximum height, leading z_{me} to increase rapidly also. This behaviour is plotted in Figure 3.4. Although the corrections to the entrainment coefficient α outlined earlier (see Equation 3.16) enabled Q to not *decrease* in value as $F_{Lg\star}$ went to zero, total momentum $M_\star$ is zero at the reversal point of a 90° jet, so spread $b_{g\star} = Q_\star/\sqrt{8M_\star}$ goes to infinity. It is true that due to the nature of vertical fountains, modelling assumptions become invalid at 90°inclinations; yet a similar but less pronounced effect also occurs for other source inclinations less than 90°. It is assumed that the CorJet package employs some special post-processing treatment of this behaviour, as other trajectory data match well.

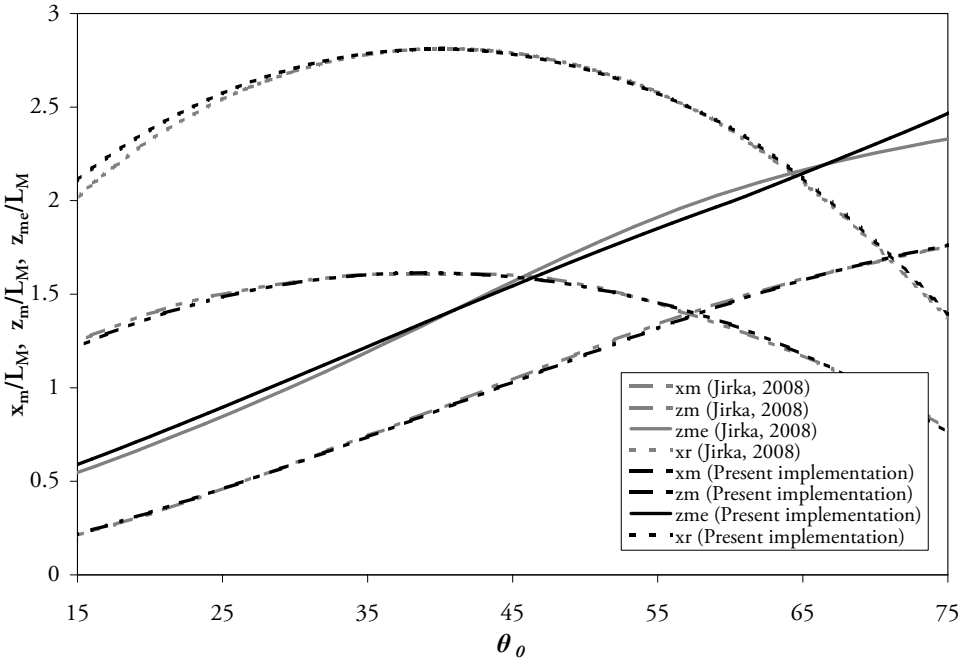

Figure 3.2: Trajectory coefficients for CorJet (from Jirka, 2008) and present implementation of Jirka (2004) model. z_{me} is defined as the $\hat{g}/\hat{g}_{cl} = 3\%$ contour. Length scale L_M is equal to $(\pi/4)^{1/4} dF_0$

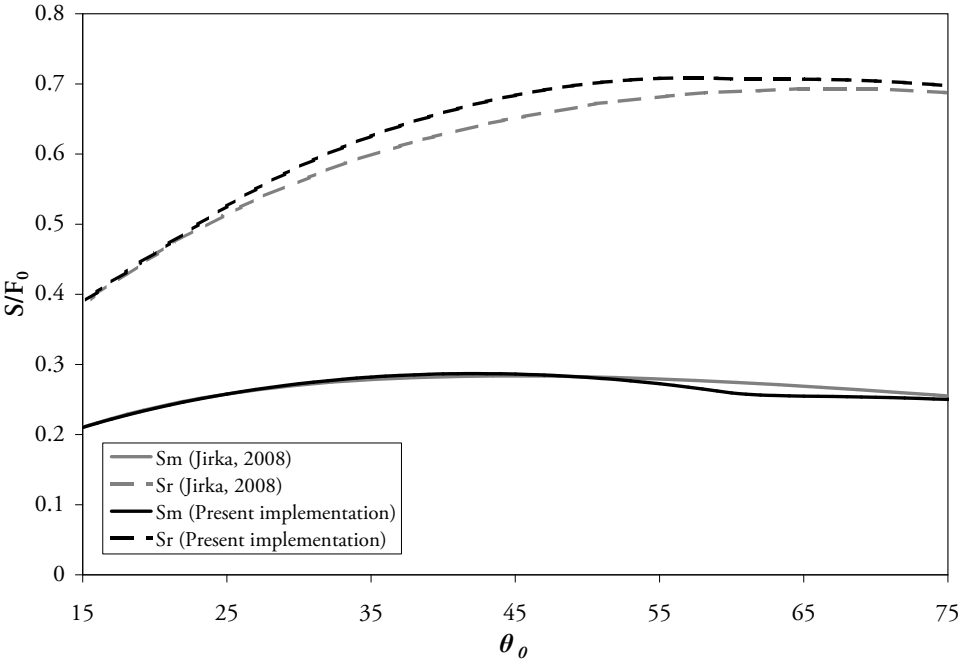

Figure 3.3: Dilution coefficients for CorJet (from Jirka, 2008) and present implementation of Jirka (2004) model

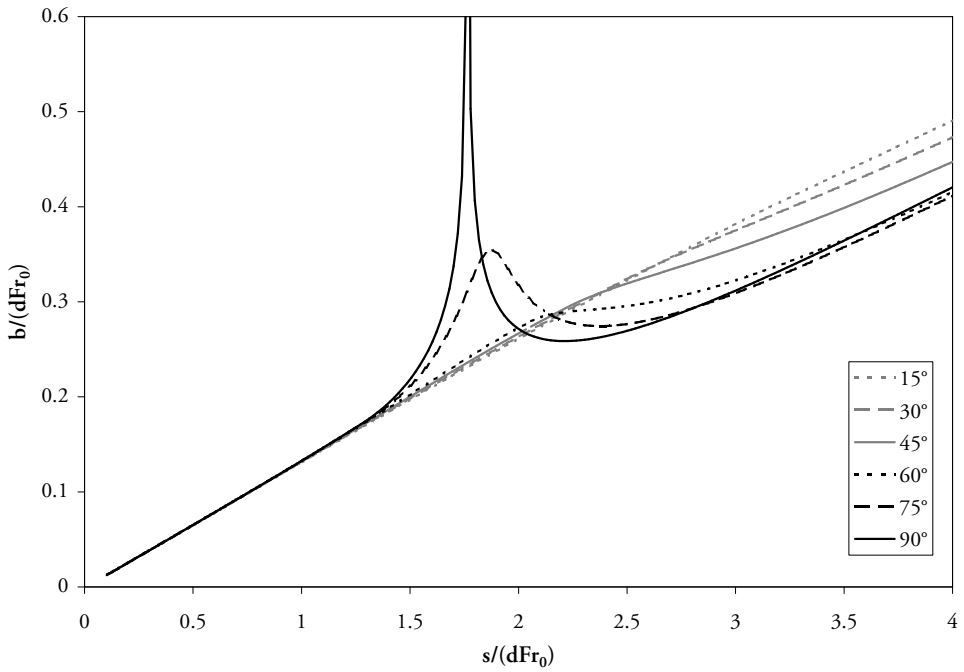

Figure 3.4: Spread as a function of path length for present implementation of Jirka (2004) model

Dilution results (Figure 3.3) are likewise similar, although return-point values show greater discrepancies for moderate inclinations. Jirka (2004) gives a point value for dilution at the reversal point of a fountain, and this value matches exactly. Nevertheless, it also gives a point value for dilution at maximum height of a 60° jet of $S_m/F_0 = 0.29$, which differs by 12% from the value generated by the present implementation of $S_m/F_0 = 0.259$. It is unclear whether this is simply a typographical error.

3.1.1.2 Form of entrainment coefficient equation

At first inspection the $\sin(-\theta)$ term in the unadjusted entrainment coefficient equation (Equation 3.12) may seem inappropriate if a constant spread rate is to be desired for the negatively buoyant jet, after the data of Kikkert (2006) and Lai (2010) discussed earlier. However, the form of this equation can be shown to be the correct form to generate linear spread rates throughout the trajectory of the flow.

By rearranging Equation 3.5, we can write

$$Q_\star = b_{g\star}\sqrt{8M_\star}$$

Differentiating this equation with respect to $s_\star$ and substituting $\frac{dM_\star}{ds_\star} = \sin\theta\frac{dM_{V\star}}{ds_\star}$, we have

$$\frac{dQ_\star}{ds_\star} = \frac{dQ_\star}{db_{g\star}}\frac{db_{g\star}}{ds_\star} + \frac{dQ_\star}{dM_\star}\frac{dM_\star}{ds_\star}$$

$$= \sqrt{8M_\star}\frac{db_{g\star}}{ds_\star} + \frac{\sqrt{2}b_{g\star}}{\sqrt{M_\star}} \cdot \sin\theta \frac{dM_{V\star}}{ds_\star}$$

Setting the spread rate to be a constant throughout the flow, $\frac{db_{g\star}}{ds_\star} = k$, we can derive

$$\frac{dQ_\star}{ds_\star} = \sqrt{8M_\star}k + \frac{\sin\theta}{u_{g\star}} \cdot \frac{dM_{V\star}}{ds_\star} \tag{3.18}$$

Equating this with Equation 3.6, we have

$$\alpha = \frac{1}{8b_{g\star}u_{g\star}}\left(\sqrt{8M_\star}k + \frac{\sin\theta}{U_\star} \cdot \frac{dM_{V\star}}{ds_\star}\right)$$

Finally, by substituting Equation 3.7 and simplifying we obtain

$$\alpha = \frac{k}{2} - \frac{\lambda^2 \sin\theta}{2F_{Lg\star}^2 F_0^2} \tag{3.19}$$

which is the same as Equation 3.12 with $\alpha_1 = k/2$ and $\alpha_2 = \lambda^2/2$.

Therefore, in order to generate a constant spread rate for the initial region of a vertical fountain, α must drop below α_{jet}, and in the limit as $z \to z_m$, tend to $-\infty$. Such behaviour is instructive for any integral modelling of negatively buoyant jets that involves the use of an entrainment coefficient: if a constant spread rate is desired, then α must be allowed to drop below α_{jet} ; particularly for steep angles ($\theta \to \frac{\pi}{2}$).

Nevertheless, as outlined earlier, allowing α to tend to $-\infty$ in a vertical fountain drives $Q_\star$ to zero. In turn, spread $b_{g\star} = Q_\star/\sqrt{8M_\star}$ becomes zero, meaning $\frac{dM_{V\star}}{ds_\star}$ becomes zero, and hence the flow ceases to move anywhere.

This scenario is directly addressed in Jirka (2004) by not allowing α to drop below 0.0275, as is seen in Figure 3.5. However, no other adjustment is made to the system of equations.

After the central flow of a fountain has reversed direction, it falls back around that core. As a result, not only does the flow re-entrain itself, but the conservation of mass and momentum equations are also significantly complicated, since fluid is now flowing in two distinct directions. As such, the equations of Jirka (2004) are invalid when applied to a vertical fountain and any other steeply-inclined negatively buoyant jet where experimental analysis shows that falling fluid is re-entrained by the initial jet region. Yet analysis of model results in this extreme case helps to highlight issues that affect predictions at other more moderate inclinations.

3.2 Papanicolaou *et al.* (2008)

Papanicolaou *et al.* (2008) presented Gaussian and top-hat integral models for negatively-buoyant

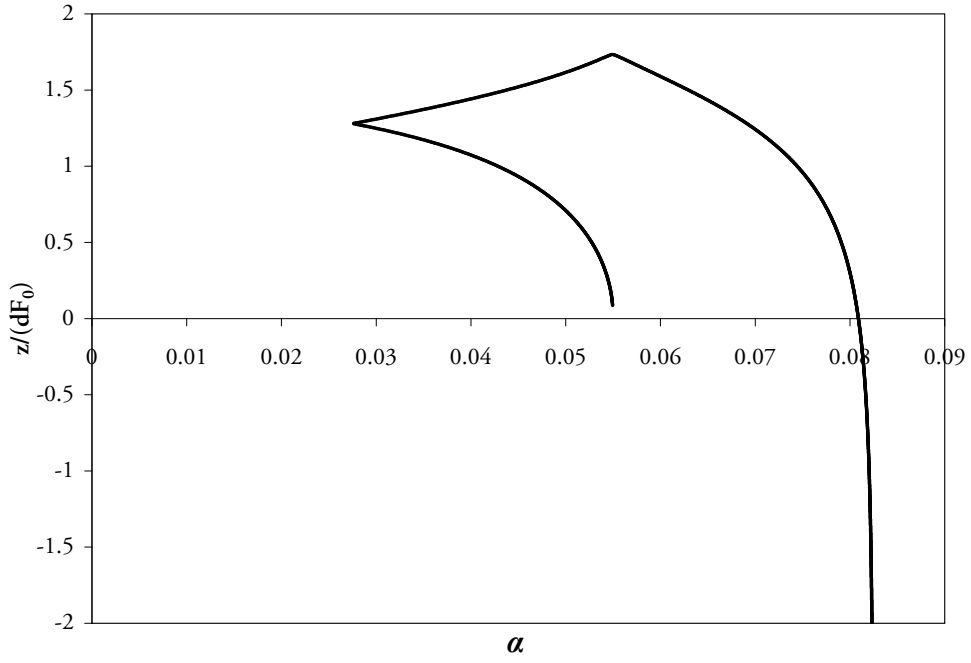

Figure 3.5: Jirka (2004) entrainment coefficient α for vertical fountain against vertical height

jets, and compared their predictions using various jet entrainment coefficient values (α_{jet}) to experimental flow-edge measurements and dilution measurements at the maximum centreline and return point locations. Although their top-hat model was presented as an alternative formulation of the same governing equations, top-hat and Gaussian model predictions were significantly different. The respective equations are presented below in non-dimensional form, and a discussion of results and their discrepancies will follow.

3.2.1 Gaussian model

Axial momentum flux $M_\star$, volume flux $Q_\star$ and buoyancy flux $B_\star$ are defined by Papanicolaou *et al.* as

$$Q_\star = 4u_{g\star}b_{g\star}^2, \quad M_\star = 2u_{g\star}^2 b_{g\star}^2, \quad B_\star = 4\hat{g}_{g\star}u_{g\star}b_{g\star}^2\frac{\lambda^2}{1+\lambda^2} \tag{3.20}$$

from which we may derive

$$u_{g\star} = \frac{2M_\star}{Q_\star}, \quad b_{g\star} = \frac{Q_\star}{2^{3/2}\sqrt{M_\star}}, \quad \hat{g}_{g\star} = \frac{B_\star}{Q_\star}\cdot\frac{1+\lambda^2}{\lambda^2} \tag{3.21}$$

The conservation equations given in section 2.1 of Papanicolaou *et al.* (2008) are as follows:

$$\frac{dQ_\star}{ds_\star} = \sqrt{32}\alpha M_\star^{1/2} \tag{3.22}$$

$$\frac{dM_\star}{ds_\star} = -\frac{1+\lambda^2}{2F_0^2}\cdot\frac{Q_\star B_\star}{M_\star}\sin\theta \tag{3.23}$$

$$\frac{d\theta}{ds_\star} = -\frac{1+\lambda^2}{2F_0^2}\cdot\frac{Q_\star B_\star}{M_\star^2}\cos\theta \tag{3.24}$$

$$\frac{dB_\star}{ds_\star} = 0 \tag{3.25}$$

$$\frac{dx_\star}{ds_\star} = \cos\theta, \quad \frac{dz_\star}{ds_\star} = \sin\theta \tag{3.26}$$

where λ is a constant equal to 1.20.

It is worth noting that Equation 3.24 can be developed by taking the derivative of $\theta = \arccos\left(\frac{M_{H\star}}{M_\star}\right)$, leading to

$$\frac{d\theta}{ds_\star} = \frac{1}{\sin\theta}\left(\frac{M_{H\star}}{M_\star^2}\frac{dM_\star}{ds_\star}\right)$$

The entrainment coefficient, α, is defined after Priestley & Ball (1955):

$$\alpha = \alpha_{jet} + (\alpha_{plume} - \alpha_{jet})\left(\frac{R}{R_p}\right)^2 \tag{3.27}$$

where R, the local Richardson number, is

$$R = \frac{Q_\star B_\star^{1/2}}{M_\star^{5/4}}\left(\frac{\pi}{4}\right)^{1/4}\frac{1}{F_0} = \frac{\pi^{1/4}\left(\frac{\lambda^2}{1+\lambda^2}\right)^{1/2}2^{5/4}}{F_{Lg\star}F_0} \tag{3.28}$$

subject to the condition

$$R \leq R_p \tag{3.29}$$

employing the definition of $F_{Lg\star}$ in Equation 3.13; and R_p is the asymptotic plume Richardson number, defined by Papanicolaou *et al.* to be $0.63/1.1^{5/4} \approx 0.56$. The coefficient α_{jet} is a variable (either 0.0545 or 0.030), and the coefficient α_{plume} is equal to 0.0875.

The solution is started with the initial conditions of $x_\star = 3.28\cos\theta, z_\star = 3.28\sin\theta, M_\star = Q_\star = B_\star = 1.0$.

3.2.2 Top-hat model

Axial momentum flux $M_\star$, volume flux $Q_\star$ and buoyancy flux $B_\star$ are defined as

$$Q_\star = 4u_{T\star}b_{T\star}^2, \quad M_\star = 4u_{T\star}^2 b_{T\star}^2, \quad B_\star = 4u_{T\star}\hat{g}_{T\star}b_{T\star}^2 \tag{3.30}$$

from which we may derive

$$u_{T\star} = \frac{M_\star}{Q_\star}, \quad b_{T\star} = \frac{Q_\star}{2M_\star^{1/2}}, \quad \hat{g}_{T\star} = \frac{B_\star}{Q_\star} \tag{3.31}$$

The conservation equations are

$$\frac{dQ_\star}{ds_\star} = 4\alpha_T M_\star^{1/2} \tag{3.32}$$

$$\frac{dM_\star}{ds_\star} = -\frac{B_\star Q_\star}{M_\star F_0^2}\sin\theta \tag{3.33}$$

$$\frac{d\theta}{ds_\star} = -\frac{B_\star Q_\star}{M_\star^2 F_0^2}\cos\theta \tag{3.34}$$

$$\frac{dB_\star}{ds_\star} = 0 \tag{3.35}$$

$$\frac{dx_\star}{ds_\star} = \cos\theta, \quad \frac{dz_\star}{ds_\star} = \sin\theta \tag{3.36}$$

where the entrainment coefficient, α_T, is the same as α in Equation 3.27, except with a modified α_{jet} value. R, the local Richardson number, is

$$R = \frac{Q_\star B_\star^{1/2}}{M_\star^{5/4}}\left(\frac{\pi}{4}\right)^{1/4}\frac{1}{F_0} = \frac{\pi^{1/4}}{F_{LT\star}F_0} \tag{3.37}$$

subject to the condition

$$R \leq R_p \tag{3.38}$$

R_p is the same as used in the Gaussian formulation, and $F_{LT\star}$ is equal to

$$F_{LT\star} = \frac{u_{T\star}}{\sqrt{\hat{g}_{T\star} b_{T\star}}} \tag{3.39}$$

The solution is started with the initial conditions of $x_\star = z_\star = 0$, $M_\star = Q_\star = B_\star = 1$.

3.2.3 Discussion

Papanicolaou *et al.* (2008) present plots of model results and experimental data for maximum edge height (z_{me}) and the horizontal distance to the outer edge of the flow at the source height (x_{re}). Top-hat modelling generally provided better predictions for these parameters than Gaussian modelling; a fact that the authors stated "does not generally agree with the findings in positively buoyant jets". This was the case regardless of whether a constant or variable λ value was

used. The authors argue that this may be because reduced gravity, acting "out of phase" with velocity—*i.e.* in the opposite direction to velocity—*decelerates* the jet 'core'. This in turn would reduce the shear stress between the jet and the ambient fluid, and thus create a more 'uniform' velocity distribution that was closer to top-hat than to Gaussian.

Such an argument finds support in the observations of flow 'asymmetry' noted by many authors. If indeed velocity and density cross-sections were non-Gaussian on the inner side of negatively buoyant jets, that distribution may in fact be better represented by a top-hat flow distribution than the commonly-assumed Gaussian distribution.

It is important to point out however that top-hat modelling, introduced by Morton *et al.* (1956), does not in itself necessitate the assumption that velocity and density profiles in the turbulent flow are top-hat in form. Rather, for the purposes of modelling it simplifies the experimentally-measured profile to a uniform distribution; assuming that as long as volume flux, momentum flux and buoyancy flux are consistent, the actual modelling distribution used is not important. In order to relate such model results back to their "real" distribution characteristics (maximum centreline value, *etc.*), conversion factors are employed. As such, it is incorrect to state that "top-hat modelling can only predict the average dilution" (Papanicolaou *et al.*, 2008, p. 463).

From an analysis of the data presented in Table 1 of Papanicolaou *et al.* (2008) it can be seen that maximum *centreline* heights differ between Gaussian and top-hat models. Thus, these models are not direct corollaries of each other; distinct formulations modelling the same flow behaviour. They instead are making fundamentally different assumptions of the underlying velocity and density distributions, causing the flow itself to travel along different trajectories.

The conclusions of Papanicolaou *et al.* are therefore intriguing. At least with respect to trajectory data, uniform distributions better replicate the velocity and density distributions of negatively buoyant jets than Gaussian distributions.

Papanicolaou *et al.* found spread in their model to increase "dramatically" for $\theta_0 > 60°$ (see Figure 3.6); becoming theoretically infinite at 90° and leading to model collapse. It is worth noting that significant effects are observed on spread rates at angles less than 60° also. They noted that this was in contradiction to what was observed experimentally, and suggested the post-numerical integration application of the limits $b_g/L_M \leq 0.3$ and $b_T/L_M \leq 0.47$, where L_M is equal to $(\pi/4)^{1/4} dF_0$ as before.

The authors also found that decreasing the jet entrainment coefficient, α_{jet}, improved predictions for both Gaussian and top-hat models. They argued that this also was because of the deceleration of the jet core (caused by the "out of phase" reduced gravity), leading the flow to entrain less fluid as it rose.

Both the Gaussian and top-hat formulations presented above were coded in Python and numerically integrated with the SciPy odeint library. Maximum centreline heights were checked against those given in Papanicolaou *et al.*, and were found to match accurately.

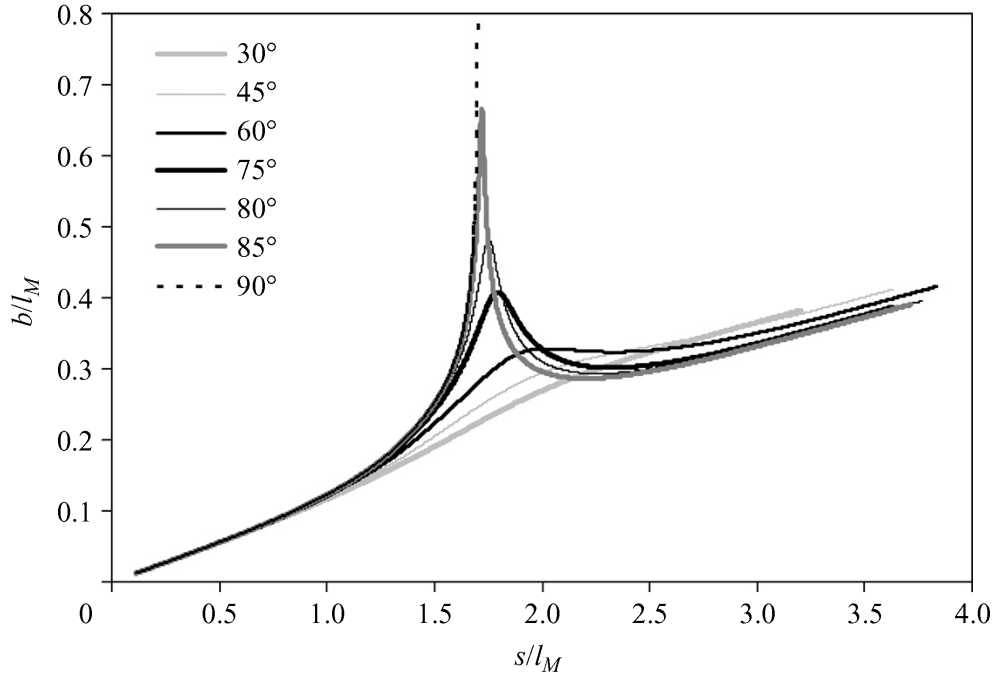

Figure 3.6: Spread rate as a function of path length from Papanicolaou *et al.* (2008)

3.2.3.1 Top-hat to Gaussian conversion factors

It is helpful to outline the process in which top-hat model results can be reconciled with Gaussian model results. A mapping of top-hat bulk parameters (u_T, $\hat{g}_T$ and b_T) to their mean Gaussian counterparts ($u_{\text{ℓ}}$, $\hat{g}_{\text{ℓ}}$ and b) can be made by equating volume, momentum and buoyancy fluxes at a given cross-section:

$$Q = \pi u_T b_T^2 = \int_0^\infty u\, 2\pi r\, dr = I_Q u_{\text{ℓ}} b^2 \tag{3.40}$$

$$M = \pi u_T^2 b_T^2 = \int_0^\infty u^2\, 2\pi r\, dr = I_M u_{\text{ℓ}}^2 b^2 \tag{3.41}$$

$$B = \pi \hat{g}_T u_T b_T^2 = \int_0^\infty u\hat{g}\, 2\pi r\, dr = I_{QC} u_{\text{ℓ}} \hat{g}_{\text{ℓ}} b^2 \tag{3.42}$$

I_Q, I_M and I_{QC} are constants of integration; which by Papanicolaou *et al.* (2008) are defined as π, $\pi/2$, and $\frac{\lambda^2\pi}{\lambda^2+1}$. A formal derivation will be carried out in Section 3.3.1.

From Equations 3.40–3.42 we can obtain

$$\frac{u_T}{u_{\text{ℓ}}} = \frac{I_M}{I_Q}, \quad \frac{\hat{g}_T}{\hat{g}_{\text{ℓ}}} = \frac{I_{QC}}{I_Q}, \quad \frac{b_T}{b} = \sqrt{\frac{I_Q^2}{\pi I_M}} \tag{3.43}$$

For Papanicolaou *et al.* (2008), these equate to $u_T/u_{\text{ℓ}} = 1/2$, $\hat{g}_T/\hat{g}_{\text{ℓ}} = \lambda^2/(\lambda^2+1)$ and $b_T/b = \sqrt{2}$.

However, it is not enough to simply equate the flux equations themselves. In order for these

relationships to hold at any arbitrary path distance s, the derivative equations must be equal also. Thus, writing Equation 3.22 and Equation 3.32 in their dimensional forms (which are the entrainment hypothesis formulations for change of volume flux) we have:

$$\frac{dQ}{ds} = 2\pi b_T u_T \alpha_T = 2\pi b u_{\mathbb{Q}} \alpha$$

Substituting Equation 3.43:

$$2\pi b_T u_T \alpha_T = 2\pi b_T \sqrt{\frac{\pi I_M}{I_Q^2}} u_T \frac{I_Q}{I_M} \alpha$$

or

$$\alpha_T = \left(\frac{\pi}{I_M}\right)^{1/2} \alpha \tag{3.44}$$

For Papanicolaou *et al.* (2008), this relationship is $\alpha_T = \sqrt{2}\alpha$. They make note of this, stating "the entrainment coefficient α in Gaussian modelling has been replaced by $\alpha\sqrt{2}$ in top-hat modelling" (p. 452). However in implementing their model it became evident that only α_{jet} had been modified, and α_{plume} remained unchanged. As a result, $\frac{dQ}{ds}$ was different for the Gaussian and top-hat models when provided the same input parameters (particularly in the plume region).

Likewise, equating the change in vertical momentum flux equations used by Papanicolaou *et al.* (Equations 3.23 and 3.33) in their dimensional forms we have:

$$\frac{dM_V}{ds} = -\pi b_T^2 \hat{g}_T \sin\theta = -I_C \hat{g}_{\mathbb{Q}} b^2 \sin\theta$$

where $I_C = \lambda^2 \pi$. In substituting Equation 3.43, this becomes:

$$-\pi b_T^2 \hat{g}_T \sin\theta = -I_C \hat{g}_T \frac{I_Q}{I_{QC}} b_T^2 \frac{\pi I_M}{I_Q^2} \sin\theta$$

Employing the values used by Papanicolaou *et al.* for I_C, I_Q, I_{QC} and I_M, it can easily be seen that this is an inequality. As a consequence, the top-hat model presented by Papanicolaou *et al.* does not predict the same momentum flux as the Gaussian model.

This discrepancy is a direct result of the fact that although Gaussian velocity and tracer spread factors differ by a factor of λ, where $\lambda > 1$, only one spread factor is used for the top-hat formulation (b_T). If we introduce a top-hat tracer spread parameter, b_{TC}, we may write:

$$\frac{dM_V}{ds} = -\pi b_{TC}^2 \hat{g}_T \sin\theta = -I_C \hat{g}_{\mathbb{Q}} b^2 \sin\theta$$

from which we may obtain:

$$\left(\frac{b_{TC}}{b_T}\right)^2 = \frac{I_C I_M}{I_Q I_{QC}} \tag{3.45}$$

For Papanicolaou *et al.* (2008) this evaluates to $\left(\frac{b_{TC}}{b_T}\right)^2 = \frac{\lambda^2+1}{2}$. When the change of momentum and angle equations are re-calculated, they come to be exactly the same as the Gaussian-formulation equations (Equations 3.23 and 3.24). If the models are then re-run with the corrected α_{plume} value and the same initial conditions, their results become identical.

It should be noted that b_{TC} is not important in Equation 3.42, because $b_{TC} > b_T$ and velocity is zero past the edge b_T, so the integration is unaltered.

3.3 New 'Forced Jet' Model

For a top-hat flow that simply entrains fluid equally around its circumference—or as alternately formulated, a flow which spreads equally in all directions—conservation of mass (Equation 3.2) reduces to

$$\hat{g}_{T\star} Q_\star = 4 \hat{g}_{T\star} u_{T\star} b_{T\star}^2 = 1 \tag{3.46}$$

In Gaussian terms, this equates to $\hat{g}_{g\star} Q_\star = 1$. To the author's knowledge, all integral models to date that have been developed for or applied to negatively buoyant jets have employed this relationship. In the model of Jirka (2004), it is Equation 3.9; in the Gaussian and top-hat models of Papanicolaou *et al.* (2008), it is Equation 3.25 and Equation 3.35 respectively.

The consequence of Equation 3.46 is that as $\theta_0 \to 90°$ and time averaged velocity ($u_{T\star}$ and $u_{g\star}$) goes to zero at z_m, concentration, spread or both must go to infinity. Experimental studies of turbulent fountains have shown that neither result occurs in reality. This is because mass flux is conserved not in the time-averaged sense but in the instantaneous, point-wise sense. As such, the assumptions made in modelling the flow have become invalid or inappropriate assumptions by the time $\theta_0 = 90°$.

Both Jirka (2004) and Papanicolaou *et al.* (2008) allow spread in their models to go to infinity at z_m as $\theta_0 \to 90°$. While this is a physically incorrect result, it allows the dilution rate to stay 'correct' at steep angles.

It has already been discussed that integral modelling of turbulent fountains is problematic due to the continuous re-entrainment of falling discharge fluid. For the assumptions made by any such model to make physical sense in such a scenario—or to simply generate good predictions—special formulations must be made. Carazzo *et al.* (2010) for example presents a "confined top-hat model" which separates upward and downward moving flow at the boundary where $u_z = 0$.

Nevertheless, it may be argued that it is precisely the ability of an integral model to produce finite and relatively reasonable results for a fountain that predicts its ability to model negatively buoyant jets as a whole. This can be seen in the spread results of Jirka (2004) and Papanicolaou

et al. (2008) (plotted in Figures 3.4 and 3.6 respectively), where spread predictions are artificially elevated even at moderate inclinations. Time-averaged velocity need not drop completely to zero for concentration or spread to be affected if Equation 3.46 holds.

Based on the assumption that a turbulent flow in a stagnant ambient is jet-like when initial momentum flux M_0 is greater than buoyancy-generated momentum flux M_B, Kikkert *et al.* (2007) stated that the maximum height of a negatively buoyant jet must always be reached within the jet region. At this location, vertical momentum components must match, meaning that $M_B/M_0 = \sin(\theta_0)$. Modelling geometrical behaviour at the maximum centreline height using an analytical approach based on jet solutions was found to generate reasonably accurate predictions. Section 5.4.5 will show that this model predicts centreline dilutions with relatively good accuracy also. This assumption of jet-like behaviour is supported by the observations of Lai (2010) that centreline velocity decay is jet-like up until the maximum centreline height. It therefore appears to be advantageous to force integral model predictions to mimic the jet dilution rate up to maximum rise height.

Numerous workers (Lane-Serff *et al.* (1993); Papakonstantis *et al.* (2011b); Ferrari & Querzoli (2010, *etc.*)) have highlighted the asymmetric nature of inclined negatively buoyant jet cross-sections; noting that the upper half of the flow remains essentially Gaussian and self-similar, while the lower half is severely distorted because of buoyancy-induced instabilities. From the data to date it is evident that the buoyancy flux of the main flow is not conserved because of these instabilities. Here an integral model is developed which builds on the success of analytical solutions presented by Kikkert *et al.* (2007) in predicting the flow behaviour. In doing so it incorporates the concept of a *reducing* buoyancy flux as the flow rises to maximum height; abandoning the common assumption that buoyancy flux cannot change (Equation 3.46)[1]. For simplicity the model is top-hat in form.

Axial momentum flux, $M_\star$, volume flux $Q_\star$ and buoyancy flux $B_\star$ are defined in the the same manner as in the Papanicolaou *et al.* (2008) top-hat model: *i.e.* Equation 3.30. Therefore $Q_\star = 2b_{T\star}\sqrt{M_\star}$ and,

$$\frac{dQ_\star}{ds_\star} = \frac{b_{T\star}}{\sqrt{M_\star}}\frac{dM_\star}{ds_\star} + 2\sqrt{M_\star}\frac{db_\star}{ds_\star} \tag{3.47}$$

Instead of using the entrainment hypothesis, spread rate is assumed constant here; *i.e.* $\frac{db_{T\star}}{ds_\star} = k_T$. In a pure jet, $\frac{dM_\star}{ds_\star} = 0$ and consequently $M_\star = 1.0$ always. Thus we have,

$$\frac{dQ_\star}{ds_\star} = 2k_T \tag{3.48}$$

As $\hat{g}_{T\star} = B_\star/Q_\star$, we may derive from this the relationship for change in concentration with

[1] In this study the details of how buoyancy flux may change whilst still conserving mass are not developed: this process is assumed to be complex yet one which has a negligible effect on the formulation of other integral relationships.

respect to path in a pure jet:

$$\frac{d\hat{g}_{T\star}}{ds_\star} = -2k_T\hat{g}_{T\star}^2 \tag{3.49}$$

If rather than being equal to a constant 1.0, $\hat{g}_{T\star}Q_\star$ was equal to the variable parameter $B_\star$, this may be differentiated as follows:

$$\frac{d\hat{g}_{T\star}}{ds_\star} = \frac{1}{Q_\star}\frac{dB_\star}{ds_\star} - \frac{B_\star}{Q_\star^2}\frac{dQ_\star}{ds_\star} \tag{3.50}$$

Equating Equation 3.49 and Equation 3.50 we find,

$$\frac{dB_\star}{ds_\star} = \frac{B_\star}{Q_\star}\frac{dQ_\star}{ds_\star} - 2Q_\star k_T\hat{g}_{T\star}^2 \tag{3.51}$$

which is the change in $B_\star$ with respect to path necessary to maintain pure jet dilution rate in an arbitrary flow.

This condition may be applied until the transition from jet region to plume region, or simply until maximum centreline height is reached. Both forms of the model were developed, and differences were found to be small. Thus for the sake of simplicity, Equation 3.51 will be applied only until the maximum centreline height. Applying $\frac{dB_\star}{ds_\star} = 0$ afterwards, a complete set of equations may be written, following an otherwise-standard approach:

$$\frac{db_{T\star}}{ds_\star} = k_T \tag{3.52}$$

$$\frac{dM_{H\star}}{ds_\star} = 0 \tag{3.53}$$

$$\frac{dM_{V\star}}{ds_\star} = -\frac{4\hat{g}_{T\star}b_{T\star}^2\left(\frac{b_{TC}}{b_T}\right)^2}{F_0^{\,2}} \tag{3.54}$$

$$\frac{dM_\star}{ds_\star} = \frac{M_{V\star}}{M_\star}\frac{dM_{V\star}}{ds_\star} \tag{3.55}$$

$$\frac{dQ_\star}{ds_\star} = \frac{b_{T\star}}{\sqrt{M_\star}}\frac{dM_\star}{ds_\star} + 2\sqrt{M_\star}\frac{db_\star}{ds_\star} \tag{3.56}$$

$$\frac{dB_\star}{ds_\star} = \begin{cases} 0.0 & \frac{dz_\star}{ds_\star} < 0 \\ \frac{B_\star}{Q_\star}\frac{dQ_\star}{ds_\star} - 2Q_\star k_T\hat{g}_{T\star}^2 & \frac{dz_\star}{ds_\star} \geq 0 \end{cases} \tag{3.57}$$

$$\frac{dx_\star}{ds_\star} = \frac{M_{H\star}}{M_\star}, \quad \frac{dz_\star}{ds_\star} = \frac{M_{V\star}}{M_\star} \tag{3.58}$$

where $k_T = 0.15$, $\hat{g}_{T\star} = B_\star/Q_\star$ and $u_{T\star} = M_\star/Q_\star$. $\frac{b_{TC}}{b_T}$ is defined as per Equation 3.45:

$$\left(\frac{b_{TC}}{b_T}\right)^2 = \frac{I_C I_M}{I_Q I_{QC}}$$

and I_C, I_M, I_Q & I_{QC} will be defined in Section 3.3.1. Initial conditions include $x_\star = z_\star = 0$; $M_\star = B_\star = 1$; $M_{V\star} = \sin\theta_0$ and $M_{H\star} = \cos\theta_0$. A point-source may be simulated by setting $b_\star$ equal to a small number; e.g. 0.05. The final initial conditions are then $U_\star = \sqrt{M_\star/(4b_\star^2)}$ and $Q_\star = 4U_\star b_\star^2$.

Equations 3.52 to 3.58 will be referred to as the 'forced jet' model. Figure 3.7 plots $B_\star$ values generated when running the model at different inclinations.

As with all integral models, the forced jet model has limitations. In particular, as discussed in Section 3.3.1, this model is unable to predict attributes of the distorted lower side[2] of the flow, and therefore spread rates predicted by the forced-jet model will refer only to spread rates observed on the upper side[3]. Derived centreline parameters may be assumed to remain accurate, however. Section 3.3.1 will discuss in detail the derivation of Gaussian parameters from the top-hat predictions of the forced jet model.

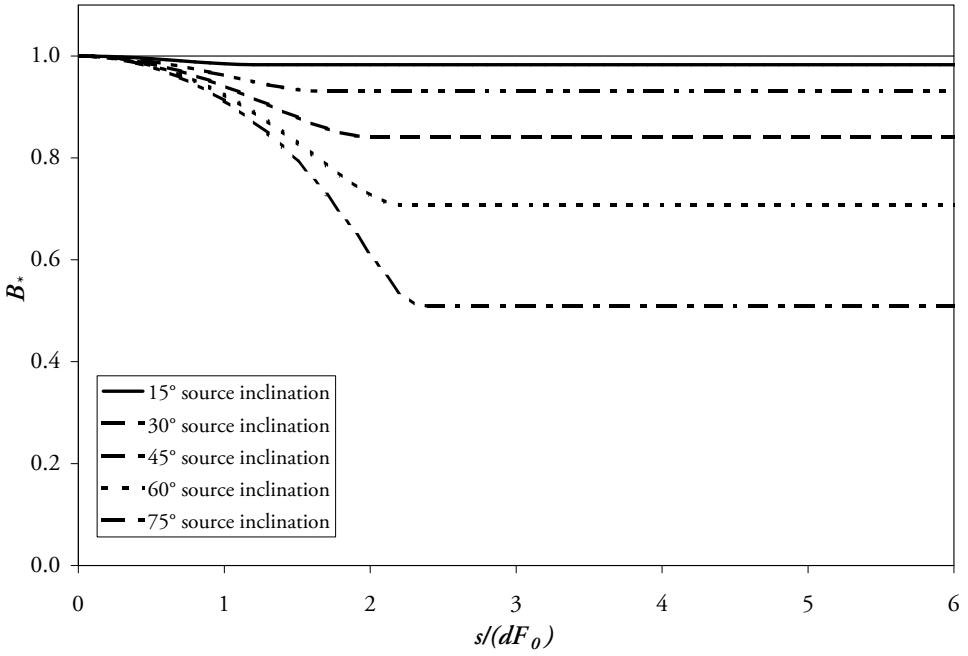

Figure 3.7: $B_\star$ values generated when forced jet model is run at different inclinations. Solid line drawn at $B_\star = 1.0$

It is instructive to consider how letting $\frac{dB_\star}{ds_\star}$ become non-zero does in fact affect dilution rate. If top-hat dilution rate $S_{T\star}$ is the reciprocal of concentration, then $S_{T\star} = Q_\star/B_\star$ and differentiating

[2] More accurately, the inner side: see Figure 5.1

[3] More accurately, the outer side

yields

$$\frac{dS_{T\star}}{ds_\star} = \frac{1}{B_\star}\frac{dQ_\star}{ds_\star} - \frac{Q_\star}{B_\star^2}\frac{dB_\star}{ds_\star} \tag{3.59}$$

Therefore dilution rate is increased if $\frac{dB_\star}{ds_\star} \leq 0$ is negative and $B_\star < 1$ (other scenarios may also lead to increased dilution rate). As Figure 3.7 demonstrates, $\frac{dB_\star}{ds_\star} < 0$ on the rising side.

If however Equation 3.51 was applied throughout the entire flow, Figure 3.8 demonstrates that $\frac{dB_\star}{ds_\star} > 0$ on the falling side. Consequently dilution rate *decreases* rapidly; in many cases becoming negative—that is, the flow becomes more concentrated than it was. In practice, while falling fluid may re-entrain fluid that had earlier "fallen out" of the flow, this effect will never increase overall flow concentration. Therefore such predictions are clearly non-physical. It is assumed that in the plume region the influence of the buoyancy induced instabilities is no longer significant, and therefore the buoyancy gradient here is such that $B_\star$ is a constant.

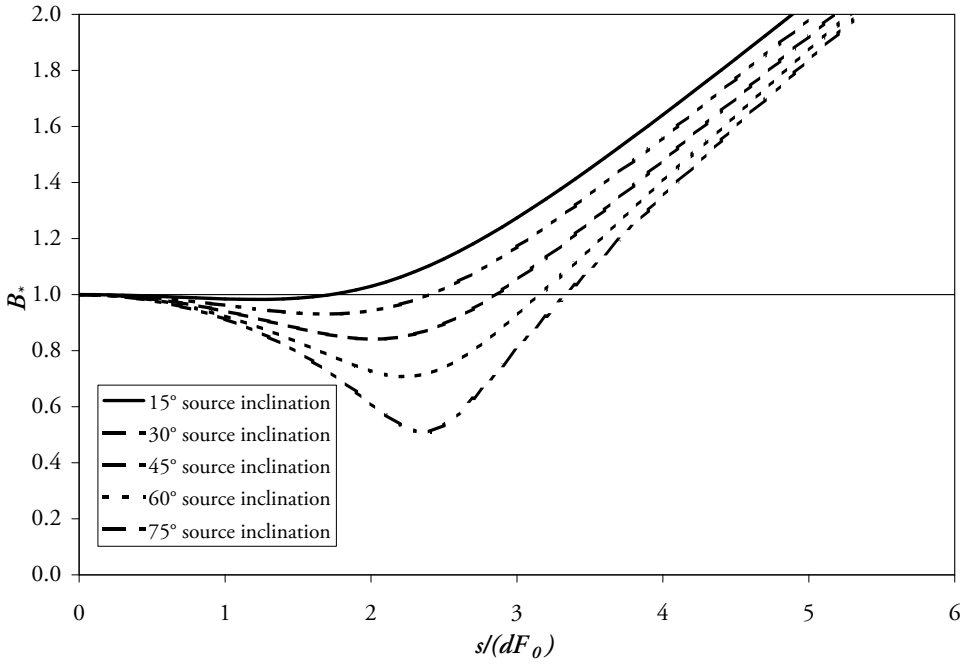

Figure 3.8: $B_\star$ values generated when forced jet model is run at different inclinations, but with Equation 3.51 applied at all locations. Solid line drawn at $B_\star = 1.0$

While switching directly to $B_\star = 1$ after the maximum centreline height would return the model equations to their "unaffected" state, this has no physical backing. Regardless, a step change such as this would mean $\frac{dB_\star}{ds_\star} = \infty$ at that point, and by Equation 3.59, dilution would go to zero.

A complete presentation of model results will be made in Section 5.4. However an important limitation of the forced jet model is that it is unable to predict dilution rates at steep inclinations; $\theta_0 \gtrsim 60°$. This is due to two separate reasons.

Firstly, at the maximum centreline height, dilution rates in steeply-inclined negatively buoyant jets are constricted because flow mixing in the inner side of the flow is constricted. That is,

unmixed ambient fluid cannot be brought into the flow as effectively at steep inclinations, where tracer fluid is being (re-)entrained as well as ambient fluid. Although dilution rates on the rising side of negatively buoyant jets are jet-like for low-to-moderate source inclinations, they cannot be jet like when such self-entrainment processes are significant. This is certainly the case for vertical fountains but is also true at lower inclinations. Figure 3.9, which presents time-averaged concentration images for experiments at 60° and 75° inclinations, clearly shows inner-side flow constriction that is present at the 75° inclination.

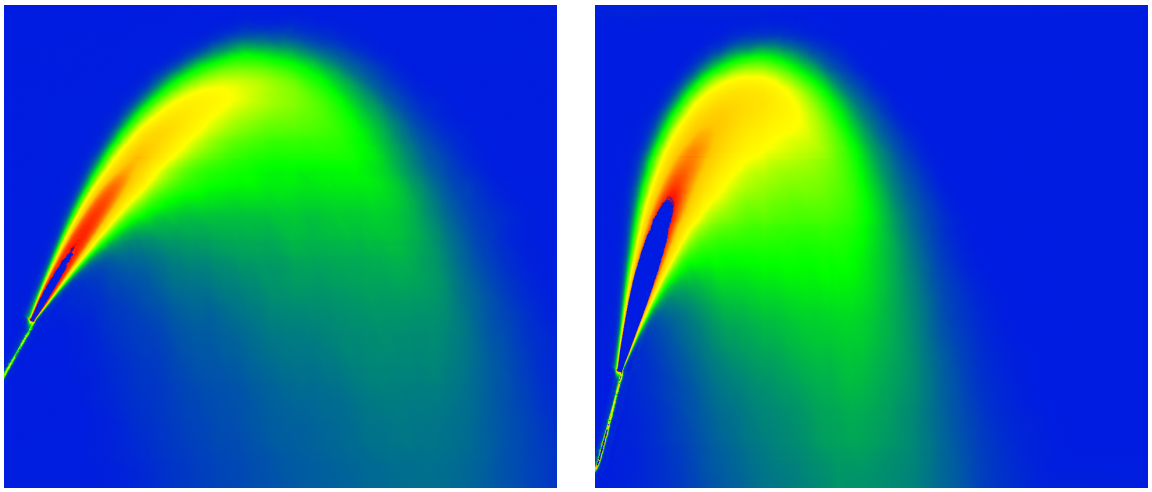

(**a**) 60° inclination; $F_0 = 30.95$ (**b**) 75° inclination; $F_0 = 30.81$

Figure 3.9: False-colour images of temporally-averaged concentration at 60° and 75° inclinations. Blue area near source demarks area of no signal

Secondly, at the return point, model predictions for dilution rate (S_r) tend to infinity as $\theta_0 \to 90°$: clearly a non-physical result. No such observation has been made in experimental results. As has been discussed, in the forced jet model, $B_\star$ is reduced on the rising side and from the maximum centreline height onwards, $\frac{dB_\star}{ds_\star}$ is made zero. However, the limit of the value to which $B_\star$ reaches at s_m as $\theta_0 \to 90°$ is zero[4]. Therefore, by Equation 3.59, dilution rate must tend to infinity.

For these reasons, dilution predictions made by the forced-jet model are assumed invalid for steep inclinations. Trajectory predictions are likewise cast into doubt; however these will be examined in detail in Section 5.4.

Conversion factors from Gaussian to tophat parameters will be discussed in the following section.

3.3.1 Top-hat to Gaussian conversion factors

On the lower side of the negatively buoyant discharge it can be difficult to distinguish between the material that remains part of the 'primary' flow and that which is detrained from it due to the

[4]This is because $B_\star$ is a function of $Q_\star$ (see Equation 3.51), and as $\theta_0 \to 90°$, $Q_\star = 4u_{T\star}b_{T\star}^2$ tends to zero

buoyancy-induced instabilities. The mean parameter profiles are also distorted and no longer self-similar. These features could potentially make conversion factors for a top-hat model difficult to define. Here we assume that half of the axial volume flux is above the centreline[5]. This effectively defines the lower boundary of the control volume in the real flow. Conversions will then be made based only upon the top half of the top-hat control volume:

$$Q_{\text{top-half}} = \frac{\pi}{2} u_T b_T^2 = \int_0^\infty u \, \pi r \, dr = \frac{I_Q}{2} u_{\text{℄}} b^2 \tag{3.60}$$

$$M_{\text{top-half}} = \frac{\pi}{2} u_T^2 b_T^2 = \int_0^\infty u^2 \, \pi r \, dr = \frac{I_M}{2} u_{\text{℄}}^2 b^2 \tag{3.61}$$

$$B_{\text{top-half}} = \frac{\pi}{2} \hat{g}_T u_T b_T^2 = \int_0^\infty u \hat{g} \, \pi r \, dr = \frac{I_{QC}}{2} u_{\text{℄}} \hat{g}_{\text{℄}} b^2 \tag{3.62}$$

where the integral constants I_Q, I_M, I_{QC} are consistent with definitions given in Equations 3.40–3.42. Similarly, the definition of I_c remains the same, as

$$I_C = \int_0^\infty \frac{\overline{\hat{g}}}{\hat{g}_{\text{℄}}} 2\pi \frac{r}{b} d\left(\frac{r}{b}\right) \tag{3.63}$$

Mean Gaussian distributions for velocity and reduced gravity were defined in Equation 1.4 as

$$\frac{\bar{u}}{u_{\text{℄}}} = e^{-r^2/b^2}, \quad \frac{\bar{g}'}{\hat{g}_{\text{℄}}} = e^{-r^2/(\lambda b)^2}$$

However, velocity and reduced gravity can both be segregated into their average and fluctuating components: $u = \overline{u} + u'$ and $\hat{g} = \overline{\hat{g}} + \hat{g}'$. While the average of each fluctuating component is zero, the average of two fluctuating components multiplied together is not zero. Thus we may write:

$$I_Q = \int_0^\infty \frac{\bar{u}}{u_{\text{℄}}} 2\pi \frac{r}{b} d\left(\frac{r}{b}\right)$$

$$I_M = \int_0^\infty \left[\left(\frac{\bar{u}}{u_{\text{℄}}}\right)^2 + \overline{\left(\frac{u'}{u_{\text{℄}}}\right)^2} \right] 2\pi \frac{r}{b} d\left(\frac{r}{b}\right)$$

$$I_{QC} = \int_0^\infty \left[\frac{\bar{u}}{u_{\text{℄}}} \frac{\hat{g}}{\hat{g}_{\text{℄}}} + \overline{\frac{u'}{u_{\text{℄}}} \frac{\hat{g}'}{\hat{g}_{\text{℄}}}} \right] 2\pi \frac{r}{b} d\left(\frac{r}{b}\right)$$

$$I_C = \int_0^\infty \frac{\bar{g}'}{\hat{g}_{\text{℄}}} 2\pi \frac{r}{b} d\left(\frac{r}{b}\right)$$

[5]Although the validity of such an assumption is unclear, its accuracy is deemed here to be unimportant compared to the modification in $\frac{dB_*}{ds_*}$ relationship made by the forced jet model.

Hussein *et al.* (1994) and Wang & Law (2002) found that the momentum flux in a buoyant jet contributed by turbulence was 10% of the mean momentum flux; that is, $\left(\frac{u'}{u_{\mathbb{C}}}\right)^2 = 0.1\left(\frac{\bar{u}}{u_{\mathbb{C}}}\right)^2$. Papanicolaou (1984) found that 7% of the total mass flux was carried by turbulence; while Wang & Law (2002) found this value to be 7.6% and 15% in the jet and plume regions respectively. Adopting the values of Wang & Law, we may therefore write $\overline{\frac{u'}{u_{\mathbb{C}}}\frac{\hat{g}'}{\hat{g}_{\mathbb{C}}}} = 0.076\frac{\bar{u}}{u_{\mathbb{C}}}\frac{\hat{g}}{\hat{g}_{\mathbb{C}}}$ for a jet and $\overline{\frac{u'}{u_{\mathbb{C}}}\frac{\hat{g}'}{\hat{g}_{\mathbb{C}}}} = 0.15\frac{\bar{u}}{u_{\mathbb{C}}}\frac{\hat{g}}{\hat{g}_{\mathbb{C}}}$ for a plume. Accurate factors are important to employ, however as illustrated in Section 3.2.3.1, it is essential that these factors are applied consistently.

By substituting the Gaussian distributions of Equation 1.4 and employing the definite integral $\int_0^\infty e^{-ax^2} x\,dx = \frac{1}{2a}$, we derive:

$$I_Q = \pi \tag{3.64}$$

$$I_M = 1.1\frac{\pi}{2} \approx 1.7 \tag{3.65}$$

$$I_{QC} = \begin{cases} \frac{1.076\pi}{1+1/\lambda^2} & \text{in jet} \\ \frac{1.15\pi}{1+1/\lambda^2} & \text{in plume} \end{cases} \tag{3.66}$$

$$I_C = \lambda^2\pi \tag{3.67}$$

The ratio of concentration spread to velocity spread, λ, was found by by Wang & Law (2002) to be equal to 1.217 in a jet and 1.038 in a plume. As proposed by these authors, we will employ the empirical interpolation function,

$$\lambda = \lambda_j - (\lambda_j - \lambda_p)\left(\frac{F_{Lp,T\star}}{F_{LT\star}}\right)^{3/2} \tag{3.68}$$

where $\lambda_j = 1.217$ and $\lambda_p = 1.038$. We will also employ the like function for ratio of total mass flux to the mean, k_H:

$$k_H = k_{jH} - (k_{jH} - k_{pH})\left(\frac{F_{Lp,T\star}}{F_{LT\star}}\right)^2 \tag{3.69}$$

with $k_{jH} = 1.076$ and $k_{pH} = 1.15$.

The local Froude number, $F_{LT\star}$, is

$$F_{LT\star} = \frac{u_{T\star}}{\sqrt{\hat{g}_{T\star} b_{T\star}}} \tag{3.70}$$

It can be verified that in the same manner as Equation 3.14, this tends to the value $F_{Lp,T\star}$ in the plume region where

$$F_{Lp,T\star} = \frac{2\cdot\sqrt{\frac{5}{4}\left(\frac{b_{TC}}{b_T}\right)^2}}{F_0} \tag{3.71}$$

A reference implementation of this 'forced jet' model is given in Appendix C. This model must now be evaluated against existing and new experimental data. Experimental systems for the current study are outlined in the following chapter, and experimental results will be discussed in Chapter 5. Evaluation of the forced jet model will be carried out in Section 5.4.

Chapter 4

Experimental Systems

"Failed? Why, we haven't failed, we only know the thousands of ways that won't work."
Thomas Edison; quoted in Association of American Railroads (1924, p. 23)

The goal of the experimental programme incorporated into this thesis was to gather high-quality laboratory data on the dilution rate of singly-diffusive inclined negatively buoyant jets in stagnant unstratified environments, without boundary influence. By implication this also included the collection of data regarding the spatial extent of that concentration field. Laser Induced Fluorescence (LIF) was the primary experimental technique employed for this purpose. This chapter describes in detail the experimental systems utilised.

4.1 Laser Induced Fluorescence: An Introduction

4.1.1 Fluorescence

The light we see with our eyes every day—visible light—is electromagnetic radiation within a narrow spectrum of wavelengths (approximately 400–700 nm). The elementary unit of an electromagnetic radiation field is the *photon*. Photons have been shown to exhibit properties of both waves and particles; described as the 'wave-particle duality'. The energy of photons depends only on their frequency, ν, or equivalently, their wavelength, λ (Planck, 1901):

$$E = h\nu = hc/\lambda \tag{4.1}$$

where h is Planck's constant, and c is the velocity of light within a vacuum; understood to be a constant also. Thus red light, with wavelengths on the high end of the visible spectrum (approx. 700 nm), will have less energy than violet light, with wavelengths on the low end of the visible spectrum (approx. 400 nm).

Fluorescence is the phenomenon where a photon that hits a molecule triggers the rapid emission of another photon, of equal or longer wavelength (thus, with an equal or reduced energy

level). This takes place when the incident photon causes the molecule to enter an excited energy state, that, upon decaying, transforms much of its absorbed energy into an outbound photon. The outbound—or 'fluoresced'—photon is emitted in an essentially random direction, not related to the direction at which the incident photon was travelling.

The word 'fluorescence' was coined by George Gabriel Stokes (Stokes, 1852) in order to refer to light coming from an illuminated object that had not been reflected off that object and had not simply passed directly through that object. Stokes correctly identified that this light had a different colour to that with which the object was illuminated. He named the phenomenon after fluorspar, a mineral that commonly fluoresces in the visible spectrum when illuminated by ultra-violet light.

Today, fluorescence is used extensively in lighting, analytical chemistry and biochemistry applications. Fluorescent light tubes would perhaps be the most ubiquitous use of the phenomenon. These tubes contain small amounts of mercury that emit light in the ultraviolet range, but are lined with a fluorescent material that absorbs the ultraviolet light and emits visible light.

Like fluorspar, many gemstones fluoresce under the correct lighting conditions. Figure 4.1 shows a selection of these minerals.

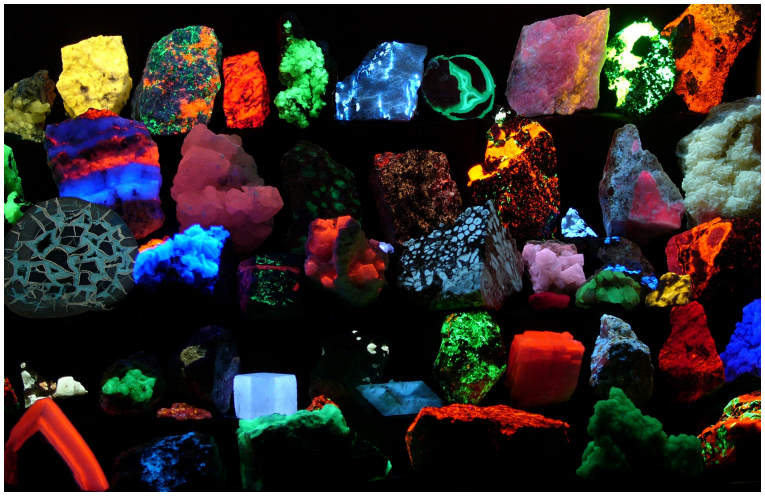

Figure 4.1: Collection of various fluorescent minerals under UV-A, UV-B and UV-C light. Hannes Grobe, 7 April 2005

4.1.2 Fluorescence in Fluid Mechanics

Dyes that fluoresce under appropriate lighting conditions can be useful tracers in fluid mechanics experiments. A known quantity of fluorescent dye is mixed into a flow at a certain point, and some type of illumination & sensing system is used to determine the fluorescence of the liquid—and by correlation, the quantity of dye—at further points of interest during the testing period. In such a way, dilution measurements and even flowrate measurements can be made using fluorescent dyes.

In many applications the illumination-sensing system used is a *fluorometer*; a compact device which measures the light emitted from a sample under a specific lighting spectrum (usually light emitted from a broad spectrum lamp is filtered to provide specific wavelengths). However, any type of light source can be used; the light needs only to match in some part the absorption spectrum of the fluorescent material being used.

Laser Induced Fluorescence (LIF) is the technique that uses a laser light source to illuminate fluorescent molecules (known as *fluorophores*). Lasers have many appealing properties, but within fluid mechanics the primary property of interest is the high collimation of their light (*i.e.* light rays are nearly parallel). This means laser light may be used to illuminate only a narrow plane through an experimental vessel; isolating a small portion of the three-dimensional flow field.

Worthy of note is the ability of many lasers to produce a single wavelength of light (or more precisely, a very narrow spectrum of light). This is helpful in avoiding the inadvertent excitation of other fluorescent molecules which may be within the illumination area.

LIF has been used by a wide range of workers within the Fluid Mechanics field. Ferrier *et al.* (1993), Law & Wang (2000) and Crimaldi (2008) provide details on rigorous experimental and calibration techniques that have been employed. The current system is different to many used to-date in that calibration is made on a per-pixel basis.

For the current experiments, Rhodamine 6G was the fluorescent dye of choice. Figures 4.2 and 4.3 plot the absorption and emission spectra, respectively, for Rhodamine 6G dissolved in ethanol. It is known that the solvent with which fluorophores are dissolved can have some influence over these spectra, so this data should be treated as indicative rather than absolute. Eggeling *et al.* (2005) gives the absorption maximum of Rhodamine 6G in water to be 524 nm and the fluorescence maximum of the same to be 553 nm.

4.2 Equipment

All experiments were conducted in a 5000 L glass-walled tank, measuring 1.78 m high by 2.30 m wide by 1.23 m deep. An image of this tank is presented in Figure 4.4. The tank was filled with fresh tap water (filtered to 5 μm) and emptied to the city sewage system. Filling and emptying both took 30–45 minutes. A frame was constructed inside the tank at one end to support the discharge source pipe. This frame allowed the source to be located at any point vertically and at a variety of locations horizontally. During the experiments conducted it was never positioned closer than 500 mm from any tank boundary. The source itself was mounted on a hinged plate so that it could be rotated out of the way during calibration procedures.

A 2000 L header tank was positioned on a mezzanine floor above the primary tank and filled with the discharge fluid (minimum head difference of 2100 mm). Its diameter was 1.5 m. This diameter was such that at typical jet flowrates, the depth of water in the tank would drop at a slow enough rate to have an insignificant effect on the pressure head. For instance, at a jet flowrate of 1 L/min (high for the current experimental setup), the depth in the tank would drop

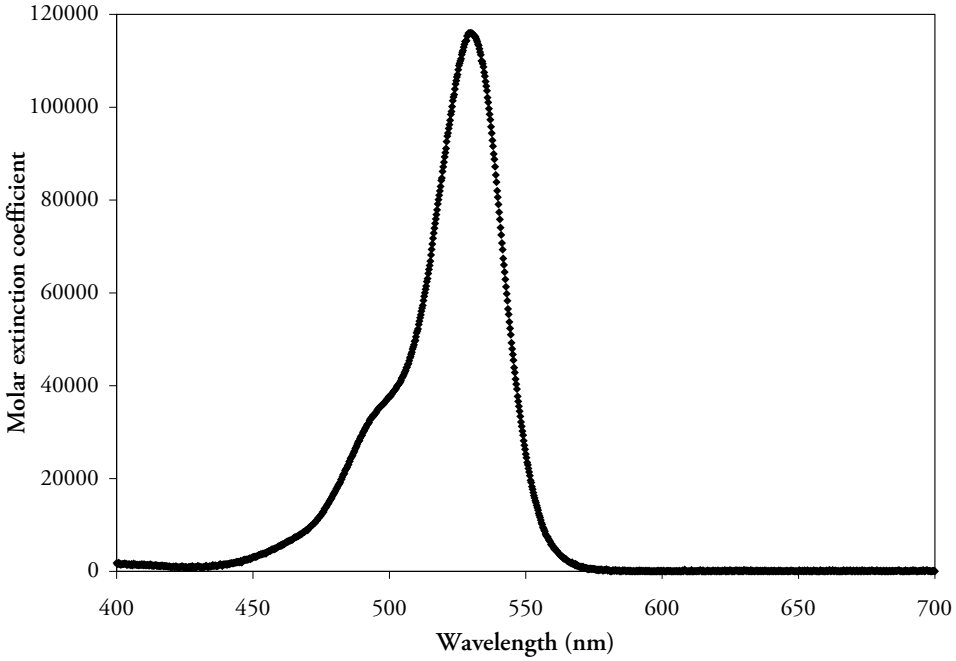

Figure 4.2: Molar extinction coefficient (also known as molar absorptivity) for Rhodamine 6G dissolved in ethanol, from Du *et al.* (1998)

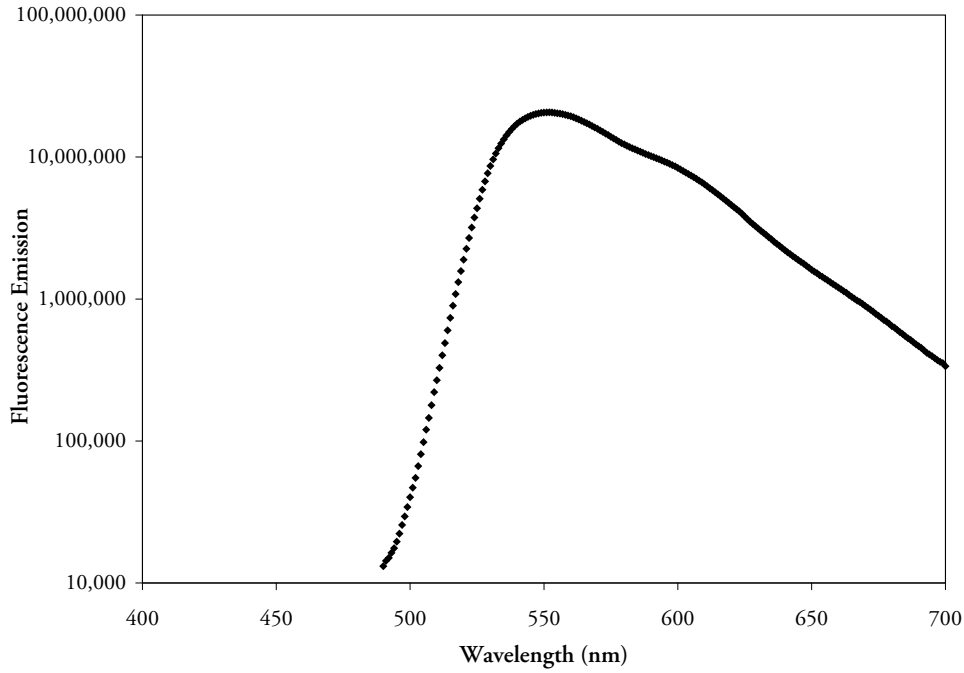

Figure 4.3: Fluorescence emission spectrum of Rhodamine 6G dissolved in ethanol, from Du *et al.* (1998)

Figure 4.4: Experimental tank used in current study

at only 0.57 mm/min. The source fluid used for experiments was fresh tap water (also filtered to 5 μm) mixed with Rhodamine 6G, and for experiments requiring a density difference, mixed with approximately 3% salt by weight. Densities were measured using an Anton Paar DMA 5000 density meter, which operated at 20°C. Density differences between source fluid and ambient tank fluid in negatively buoyant jet experiments ranged between 2.94% and 2.98%.

Experimental discharge flowrates were logged every 0.3 seconds by a computer connected to a Krohne IFC 010D flowmeter. A stopwatch-and-bucket calibration was undertaken to determine an accurate relationship between logged flowrate and true flowrate. Header tank and experimental tank temperatures were measured directly following each experiment. On average, header-tank temperatures were 2.9°C greater than experimental tank temperatures, where the average experimental tank temperature was 15.4°C. Table 4.1 demonstrates that the density changes due to these temperature differences were insignificant; unlikely to affect flow buoyancy or generate any double-diffusive effects.

A visible continuous laser was used to induce fluorescence in the Rhodamine dye mixed with the discharge fluid. This laser was a Spectra-Physics Millennia IIs, a high stability ($\pm$0.1%) diode-pumped Nd:YAG laser which was frequency-doubled to 532 nm. Its maximum intensity

Table 4.1: Density of water at various temperatures, from (Lide, 2004, p. **6**-6); and relative differences to average experimental tank temperature (15.4°C). Lowest recorded experimental tank temperature was 13.0°C, and highest 16.7°C. Temperature increments in table equal to average difference between header tank and experimental tank temperatures

Temperature (°C)	Density (g/cm^3)	$\Delta\rho$
12.5	0.9994410	-0.040%
15.4	0.9990403	—
18.3	0.9985416	0.050%
21.2	0.9979513	0.109%

was 2.00 W. The laser beam was directed into a box which contained an 8-sided glass scanning mirror that rotated at 10,000–15,000 RPM and a parabolic perspex mirror. As the scanning mirror rotated it reflected the incident laser beam across the length of the parabolic mirror, which was designed in such a way that it would in turn reflect the laser beam into a horizontal beam at all locations. The net result was a coherent sheet of laser light, approximately 6 mm thick (±2 mm) and 700 mm tall. This light sheet was directed down the centre of the experimental tank, along a vertical plane. The discharge pipe (supplying fluid from the aforementioned header tank) was located at the opposite end of the experimental tank, and was aligned such that the light sheet intersected both the discharge pipe and the flow out of that pipe when turned on with the surrounding tank still empty. Figure 4.5 illustrates this configuration. It is important to note that in all cases the lowest part of the light sheet (and thus the lowest part of the measurable flow) was at least 500 mm above the bottom tank boundary. This allowed dense fluid to accumulate at the bottom of the tank, without influencing flow in the area of interest.

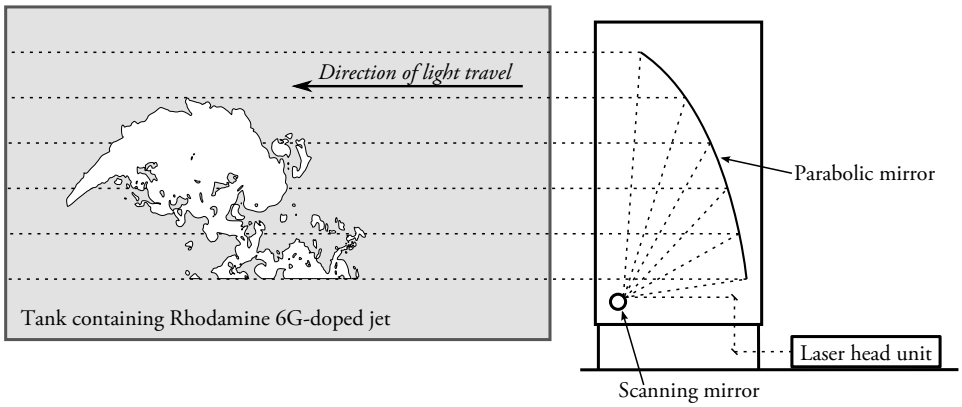

Figure 4.5: Configuration image, looking horizontally towards tank from alongside video camera. Dashed lines indicate light ray paths. Representative outline shown of flow image generated by fluorescence. Dimensions only approximate, and details of tank design omitted

Recordings of the flow as illuminated by the laser light sheet were taken using a video camera looking through one of the two largest panels of glass in the tank: a 1250 mm by 1250 mm panel along the longest side or a 1120 mm by 1200 mm panel along the shortest side. The camera used

was a JAI Pulnix TM-2030CL, a greyscale 12-bit progressive-scan digital video camera. This camera operated at a frame rate of either 16 Hz or 32 Hz, employing a 'dual tap system' for the latter frame rate, where the image sensor was read by two separate Analogue-to-Digital (ADC) devices.

The camera was mounted perpendicular to the light sheet direction, on a modified survey tripod positioned approximately 3.2 m from the tank. A plan-view configuration diagram is given in Figure 4.6. A Goyo Optical high transmission 50 mm TV lens was used ($f/0.95$; part number GMY45095MC), with the effective recording area of approximately 1075 mm wide by 604 mm high. The lowest part of this recording area was 450 mm above the base of the experimental tank.

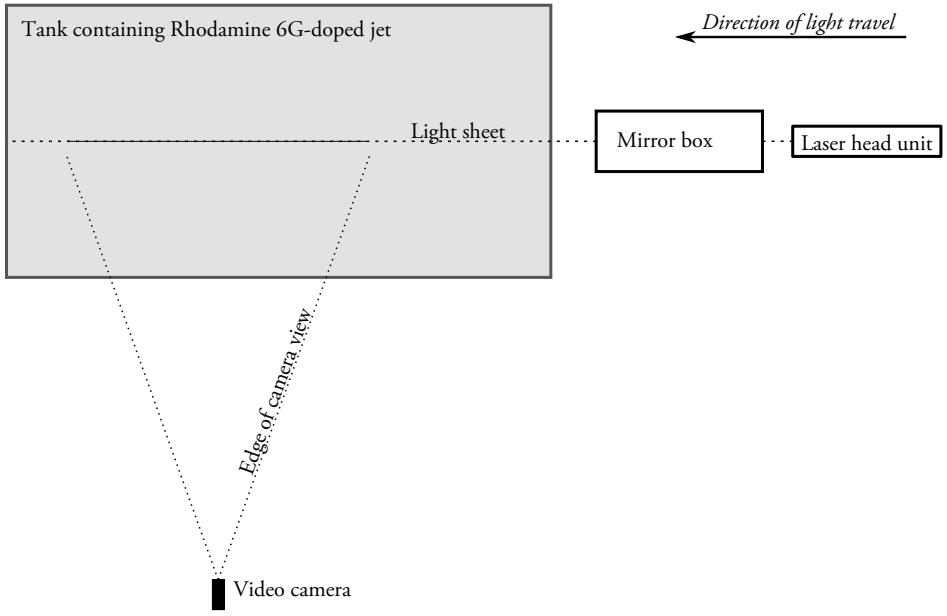

Figure 4.6: Configuration image, looking down in plan view on tank. Dimensions only approximate, and details of tank design omitted

The digital video camera was connected to a computer via a CameraLink interface and a Correco capture card. JAI software was used to control camera settings, while Correco IFC software was used to analyse the frequency distribution of greyscale intensities in real-time images. Software was developed using the IFC Application Programming Interface (API) to capture images to memory and concurrently write to disk as individual uncompressed files of approximately 4 MB each. Because the most important data to be generated for the present study were averaged images, maintaining a high frame rate was not important. Thus the camera was set in single-tap mode, providing a frame rate of 16 Hz. With this reduced frame rate however, it was still not possible for standard hard drives to save the data in real time. High speed Western Digital Raptor hard drives (nominally rated at 10,000 RPM) were found to be adequate—two up until they were 40–50% full, and another newer-generation drive for its entire capacity. This is demonstrated in Figure 4.7.

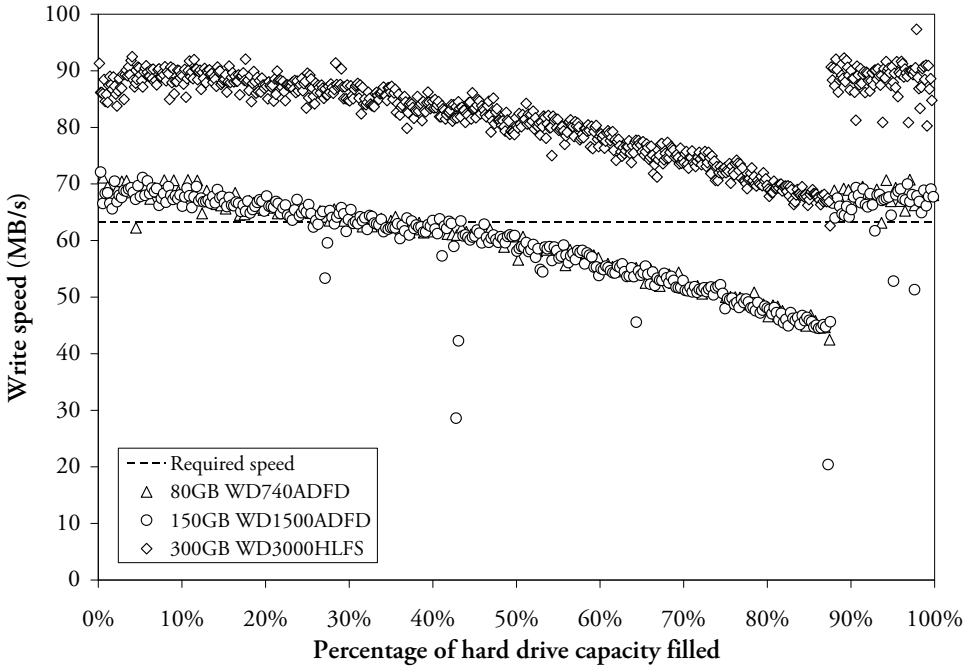

Figure 4.7: Speed of three Western Digital high-speed NTFS-formatted hard drives used for image capture, as determined by measuring the length of time taken to save batches of one hundred 4 MB files at a time. Sudden jump in speed at 88% hard drive capacity is due to the operating system allowing the hard drive to write files in the region close to the outer edge of the disk that was initially reserved for the NTFS Master File Table (MFS)

4.3 Signal Quality

While it was relatively straightforward to generate visually appealing experimental images, it was important to ensure those images were a fair representation of the flow behaviour that was being investigated, and not unduly tainted by artifacts of the recording process. Issues such as image distortion and repeatability needed to be dealt with in this context.

Ultimately, the goal was to relate the greyscale intensities recorded by the camera to specific concentrations of source fluid. If the incident light intensity is held constant, the brightness of fluoresced light from a given point increases as the number of fluorophore molecules at that location increases (up to a certain point that is; see Section 4.3.3.2). Here Rhodamine 6G molecules mixed in the discharge fluid were the fluorophores, and thus the brightness of fluoresced light was directly proportional to the concentration of discharge fluid within the light sheet. The process of calculating this relationship was the *calibration* process, and will be discussed later in Section 4.4.1. Yet, without a reliable intensity field, such a process was meaningless.

In this section, experimental signal quality will be discussed under three categories: light-sheet generation (Section 4.3.1), camera accuracy (Section 4.3.2) and fluorescent image behaviour (Section 4.3.3). These three categories encompass the range of factors that are important for the derivation of reliable quantitative concentration data.

All experimental equipment outlined in the previous section was fixed in place, and calibra-

tions were carried out again if anything was intentionally moved. Nevertheless, because it was possible for components to be bumped accidentally or displaced slightly by room heating and cooling cycles, calibrations were carried out on a regular and ongoing basis.

4.3.1 Light sheet

4.3.1.1 Laser power stability

Power output of the laser described earlier was set by a digital controller unit. This unit also displayed a measured power-output reading, to three significant figures. This measured reading was found to stabilise quickly after a different power output was set. After this initial stabilisation period no further fluctuations were ever observed.

Nevertheless, it was important to independently verify the power stability of the laser. Figure 4.8 plots the power measured by a relatively simple thermal power meter, logged on a regular basis to a computer for a period of almost three days. After an initial rise (likely due to heat stabilisation in the detector unit), fluctuations remained within ±0.5%.

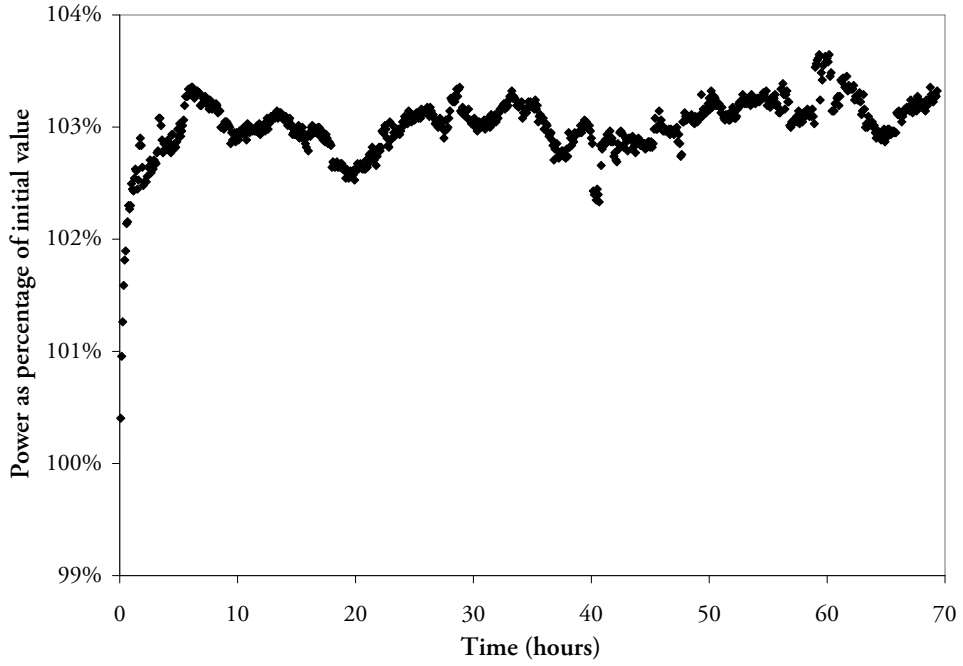

Figure 4.8: Laser power while running continuously for 69 hours, as measured by Spectra-Physics 407A CW Laser Power Meter, with voltage from output logged to computer. 300 seconds (5 minutes) between each data point plotted

4.3.1.2 Fixed mirrors

Fixed mirrors—including the parabolic mirror and those used to direct the laser beam to the scanning mirror—were assumed to be reliable and consistent. Although there was a possibility

of variability in reflectance levels, no evidence of this was found. The calibration process, outlined later, negated the effect of fixed spatial variations in light sheet intensity.

Nonetheless, it was important also that the light sheet generated was as planar as was possible. As such, this was dictated by the alignment of the parabolic mirror. This mirror was held by tensioned tape against two flat metal pieces that created the parabolic shape. Twisting the mirror—manually or otherwise—at any point would distort the light sheet at that corresponding position.

Because the supporting metal pieces were not positioned precisely, some fine tuning was required in order to create a relatively straight light sheet. This involved placing shims of suitable thicknesses between the mirror and one of the supporting pieces.

Figure 4.9 shows vertical traces of the light sheet at each side of the recordable area in the experimental tank. On the side closest to the scanning mirror box, the light sheet was fairly flat, with some small deviations at the bottom. However, on the side furthest from the spinning mirror box, much larger deviations can be seen at the bottom of the sheet. This section was invariably below the source height, and illuminated areas of low concentration gradients. As such it was not assumed to be of concern.

4.3.1.3 Scanning mirror

Two features of the scanning mirror employed had the potential to affect results. The first was its rotational speed. Although fluctuations in rotational speed were unlikely to change the total light power transferred to a given section of the light sheet over a 'long enough' time period, that light or its effect (*i.e.* the fluorescent light) could be detected differently by video cameras or power meters. A high-speed photo-diode was used to count the rotational frequency of the scanning mirror, and for both motor-controllers employed it was found to be extremely precise ($\pm 0.013\%$).

Secondly, there was the possibility that the mirror might move on its bearings, and that this could alter the input signal. Directly checking for this was difficult, and therefore the standard calibration systems were relied upon to make appropriate corrections.

4.3.2 Camera

4.3.2.1 Static optical distortion

Many types of optical distortion are possible in the recording of images by some device. The most common is that of barrel or pincushion distortion, generated typically within camera lenses. These distortions, demonstrated diagrammatically in Figure 4.10, are radially symmetric about a central point that may or may not be at the image centre. They may be corrected by altering the constants c_0, c_1, c_2 and c_3 of the following equation, after Ojanen (1999):

$$\vec{r_u} = (c_0 + c_1 \cdot ||\vec{r_d}|| + c_2 \cdot ||\vec{r_d}||^2 + c_3 \cdot ||\vec{r_d}||^3) \cdot \vec{r_d} \tag{4.2}$$

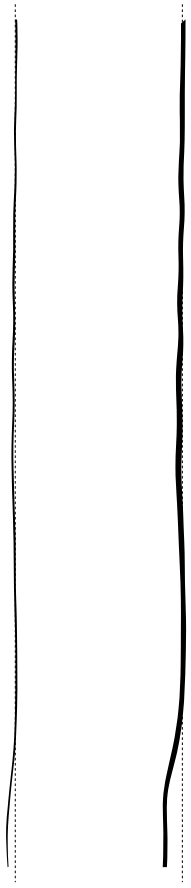

(a) (b)

Figure 4.9: Vertical traces of laser light sheet at right (4.9a) and left (4.9b) extremeties of area visible to digital video camera (nearest and furthest away from parabolic mirror respectively), with straight dashed lines plotted behind

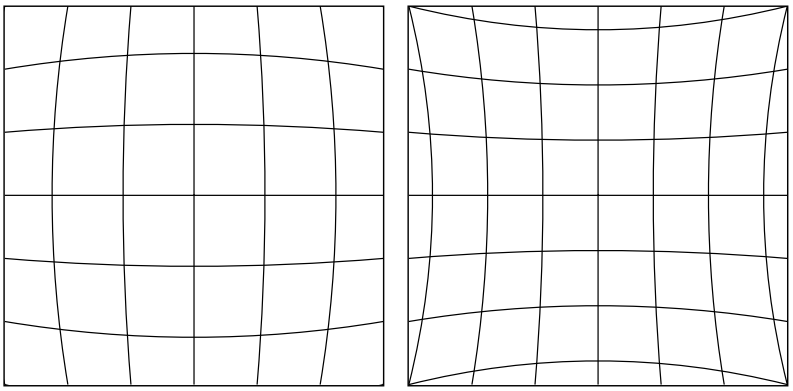

(**a**) Barrel distortion (**b**) Pincushion distortion

Figure 4.10: Barrel and pincushion distortion simulations

where $\vec{r_u}$ is the undistorted (or destination) pixel location and $\vec{r_d}$ is the distorted (or source) pixel location.

A frame holding a regular grid of tensioned string was constructed in order to test for barrel or pincushion distortion. When placed in the camera's field of view and recorded, a slight pincushion distortion was evident, but this was deemed to be small enough to be insignificant.

Camera focus was also potentially significant under this category. In most cases the jet source was used as a focus reference, and live images were magnified to increase focusing accuracy. PTV images recorded by a later worker using the same camera and light sheet system were found to be slightly out of focus in the central area, although attempting to correct this caused outer parts of the image to go out of focus instead. Out of focus areas do not reduce light intensity in the camera, but rather smear that light over a greater number of pixels than it should be. Thus, high concentration-gradient areas would not have been quite so distinct. Although this will have affected temporal statistics somewhat, its effect can be assumed to be small as camera focus was still largely correct. Errors on temporally-averaged data likewise can be assumed negligible[1].

Bubbles and other smearing on glass panels could in a similar manner distort the fluoresced light as it travelled towards the camera. Before tank filling, glass walls were cleaned with glass cleaner such as *Mr. Muscle* (JohnsonDiversey). Often surfaces were also wiped with methylated spirits in order to hinder bubble formation. Prior to each experiment bubbles were wiped off walls with a sponge brush.

Parallax was unimportant for the current experiments. This was because the camera was stationary, and, although the fluoresced light travelling from the light sheet to the camera did not pass through the same amount of water in every part of the image, the attenuation of fluoresced light by water was constant. That is, its effect would be accounted for in the calibration process.

4.3.2.2 Extraneous light sources

It was essential that the ambient room lighting—in particular, ambient lighting as perceived by the camera—did not change during experiments and calibration recordings, and did not change between each experiment and its corresponding calibration recording. Therefore in all cases experiments were conducted in blackout conditions. Care also had to be taken that torches or computer screens used during periods when room lighting was off did not create inconsistent reflections. In one example, a computer screen left on during part of an early calibration run created a reflection off the adjacent roller door, and then off the glass on the primary tank. An image of a person leaning over a computer screen was clearly evident in a plot of RMS error for the subsequent pixel calibration fits.

Reflected laser light was an additional issue to be considered. If the primary tank was filled with water that contained dust particles or similar, the laser light would reflect off those particles

[1] This assumption can safely be made if it can be assumed that intensity fluctuations either side of the mean were approximately equal, and that the change of (true) temporally-averaged concentration over the distance affected by a given pixel's smearing was small. While these assumptions do not hold true in every part of the flow field, the extent of blurring was minor, and therefore errors can safely be assumed negligible overall.

and be detected by the camera. This would create a 'starry night' effect on recorded images, as direct laser light was much brighter than fluoresced light and the particles would often enter and exit the light sheet quickly.

A Schott OG 550 optical filter (50 mm by 50 mm by 2 mm thick) was used to block laser light (532 nm) while allowing fluoresced light—of longer wavelength—to pass through. It was found to be effective at cutting out all but the brightest reflections (that is, those from the largest particles), and transmitting the majority of the fluoresced light through to the camera. Pre-cleaning the tank and filtering its inlet water significantly reduced the likelihood of large particles entering the water.

Occasionally, laser light reflected off the source pipe or framing during experiments in a way that differed from its reflections during the calibration recordings. This was due to the fact that a portion of the framing was tilted out of the way during calibrations. This light was in turn reflected off the rear glass wall and towards the camera. Although not strong, it could be discerned in the recorded experimental images. In order to obstruct this light, the rear wall was painted with a non-reflective matt black acrylic paint.

4.3.2.3 Signal amplification and camera noise

All digital video cameras contain photo-detectors that convert light energy to a voltage. Analogue-to-digital converters are then used to digitise—and thus discretise—this signal. The camera used in the current research, a JAI Pulnix TM-2030CL, is a 12-bit camera, meaning $2^{12} = 4096$ discrete levels could be used to represent the analogue voltage level. Yet, in practice a fixed input light intensity to a digital video camera does not result in a completely fixed digital signal. This is because all electronic circuits are subject to random fluctuations in electrical signals, arising from a variety of sources. These random fluctuations are collectively termed 'noise'.

Digital video cameras are particularly prone to *thermal noise*, generated by the thermal agitation of electrons. Heating such cameras increases the level of thermal fluctuations. Because cameras generate their own heat, the present camera was left on continuously; allowing temperatures to remain at a stable level.

As with camera focus, noise was not a problem for temporally averaged data. More precisely stated, the fluctuation period of noise was much shorter than the fluctuation period of most turbulent eddies under consideration, so if averages were long enough to smooth the details of the turbulent field, the effect of noise would also be removed. Nonetheless, significant levels of noise can render temporal statistics unreliable—or at the least, difficult to calculate.

It was desirable to maximise the dynamic range between strongest and weakest digital intensities recorded on-camera, as this would maximise the number of discrete concentration levels that were detectable. Dynamic range could be increased by amplifying the analogue pixel voltages on-camera, prior to being converted to discrete digital greyscale levels. This was referred to as 'gain', and could be adjusted via the JAI Camera Control software.

An investigation was carried out to determine the effect of camera gain level on noise for the camera used in this study. A summary of the results is presented in Figure 4.11, which plots average fluctuation levels against average intensity for five different gain levels. It was determined that a 100% gain level was suitable provided the fluorescent intensities were (predominantly) in the upper end of the range. If for example, mean intensities were above 1760, pixel noise levels would be 3% or below. Maximising gain also had the advantage of permitting lower dye concentrations, for reasons that will be discussed in Section 4.3.3.2.

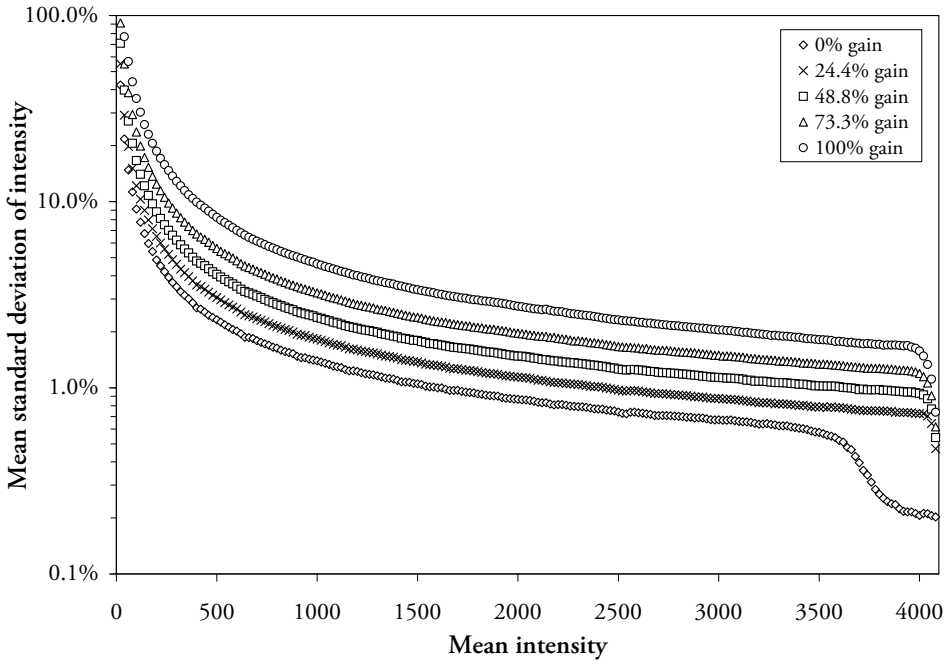

Figure 4.11: Noise as a function of mean intensity value and camera gain level (at zero offset). Every 20th data point plotted. Noise is calculated as the sample standard deviation of intensities for each pixel over 450 consecutive frames, and is averaged together with all other pixels that had the same mean intensity over those 450 frames (in all cases this was at least 150 pixels). Data were generated by recording images of a smooth greyscale gradient printed on paper, and positioned in a fixed out-of-focus location in front of the camera. Camera was left out-of-focus to reduce the effect of high-frequency content in the observed images, after Irie *et al.* (2008). A DC lamp was used to provide appropriate illumination of the gradient

4.3.2.4 CCD sensitivity

The image sensor on the experimental camera used is a 1" progressive-scan Charge-Couple Device (CCD). CCD sensors are highly reliable, and aside from the influence of noise, are known to produce temporally repeatable results. Informal tests were made to check the response of the camera to fluorescent light after room lights had been switched on for a period, and thus had saturated the camera for that time. In all cases, camera sensitivity was found to be the same as when the camera had been kept un-saturated for a reasonable length of time.

4.3.2.5 Vignetting

Vignetting (or light fall-off) is an effect where more light reaches certain regions of the image than reaches other regions. Vignetting can be caused by various forms of light obstruction, and less commonly due to spatial variation in CCD sensitivity[2]. Typically vignetting effects mean that the center of an image receives more light than the edges.

In the present study, while the lens specifications matched the camera image-sensor size, a weak vignetting effect was observed. The brightest part of the image was slightly offset from the centre. However, as calibration was performed on a per-pixel basis (see Section 4.5), the result of this effect was simply a loss of dynamic range. Therefore vignetting was not deemed to be a concern.

4.3.3 Fluorescent image

4.3.3.1 Photobleaching and stability of fluorescence level

Once a fluorophore has been raised to an excited state, it can decay back to a ground state by a number of mechanisms. The most obvious event is the emission of a photon—that is, the emission of fluoresced light. The relative fraction at which light is emitted is defined as the *quantum yield*; the ratio of the number of photons emitted to the number of photons absorbed. Magde *et al.* (2002) found the quantum yield of Rhodamine 6G in water to be 0.90 ± 0.02.

Alternate decay mechanisms can leave a fluorophore in comparatively long-lived states that allow the possibility of chemical reaction with molecular oxygen or similar. These reactions invariably destroy the fluorescent properties of the compound, and thus are broadly referred to as *photobleaching*. A fluorescent dye that is susceptible to photobleaching will gradually emit less fluorescent light over time as it is irradiated at its excitation frequencies.

To test whether photobleaching was a significant effect for the current experiments, a small (4 L) perspex box was filled with a 0.006 mg/L solution of Rhodamine 6G and irradiated by the laser light sheet for 22 hours. The results, plotted in Figure 4.12, do not show any evidence of such a phenomenon. While the difference between maximum and minimum intensities during the experiment was 4.5%, the largest fluctuations happened only over a very long time scale (a matter of hours). This can be seen in Figure 4.13, which plots normalised RMS values over periods typical of the current experiments. Fluctuations are typically only 0.3% of the intensity range for these periods. No gradual change in intensities (as might be expected with photobleaching) could be seen imposed over top of the fluctuation patterns.

4.3.3.2 Attenuation and saturation

When discussing attenuation it is useful to imagine for a moment a narrow vessel containing fluorophores mixed in water that is exposed to a laser light sheet, such that any given photon

[2]Note that Section 4.3.2.4 referred to temporal variations in CCD sensitivity, as opposed to spatial variations.

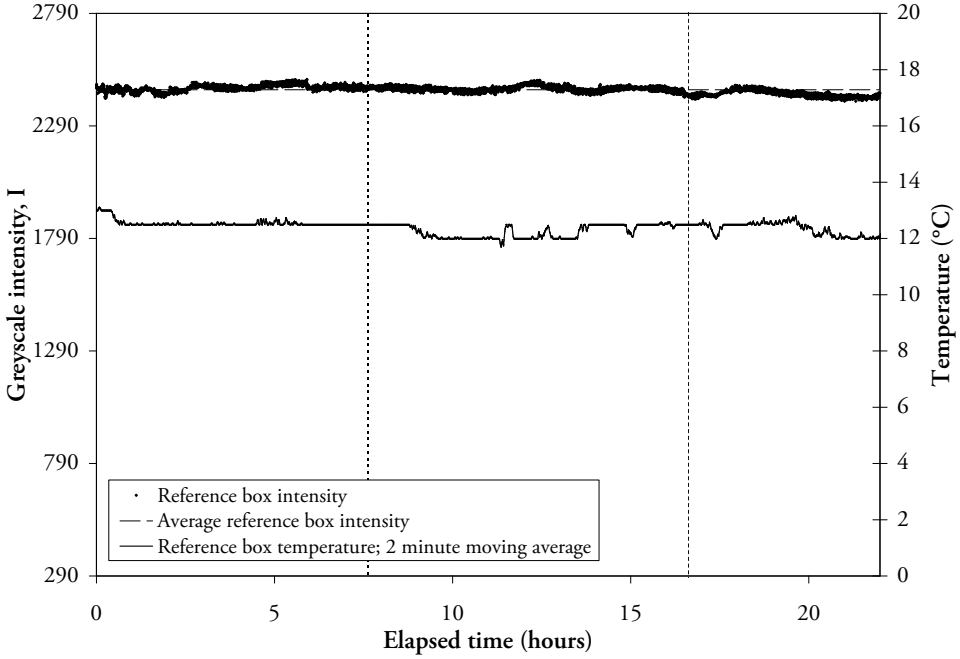

Figure 4.12: Intensity of fluoresced light from perspex box filled with 0.006 mg/L solution of Rhodamine 6G and centred across light sheet, with laser left on continuously at 2.00 W. Camera set at 100% gain and an offset of 2000; minimum of greyscale intensity axis is the corresponding zero-concentration level, 290. Temperature probe was located behind light sheet, 40 mm below surface, and 20–30 mm from lateral edges. It was sensitive only to 0.5 °C increments, so a two-minute moving average has been plotted to give a more realistic picture. When experiment was stopped a single bubble could be seen on the perspex wall facing the camera

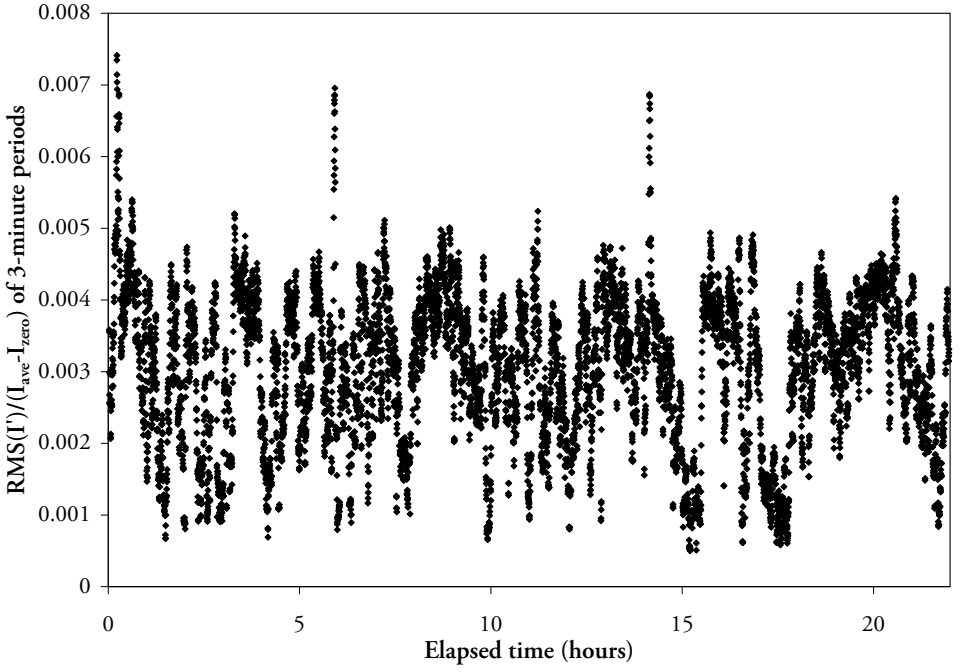

Figure 4.13: Root mean square of fluctuations from data in Figure 4.12 over moving 3-minute periods, normalised by average intensity range. Samples taken every ten seconds, so 19 samples used in each calculation

does not travel a 'long' distance through the water.

Consider two scenarios. In the first, there are very few fluorophores in the vessel, but the irradiating light intensity is very great: so much so that each fluorophore is almost constantly being hit by photons. Even though there is a vast distance between each fluorophore (on the atomic scale), there are so many photons being fired through the vessel that there is a high probability that each fluorophore will be hit within some arbitrary "short" period of time. This scenario is referred to as *saturation*. Increasing laser power (*i.e.* adding more photons) cannot further increase the amount of fluoresced light that is being emitted from the cell, and it is likely that decreasing laser power somewhat will have very little effect also. In other words, the output signal is no longer dependent on the input power level.

In the second scenario, there are many fluorophores in the vessel, and the irradiating light intensity is relatively low. Whilst the vessel is 'thin', the fluorophore molecules are small enough (and at a great enough concentration) that a significant proportion will in fact be sitting directly behind other fluorophores—that is, in the direction that light photons would be travelling. Because of this, the fluorophores on the edge closest to the light source will be more likely to be hit by photons than will fluorophores on the opposite edge, furtherest away from the light source. In this second scenario, the laser light is being *attenuated* as it travels through the tank: there is distinguishably less light getting through to the far side of the vessel, and thus distinguishably less fluorescent light generated on the far side.

It is the latter scenario—that of attenuation—that is more likely to occur in practice. In order for (full) saturation to occur, the irradiating light source must be very intense; either focused to a very small point or being emitted from a very powerful lasing device. As such it is unlikely to be a problem for practical Fluid Mechanics LIF experiments. Attenuation on the other hand is much more probable. Most fluids-related experiments are not conducted in very thin vessels, and most experiments do not use concentrations so low that one could speak of there being 'few' fluorophores in the vessel under question.

Attenuation by itself is not problematic. It must be pointed out that water itself is known to attenuate light to some extent. This can be seen from Table 4.2, which will be discussed in Section 4.3.3.4. Yet because the light travels through a constant amount of water to reach the location measured by each given pixel in an image, the effect of attenuation is fixed—in much the same way as the effect of camera vignetting is fixed. As calibration (in the current study) is performed on a per-pixel basis, and as the camera remained unmoved between experiment and calibration recording, attenuation by water is accounted for automatically.

The difficulty however lies in *changing* attenuation levels; changing either between various locations in an experiment, or between the experiment and its corresponding calibration recording. This of course is where fluorophore attenuation becomes important. When attenuation can be shown to change fluoresced intensities in a non-negligible manner over the distances and concentrations involved in an experiment, and when that attenuation is not constant, quantitative concentration data can no longer be reliably attained. Either some model must be developed to

correct for the attenuation (and possibly run in a time-dependent manner), or concentrations must be reduced to the point where attenuation over the distances of concern is insignificant.

4.3.3.3 Determining appropriate flurophore concentrations

It was important therefore to determine the concentration of Rhodamine 6G at which laser attenuation began to occur.

Figures 4.14 and 4.15 plot greyscale intensity across a horizontal line in a medium-sized (750 mm long by 380 mm high by 100 mm deep) perspex tank for different fully-mixed Rhodamine 6G solutions, created by repeatedly diluting a 1 mg/L solution by a factor of two. The laser light enters from the left hand side of the figure and exits on the right. It can be seen that for high concentrations, greyscale intensity plunges dramatically in a short length, leaving very little signal through the remainder of the tank. Greyscale intensity for low concentrations is not entirely uniform, due to the vignetting effect mentioned in Section 4.2. Beyond 0.0078 mg/L, attenuation appears to have become minimal.

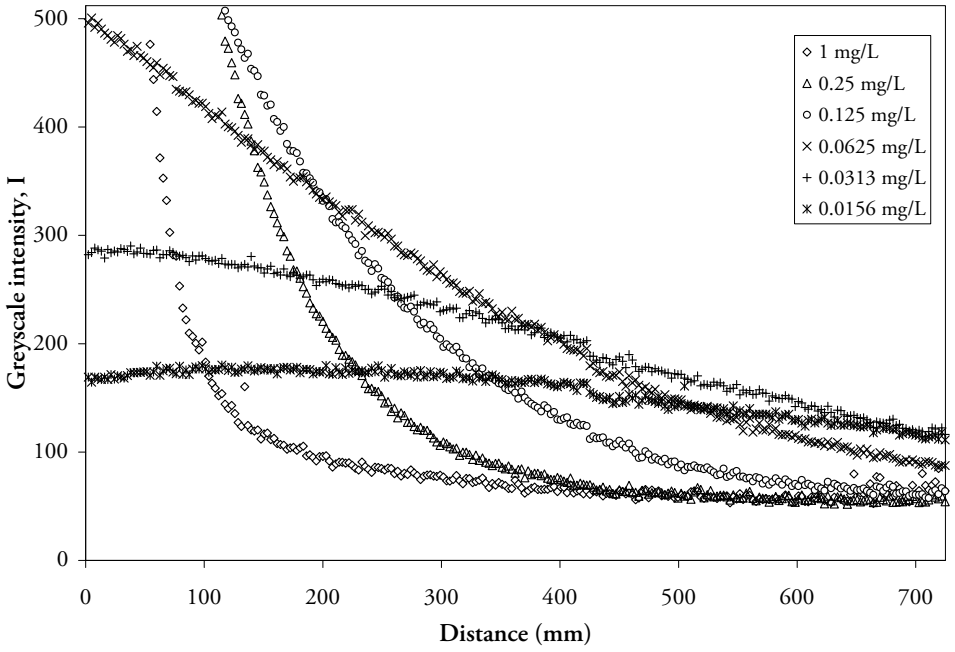

Figure 4.14: Greyscale intensity along an image line for various concentrations of Rhodamine 6G. Every fifth data point plotted. Laser power at 2.00 W, camera gain at 0%, and camera offset at 1000. Dual-tap mode used, meaning the left and right side of the images are digitised by different analogue-to-digital converters; each with slightly different sensitivities. As a result there is a slight signal discontinuity at approximately 425 mm

In order to verify this in a more precise manner, a perspex cell 1200 mm wide (slightly less than the maximum possible viewing width) was filled with concentrations of Rhodamine 6G between 0.012 mg/L and 0.0006 mg/L, paying particular attention to dilution accuracy. Figure 4.16 plots vertically-averaged greyscale intensity, from the first 160 mm of this cell that light travelled through, with each data set normalised against its average greyscale intensity value over

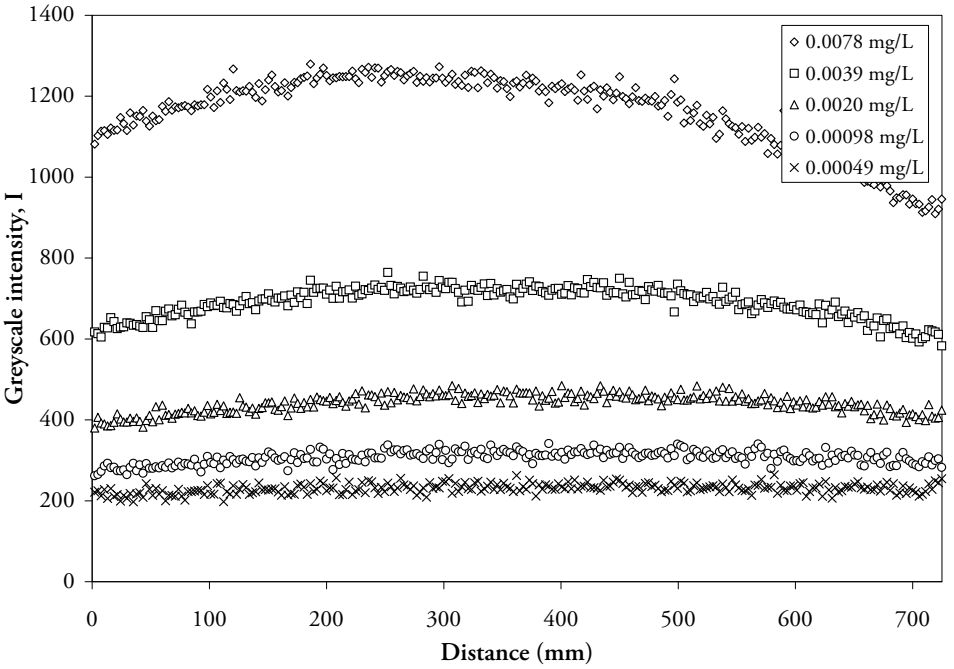

Figure 4.15: Same as Figure 4.14, but with camera gain at 100%, camera offset at 1700, and single tap mode used (meaning no artificial signal discontinuities)

the same area. Data sets fall almost entirely upon each other, and follow a remarkably consistent pattern. This confirms that attenuation is not significant over this distance at these concentration levels. Note that while the cell was filled to a uniform concentration, and likely fluoresced at a similar rate across its width, camera vignetting[3] meant that in this area (on the edge of the image), recorded greyscale intensities were rising with respect to distance.

Figure 4.17 plots Rhodamine 6G concentrations against raw greyscale intensities for three discrete locations within this same area, and demonstrates that, in these conditions, the data follows a very linear relationship at least until 0.012 mg/L of Rhodamine 6G.

Figure 4.18 extends the horizontal axis of Figure 4.16 out to the far edge of the cell. It is immediately apparent that the data does not continue to collapse upon itself indefinitely. In each case camera vignetting creates an 'arch' upwards and then back down, but the three highest concentrations (0.006 mg/L and above) show progressively greater intensity deviations from that of the two lowest concentrations. If attenuation through the cell was insignificant, each normalised data set could be expected to have a consistent shape: either to collapse onto each other or to be 'stretched' to the same extent either side of its maximum. Thus this data shows evidence of attenuation in concentrations of 0.006 mg/L and above.

By way of additional confirmation, Figure 4.19 plots the greyscale intensities from the 0.0024 mg/L and 0.003 mg/L data sets; this time normalised by the average value of each across the entire visible width (1012 mm) and shown with a much narrower vertical scale. These two datasets are very consistent, suggesting minimal attenuation.

[3] See autorefs:vignetting

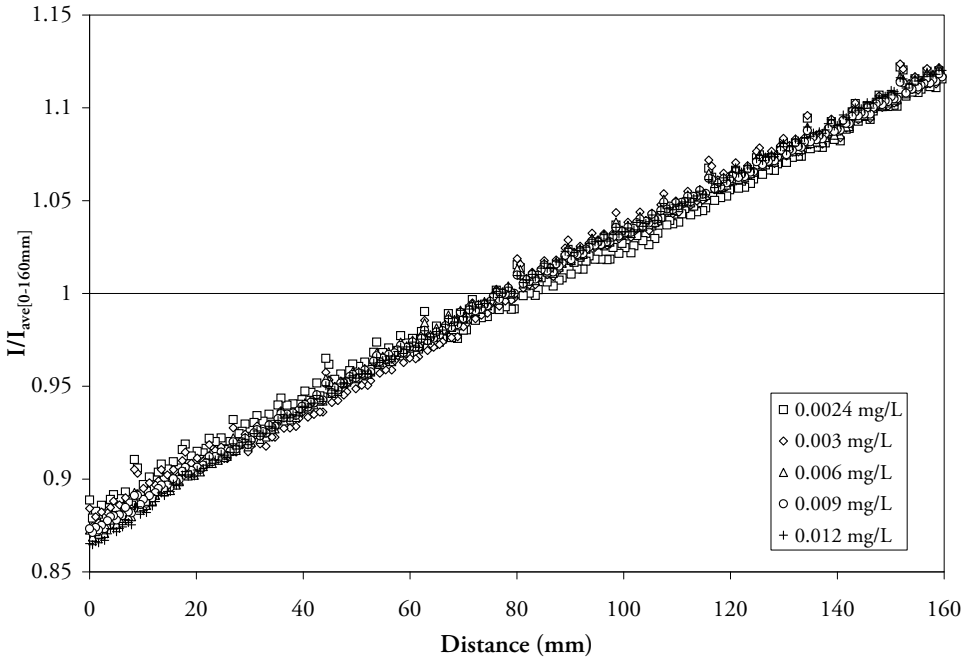

Figure 4.16: Greyscale intensity, I, averaged vertically across 72 mm (130 pixels); plotted as a function of horizontal distance for the first 160 mm of the image and normalised by the average intensity across this same distance. Distances are measured from side closest to light source; cell started approximately 180 mm prior to edge of image. Solutions were dilutions of header tank fluid containing 0.06 mg/L Rhodamine 6G and 3.3% salt by weight. Laser power was 2.00 W, camera gain was at 100% and camera offset at 2000

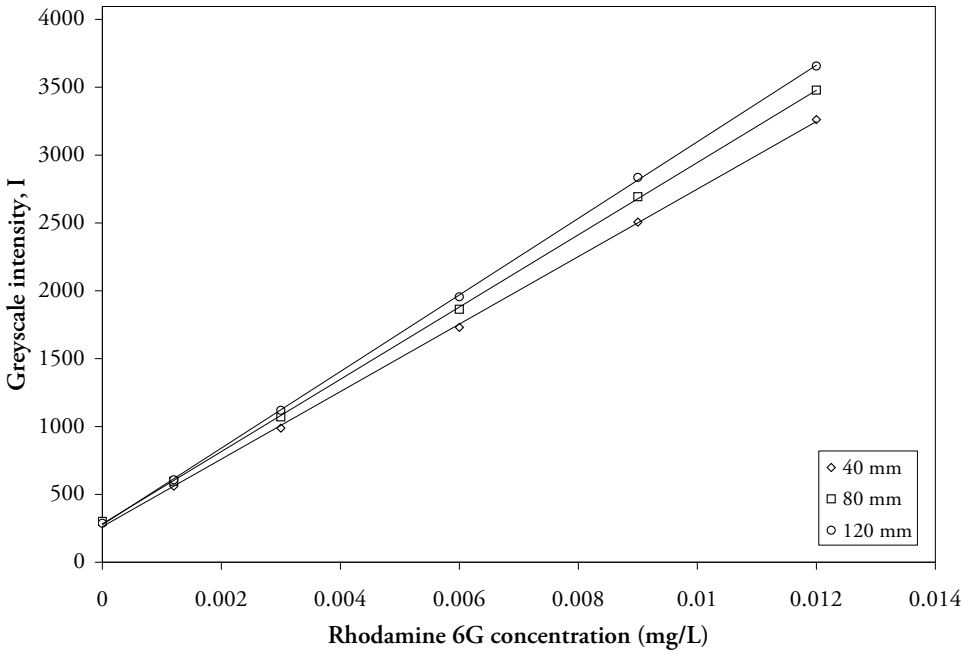

Figure 4.17: Greyscale intensity averaged vertically across 72 mm (130 pixels) at different horizontal locations from edge of cell, as a function of Rhodamine 6G concentration. Linear best-fit lines are fitted to each data set. Laser power was 2.00 W

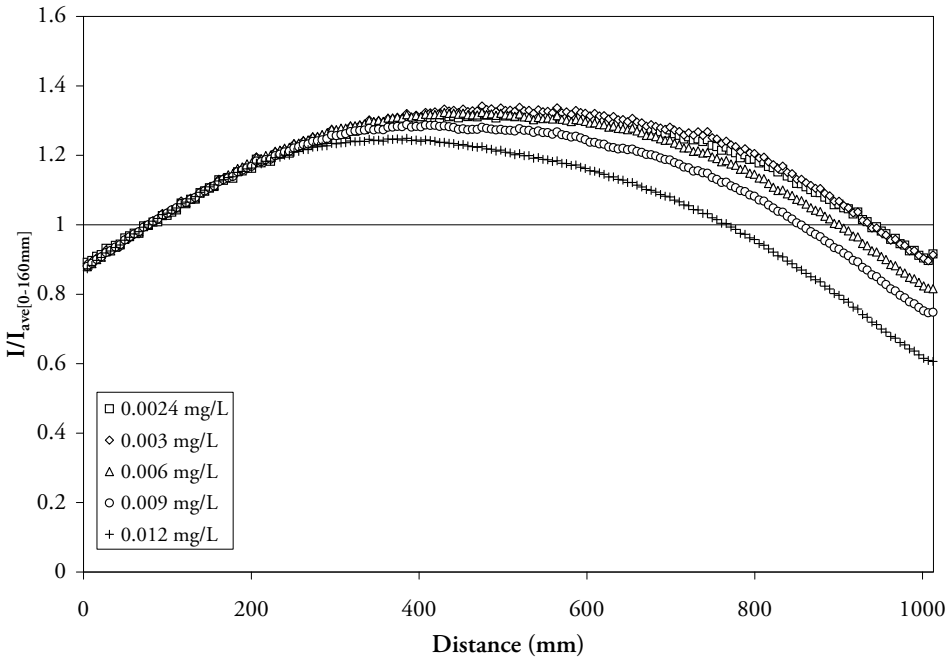

Figure 4.18: Same as Figure 4.16 but data plotted across all of calibration cell within image (1012 mm), and only every tenth data point displayed

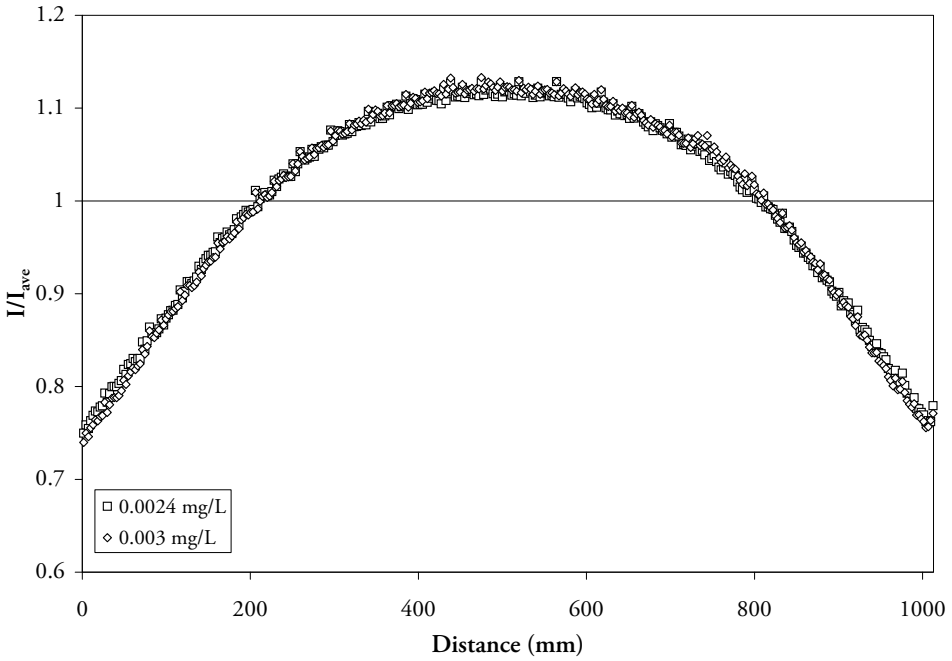

Figure 4.19: Greyscale intensity averaged vertically across 72 mm (130 pixels); plotted as a function of horizontal distance across all of calibration cell within image (1012 mm) and normalised by the average intensity across the same area. Distances same as defined in Figure 4.16. Every fifth data point plotted

The plots given thus far (Figures 4.14, 4.15, 4.16, 4.18 and 4.19) have been given in terms of a spatially-fixed perspex cell; with only concentration being varied. In experiments, mixing will mean typical concentrations are in fact much less than the maximum which we desire to detect. Yet, the distance which light must travel through fluorophores to get to any given location will change with time. Thus it is important to verify the consistency of light generated from a perspex cell placed in different locations, with respect to some fixed ('calibration') location.

Figure 4.20 plots fluoresced light intensity from a fixed area in the aforementioned perspex cell, as the cell is moved closer or further from the light source—that is, as light passes through more or less fluorescent dye. A Rhodamine 6G concentration of 0.003 mg/L is used. Each dataset is plotted with respect to calibration images taken with the cell furthest away from the light source. It is apparent that at the concentration under consideration, attenuation was insignificant up to a 143 mm offset from this reference location (or thereabouts). That is, the laser intensity back-calculated for each pixel using images obtained at the reference location was approximately what it actually was (2.00 W) up to 143 mm away. The exact method used to perform image calibration is discussed in the following sections; it is enough at this point to note that given the data in this figure and in Figure 4.16, attenuation of 0.003 mg/L Rhodamine 6G across distances of 160 mm can safely be assumed insignificant.

4.3.3.4 Laser power as an analogue for concentration

Although the above data were generated using a laser power of 2.00 W, tests carried out at 1 mg/L of Rhodamine 6G revealed that lowering laser power alone did not reduce attenuation. This can be expected, as the probability that a given photon will pass through a region of fluorophores unabsorbed is dependant only on the density of fluorophores in that region, not on the number of other photons that are passing through at the same time. Nevertheless, at concentrations below 0.006 mg/L it was observed that relative laser power was a good analogue to relative Rhodamine 6G dilution. This was a useful result, as it enabled calibrations to be carried out with a single solution of Rhodamine 6G—simply by varying laser intensity.

Figure 4.21 plots spatially-averaged intensity in a small perspex box for varied concentration and then varied wattage, while keeping the other parameter fixed. The intensity recorded over the same area for a fresh water (0 mg/L) cell under 2 W laser power was subtracted from each value. Both datasets show a strongly linear behaviour, and almost identical values for equivalent concentrations and wattages[4]. No evidence can be seen for saturation or attenuation in the concentration dataset.

Calibration under varied wattage rather than varied concentration is not a new concept. Pun (1998) found the same type of behaviour as seen here for Rhodamine 590 illuminated by a 6 W Argon laser (514 nm).

[4]The linear best-fit through the varied-wattage dataset was 0.00151638 W/I, and through the varied-concentration dataset was 0.0014968 W/I (assuming 0.006 mg/L Rhodamine 6G was the same as 2 W); or 1.3% different. NB: fits enforced a crossing at (0,0).

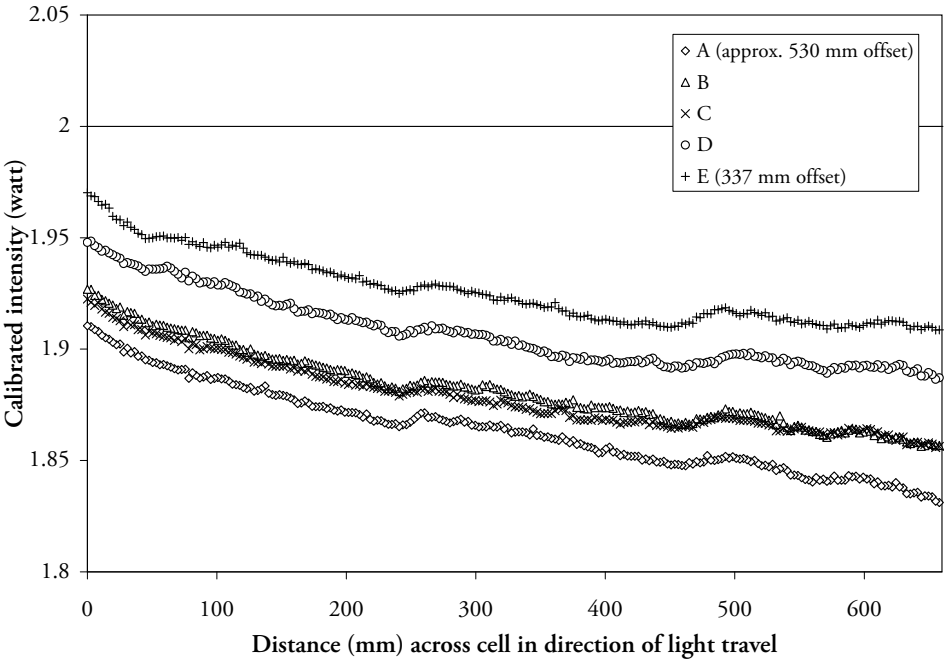

(**a**) Locations closer to light source

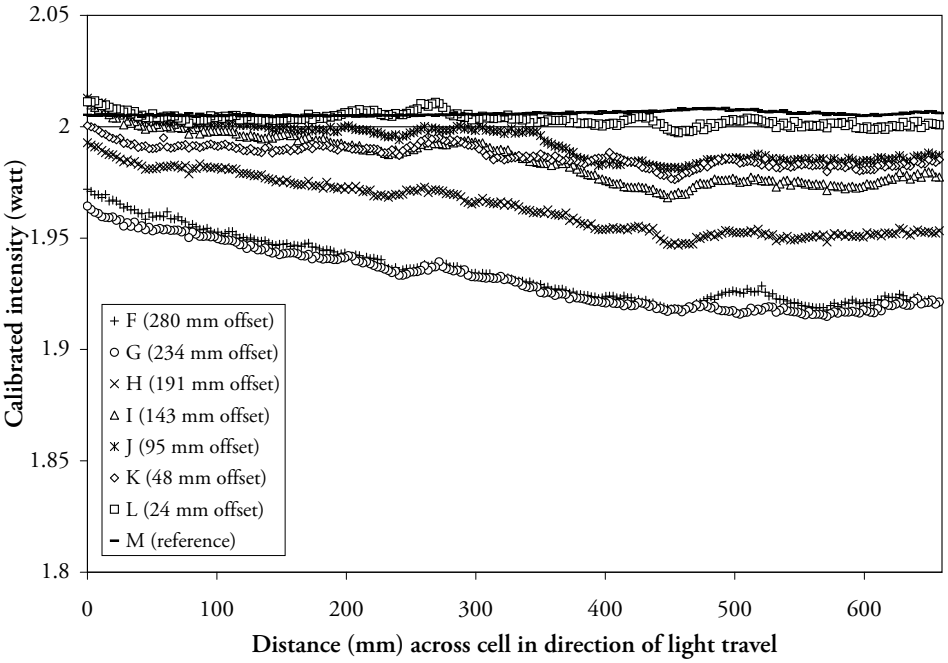

(**b**) Locations further from light source

Figure 4.20: Calibrated signal intensity across fixed area within tank filled with fixed 0.003 mg/L Rhodamine 6G solution in calibration cell, as cell itself was moved away from light source and towards the reference location ('M' in 4.20b). Data is calibrated with respect to images from reference location, and spatial offset values given in legend are the distance of the cell from that position. Data is averaged vertically over 448 mm and is plotted in terms of wattage (as an uncorrected artifact of the calibration procedure); where 2 W is equivalent to a concentration of 0.003 mg/L Rhodamine 6G, and 0 W is equivalent to a 0 mg/L solution. Every fifth data point plotted

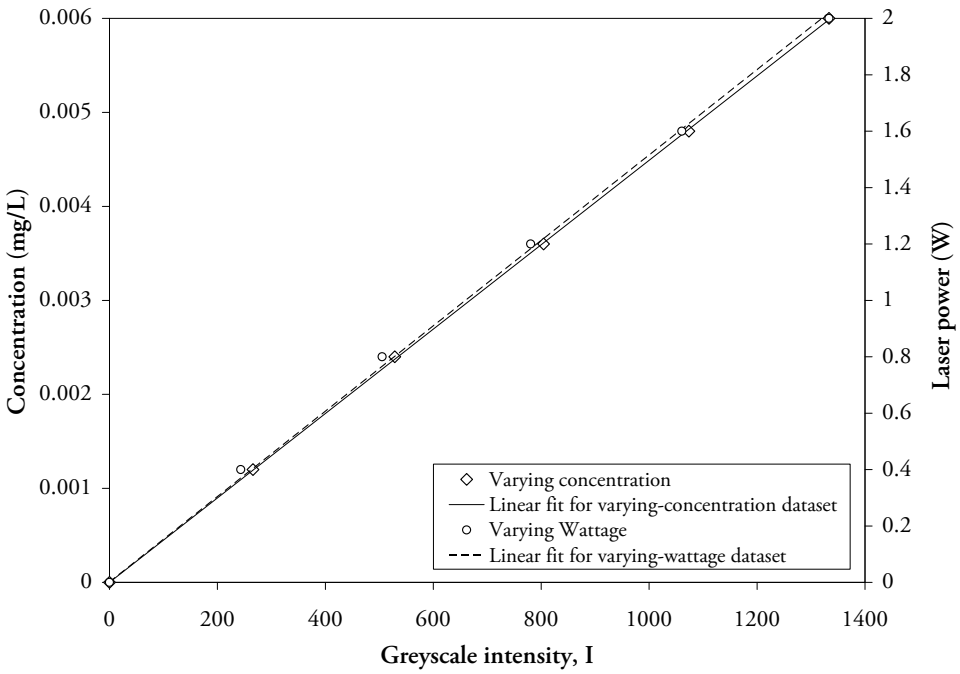

Figure 4.21: Spatially- and temporally-averaged greyscale intensity for small (4 L) perspex box under varying wattage levels (with Rhodamine 6G concentration fixed at 0.006 mg/L) and varying concentration levels (with laser power fixed at 2 W). Averaging made over an area 118 mm wide by 140 mm high, and over a time period of approximately 30 seconds

An additional factor of concern was whether or not the calibration apparatus itself—built of perspex—was attenuating light. Perspex pieces were placed on laser and camera sides of a cell containing Rhodamine 6G, and the greyscale-intensity of fluoresced light was recorded. Table 4.2 outlines the results, and demonstrates that the attenuation of light by these additional pieces of perspex is small. In the scenario where the surrounding tank was full of water (Figure 4.2), the results are likely within the margin of error of the recording apparatus.

Table 4.2: Attenuation of laser light and fluoresced light by water and perspex. Greyscale intensity I averaged spatially over approximately 80 mm by 190 mm, and temporally over 200 frames (12.5 s)

(**a**) Cell sitting in empty tank

	I_{ave}	I_{ave}/I_{ref}
Cell only	974.560 ($=I_{ref}$)	—
Perspex on laser side	940.587	96.5%
Perspex on camera side	952.903	97.8%
Perspex on both sides	931.264	95.6%

(**b**) Cell with surrounding tank full of water

	I_{ave}	I_{ave}/I_{ref}
Cell only	941.255 ($=I_{ref}$)	—
Perspex on laser side	939.946	99.9%
Perspex on camera side	944.890	100.4%

4.3.3.5 Dynamic optical distortion

When a wave changes its speed after passing from one medium to another, its frequency remains constant but its wavelength changes. Additionally, if the wave did not strike the interface between the two mediums from a perfectly normal direction, the wave will change direction. This change in direction is known as *refraction*, and is governed by Snell's law, which can be written as

$$n_1 \sin\theta_1 = n_2 \sin\theta_2 \tag{4.3}$$

where subscripts denote the medium, θ is the angle between the normal to the interface and the direction at which the wave was travelling, and n is the refractive index, defined as

$$n = \frac{c}{\upsilon_p} \tag{4.4}$$

where c is the speed of light in a vacuum and υ_p is the phase velocity of light through the medium under consideration (in this case the phase velocity is simply the wave velocity). Air has a refractive index of approximately 1.0.

Refraction through fresh water ($n \approx 1.33$) and glass ($n \approx 1.5$) between the camera and the light sheet was not important if in fact the camera view was aligned perpendicular to tank, as it was set up to be. This refraction would only serve to slightly narrow the camera's field of view.

Much more problematic however, was the difference in refractive index between fresh water and salt water. Table 4.3 demonstrates this difference for salt concentrations up to 6% by mass. As mentioned in Section 4.2, salt was used to create an elevated density in the source fluid. Thus, during an experiment involving a positively- or negatively-buoyant jet, laser light would travel through a mixture of both fresh water and salty water at a variety of concentrations. Turbulence would ensure that any interfaces were continually moving, and that their orientation was rapidly changing. Because the source fluid was being rapidly diluted, differences of refractive index were typically small.

Across small distances—approximately up to 200 mm—refraction was observed to be minimal; often even undetectable. However, at larger distances, refraction caused the light sheet to 'flicker'. In places the light sheet became darker, much like it had been shadowed by some object nearer the light source. In other places the light sheet became brighter. Distinct horizontal 'lines' appeared and disappeared rapidly. These lines were a product of the light sheet being deflected, widened or narrowed in various locations. Figure 4.22 plots an instantaneous image of lines generated in a fixed-concentration cell by a vertical buoyant jet. When the jet was turned off, no lines were visible.

As a consequence, instantaneous concentrations calculated from negatively buoyant jets were less reliable, and particularly so furtherest away from the light source; that is, nearest the discharge source (see Figure 4.5).

Various authors have proposed methods to match experimental refractive indices while re-

Table 4.3: Density and refractive index of various concentrations of Sodium Chloride (NaCl) dissolved in water (H_20) at 20 °C, from Lide (2004, p. **8**-78). Mass % is the mass of solute divided by the total mass of solution, expressed as a percentage. Refractive index is measured relative to air, at a wavelength of 589 nm

NaCl Mass %	Density (g/cm^3)	$\Delta\rho$	Refractive Index
0.0	0.9982	—	1.3330
0.5	1.0018	0.36%	1.3339
1.0	1.0053	0.71%	1.3347
2.0	1.0125	1.43%	1.3365
3.0	1.0196	2.14%	1.3383
4.0	1.0268	2.86%	1.3400
5.0	1.0340	3.59%	1.3418
6.0	1.0413	4.32%	1.3435

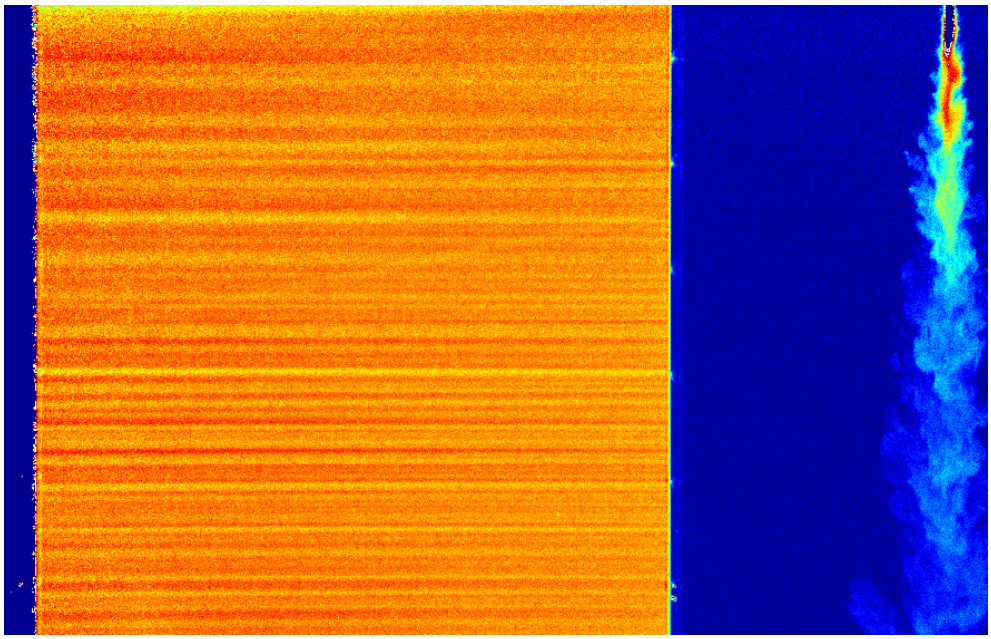

Figure 4.22: Calibrated instantaneous image of a vertical buoyant jet beside perspex cell containing a fixed concentration of Rhodamine 6G. Light sheet entered from right hand side of image. Jet source fluid contained 0.03 mg/L Rhodamine 6G, and had a density 2.94% greater than the ambient fluid (fresh water). Perspex cell was filled with a 1:10 dilution of the header tank fluid. Horizontal scale is 1075 mm

taining density differences. McDougall (1979) used Epson salt and sugar in such a manner that avoided double diffusive (fingering) effects. Hannoun (1985) investigated other solutes and concluded that ethanol and common salt (NaCl) was a better combination, particularly with respect to cost per unit volume. Daviero *et al.* (2006) extended this approach to LIF experiments in a 3400L density-stratified tank. Yet to obtain the desired density difference ($\Delta\rho \approx 0.03 g/cm^3$) in the current facilities, their method required the use of approximately 380 L of ethanol for each individual experiment. The cost, safety risk and mixing difficulty made this a prohibitive option.

Nevertheless, although refractive-index induced light sheet fluctuations altered temporal con-

centration statistics, these did not alter the temporally-*averaged* concentration field. This was because turbulence is unsteady and chaotic in nature, meaning light was refracted in a random pattern. A test was performed where a turbulent jet was discharged next to a fixed-concentration cell, and average intensity in the cell was found to be the same as it was before the jet was turned on. This data is plotted in Figure 4.23. Measured values for RMS of concentration fluctuations were also consistent with previously observed values in the jet and plume regions.

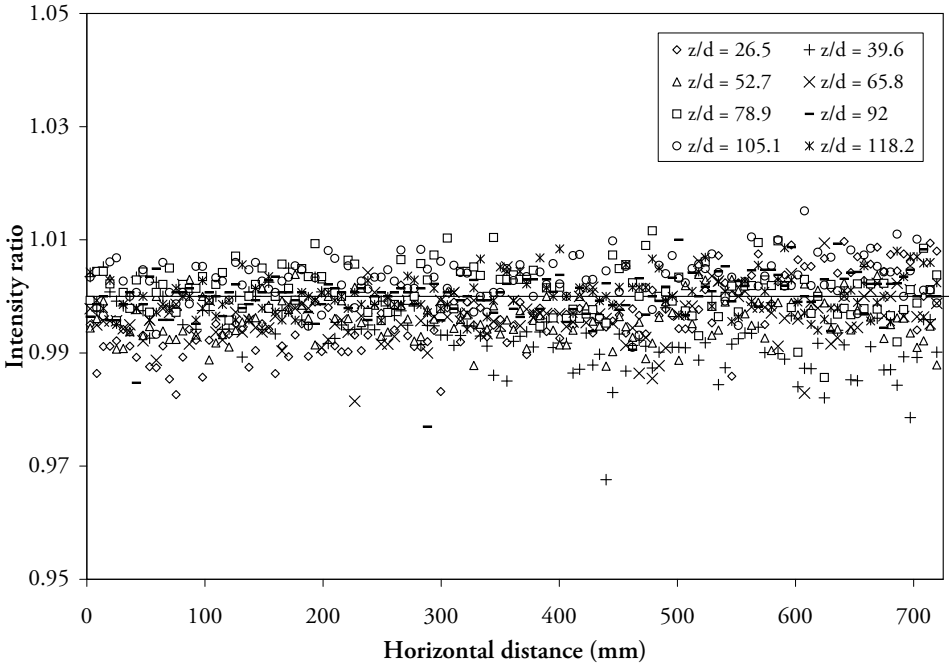

Figure 4.23: Temporally-averaged intensity values from cell with vertical buoyant jet (VBJ) running on light source side, divided by temporally-averaged intensity values of the same configuration but with VBJ turned off. Cell contained a fixed 0.003 mg/L concentration of Rhodamine 6G. VBJ source was located at -100.8 mm on horizontal axis, and fed from a 0.03 mg/L concentration of Rhodamine 6G. Every tenth data point plotted

A similar refractive effect, though likely not so severe, was assumed to be occurring with the fluoresced light travelling toward the video camera. This would have served to degrade the apparent image focus.

It should be noted that the extent of refractive distortions is largely a function of concentration gradients at the smallest eddy sizes; known as the Kolmogorov microscale η. These gradients can be shown to be greater than those generated by the the largest flow eddies for $\mathrm{Re} > 1$. Following Pope (2000, p. 186) we may write

$$\frac{\eta}{\ell} \sim \mathrm{Re}^{-3/4} \tag{4.5}$$

$$\frac{C_\eta}{C} \sim \mathrm{Re}^{-1/4} \tag{4.6}$$

where ℓ and C are length and concentration scales of the largest eddies in the flow and η and C_η

are the length and concentration scales of the smallest eddies. Thus we may write,

$$\frac{C_\eta}{\eta} \sim \frac{C}{\ell}\sqrt{\mathrm{Re}} \tag{4.7}$$

Therefore, as Re increases, so do the relative concentration gradients at the smallest scales. Yet because the largest eddy sizes are not a function of Reynolds number, this also means that absolute concentration gradients increase as Re increases. Such a result is observed and often exploited by experimentalists conducting shadowgraph and Schlieren-photography experiments, but here means that Re should be kept as low as reasonably possible. This was done by changing the source diameter, and had the practical advantage of allowing experiments at a greater range of F_0 values to be conducted within the same tank and viewing area.

It should also be noted that temperature changes can also modify the refractive index of water. Table 4.4 tabulates this effect for the range of 0–100°C. Recalling that on average, header-tank temperatures were 2.9°C greater than experimental tank temperatures—where the average experimental tank temperature was 15.4°C—it can be seen that temperature-induced refractive index changes were insignificant with respect to those generated by the salt solution.

Table 4.4: Refractive index of water at various temperatures, measured relative to a vacuum at a wavelength of 589 nm; from Lide (2004, p. **10**-232)

Temperature (°C)	Refractive Index
0	1.33432
10	1.33408
20	1.33336
30	1.33230
40	1.33095
50	1.32937
60	1.32757
70	1.32559
80	1.32342
90	1.32109
100	1.31861

4.4 Experimental Procedures

4.4.1 Calibration

The goal of the calibration process was to derive the relationship between light intensity (as recorded by the digital video camera) and the concentration of the discharge fluid—containing fluorophores—within the light sheet. Provided attenuation was not significant, this relationship would be accurate for the duration of any given experiment.

Figure 4.17 showed that attenuation of 0.003 mg/L Rhodamine 6G across distances of 160 mm can be assumed insignificant. Nevertheless, because turbulent jets mix rapidly, typical centre-plane concentrations were much less than the source concentration. Therefore in order to maximise dynamic range in the recorded images, the header tank (and thus source) concentration was set at 0.03 mg/L Rhodamine 6G. Calibrations were performed at approximately 10% solutions of the header tank fluid (*i.e.* 0.003 mg/L), in a 160 mm wide perspex cell. The cell was positioned in multiple locations in order to cover the complete camera viewing area.

Section 4.3.3.4 showed that relative laser power can be a good analogue of relative concentration, at least up until 0.006 mg/L at 2 W. This result was employed for the calibration process, so as to simplify the procedure necessary.

Calibration images were recorded approximately every week while carrying out experiments. The procedure that was developed involved lowering the aforementioned cell onto rails positioned directly above the position of the laser light sheet. After filling this cell with the appropriate header-tank solution, images were recorded from the camera for approximately ten seconds with the laser operating at 2.00, 1.60, 1.20, 0.80 and 0.40 watts respectively. In all cases the primary tank was filled with fresh water also. The cell was then moved along the rails some distance and further images recorded at the same laser wattages. In total, eight positions were required in order to cover the complete viewable area. These positions were marked out along one of the rails in order to facilitate easy location, and were determined such that there was always some overlap of area occupied by the cell when in adjacent positions.

Since the camera in use operated at a frame rate of 16 Hz, around 160 images were recorded at each location and laser power. These images were later averaged together, resulting in 40 separate averaged images. One image from each location was then displayed on screen, and the left and right edges of the cell located. These positions were then fed into software which stitched the images together, using a smooth merging curve for overlapping regions. An additional image was inferred for a 0.0 W laser power by stitching together 2.0 W images where the cell was in other locations (preferably, further away from the laser than the location in question).

4.4.2 Experiments

The procedures carried out prior to, during and after experiments were as follows.
Prior to experiments:

- Check percentage of capture hard disks used and empty if necessary
- Clean tank windows with glass cleaner and wipe down with methylated spirits
- Drain enough water from header-tank pipeline to flush pipe thoroughly

Experiments themselves:

1. Fill primary tank to set depth

2. Wait for 15 minutes and wipe off any bubbles that have formed on tank windows and surfaces of concern

3. Wait a further 15 minutes and wipe surfaces to remove bubbles again.

4. Wait one hour without disturbing tank before proceeding with experiment. If bubbles have formed again on important surfaces, wipe and wait a further hour. Check ambient motions by dropping Potassium Permanganate crystals in corner of tank: if still substantial, wait longer.

5. Close doors (mounting appropriate laser warning signs). Start flowmeter logger and laser. Turn off room lights

6. Start image capture, turn on flow to correct level, estimate time at which jet becomes established then record for further 6-10 minutes

7. Stop image capture, turn off jet and laser and stop flowmeter logger. Measure primary and header tank temperatures, then drain primary tank.

After experiments:

- Feed data through post-processing tool-chain (see Section 4.5)
- Back up data to non-capture hard disks, including at least one off-site

4.5 Post-Processing Systems

Post-processing was the means of deriving quantitative statistics from the instantaneous images collected during an experiment. Generally this involved correcting each image by the calibration data associated with that experiment. Because of the sheer volume of data collected during experiments—and in fact the level of precision attained in that data—for the most part manual analysis was neither feasible nor desirable. Computer algorithms were employed heavily to automate the majority of the post-processing chain. Human intervention was necessary for choosing which parts of each experiments to analyse, and initiating each step in the correct manner.

4.5.1 Calibration

The process of intensity-correction—and by implication concentration lookup—was carried out by fitting linear or polynomial best-fit curves for every pixel in the corresponding set of stitched calibration images, and then looking up those fits to calculate the real value of a given pixel in a given frame. That is, best-fit curves were calculated between *recorded intensity* and *laser power* for *each* of the (two million) pixels recorded by the camera, and it was those curves that determined the real value of each pixel in each frame of an experiment.

Typically second-order polynomial fits were used for this process, although in some instances first-order (*i.e.* linear) fits were made. The vast majority of pixels fitted linear curves very accurately. Frequency plots of one goodness-of-fit statistic, the R^2 value, are given in Figure 4.24 for a calibration performed on 18th Jan 2010.

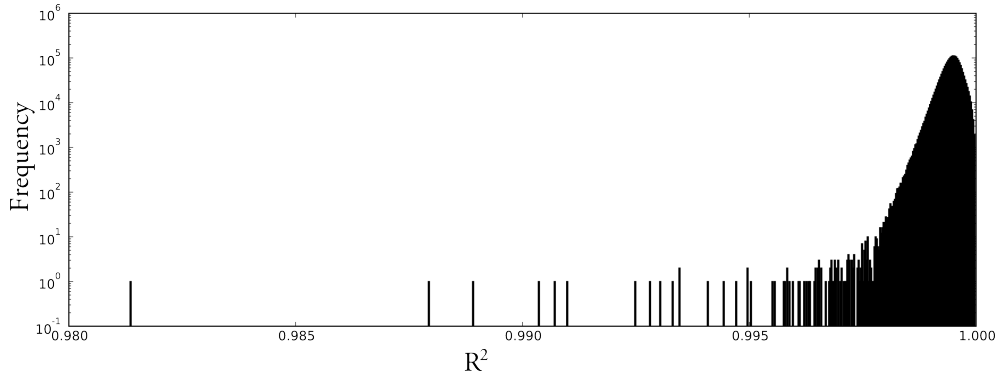

(**a**) First-order curve fits

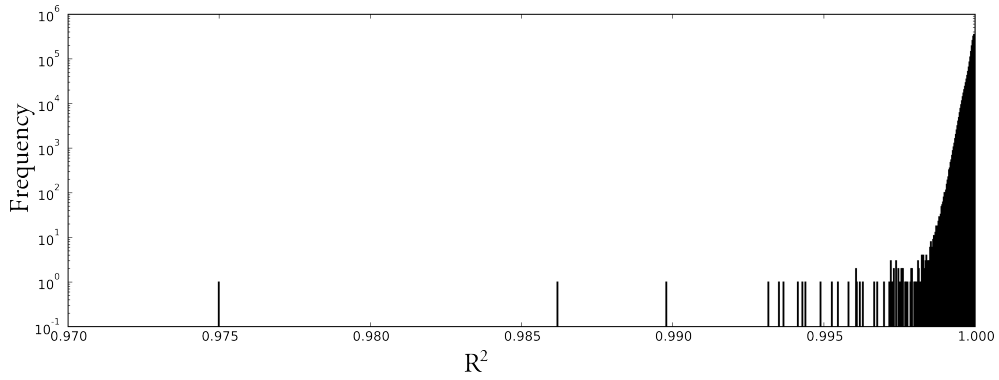

(**b**) Second-order curve fits

Figure 4.24: Frequency plot of coefficient-of-determination (R^2) values for curve fits between pixel intensities recorded during calibration and the corresponding laser power, for each pixel in camera image. R^2 calculated as $1 - SS_{\text{err}}/SS_{\text{tot}}$. $SS_{\text{tot}} = \sum_i (y_i - \bar{y})^2$ and $SS_{\text{err}} = \sum_i (y_i - f_i)^2$, where data set values are y_i and modelled values are f_i

Curve extrapolation was allowed below the minimum laser power considered and above the maximum; up to 50% of the total range. Invariably the maximum and minimum laser powers were 2 W and 0 W; thus extrapolation was made out to the equivalent of 3 W, or 0.0045 mg/L Rhodamine 6G. This extrapolation was considered acceptable because these concentrations only occured in a narrow area near the discharge, furtherest away from the light source. As such, extrapolation allowed the extraction of near-discharge data that was greater than the nominal 10% calibration dilution but was below the camera saturation level.

Figure 4.25 plots spread rate and dilution rate from four separate pure jet experiments conducted with the present apparatus against data by two other experimentalists. Datasets in both plots are very consistent, providing assurance that the system as a whole was collecting accurate data.

Some experiments conducted during the present study were discarded because of faults in the calibration or experimental difficulties such as bubbles forming on tank walls during the

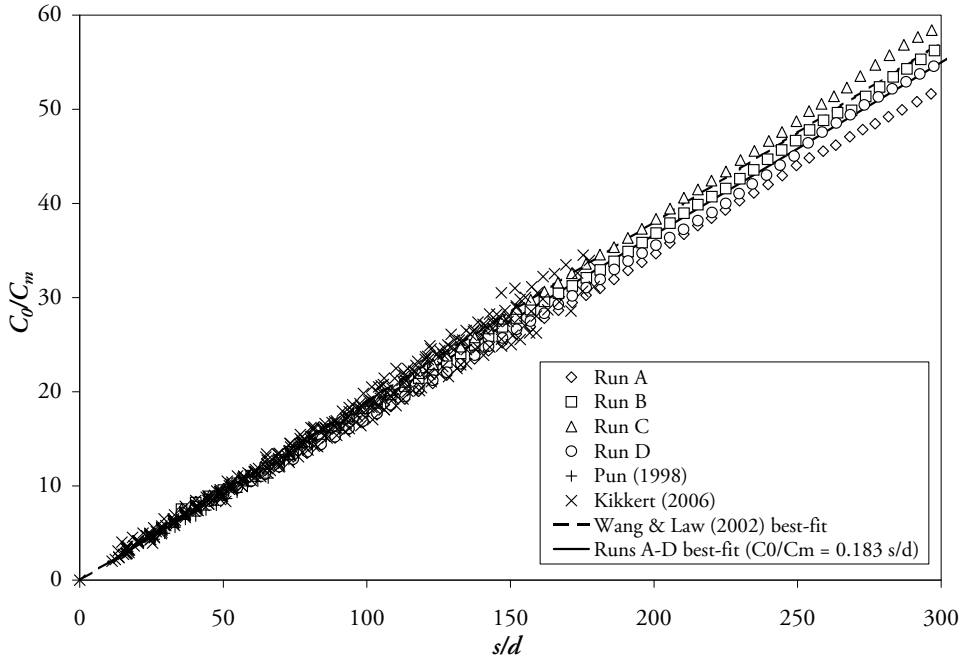

(**a**) Dilution rate for pure jet

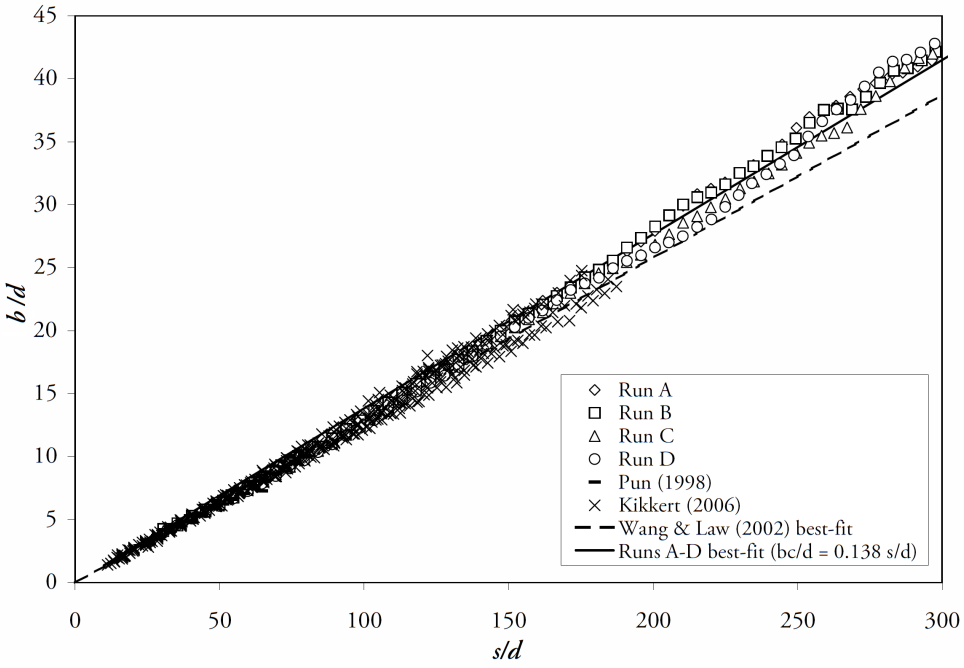

(**b**) Spread rate for pure jet

Figure 4.25: Dilution and spread rates of pure jet, compared with data from Pun (1998) and Kikkert (2006)

recording period.

4.5.2 Determination of initial concentration

Although the calibration process provided a preliminary estimate of the initial source concentration (C_0), where possible this was determined based on analysis of dilution behaviour in the jet region. This was considered to be the most reliable method, and reduced the possibility of accumulated error.

In the jet region, any buoyancy-induced instabilities are small, and their effect is not expected to extend far into the flow. Kikkert *et al.* (2007), Lai (2010) and others support the fact that flow behaviour is jet-like as it rises to maximum height; particularly with respect to centreline dilution rate. This dilution rate can be readily derived, and shown to be a simple function of distance from the source.

In a jet, buoyancy-generated momentum is negligible and momentum flux is conserved. In top-hat terms, we may write:

$$\frac{dM_\star}{ds_\star} = 0$$
$$\frac{d}{ds_\star}(\hat{g}_{T\star} Q_\star) = 0$$

Recalling that at the source the non-dimensional variables $M_\star$, $\hat{g}_{T\star}$ and $Q_\star$ are equal to 1.0, we have

$$\frac{1}{\hat{g}_{T\star}} = Q_\star = 4u_{T\star} b_{T\star}^2$$

Rearranging the relationship $M_\star = 4u_{T\star}^2 b_{T\star}^2$ in terms of $u_{T\star}$ and substituting:

$$\frac{1}{\hat{g}_{T\star}} = \frac{4b_{T\star}^2}{\sqrt{4b_{T\star}^2}} = 2b_{T\star}$$

Finally, employing the observation of constant spread rate with respect to path length in a turbulent jet, we write

$$\frac{1}{\hat{g}_{T\star}} = 2k_T s_\star$$

where k_T is equal to $\frac{db_{T\star}}{ds_\star}$.

From literature and from experimental dilution plots presented in Chapter 5, it can be deduced that negatively buoyant flows are jet-like up to—and possibly beyond—$s/F_0 d = 2.0$. Based on linear slope-fitting of negatively-buoyant experimental spread data up to this point, the

average concentration spread rate in the jet region of this flow is calculated to be

$$\frac{d(\lambda b)}{ds} = 0.1253 \tag{4.8}$$

Employing the top-hat conversion factors in Section 3.3.1 and assuming a standard jet λ value ($\lambda = 1.217$ as per Section 3.3.1), we find $k_T = \frac{0.1253}{1.217}\sqrt{2/1.1} = 0.139$. Consequently, $\frac{1}{\hat{g}_\star} = 2 \times 0.139 s_\star \times \frac{1.076}{1+1/1.217^2} = 0.1783$. Alternatively we may write,

$$\frac{\hat{g}_0}{\hat{g}_\ell} = \frac{1}{k_{jc}} s_\star \tag{4.9}$$

where, reflecting the limited accuracy of the underlying coefficients, we define k_{jc} to be equal to 5.6.

Figure 4.26a plots dilution data from selected inclined negatively buoyant jet experiments, where C_0 has been initially estimated from the calibration process. Two experiments in this figure are clearly inconsistent (and are in fact extreme examples of this behaviour). By fitting a best fit slope to the data (*i.e.* the relationship $C_0/(C_m F_0) = m \times s/(dF_0)$, where m is an unknown), we may calculate a more accurate example of C_0. Figure 4.26b shows the same plot after dilutions from these two experiments were adjusted based on this more accurate estimate.

Where estimates based on the jet solution were within 5% of those based on the calibration process, the latter were adopted. The frequency of this situation had no correlation with inclination, source diameter or initial Froude number. Some experiments had no data collected within the $s/F_0 d \leq 2.0$ region, so likewise used the calibration process estimate of C_0. It is important to point out that the accuracy of trajectory and spread data was not affected in any way by the estimate of initial concentration value.

In some early experimental data, the condition that an average would only be calculated for a pixel "if not more than 5% of frames had been ignored" (Section 4.5.4.1) was not applied. As a result, some average concentration data near the source was lower than would be expected, and thus the corresponding dilutions were higher. This potentially affected the first few data-points in series plotted in Figure 4.26 and similar figures, but was highly unlikely to cause anomalous estimates of C_0.

4.5.3 Selection of images for analysis

Turbulence is by definition a flow behaviour characterised by random and chaotic flow behaviour; yet simultaneously this behaviour also has an element of orderliness and predictability. That is, over large enough temporal or spatial scales, distinct patterns can be discerned. For the current study, the statistic of most interest was the *average* of the concentration field over time, for a constant set of source conditions. In particular, source flowrate and concentration (the latter as perceived via fluorescence) were required to be steady, and ambient motions in the tank were to

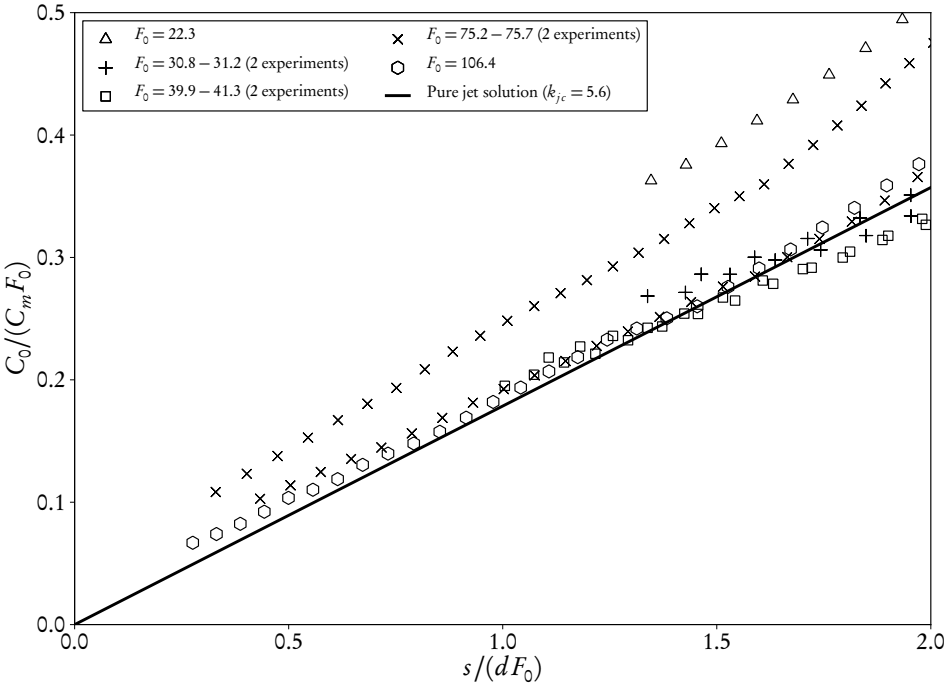

(**a**) C_0 estimated from calibration process

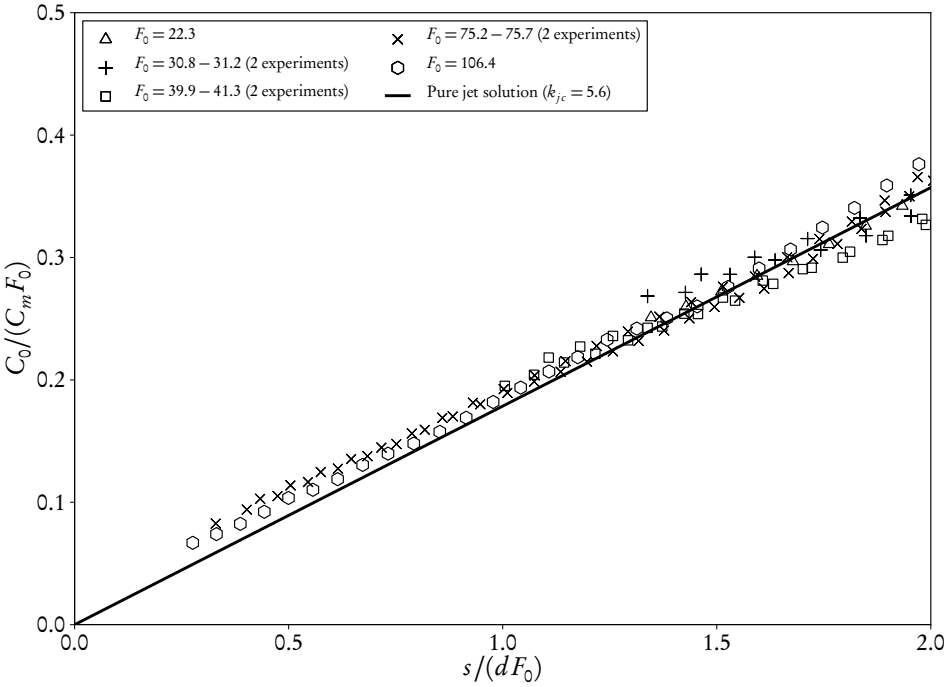

(**b**) C_0 estimated from pure jet solution ($k_{jc} = 5.6$)

Figure 4.26: Minimum dilution in jet region from selected 30°, 45°, 70° and 75° experiments

be negligible.

Readings from a flowmeter installed upstream of the source were logged to computer for the majority of experiments performed in the current study, providing a reliable measure of changes in source flowrate. These data were analysed after each experiment, and almost as a rule fluctuations were negligible with respect to the average value. A typical plot is given in Figure 4.27.

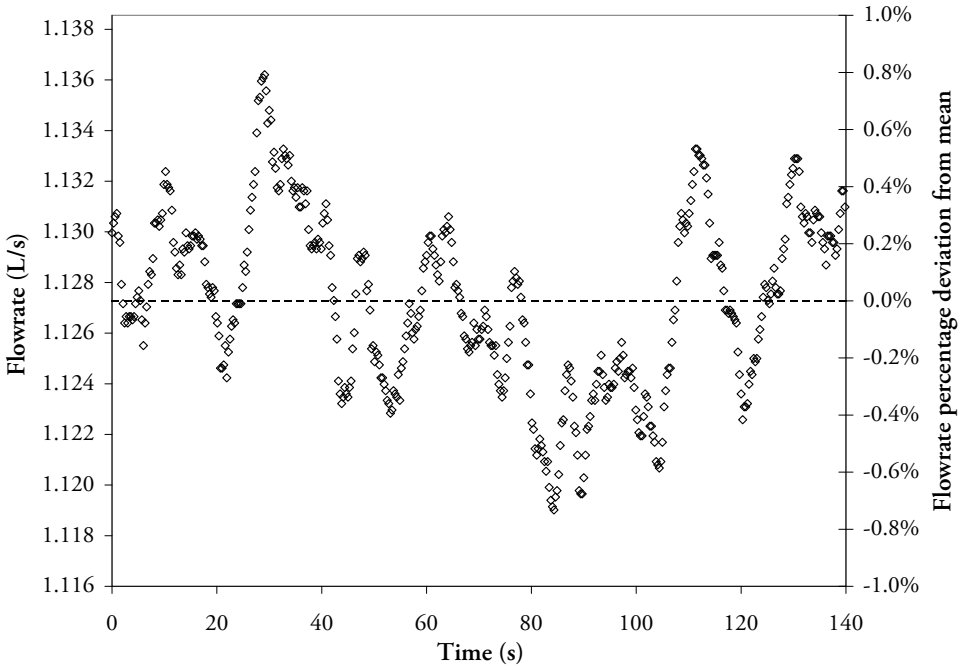

Figure 4.27: Flowmeter log for experiment performed on 7 Dec 2009 at $F_0 = 10.2$, $\theta = 45°$

However, in order to quality assure the 'stability' of conditions in the recorded images—that is, the stability of concentrations in the flow as discerned by the camera—two statistics were calculated. The first was the spatial-average of the raw (*i.e.* uncalibrated) pixel intensities across each frame. Although the camera did not have a uniform intensity response over its entire area, its response in the area that the flow typically occupied was stable enough that averaging raw intensities provided a useful indication of the amount of fluorescent dye present in the centreline cross-section at that instant. Turbulence dictated that a plot against the frame number would always display some temporal fluctuations; yet for a constant flowrate those fluctuations could be expected to be centred around a fixed mean value. Thus a gradual increase in average intensity at the beginning of a recording could indicate that the flow had not yet reached steady state, or alternatively that the fluorescent dye in the initial fluid had been diluted in some way; perhaps by water entering the discharge pipeline as the tank was first filled. Likewise, a gradual increase in average intensity after the flow had been running for some time could indicate that the dense layer of fluid settling on the base of the tank was growing to the point where it was intruding into the bottom of the recorded image. Sudden changes part way through the flow were of more concern, prompting a more in-depth investigation when observed (thankfully, these were rare). More often than not, the gradual changes that this statistic made evident had not been noticed

visually among the consistent turbulent fluctuations that were occurring.

The second statistic was a measure of the area occupied by the flow. By employing the calibration data associated with that experiment, the number of pixels above a user-supplied threshold concentration level—or in practice, a threshold laser power—were calculated for each frame of interest in the recording. This threshold was chosen in such a way as to avoid detection of the background noise, but account for as much of the flow as possible. Whilst more computationally demanding, this statistic was a much more direct measure of changes in the flow as a whole over time than the raw average pixel intensity. Figure 4.28 plots average pixel intensity and number of pixels above a threshold of $0.015\,C_0$ against time, recorded during the same experiment (and time period) as Figure 4.27. It can be seen that these two statistics follow a very similar pattern, following the same peaks and troughs; albeit with the average intensity series being somewhat smoother than the other.

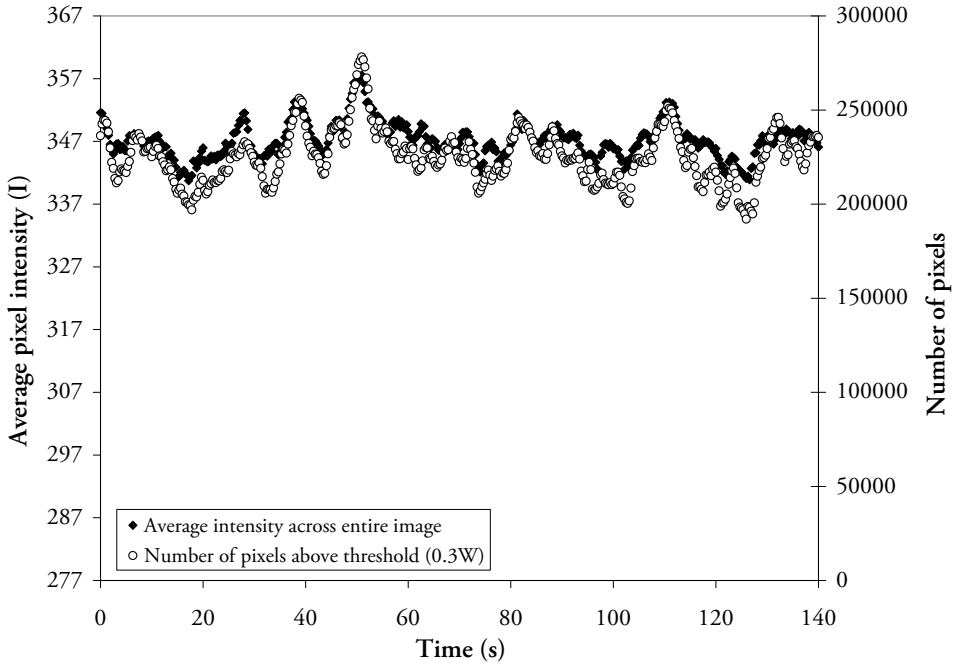

Figure 4.28: Average pixel intensity across image, and number of pixels with calibrated value above threshold of 0.3 W but within extrapolation limits (*i.e.* a concentration of $0.015C_0 \leqslant C \leqslant 0.15C_0$), for same experiment and time period as Figure 4.27. Every fifth data point plotted. X-crossing on vertical axis is lights-off average intensity (276.45). NB: 2,073,600 pixels in image total, and each pixel is the equivalent of $0.316\,\mathrm{mm}^2$

Both of these statistics are bulk parameters and as such will mask many of the changes that are occurring across the extent of the flow. Thus of particular note in Figure 4.28 is simply the size of the fluctuations. Both series show proof of significant large-scale changes, and this over significant time periods. Visual observation of images suggested that the peaks are associated with the development of large eddies in the flow, and the troughs are associated with large 'holes' or 'gaps' in the flow. It is possible that the size of the fluctuations are accentuated by the fact that the flow was partially falling down upon itself. Nevertheless, it was important that any

temporal averaging of the concentration field be carried out over a long enough time period so as to encapsulate the effect of these intermittent events.

Based on analysis of experimental data, Wang (2000a, p. 52) concluded that in order to generate high-quality averaged results, at least 35 'independent eddy motions' should be considered. Because the data recorded in the current experiments were of concentration not velocity, and the statistics in Figure 4.28 are bulk statistics, independent eddy motions can only be guessed at. Thus experiments were recorded for as long as reasonably possible, which typically meant 6 minutes or more. Section 5.5 discusses the bulk timescales that were back-calculated from experimental data.

After finishing each experiment, the average intensity was calculated for all recorded frames: firstly across the entire image and then secondly across a small area near the bottom of the image. A decision was made regarding which range of frames should be used for concentration-field analysis (averaging *etc.*), with the second average-intensity plot used to more precisely determine the point where the bottom layer started intruding into the flow, if at all. This frame range generally began at around a minute after the flow was first turned on. At least 100 seconds of actual experimental data were used for analysis.

4.5.4 Concentration-field statistics

A variety of statistics could be derived from concentration field data. Because for each temporal realisation (*i.e.* frame) this data consisted of an array of discrete values on a spatial plane, statistics were also calculated in discrete locations. Where two-dimensional profile cuts were required in directions other than horizontal or vertical, interpolation was performed between nearest neighbours.

4.5.4.1 Averaging

As already mentioned, the bulk statistic of most interest was the average of the concentration field over time, for a constant set of source conditions. This array was calculated by loading frames into memory one at a time, looking up the polynomials fitted during the calibration process (Section 4.5.1) to compute each pixel's concentration, and then adding these concentration values to a summation array if they were within the extrapolation bounds. A record was made of the number of frames used for each individual pixel, and if not more than 5% of frames had been ignored, the pixel's average was determined by dividing the summed value by the number of frames.

Considering the factors discussed in Section 4.3 (Signal Quality), it is estimated that spatial and concentration data were accurate to $\pm 5\%$.

Trajectory, spread and centreline dilution were all calculated by fitting Gaussian profiles to the averaged concentration data. This procedure was carried out algorithmically; an advantageous approach due to its speed and mathematical precision. However, an algorithmic approach

was also non-trivial due to issues such as experimental noise and deviations from the 'expected' Gaussian profile shape.

The algorithm developed for the current study was known as the *scalar traverse* algorithm. This algorithm used an iterative method to improve upon accuracy of its calculations incrementally whilst smoothing out the effect of experimental artifacts. These steps were followed:

1. Scalar concentrations were interpolated from input field along a cut line from a central origin, out to some pre-defined radius. This origin was located manually in such a way that cut lines made at incremental angles would intersect with the complete flow path—that is, it was positioned on the inner side of the flow, often approximately at $[x_m, 0]$.

2. The maximum concentration on that cut line was identified, as was the location on the outer side where concentrations dropped to 37% of that maximum. This enabled the estimation of the centreline location and the cross-section width b_c.

3. A new set of data were interpolated between $-0.25 \leqslant \frac{r}{b_c} \leqslant 1.0$ (where r is radial distance as in Equation 1.4), and a Gaussian distribution was fitted to this data (see below).

4. Trajectory coordinates [x, y] were back-calculated from corrections derived from fitted distributions[5], and distribution width b recorded.

5. Parts 1-4 were repeated for further cut lines, made at 2° increments around a complete circle. Where cut lines did not intersect experimental data or no Gaussian profiles were identified, trajectory coordinates were not recorded.

6. Where possible, x and y values were averaged over sets of three successive trajectory coordinates.

7. Trajectory angle (θ) values were back-calculated from [x, y] data; using central differencing where possible.

8. Angle values (θ) were averaged over sets of three then five successive angles.

9. For each trajectory step, a new set of data were interpolated between $-0.25 \leqslant \frac{r}{b_c} \leqslant 1.0$, perpendicular to the revised trajectory. A Gaussian distribution was fitted to this data, and trajectory coordinates corrected by the new r_0 value.

10. Parts 6-9 were repeated until the trajectory no longer changed significantly. Typically this meant five iterations.

[5] r_0 values in Equation 4.10

Gaussian fitting It is important to outline the procedure employed to fit Gaussian distributions to the mean concentration data. An equation for concentration C against radial distance r can be written as follows:

$$\frac{C}{C_m} = e^{\left(\frac{-(r-r_0)^2}{b_c^2}\right)} \tag{4.10}$$

where C_m is the maximum value of the distribution; b_c the radial width of the distribution ($b_c = \lambda b$); r_0 the (true) distance from the origin that the distribution is centred upon.

Taking the natural logarithm of both sides and rearranging:

$$\ln C - \ln C_m = \frac{-r^2 - r_0^2 + 2r\,r_0}{b_c^2}$$

$$\ln C = \left(\frac{-1}{b_c^2}\right) r^2 + \left(\frac{2r_0}{b_c^2}\right) r + \left(\ln C_m - \frac{r_0^2}{b_c^2}\right)$$

If a second-order polynomial fit is performed between r along the x-axis and $\ln C$ on the y-axis—*i.e.*, $y = p_0x^2 + p_1x + p_2$—the parameters C_m, b_c and r_0 can be calculated as follows:

$$b_c = \sqrt{\frac{-1}{p_0}}$$

$$r_0 = \frac{b^2 p_1}{2}$$

$$C_m = e^{p_2 + \frac{r_0^2}{b^2}}$$

Choice of fitting bounds In part 3 of the scalar traverse algorithm outlined above, it was stated that data were interpolated between the bounds $-0.25 \leqslant \frac{r}{b_c} \leqslant 1.0$. These bounds were chosen in large part by trial and error, and could not be symmetrical because the inner side of the flow ($\frac{r}{b_c} < 0$) was not Gaussian in form (especially at and past the maximum rise height location). This is consistent with the observations of Kikkert *et al.* (2007) and others. Concentration data on the outer edge of the flow was found to closely match the Gaussian distribution, and thus this was the target region for matching.

Nevertheless, camera noise (even if very small) meant that the bound on the outer edge could not be extended to infinity. The Gaussian distribution tends to zero in the limit of $r \to \infty$, yet by contrast experimental data fluctuates by a small but relatively constant amount around zero: sometimes above, sometimes below. Ignoring the complications caused by taking the logarithm of a negative number, it can be seen that when fitting distributions using the technique outlined above, these deviations can quickly cause the fitted shape to be significantly incorrect. The bound at which this became a problem was a function of the signal to noise ratio, and thus the 'best' bounds for one experimental setup might easily be non-optimal in another.

In order to ascertain how sensitive fits were to various noise levels, a simulation was per-

formed where software (pseudo-random) noise at varying levels was added to a pure Gaussian distribution, and a Gaussian fit back-calculated. A plot of calculated goodness-of-fit values is shown in Figure 4.29. The magnitude of noise that best matches experimental conditions will change across the flow field as C_m reduces, and change between experiments as averaging length varies. In the shortest experiment made during the current study (1 minute and 40 seconds long; 45° source inclination), σ/C_m at the return point was 0.05, where σ is the (estimated) standard deviation of noise. In a long experiment (7 minutes and 45 seconds long; 45° inclination), σ/C_m at the return point was approximately 0.009. Taking this into account, it appears that a fit bound of $|r/b_c| = 1.0$ is a good compromise.

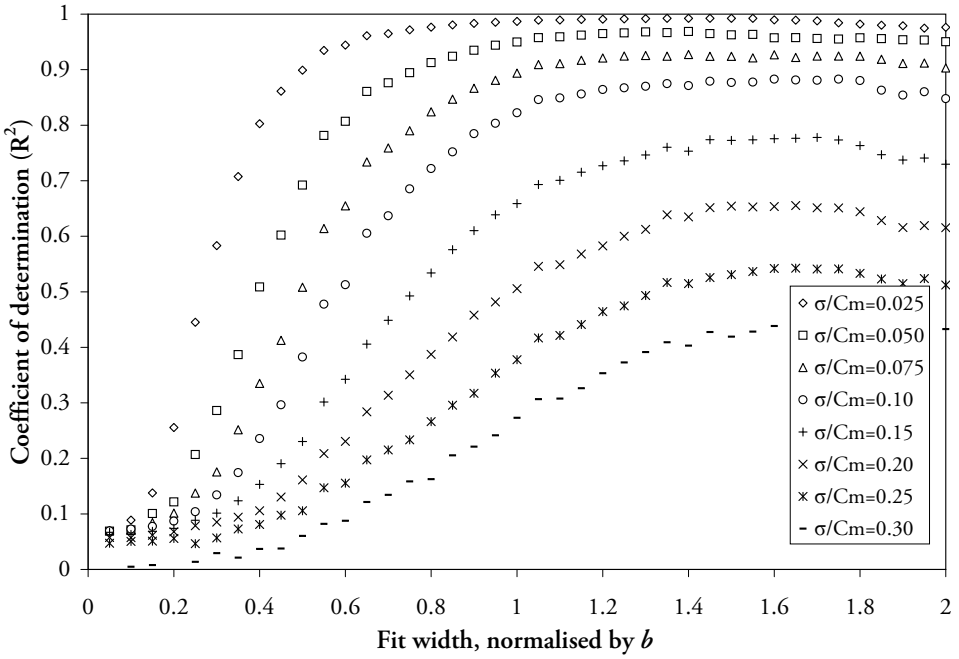

Figure 4.29: Average coefficient of determination (R^2) for fitting of Gaussian shape ($\frac{C}{C_m} = e^{-(\frac{r-r_0}{b})^2}$) to a series constructed by superimposing random noise on a pure Gaussian ($C_m = 0$, $x_0 = 0$) shape, out to various $|r/b|$ widths. Noise is Gaussian-distributed, with average of zero and of various standard deviations (σ). R^2 is calculated in same manner as for Figure 4.24. Each plotted value is the average for 1000 fits

Although the inner edge of the flow was of little interest for the fitting of Gaussian profiles, the sensitivity of the above-mentioned fitting procedure (in particular regarding r_0 values) meant that the bound on the inner edge could not be zero. The bound of $0.25\ b_c$ on this edge was chosen by visual inspection of the profiles fitted for a range of different bounds.

4.5.4.2 Temporal statistics

Although the average concentration field is the primary data of interest to industry practitioners, temporal data can provide valuable insights into flow structure and behaviour. Two are of particular interest in the current research.

RMS The *root mean square* (RMS) is a measure of the magnitude of a varying quantity. Of interest with regards to a turbulent field is the magnitude of its *fluctuations*; that is, the magnitude of differences around the mean. For a concentration field, this quantity is defined as:

$$\mathrm{RMS}(C') = \sqrt{\overline{C'^2}} = \sqrt{\frac{\sum_{i=1}^{n}(C_i - \overline{C})^2}{n}} \tag{4.11}$$

As a turbulent signal (under discrete sampling) may be described as a random variable, this parameter is identical to the standard deviation of the statistical population.

In a measured concentration signal—calibrated or not—the calculated value for RMS-of-fluctuations will be a combination of true experimental fluctuations and of noise from the measuring system. If C'_e is the fluctuating component of the true experimental concentration and C'_n is the system noise fluctuations, the measured fluctuating component is $C'_m = C'_e + C'_n$. The RMS of C'_m is therefore,

$$\mathrm{RMS}(C'_m) = \sqrt{\frac{\sum_{i=1}^{n}(C'_e + C'_n)^2}{n}} = \sqrt{\frac{\sum_{i=1}^{n}(C'^2_e + C'^2_n + 2C'_e C'_n)}{n}} \tag{4.12}$$

It may be assumed that C'_e and C'_n are statistically independant. Therefore $2C'_e C'_n$ may be neglected and $\mathrm{RMS}(C'_m)$ is simply

$$\mathrm{RMS}(C'_m) = \sqrt{\frac{\sum_{i=1}^{n}(C'^2_e + C'^2_n)}{n}} \tag{4.13}$$

$$= \sqrt{\mathrm{RMS}(C'_e)^2 + \mathrm{RMS}(C'_m)^2} \tag{4.14}$$

Thus, in order to obtain just the real experimental fluctuations, recordings were made prior to experiments with the laser on but no dye present (known as the "black-level") and $\mathrm{RMS}(C'_e)$ was calculated using Equation 4.14 on a per-pixel basis.

Intermittency *Intermittency* refers semantically to the property of not being continuous or steady. With respect to turbulent flows, the "intermittency surface" is the boundary between turbulent, vortical eddy fluid and irrotational (non-turbulent) fluid (Townsend, 1976). As velocity measurements have not been taken in the present study, intermittency surfaces cannot be directly measured. Here the term "intermittency" specifically refers to the degree to which discharge fluid is broken up by ambient fluid. The intermittency *statistic* is defined as the measured proportion of time in which concentrations in a given location are lower than a specified threshold value; ranging from 0 (never) to 1 (always). It must be noted that this statistic has been defined by Papantoniou & List (1989), Davidson & Pun (1999) and others as the inverse

scenario: the proportion of time in which concentrations are *above* a threshold value. However the current approach allows statistical and semantic meanings of "low intermittency" and "high intermittency" to converge.

Papantoniou & List (1989) derived intermittency profiles for jets and plumes. They found negligible intermittency on and around the jet centreline ($|r/b_c| \lesssim 0.2$), but a minimum intermittency of 0.9 on the plume centreline (using the present definition). Based on this data they remarked that "not much ambient fluid reaches the jet centreline" but "a substantial amount of very low-concentration fluid or clear fluid can be found in the plume interior". These observations are consistent with visual observations by many workers that plume eddies are much more 'broken' or 'distinct' than jet eddies; particularly along the flow centreline. As such, the intermittency statistic can indicate the demarcation between jet- and plume-dominated regions.

Papantoniou & List used a threshold of 10% of the mean centreline value. While this is easily understood, such an approach derives the proportion of "low concentration" fluid rather than the proportion of "essentially unmixed" fluid. For the present experimental data, the threshold was set at a constant concentration level, slightly above the noise floor.

It should be noted that sharp concentration interfaces may be below camera resolution (in both spatial and temporal senses) or light sheet thickness, and thus as such intermittency data should be viewed as a lower limit of the true value obtained from an ideal measuring device.

4.5.5 Database and multi-experiment plotting

Throughout the experimental period, data were recorded on a custom database system. This system was built using Django and PostgreSQL, and written in the Python programming language. For each experiment undertaken, the following information was recorded:

- date/time, Q_0, θ_0, d, tank temperature, header-tank temperature, camera gain, camera offset, and laser wattage[6];
- the calibration, source density, ambient density, source concentration (mg/L Rh6G), flowmeter calibration and camera pixel-scale associated with that experiment;
- results such as spatial-average, number of pixels above threshold, flowmeter log, recording length, intermittency array, RMS array, and the average array;
- source coordinates in image (for algorithmic calculation of path length);
- trajectory and Gaussian-fit information calculated by scalar-traverse algorithm;
- check-boxes indicating whether data from the experiment should be plotted or not.

[6] Invariably this was 2.00 W.

Scripts were written to analyse the trajectory and Gaussian-fit information and create graphs of statistics such as the maximum rise-height. These graphs, produced using *matplotlib*, were invaluable for quick plotting of new experimental data and comparing different sets of experiments against each other. Statistics were also saved in tabular form for use in spreadsheet software.

Binary data such as images and concentration arrays were synchronised to an external storage service (Amazon S3). A revision-control tool (Mercurial) was used to record changes to a textual 'dump' of the database, and these changes likewise were synchronised to an external storage service (Bitbucket).

4.6 Summary

At the beginning of this chapter, it was stated that the goal of the present experiments was to gather high-quality data regarding the dilution of *singly-diffusive inclined negatively buoyant jets in stagnant unstratified environments, without boundary influence*. Section 4.3 (Signal Quality) discussed many factors that could influence the accuracy and reliability of data recorded in these experiments. Unless each of these factors were addressed appropriately, data collected would largely be a by-product of the experimental apparatus and systems, rather than a fair representation of the intended flow regime. Where feasible, processes were implemented in order to mitigate potential problems. In other instances, errors were simply characterised, and accepted as limitations on data precision. As far as reasonably possible, system quality has been investigated and upheld.

Chapter 5

Experimental Results

"To myself I seem to have been only like a boy playing on the sea-shore, and diverting myself in now and then finding a smoother pebble or a prettier shell than ordinary, whilst the great ocean of truth lay all undiscovered before me."
Sir Isaac Newton; quoted in Brewster (1855, p. 407)

This chapter will discuss various experimental results; both qualitative and quantitative. These results must be viewed in a holistic manner, as different clues to the behaviour of the same flow type. It is only in the context of a broad data analysis that reliable deductions may be drawn.

Figure 5.1 outlines nomenclature that will be used in this chapter. Notably, the terms "inner side" and "outer side" are introduced, which refer to the inner and outer sides *of the flow centreline*. Broadly speaking, the discharge may be divided into a "rising side" where flow is moving upwards, and a "falling side" where flow is moving downwards. The "transverse" direction is that which is not plotted here; *i.e.* that which extends in a perpendicular manner from the centre plane.

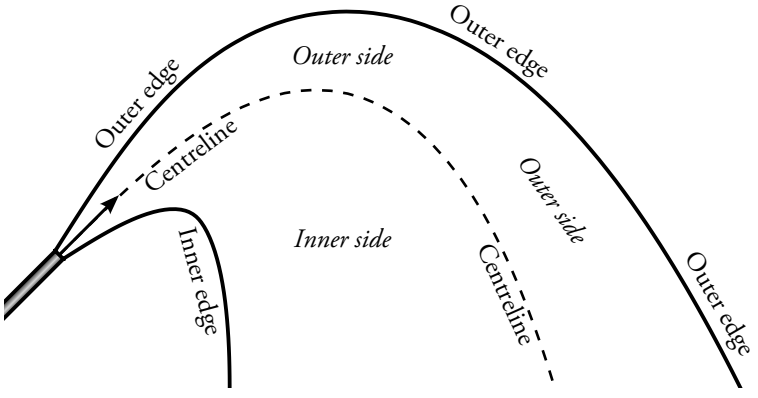

Figure 5.1: Nomenclature for regions within negatively buoyant jet

5.1 General Observations

The following section will discuss observations made visually while watching experiments. For the purpose of this discussion, a sequence of eight instantaneous images selected from an experiment conducted on 6 Nov 2009 are presented in Figure 5.2. This experiment had a 60° source inclination, with $F_0 = 23.21$ and $Re = 3455$. Images were recorded for over 13 minutes[1], but only 8 minutes & 57.5 seconds of this (frames 2400–11000) were used for data analysis purposes. It is important to note that the spatial-average plot (introduced in Section 4.5.3) for the analysed images was very stable, with fluctuations around the mean of up to $\pm 11.5\%$. The flowmeter log was also very stable, with fluctuations around the mean of up to $\pm 1.6\%$.

Before proceeding, it is worthwhile to emphasise that the data presented from the current experimental study is concentration data, or that which is derived from the concentration field. Instantaneous images such as those in Figure 5.2 highlight the presence of discharge fluid at various levels of dilution. Because the flow under consideration is fully turbulent and mixing vigorously, it may be assumed that all discharge fluid visible in these images is fluid which is *rotational*—that is, fluid which has non-zero vorticity, ω. Conversely, unmixed ambient fluid can be assumed to be *irrotational*—that is, non-turbulent fluid which has no vorticity. Eddies, which are a property of the velocity field, constantly distort and deform the boundaries between turbulent rotational fluid and non-turbulent irrotational fluid. Indeed a number of eddies may act upon different parts of the same boundary concurrently. Eddies vary significantly in size. Large eddies contain most of the turbulent energy and are responsible for transport effects, while small eddies dissipate the energy by viscous work (Streeter, 1961, p. 10-8). While tracer fields do not provide a direct measure of eddy behaviour, the effects of eddies may be observed in a tracer field. Here the phrase "tracer patches" will describe distinct parcels of (rotational) discharge fluid that are seen within the concentration field; altered by but generally distinct from eddies.

In Figure 5.2, the region immediately surrounding the flow centreline (*i.e.* location of maximum concentration) up to the maximum rise height demarks what appeared to be the jet (*i.e.* initial-momentum dominated) region. This region was characterised by large velocity magnitudes, low intermittency levels and relatively small trajectory deflections. The flow here was frequently observed to "punch up" through surrounding slower-travelling discharge fluid. Although density differences created a continued tendency for the flow to bend downwards, the "punching" action (due to large velocities) acted to re-straighten the jet-region trajectory.

The outer edge of the jet region—and indeed, of the entire flow—was in most cases very sharp and defined. This was due to the inherent stability of this region. Where small patches of tracer fluid were flung outwards, away from the flow, they fell naturally back into the flow; drawn both by the entrainment velocities surrounding the jet and the buoyancy forces acting upon the patch.

In contrast, the lower boundary of the jet region was ill-defined. Beyond some initial location,

[1] That is, after the discharge was turned on.

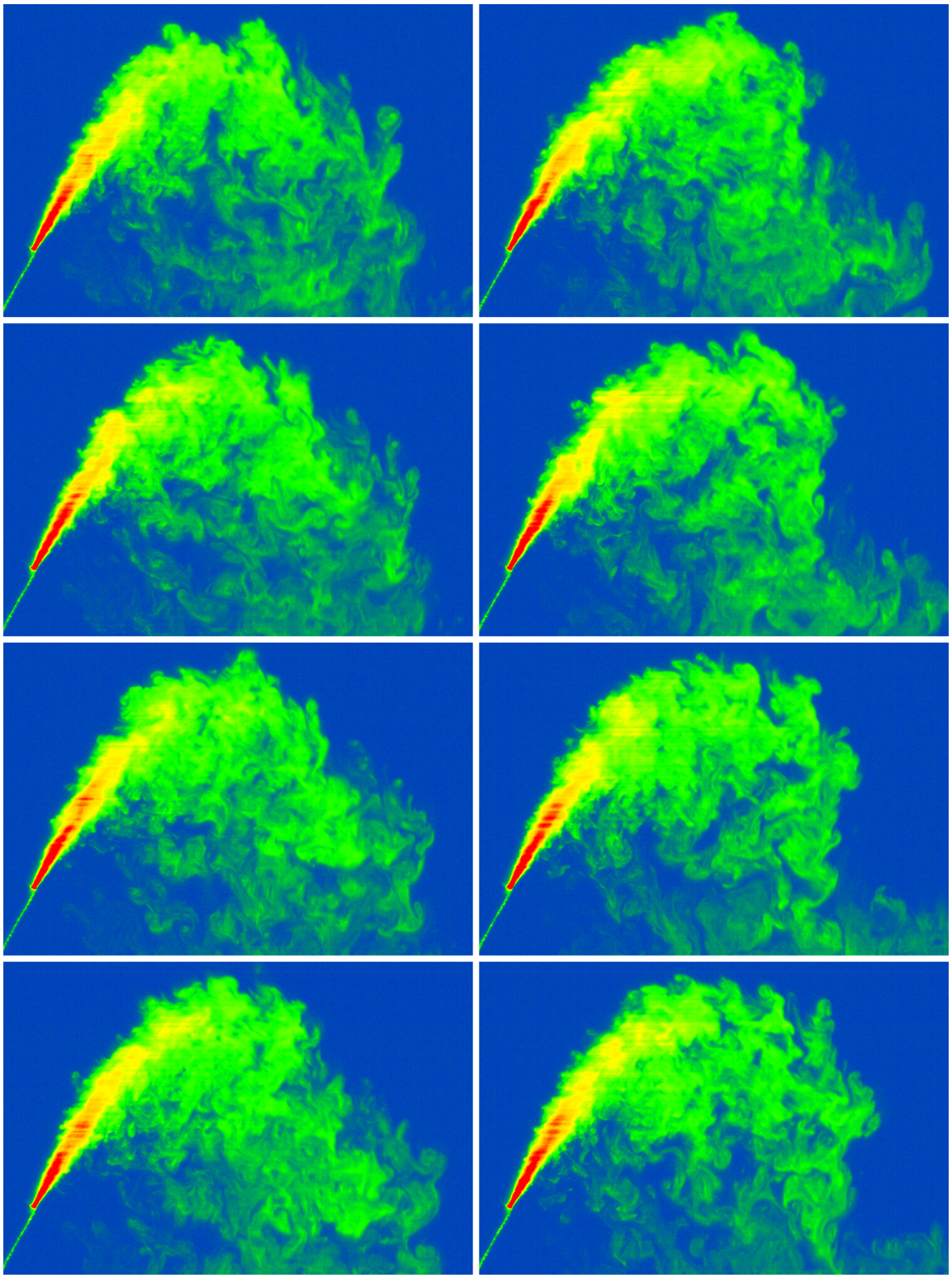

Figure 5.2: Sequence of false-colour instantaneous images, each spaced 1.0 second apart, from experiment on 6 Nov 2009 (60° source inclination, $F_0 = 23.21$, $Re = 3455$). First image is in top-left corner, second image is directly below this, and so on; such that image sequence follows down left column and then down right column. Sequence begins at frame 3731; $t = 83.1$ s from beginning of analysed section

discharge fluid began consistently falling away from the main flow. This fluid had little streamwise velocity, and appeared to originate from small patches that escaped from the edge of the fast-moving jet flow: the same type that on the outer edge were naturally drawn back into the flow. On this side of the jet region, the buoyancy forces on these patches acted to draw them *away* from the primary flow. Evidently the entrainment force exerted by the jet was not completely destroyed: rather, it was overcome by the inherent instability of interfacial fluid. Because the escaping fluid did not carry significant amounts of momentum, the velocities in the primary jet flow remained high and trajectories were not obviously affected. This is supported by the observation of Lai (2010) that at 60° inclinations, centreline velocity decay is jet-like up until maximum centreline height.

Consequently, it appeared that at least in some sense, the negatively-buoyant jet flow was divided into two distinct regions. The first of these was the jet region, where fluid travelled upwards at approximately the angle at which it was discharged from the source. The second region was a "curtain" of fluid falling from the jet region, travelling in a predominantly vertical direction. This latter region often had the appearance of fluid "smeared" out from the jet region, giving the flow a somewhat artistic form. Lane-Serff *et al.* (1993) stated that the inner side is "convectively unstable", and this is clearly evident in these images.

The outer edge of the second region was undoubtedly plume-like—having transitioned directly from a jet-like region—but the inner side fluid in this region also looked remarkably plume-like in form; albeit wider and with a non-distinct centreline. As such the flow in this area appeared similar to a line-plume (see for example, Roberts, 1979).

Nevertheless, patches of discharge fluid on the outer edge of the falling flow were noticeably larger than patches on the inner side. As the size of the largest eddies in a turbulent flow is a function of flow width, it may be assumed that the flow on this inner side was narrower in the transverse direction than the flow on the outer edge of the falling fluid.

Discharge fluid also appeared to be more dilute on the inner side. This was likely due to entrainment of ambient fluid from the transverse direction, as the flow travelled downwards from the jet region. Such an effect may be understood as the result of increasing the flow surface area; allowing more opportunity for ambient mixing.

Reasonably frequently, large "gaps" could be seen on the outer edge of the flow. These gaps were penetrations of ambient fluid associated with significant entrainment events. Alternatively described, these were large-scale intermittency events. In one sense these gaps indicated a lack of mixing in those parts of the flow; yet in another sense, they were evidence that unmixed ambient fluid was being drawn into the centre of the flow, where it could be thoroughly mixed into the surrounding discharge fluid. Such events were a natural part of the flow, but were more significant in size than would be typically expected for jets or plumes. Analysis of flowmeter logs did not provide any evidence that source flowrates were fluctuating in a manner that caused changes in flow structure.

Occasionally, similar "gaps" appeared in other parts of the flow also. In places gaps penetrated

a significant distance into the typical flow path. Here we may assume that unmixed ambient fluid has been drawn in from one or both of the transverse edges. As discussed earlier, high intermittency levels are characteristic of plume behaviour.

Ferrari & Querzoli (2004, 2010) present instantaneous centre-plane images of a 55° negatively buoyant jet containing similar large-scale "gaps" on the outer edge (reproduced here in Figure 2.3). It is likely that such gaps were in mind when these authors[2] stated that asymmetries caused by "the detachment of descending plumes" were clearly visible in Figure 2.3a. However, data from the current experiments did not show evidence that plumes detached off the jet region—or anywhere else—in a discrete, periodic fashion. Rather, jet-region fluid was fed into plume regions on a continual basis; albeit with changing shapes and large intermittency events.

It is worth highlighting that these images represent a cut-plane through the flow, and hence are a two-dimensional picture of a three-dimensional field. A patch that appears small in size may in fact be the edge of a much larger patch. Mass need not be conserved on this plane: patches may appear and/or disappear without being "mixed" into surrounding fluid.

5.2 Profile Shapes

5.2.1 Centreline-maximum and return point profiles

Figure 5.3 plots temporally-averaged and RMS concentration profiles perpendicular to the centreline trajectory, at the maximum centreline height location (s_m). Profiles from a selection of experiments at 45° inclination are included, with a range of initial Froude numbers (22–60). The experiments used are those with black-level RMS data recorded (as per Section 4.5.4.2). Note that interpolation of all profile data in this section was performed using 3rd-order spline interpolation[3].

Temporally-averaged concentration profiles on the outer side are approximately Gaussian, although concentrations decay faster than expected on the edge: an artifact of the stabilising effect that buoyancy has on this edge. On the inner side (negative r/b_c), profiles retain their Gaussian appearance, but are progressively more 'stretched' as r/b_c decreases. In addition, the base-line value that profiles appear to return to is above zero on this side. All nine profiles in this plot follow remarkably consistent shapes. That is, the form of averaged profiles centred on the centreline-maximum location does not appear to be dependent on F_0.

By contrast, RMS profiles (Figure 5.3b) peak at approximately $r/b_c = 0.9$, with a value of $\mathrm{RMS}(C')/C_m \approx 0.31$. Fluctuations decrease rapidly between this point and the centreline ($r/b_c = 0$), then stay approximately constant until $r/b_c = -1$; beyond which they slowly decrease. All profiles follow very consistent shapes. Yet such a plot is significantly different from that of fluctuations found in a pure jet or a pure plume.

[2] in Ferrari & Querzoli (2004, p. 7)

[3] The need for interpolation was discussed in Section 4.5.4.

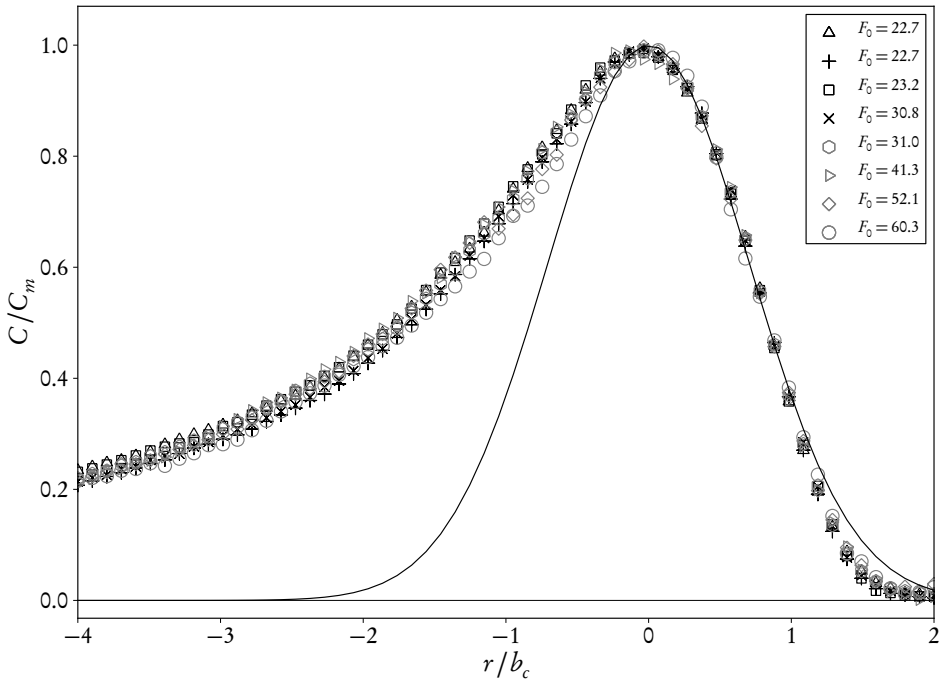

(**a**) Temporally averaged concentration. Solid line is Gaussian distribution ($C/C_m = e^{-(r/b)^2}$)

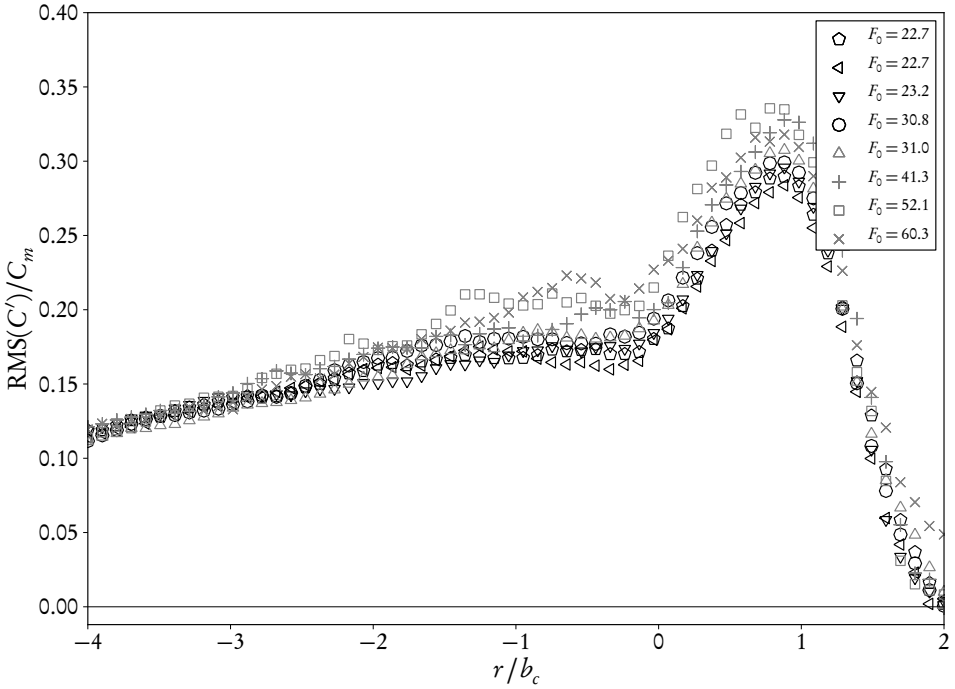

(**b**) RMS of concentration fluctuations

Figure 5.3: Average and RMS concentration profiles at centreline maximum location (s_m) of 45° negatively buoyant jets

Papanicolaou & List (1988) and Wang & Law (2002) both recorded concentration fluctuations in jets to peak with a value of $\mathrm{RMS}(C')/C_m = 0.22$ at two locations; $r/s = \pm 0.10$. Employing the spread rate given in Equation 4.8, these peak locations are calculated to be equivalent to $r/b_c = \pm 0.80$. Centreline fluctuations were only slightly smaller (approximately 20%). Conversely, concentration fluctuations in plumes peaked on the centreline axis, at values of approximately 40%. The increase in fluctuation magnitude between jets and plumes is consistent with increased intermittency levels, particularly along the centreline.

Here however, RMS profiles from the 45° negatively buoyant jet show neither two symmetric peaks nor a single axially-located peak. Rather, an offset peak is found on the outer side and an almost flat profile is found on the inner side. While outer-side fluctuations appear similar in form to those of a jet-dominated flow, it is evident that the flow structure on the inner side is dramatically different to both jets and plumes. By contrast, near the source (immediately following the zone of flow establishment) buoyancy effects are negligible and flow structure on both sides is expected to be fully jet-like. It appears therefore that between the source and the maximum centreline height, inner side turbulent fluctuations have been notably reduced because of additional mixing associated with the buoyancy-induced instabilities acting on this boundary.

The peak RMS value found on the outer side of Figure 5.3b ($\approx 31\%$ of C_m) is higher than found in pure jets, but lower than found in plumes. Hence it appears that the outer side is in transition to a plume dominated region.

Although the inner-side RMS profile has been 'flattened', fluctuations remain large in magnitude. This is evidence that vigorous mixing is still taking place here (as supported also by the gradient of averaged concentration). While flow structure is not typical of axial jet or plume flow, it is worth noting that inner-side fluid has been reorientated and is moving predominantly in the vertical direction.

Figure 5.4 plots temporally-averaged and RMS profiles at the return point. Both plots show more scattered datasets than at the centreline maximum location. Inner-side averaged concentrations follow an almost linear decay from the centreline peak. While RMS profiles continue to peak on the outer-side, this peak location is closer to the centreline axis (approximately $r/b_c = 0.5$) and is consistent with the magnitude of plume fluctuations. A slight flattening of RMS gradient may be perceived in some datasets between the region $-1.0 < r/b_c < 0.0$, but as a whole fluctuations appear to decay linearly on the inner side.

5.2.1.1 Intermittency

Intermittency profiles[4] at the maximum centreline height for shallow (30°) and steep (75°) inclinations are plotted in Figure 5.5. Low inclination profiles show almost zero intermittency between the range $-1 \leq r/b_c \leq 0.5$ for experiments below $F_0 = 42$. As already discussed, low intermittency at the centreline is typical of jet-dominated regimes. At larger initial Froude numbers the region of low intermittency becomes much smaller and profiles become more symmetric

[4] The intermittency statistic was defined in Section 4.5.4.2.

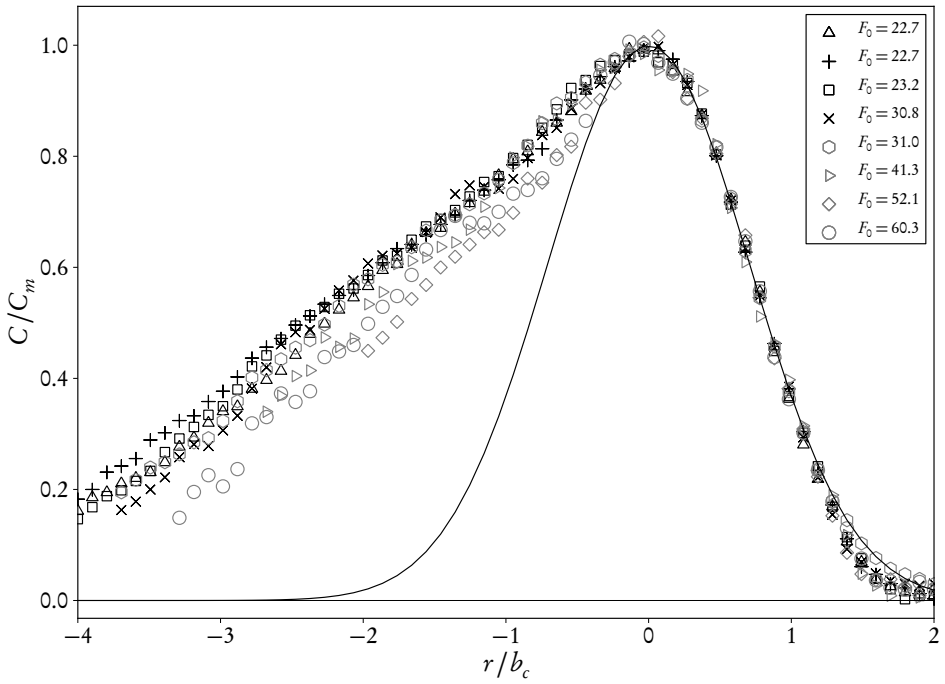

(**a**) Temporally averaged concentration. Solid line is Gaussian distribution ($C/C_m = e^{-(r/b)^2}$)

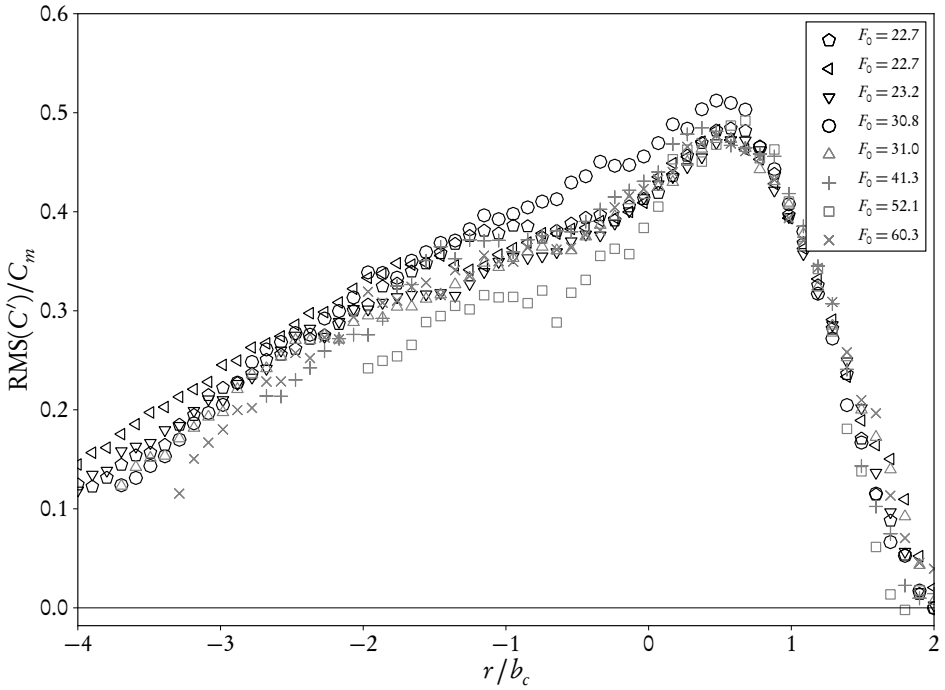

(**b**) RMS of concentration fluctuations

Figure 5.4: Average and RMS concentration profiles at return point (s_r) of 45° negatively buoyant jets

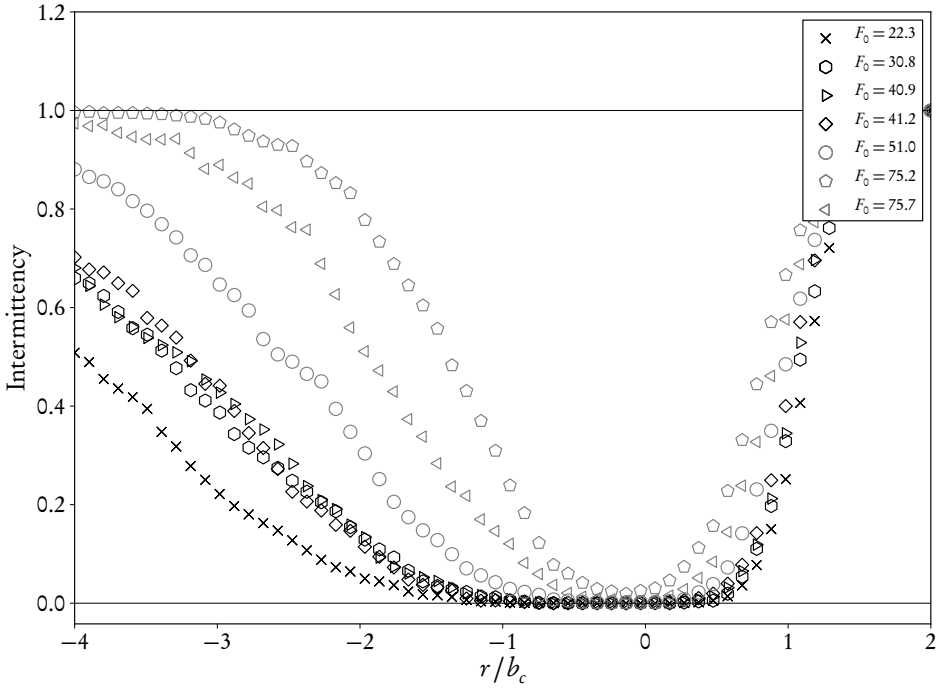

(**a**) 30° inclination

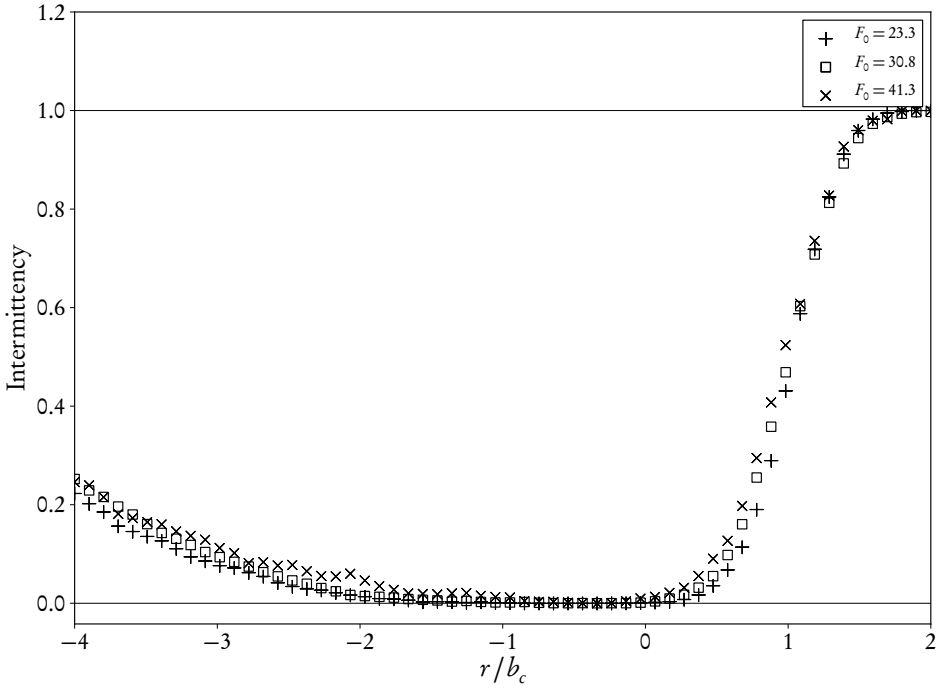

(**b**) 75° inclination

Figure 5.5: Intermittency profiles at maximum centreline height (s_m) for 30° and 75° inclination experiments. Threshold set at 0.3 W, equivalent to between 0.015 and 0.021 C_0

overall. It appears that the effect of buoyancy induced instabilities on the inner side is reduced at high F_0, and intermittency profiles at maximum centreline height more closely resemble standard jet intermittency profiles[5].

Steep inclination profiles show a low-intermittency region extending from the flow centreline to roughly $-1.5r/b_c$. This suggests that the flow at maximum height is confined, and has had a reduced ability to entrain uncontaminated ambient fluid into itself. Although dilution can still be expected to occur, in large part the flow is re-entraining its own fluid due to the rapid change in trajectory direction.

Based on the assumption that a turbulent flow in a stagnant ambient is jet-like when initial momentum flux M_0 is greater than buoyancy-generated momentum flux M_B, Kikkert *et al.* (2007) stated that the maximum height of a negatively buoyant jet must always be reached within the jet region. At this location, vertical momentum components must match, meaning that $M_B/M_0 = \sin(\theta_0)$. Intermittency profiles in Figure 5.5 for both 30° and 75° inclinations were consistent with jet-like behaviour at the maximum centreline height. Equivalent plots for other inclinations showed the same behaviour[6].

In most cases, a negatively buoyant jet reaches its return point after transitioning to plume-like behaviour. However at low angles, a negatively buoyant flow will reach the return point while still jet-like. The analytical model presented by Kikkert *et al.* (2007) predicted that the critical angle was 16.5°. That is, any negatively buoyant discharge below a 16.5° source inclination would be jet-like at the return point, and any discharge above a 16.5° source inclination would be plume-like at the return point.

Figure 5.6 plots intermittency profiles at the return point for experiments at 15° and 30° inclinations. Profiles at a 15° source inclination (Figure 5.6a) show clear evidence of jet-like behaviour along the centreline, with very little intermittency occurring. By contrast, profiles at a 30° source inclination (Figure 5.6b) show significant intermittency along the centreline, particularly for high F_0 experiments. Therefore at least for the range $22 \leq F_0 \leq 42$, the transition from jet to plume at the impact point occurs between source inclinations of 15° and 30°.

5.2.2 Single experiment profiles

Temporally-averaged and RMS profiles along the trajectory of a single 45° inclination experiment are given in Figure 5.7. Inner-side temporally-averaged concentrations consistently increase in their relative magnitude between $s/(d\,F_0) = 1.59$ and $s/(d\,F_0) = 3.06$. At $s/(d\,F_0) = 3.53$, concentration gradients on this side become steeper than earlier profiles after approximately $s/b_c = -3$. The return point profile ($s/(d\,F_0) = 4.00$) likewise has steep gradients; with its relative value at $s/b_c = -4.0$ lower even than values at the equivalent location for $s/(d\,F_0) = 1.59$.

[5]The difference in intermittency values between the $F_0 = 75.2$ and the $F_0 = 75.7$ experiments is evidence that temporal statistics such as intermittency were more sensitive to individual experimental conditions than the temporally-averaged concentration field.

[6]The 30° plot was shown here instead of the 15° plot as it contained experiments at higher initial Froude numbers.

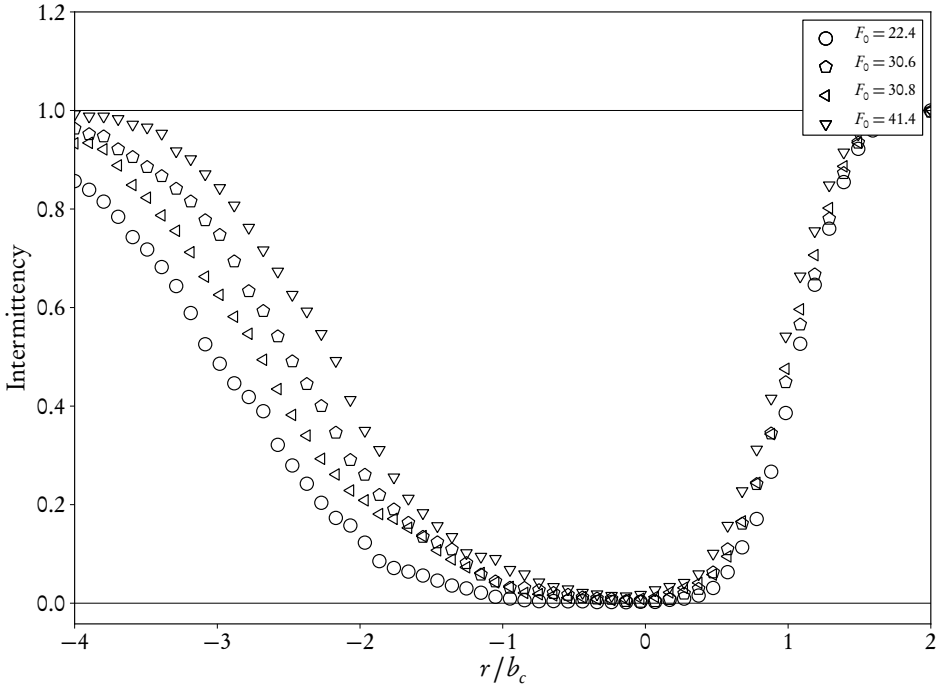

(**a**) 15° inclination

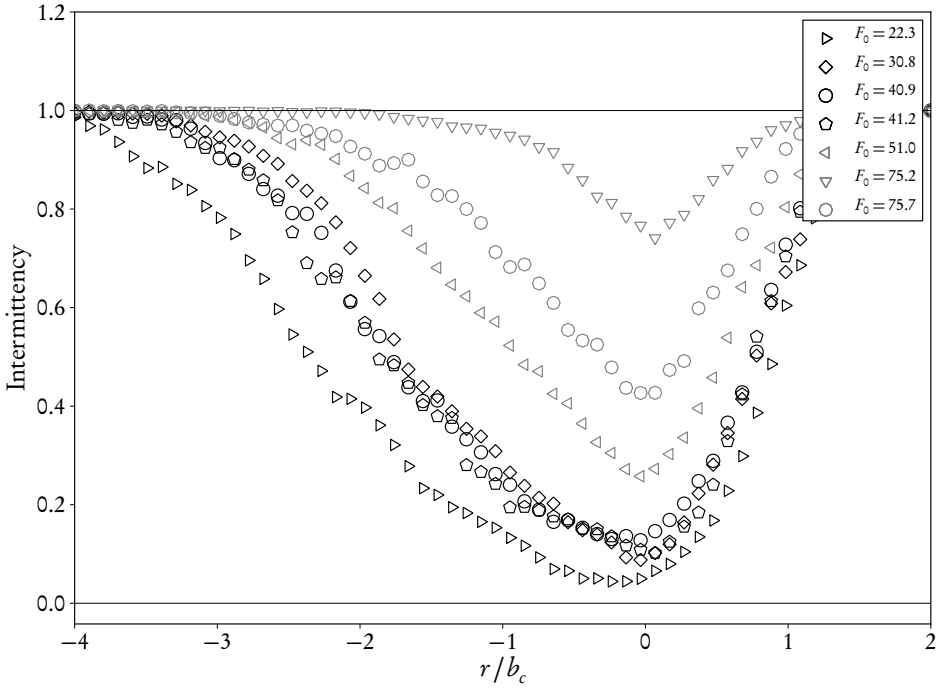

(**b**) 30° inclination

Figure 5.6: Intermittency profiles at return point (s_r) for 15° and 30° inclination experiments. Threshold set at 0.3 W, equivalent to between 0.015 and 0.021 C_0

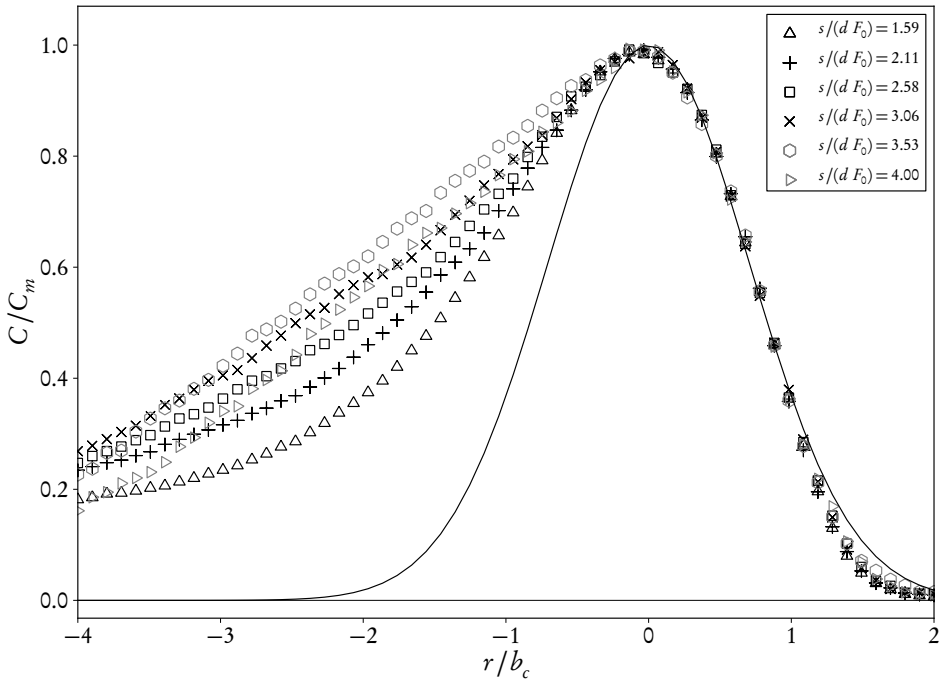

(**a**) Temporally averaged concentration. Solid line is Gaussian distribution ($C/C_m = e^{-(r/b)^2}$)

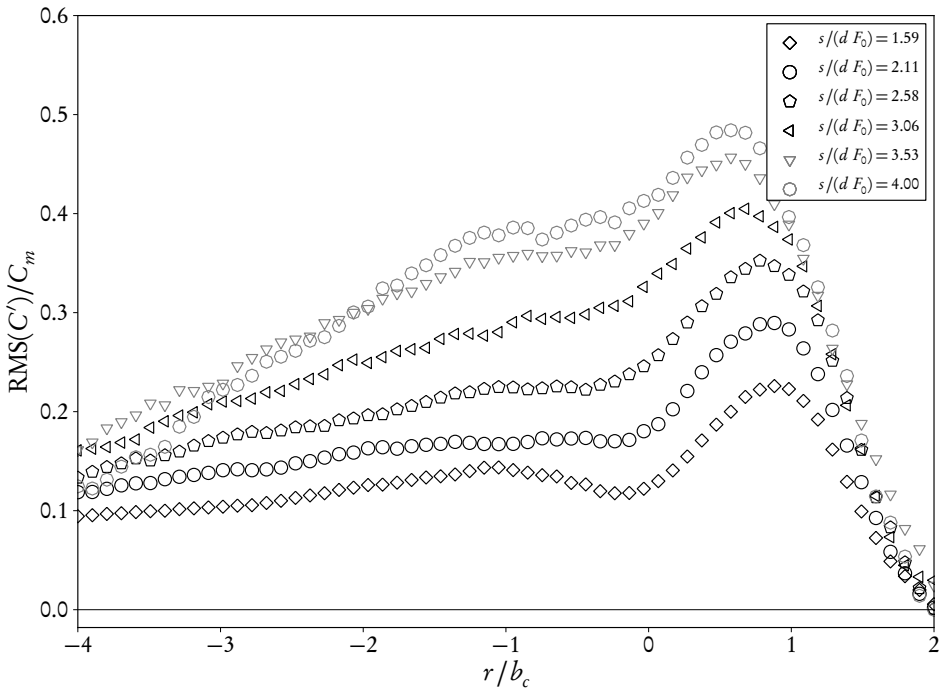

(**b**) RMS of concentration fluctuations

Figure 5.7: Average and RMS concentration profiles at various locations through single 45° inclination experiment, including maximum centreline height ($s/(d\,F_0) = 2.11$) and return point ($s/(d\,F_0) = 4.00$). $F_0 = 22.72$; Re $= 3382$

Therefore the current data does not provide any evidence that temporally-averaged profiles reach a new self-similar shape after some limiting path distance.

RMS profiles on the contrary increase in relative magnitude through the flow. Peak values rise above 40% and peak locations move closer towards the centreline axis; indicating that the flow has established a fully plume-like structure. Average and RMS images from this same experiment are given in Figure 5.8, where image intensities are based on absolute values rather than ratios with respect to the corresponding centreline value. These images provide a clear picture of how dramatically the flow structure has been altered on the inner side.

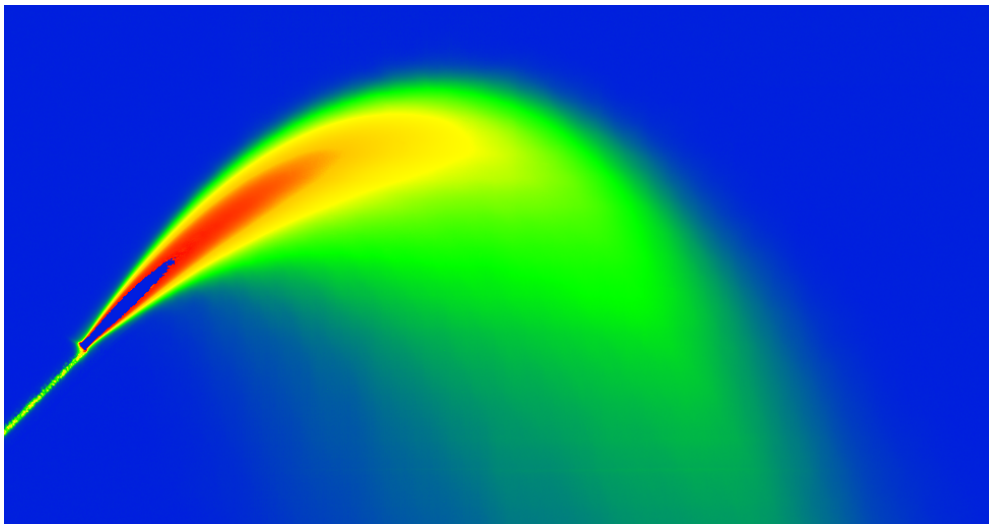

(**a**) Temporally averaged concentration

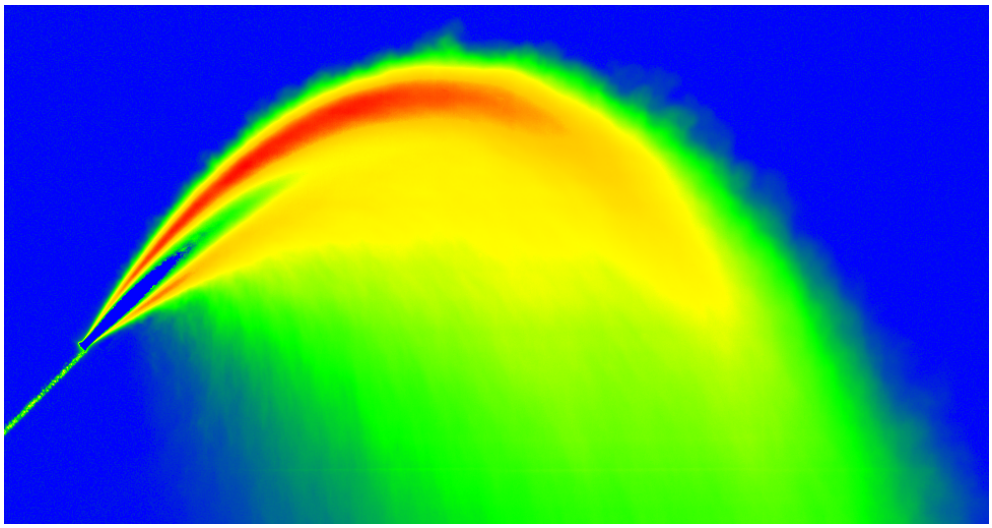

(**b**) RMS of concentration fluctuations

Figure 5.8: False-colour average and RMS images, for same 45° inclination experiment as plotted in Figure 5.7. Blue region near source in both images is area where concentrations were higher than extrapolation limits

Figure 5.9 plots intermittency and temporally-averaged concentration profiles at the same locations from a 75° inclination experiment. This experiment showed a large region of low-intermittency directly below maximum centreline height ($r/b_c < 0$ on $s/(d\,F_0) = 2.23$

profile). However, a steep decay in relative concentration may simultaneously be seen in the temporally-averaged concentration profile for the same location. This is clear evidence of flow re-entrainment. That is, eddies (of high concentration) are mixing with previously-mixed discharge fluid rather than unmixed ambient fluid.

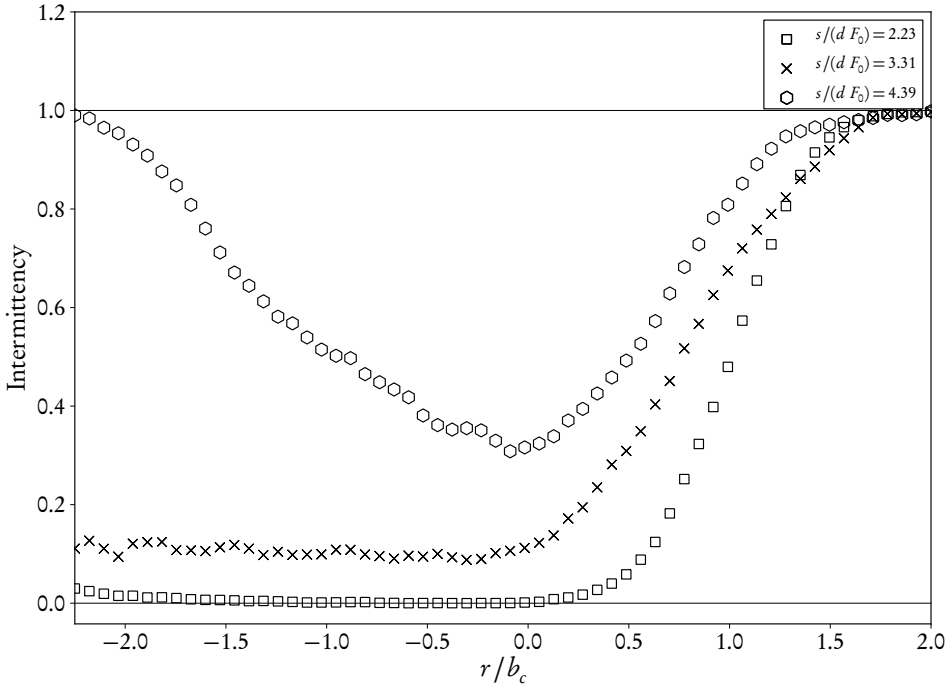

(**a**) Intermittency profile; threshold of 0.015 C_0

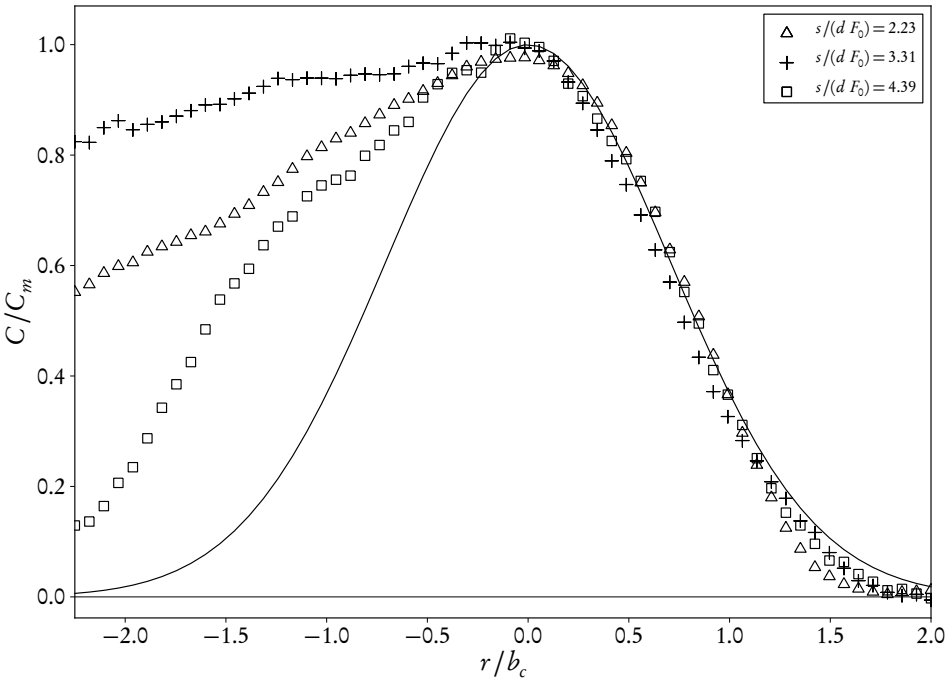

(**b**) Temporally-averaged concentration profile

Figure 5.9: Intermittency and average concentration profiles taken at same locations from experiment at 75° inclination. $s/(d\,F_0) = 2.23$ is centreline maximum height location; $s/(d\,F_0) = 4.39$ is return point location. $F_0 = 30.81$ and $\mathrm{Re} = 4586$

It is interesting to note that both intermittency and temporally-averaged concentration profiles at the return-point in Figure 5.9 ($s/(d F_0) = 4.39$) are roughly symmetric in shape. This suggests that the flow is beginning to develop a fully plume-like nature; irrespective of the conditions that generated it.

Intermittency and temporally-averaged concentration profiles from a 30° experiment may be found in Appendix A (Figure A.3).

5.2.3 Comparison with other workers

Kikkert *et al.* (2007) plotted normalised cross-sectional profiles of average concentration using both LA and LIF systems. Inner-side profiles increased in magnitude systematically with increasing distance from the source, although the data were not plotted beyond $r/b_c = -2.0$ or for locations past $1.4s_m$. LA profiles show distinct steeper-than-Gaussian decay on the outer edge, consistent with the current data. Few LIF data points were plotted for $r/b_c > 1.4$, making an equivalent comparison on this plot difficult.

Concentration and RMS profiles at the centreline maximum location of 45° negatively buoyant jets were both plotted by Papakonstantis *et al.* (2011b). Their data are much more scattered than the profiles shown in Figure 5.3, and trends are harder to discern. Relative concentrations at $r/b_c = -2.0$ were on average higher than those from the present experiments ($C/C_m \approx 0.55$ as opposed to the present 0.45), although the form was consistent. Peak RMS data were significantly higher ($\mathrm{RMS}(C')/C_m \approx 0.4$ as opposed to the present 0.31).

As discussed in Section 2.1.1, Papakonstantis *et al.* found that the ratio of the height of maximum $\mathrm{RMS}(C')$ (z_{RMS}) to the maximum centreline height (z_m) was constant, with an average value of 1.17. The distance $z_{\mathrm{RMS}} - z_m$ was more variable; having an average value of $0.76\, b_c$.

Table 5.1 tabulates averaged RMS maxima values and locations from profiles at maximum centreline height (s_m) in the present experimental data. With the exception of the 30° inclination data point, r/b_c locations are remarkably constant (overall the average r/b_c value is 0.83)[7]. However, z_{RMS}/z_m values are not constant. This ratio increases with decreasing angles; being particularly large at 15°. Such a result is intuitive because $z_m \to 0$ as $\theta_0 \to 0$. Because Papakonstantis *et al.* only conducted experiments at 45°, 60° and 75° inclinations, such a trend was easily masked in the experimental error of the available data.

Plots of concentration and RMS profiles averaged across experimental data available at each source inclination may be found in Appendix A (Figure A.4).

5.3 Trajectory, Spread and Dilution for 45° Inclination

Attention will now be turned to the bulk characteristics of negatively buoyant jets: centreline trajectory, outer edge spread, and minimum (centreline) dilution. As a large number of experiments

[7] The 30° maxima location was an outlier because the peak was relatively indistinct (see Figure A.4, which plots a coarser view of the data used for this process).

Table 5.1: Location and values of maxima in averaged RMS profiles at s_m (taken from same data used for Figure A.4b)

Inclination	RMS$(C')/C_m$ Maxima	r/b_c location	$z_{\mathrm{RMS}}/(d\,F_0)$	z_{RMS}/z_m
15°	0.220	0.90	0.42	1.74
30°	0.269	0.72	0.84	1.27
45°	0.308	0.86	1.34	1.23
60°	0.348	0.86	1.87	1.16
75°	0.370	0.83	2.16	1.14

were conducted at the 45° source inclination, these experiments will be examined specifically to ascertain characteristics of flow behaviour.

5.3.1 Trajectory

Figure 5.10 plots centreline trajectory for 26 experiments, where data are scaled upon source diameter and initial Froude number. A wide range of initial Froude numbers are used. Scatter increases with increasing path length, yet datasets all follow very consistent shapes. In contrast to the observations of Ferrari & Querzoli (2004, 2010), no changes in shape occur at or near $F_0 = 31$. Forced jet model predictions consistently fall within experimental scatter.

Figures 5.11 to 5.13 plot non-dimensional spatial scales for the same experiments as a function of F_0. Each scale is distinctly dependent upon F_0; as expected from Figure 5.10.

Best fit slopes, fitted using sum-of squares optimisation, are plotted on Figures 5.11 to 5.13[8]. For the sake of convenience, the k-notation used by Cipollina *et al.* (2005), Kikkert *et al.* (2007) and others will be employed from here on to denote trajectory scales non-dimensionalised by both source diameter and initial Froude number. Thus for example,

$$k_{xm} = \frac{x_m}{dF_0} \quad \text{and} \quad k_{zm} = \frac{z_m}{dF_0}$$

It is helpful to point out that the trajectory is not parabolic. Two statistics prove this fact. Firstly, the path length to the return point, $k_{sr} = 3.999$, is less than double the path length to the maximum height location, $k_{sm} = 2.114$. Secondly, the horizontal distance to the return point, $k_{xr} = 3.127$, is less than double the horizontal distance to the maximum height location, $k_{xm} = 1.748$. This is consistent with the integral modelling assumptions employed in Chapter 3 and the observations of Cipollina *et al.* (2005).

Nevertheless, the figures introduced thus far mask some complexity. When spatial k-coefficients are calculated on a per-experiment basis, and the results plotted against their corresponding initial Froude number, data points do not always fall evenly around the global k-coefficient line calculated earlier. Figure 5.14 displays such a plot for the horizontal and vertical distances to the centreline maximum. A weak negative slope is seen in these plots and

[8]These are also tabulated in Table 5.2, which will be discussed later.

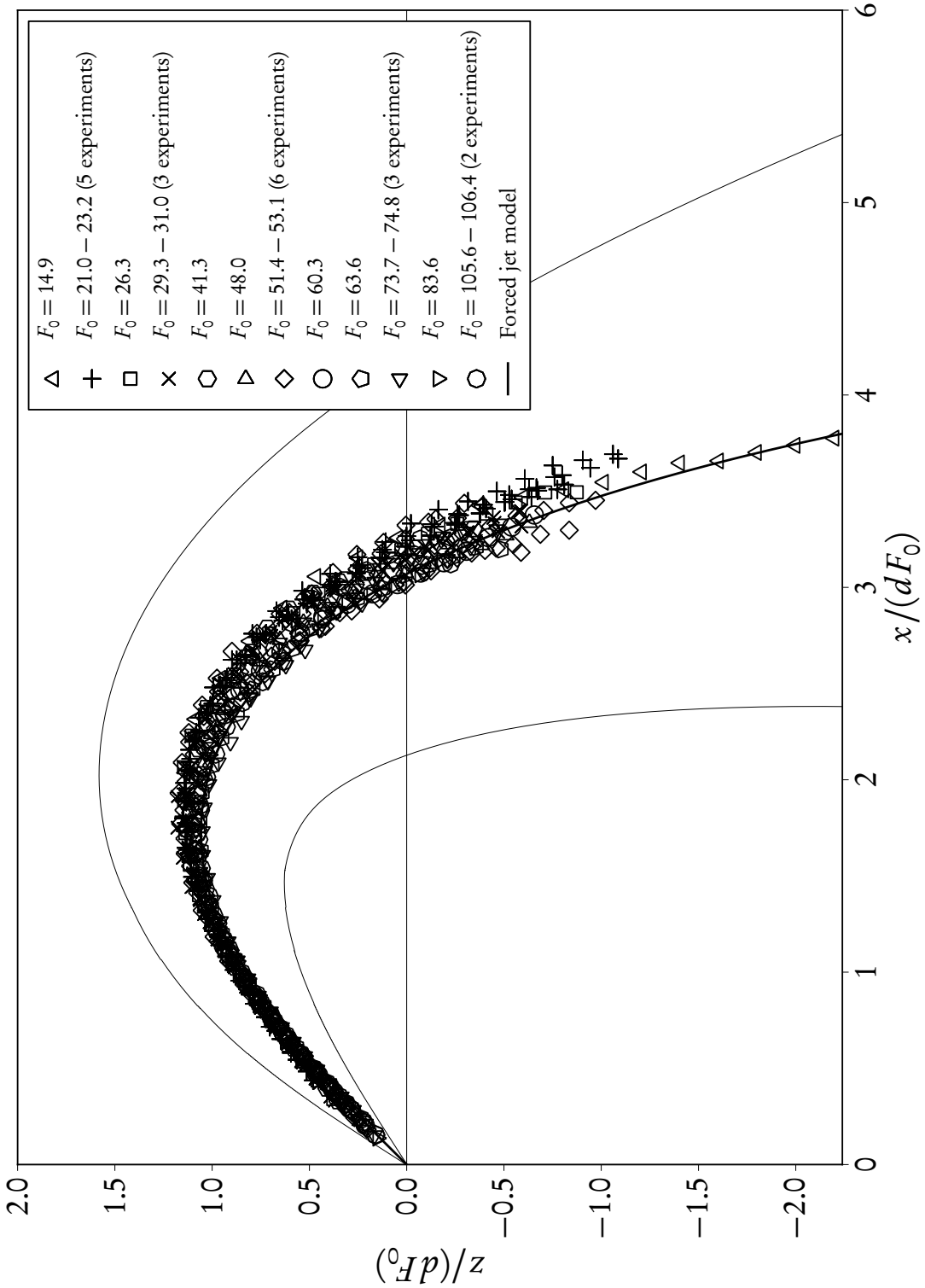

Figure 5.10: Trajectory for 45° negatively buoyant jet

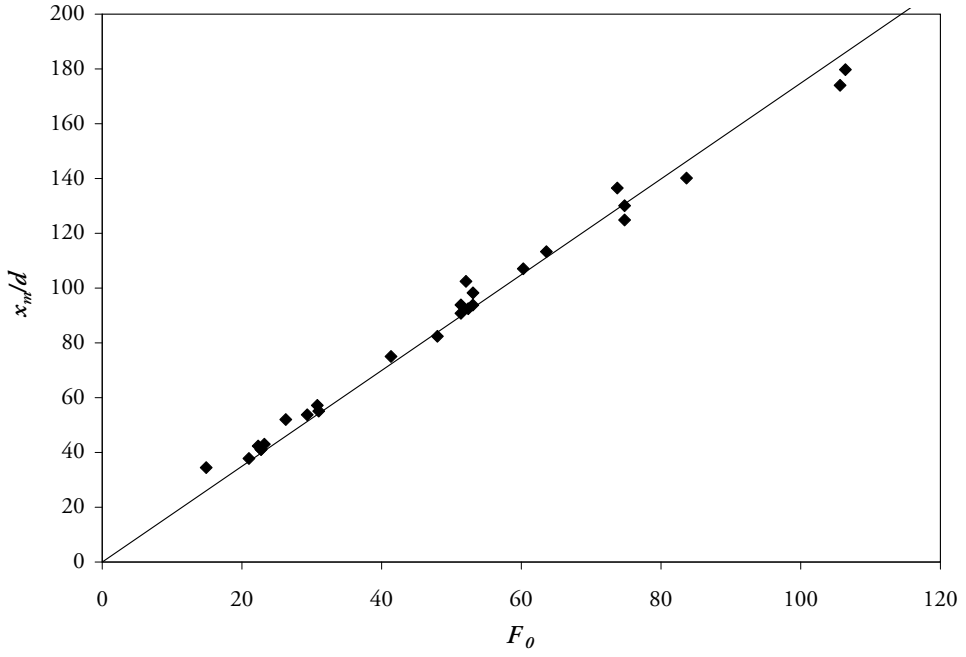

(**a**) Horizontal distance

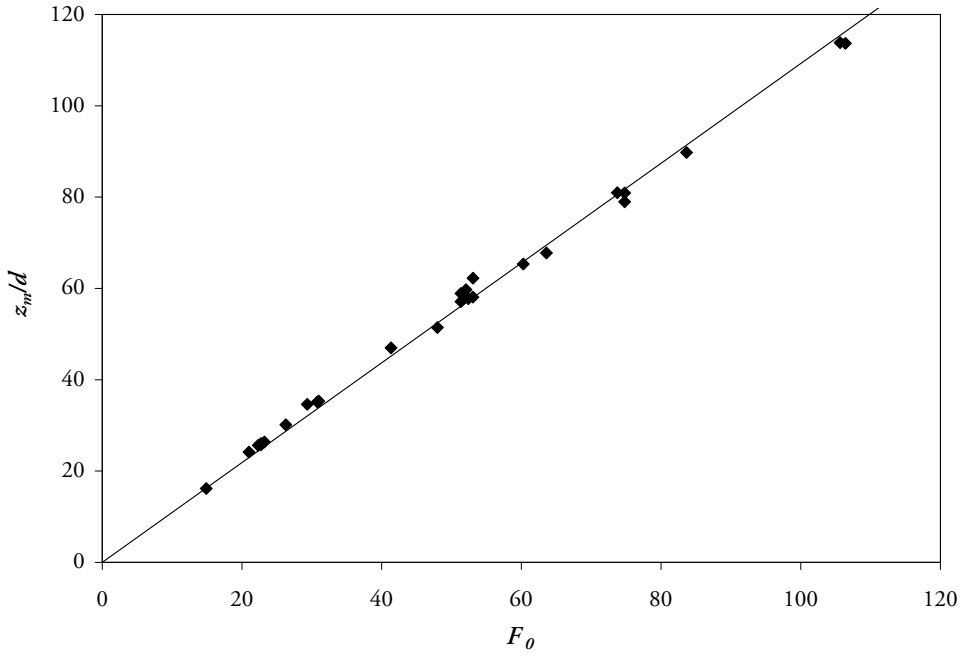

(**b**) Vertical distance

Figure 5.11: Horizontal and vertical distance to the location of maximum centreline height for a source inclination of 45°, as a function of F_0. Linear best-fit line passing through origin also plotted

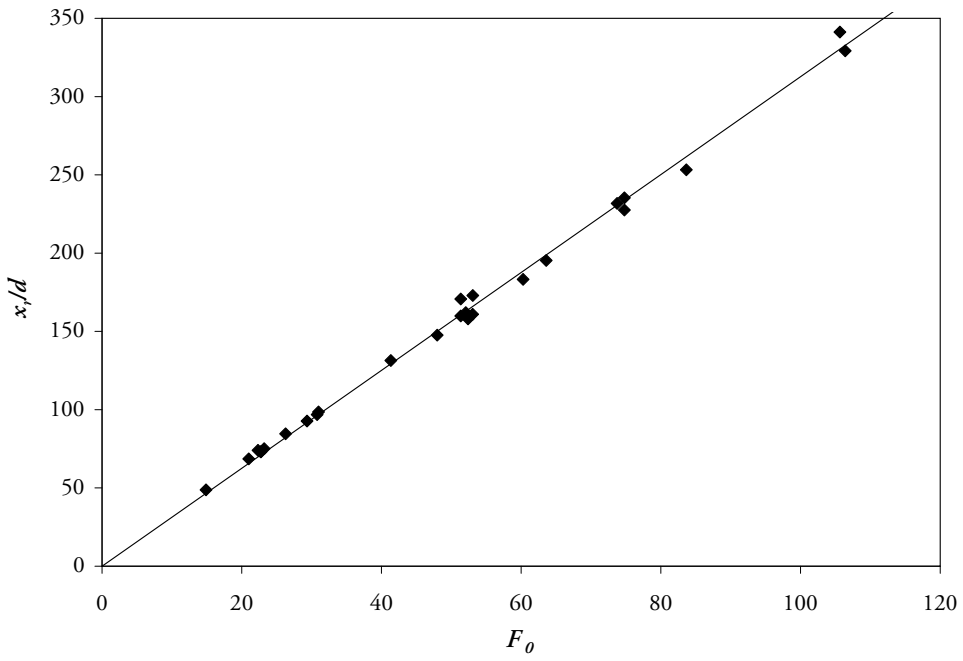

Figure 5.12: Horizontal distance to the centreline at the source height (*i.e.* the return point) for a source inclination of 45°, as a function of F_0. Linear best-fit slope also plotted

also those for k_{sm}, k_{sr}, k_{xr} and k_{xre} (which can be seen in Appendix A; Figures A.1 and A.2). Data points in Figure 5.14 are grouped by source diameter, and these slopes may also be seen within data from the same diameter. Therefore there appears to be a dependence on F_0 in spatial scales beyond that which previous workers have discussed or assumed.

5.3.2 Spread

Across the works surveyed in Chapter 2, many methods were employed to record the 'edge' of negatively buoyant jets; typically so as to determine their maximum edge height, z_{me}. Most commonly, this location has been identified visually from a small number of instantaneous flow images. However, this creates at least two problems. Firstly, the instantaneous flow edge is not always distinctly defined: at times, eddies have sharp boundaries, but at other times, their boundaries are smooth and tend to simply fade into the background colour. This issue was discussed by Jirka (2008). Secondly, because of the unsteadiness of turbulence, such a definition can only be meaningful if instantaneous measurements have been averaged over a long enough period of time. As will be seen in Figure 5.45, maximum eddy height varies significantly. There is no absolute recommendation regarding what length of time is sufficient; rather, measurements should be taken until the experimentalist is satisfied that the major periodic flow events have been encapsulated and the average is no longer changing significantly.

More rigorous definitions employed are those that are based on cross-sections taken through the time-averaged concentration field. These are based on the assumption that it is dilution rate, rather than the visual edge, that is important for practical purposes. Lai (2010) used $\frac{C}{C_m} = 0.25$

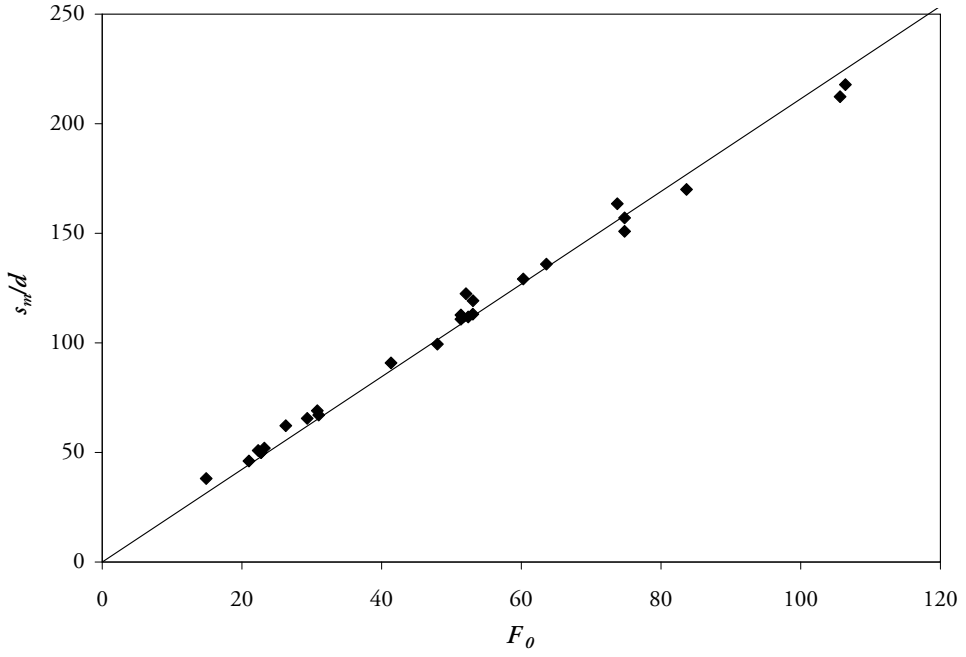

(**a**) Distance to maximum centreline height

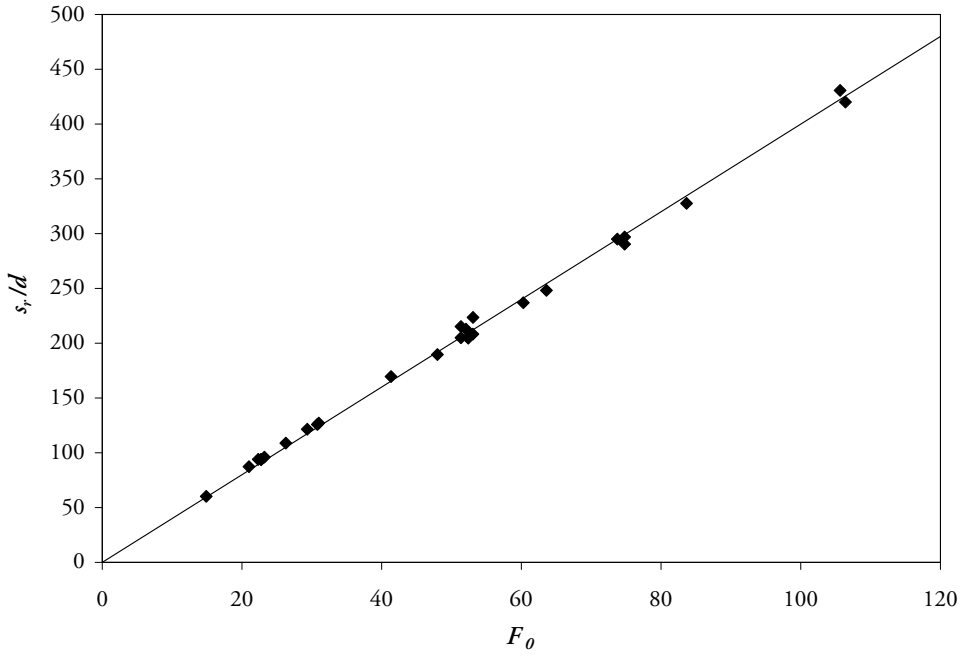

(**b**) Distance to return point

Figure 5.13: Path length to maximum centreline height and return point for a source inclination of 45°, as a function of F_0. Linear best-fit line passing through origin also plotted

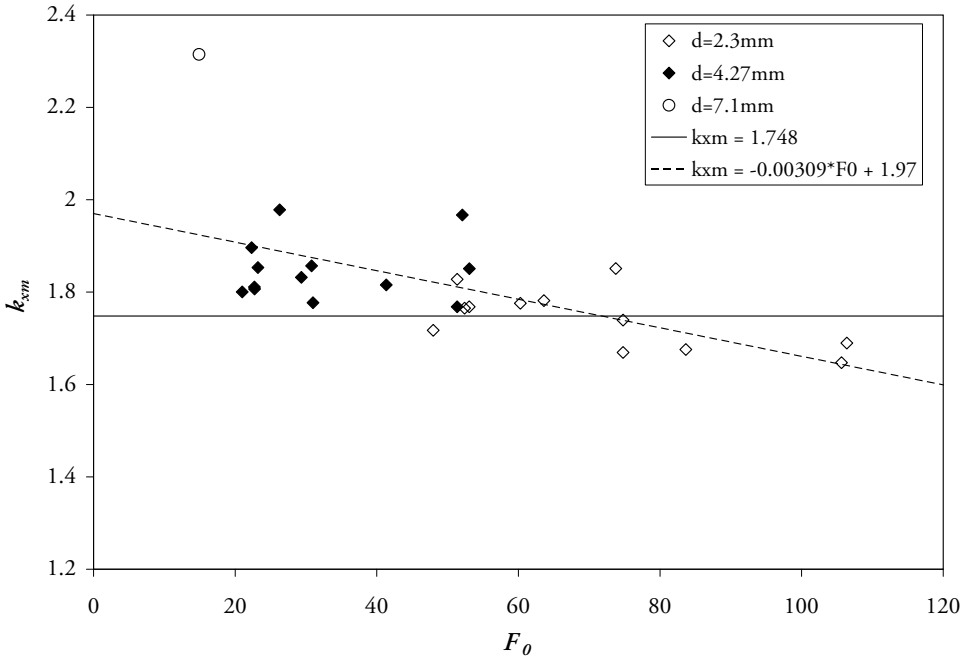

(a) Coefficient for horizontal distance. Corresponding forced jet prediction is $k_{xm} = 1.729$

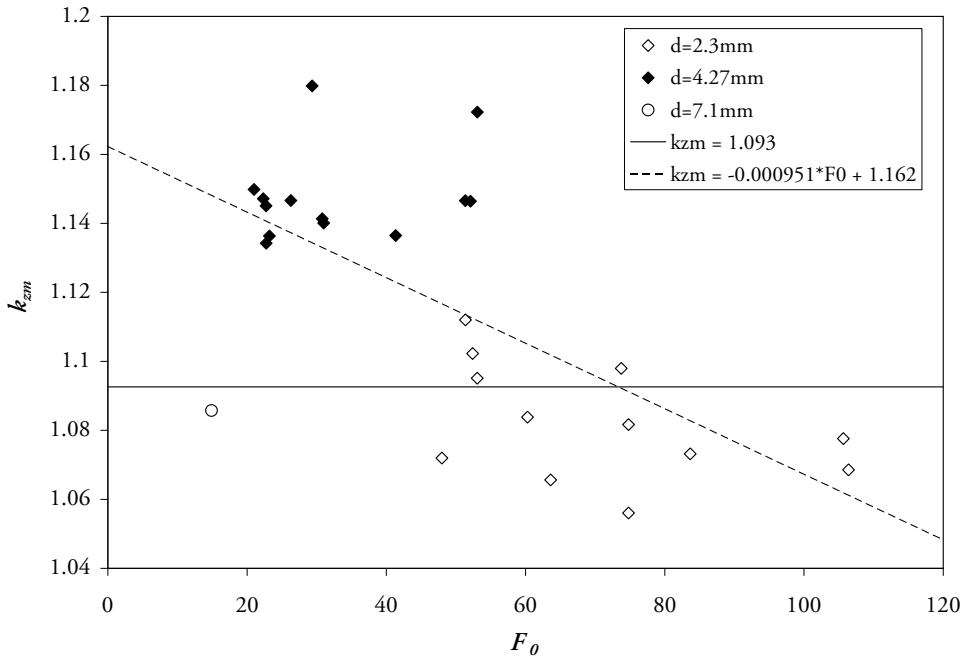

(b) Coefficient for vertical distance. Corresponding forced jet prediction is $k_{zm} = 1.057$

Figure 5.14: k-coefficients for horizontal and vertical distance to the location of maximum centreline height for a source inclination of 45°, as a function of F_0. Slope of lines plotted in Figure 5.11 plotted (here as horizontal lines), along with linear best-fit lines between the data plotted

to specify the edge of the flow, where C_m is the maximum value of the distribution in question. Kikkert *et al.* (2007) by contrast defined the flow edge to be at $\frac{C}{C_m} = e^{-4} = 0.018$, which corresponds to the location $r = 2b_c$ on the Gaussian distribution defined by Equation 4.10 (when r_0 is zero). Nevertheless, because of the asymmetry observed in the flow, this distribution was only fitted to their outer side concentration data. Of course for any of these definitions to be meaningful, concentration field data must in like manner be time-averaged over a long enough period so as to capture the major periodic flow events.

For the current study, the approach used by Kikkert *et al.* will be employed. Therefore, $z_{me} = z_m + 2b_c$ and x_{re} is approximately $x_r + \frac{2b_c}{-\sin(\theta_r)}$, where θ_r is trajectory angle at the return point. As outlined in Equation 4.10, centreline location and b_c values were based upon fits to concentration profiles between -0.25 $\leqslant \frac{r}{b_c} \leqslant$ 1.0.

Figure 5.15 plots b_c, the flow spread, against path length for 26 experiments. All data are non-dimensionalised by source diameter and initial Froude number. Locations of maximum height (s_m) and return point (s_r) are marked by dashed lines.

In the initial rising region, experimental spread rate is remarkably consistent. Below $s/dF_0 \approx$ 1.2 data follows a constant slope, but from there until the maximum height location, this slope reduces slightly. This is shown more clearly in Figure 5.16. Spread rate recovers beyond the maximum height location, and in many cases, increases further still. Forced jet model predictions largely fall within the scatter of experimental data and follow the same trends. The transition between jet and plume conversion factors (Section 3.3.1) can be clearly seen in Figure 5.16, in the range $1.1 \lesssim s/(d\,F_0) \lesssim 1.75$.

Although subtle, these are intriguing results. Concentration spread rates in pure plumes have been found by some to differ from those in pure jets: Wang & Law (2002) for instance found $\frac{db_c}{ds}$ to be 0.129 for a pure jet and 0.109 for a pure plume. Yet while it is feasible that the flow has become plume-like in its characteristics before reaching maximum height, visual observations discussed in earlier sections have indicated at least the outer side of the flow (upon which this data are based) was jet-like at this point. Additionally, centreline dilution data presented later (Figure 5.18) shows a regime-transition only after the maximum height location. Recalling that the outer side of the jet is inherently *stable*, we may thus deduce that eddy formation—and hence flow expansion—on this side has been slightly hindered in at least the region leading up to the centreline maximum.

No reasoning can be found in the literature for the apparent increase in (outer) spread rate on the falling side of a negatively buoyant jet. While not all experiments in Figure 5.15 show this behaviour, it appears to be significant over and above the increasing scatter of data as path length increases[9]. It appears that distortions on the inner side may be beginning to have an influence on outer side spread rates in the approach to—and following—the return point. This interaction would not be surprising given that large scale eddies are driving mixing on the scale of the flow,

[9]This increasing scatter is a by-product of the lengthening eddy timescales as the flow travels further from the source.

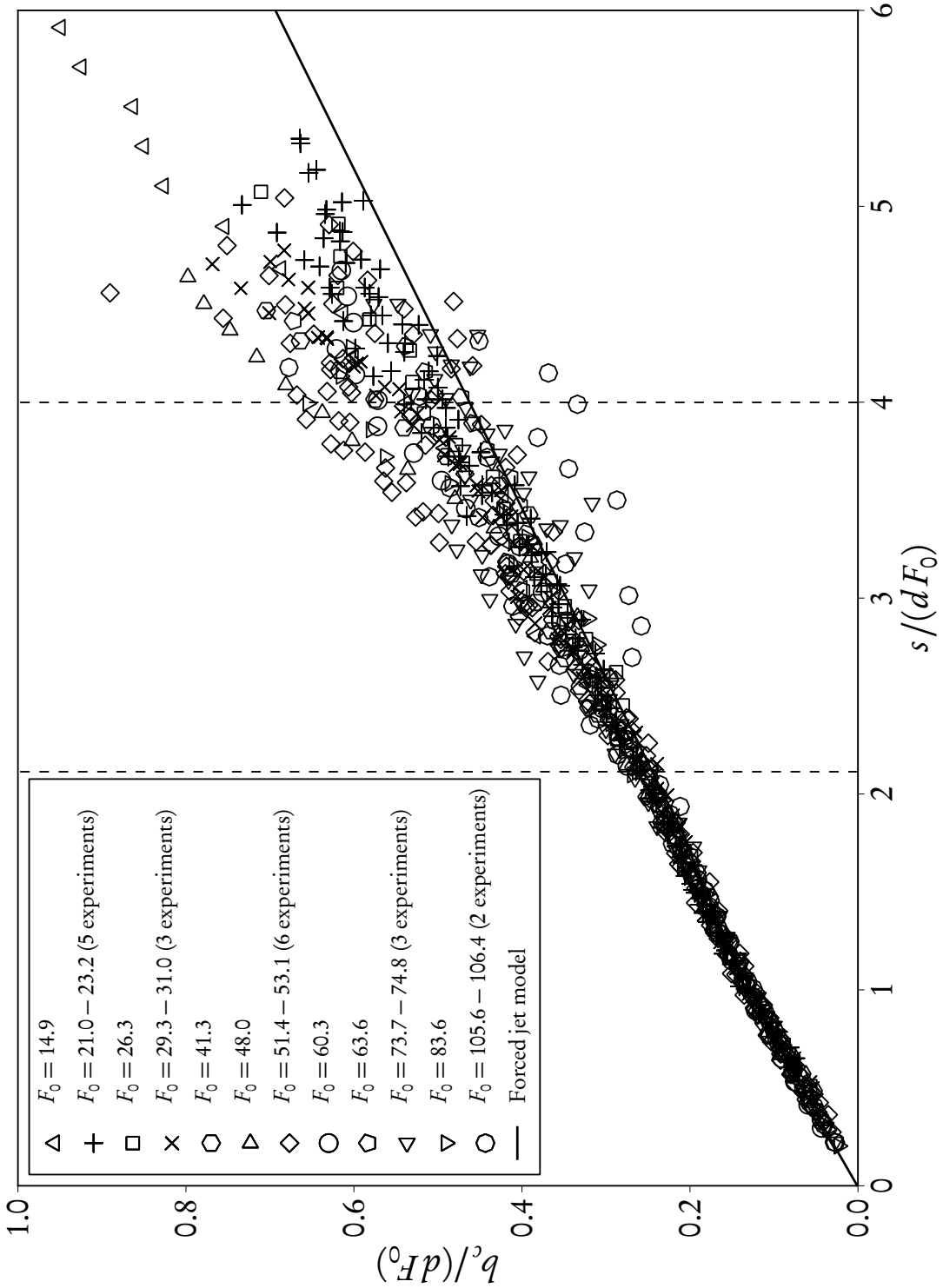

Figure 5.15: Spread against path length for for 45° negatively buoyant jet. Best-fit k_{sm} and k_{sr} locations plotted as vertical dashed lines

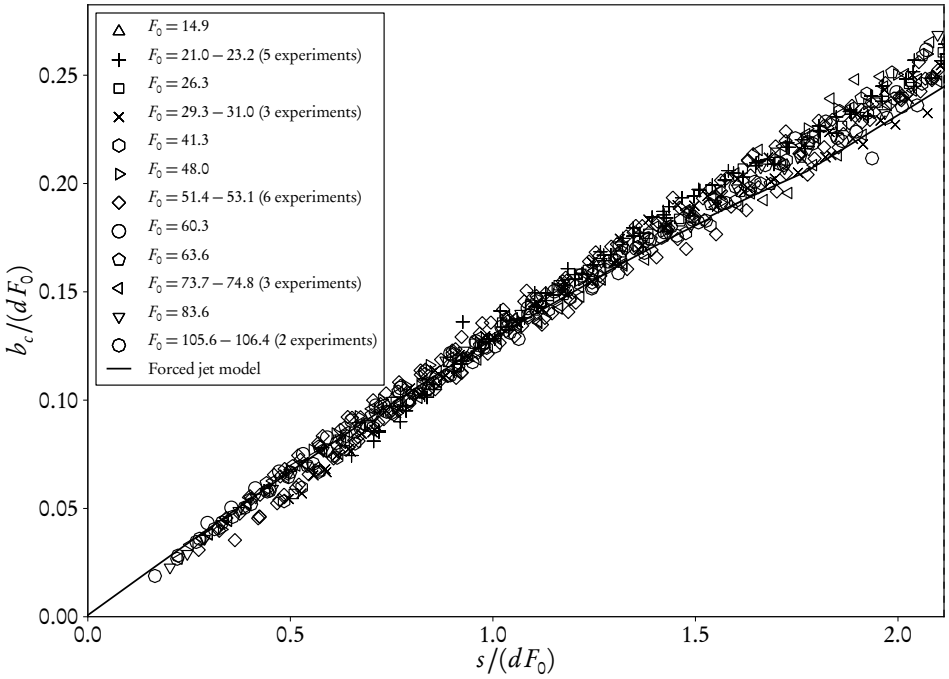

Figure 5.16: Spread against path length for for 45° negatively buoyant jet, up to k_{sm} location

as seen in Figure 5.46 and as is typical of plume-like behaviour.

Similar effects may be observed in the spread data plotted by Kikkert (his Figure 6.17), although these are not as obvious due to the limited number of experiments conducted. Unfortunately the spread data plotted by Lai (2010) was not collapsed by initial Froude number, so like analyses cannot be made.

Figure 5.17 plots non-dimensional maximum edge height and return point flow edge as a function of initial Froude number. Both scales appear to plot linearly with initial Froude number, although when per-experiment k-coefficients are plotted against F_0, a weak negative slope is also seen (refer to Figure A.2b for the k_{xre} graph).

5.3.3 Dilution

As outlined in Section 4.5.2, dilution in a jet is known to be a function of path length. Figure 5.18 plots dilution rate against path length for 45° negatively buoyant jets. Recall that initial concentrations of most datasets have been defined by the expected jet-region dilution rate, so datasets up to $s/(F_0 d) = 2.0$ have the same best-fit slope. A relatively consistent path is followed beyond the location of maximum centreline height (marked by the leftmost dashed vertical line), although the scatter in dilution rates can be seen to increase somewhat. Forced jet dilution results in the jet region are excellent; however beyond the maximum centreline height dilution rates appear to be slightly underpredicted.

In a plume, dilution rates are known to be a function of vertical height[10] rather than path

[10] Assuming that $\hat{g}$ acts vertically

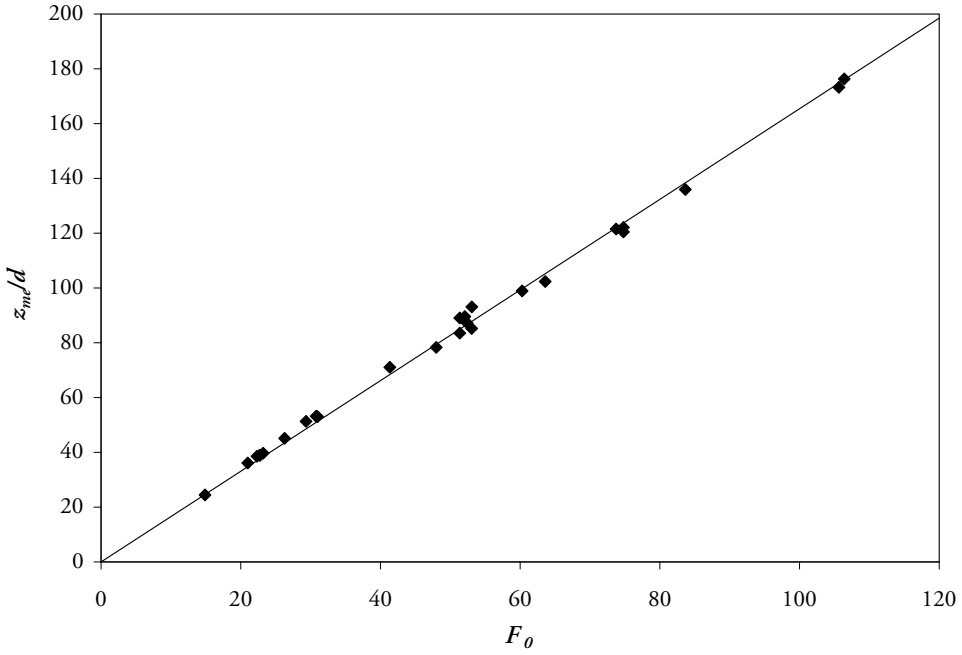

(**a**) Maximum edge height

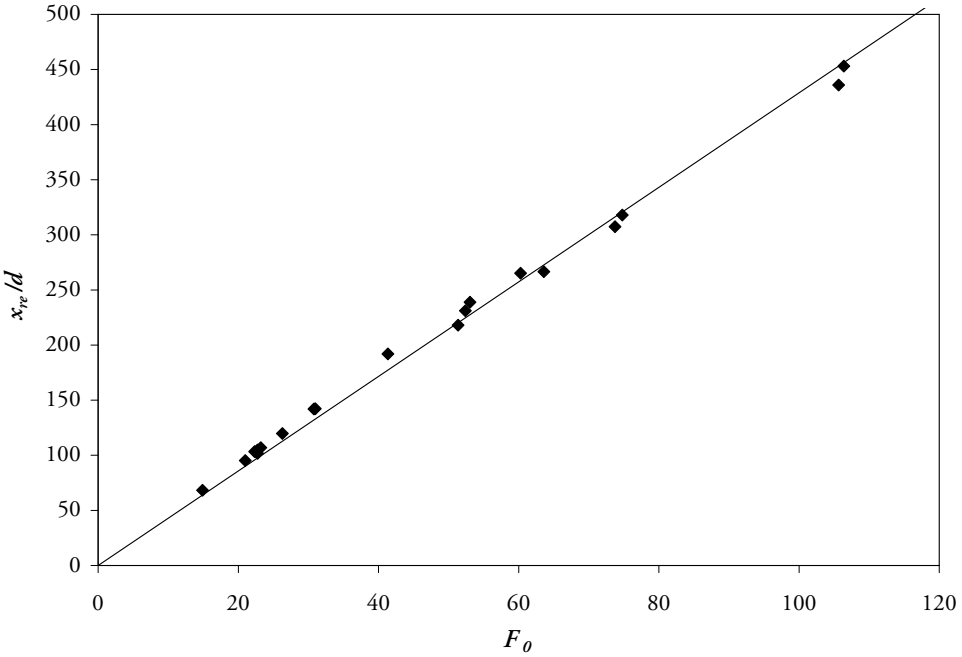

(**b**) Horizontal distance to the outer edge of the flow at the source height

Figure 5.17: Distance to outer edge of flow at maximum rise height and return point (vertically and horizontally, respectively) for a source inclination of 45°, as a function of F_0. Linear best-fit slope also plotted

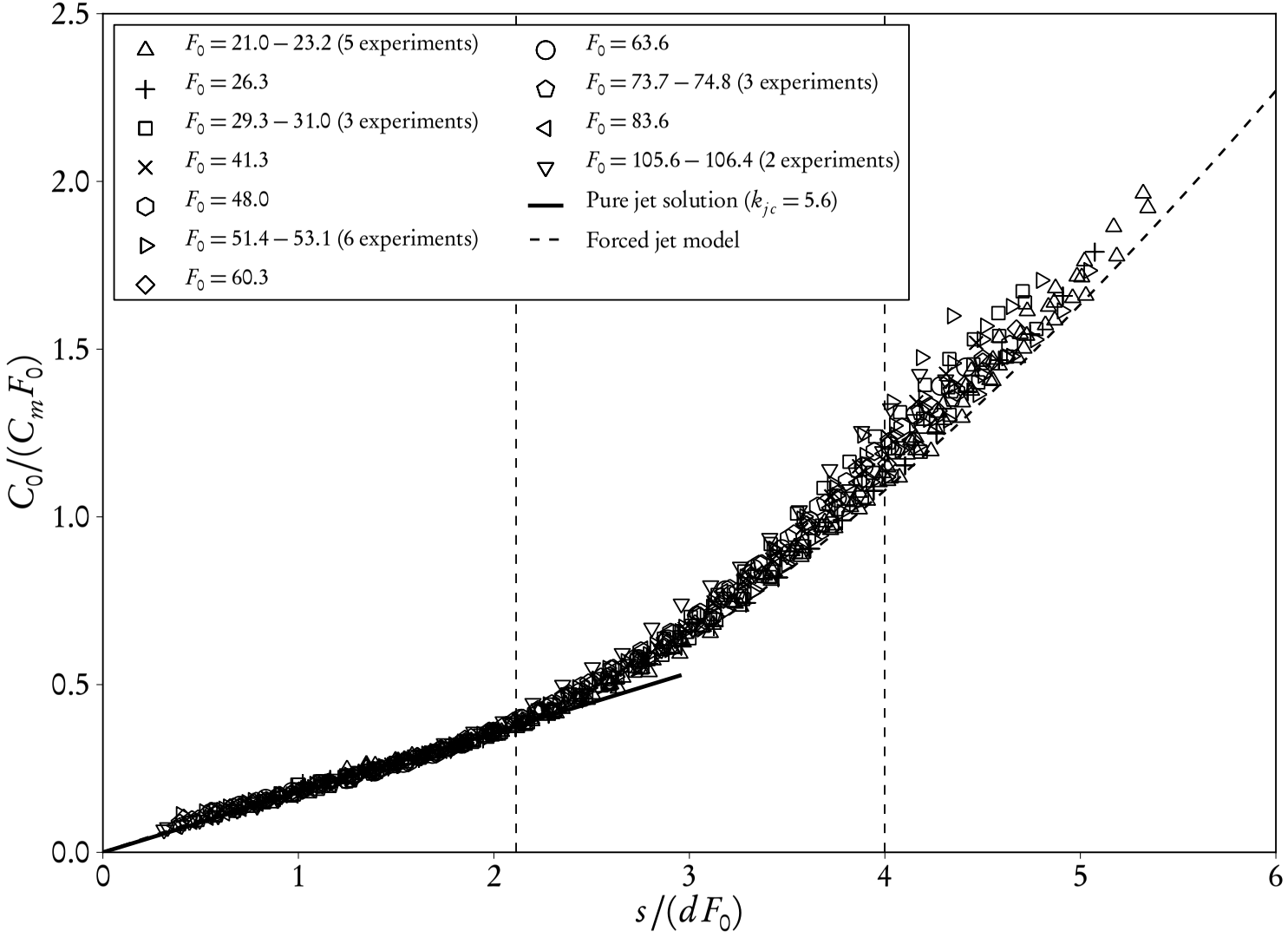

Figure 5.18: Normalised minimum dilution against path length for 45° negatively buoyant jet. Theoretical jet solution and (Equation 4.9 plume solution (Equation 5.2 with $z = s$) plotted. Best-fit k_{sm} and k_{sr} locations plotted as vertical dashed lines

length. Following Fischer *et al.* (1979), we may postulate that the quotient $\hat{g}_{\mathbb{C}}/\hat{g}_0$ can only be specified by volume flux Q_0 $[L^3/T]$, buoyancy flux B_0 $[L^4/T^3]$ and vertical distance from the source z $[L]$. Therefore we have, from this dimensional argument, that

$$\frac{\hat{g}_{\mathbb{C}}}{\hat{g}_0} = \frac{k_{pc} Q_0}{B_0^{1/3} z^{5/3}} \tag{5.1}$$

where k_{pc} is an empirical constant. Rearranging this equation and introducing the parameter F_0, we arrive at

$$\frac{\hat{g}_0}{\hat{g}_{\mathbb{C}} F_0} = \left(\frac{z}{F_0 d}\right)^{5/3} \cdot \frac{1}{k_{pc}(\frac{\pi}{4})^{2/3}} \tag{5.2}$$

Wang & Law (2002) found the constant k_{pc} to be equal to 11.3. When this relationship is plotted on a log-log scale a straight line is generated and k_{pc} controls the position of that line in the $\hat{g}_0/(\hat{g}_{\mathbb{C}} F_0)$ axis direction.

It is important to note that while this argument posits the dilution is a function of vertical height to the power of 5/3, both dilution and vertical height here are non-dimensionalised by the initial Froude number. The trajectories plotted on a linear scale in Figure 5.10 were also non-dimensionalised by initial Froude number, and their consistency indicates that after some distance, (non-dimensionalised) path length may become a good analogue to (non-dimensionalised) vertical distance. Figure 5.19, which plots the same data as Figure 5.18 on a log-log scale, gives strength to this proposition. Two distinct slopes are seen: the first matching the s^1 slope predicted by Equation 4.9[11], and the second close to a $s^{5/3}$ slope; particularly so after the return point location.

A plot of the region from maximum centreline height onwards is given in Figure 5.20. With path length s substituted for vertical height z in Equation 5.2, a good match is found beyond the return point location for $k_{pc} = 9.9$. This value is within the range tabulated by Wang & Law of k_{pc} coefficients calculated by various workers for a plume. These values of course were calculated with respect to vertical height, and standard integral models likewise operate with respect to vertical height. A visual inspection of similar plots for other source inclinations suggested that the best k_{pc} coefficient with respect to path length changed somewhat as a function of inclination, and also that the location where an $s^{5/3}$ slope was recovered was not fixed.

Figure 5.21 displays dilution against vertical height, on a linear scale. In this context, the rate of dilution on the falling side of the flow is remarkably constant. Two datasets are slight outliers, but the remaining 23 have a very consistent slope up to and beyond the return point. Forced jet dilution predictions follow approximately the same slope in this region. However, dilution predictions are too low in magnitude here with respect to vertical height. This appears to be largely due to the fact that maximum rise height (k_{zm}) predictions are on the low end of

[11] High dilutions near source are due to inadequate masking on some experiments of areas affected by extrapolation limits (as outlined in Section 4.5.4.1).

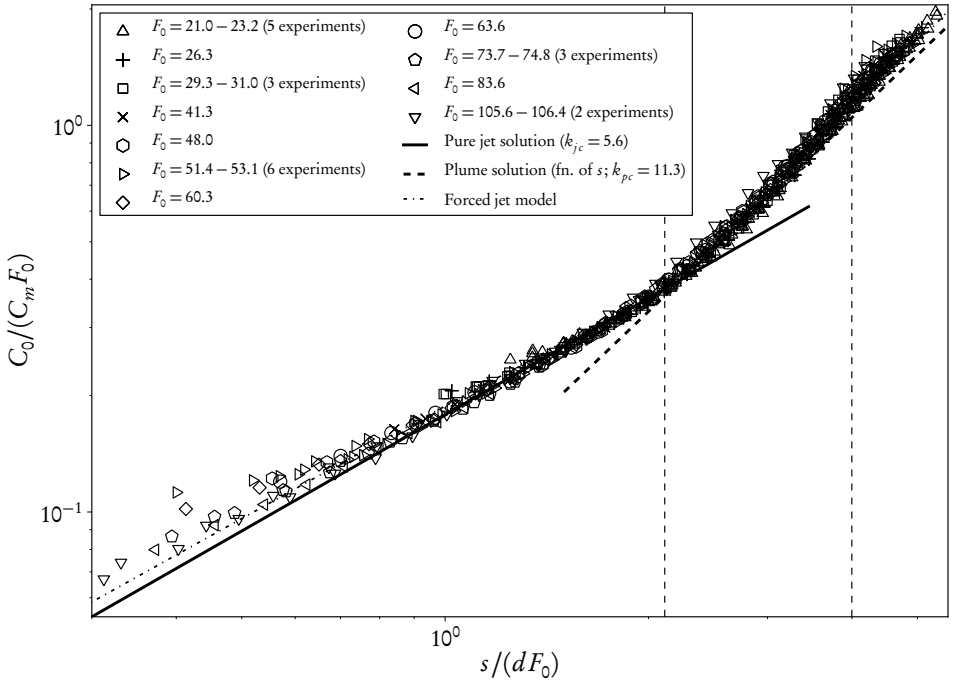

Figure 5.19: Log-log plot of normalised minimum dilution against path length for 45° negatively buoyant jet. Theoretical plume solution (Equation 5.2) plotted with $z = s$ and different values for k_{pc}. Best-fit k_{sm} and k_{sr} locations plotted as vertical dashed lines

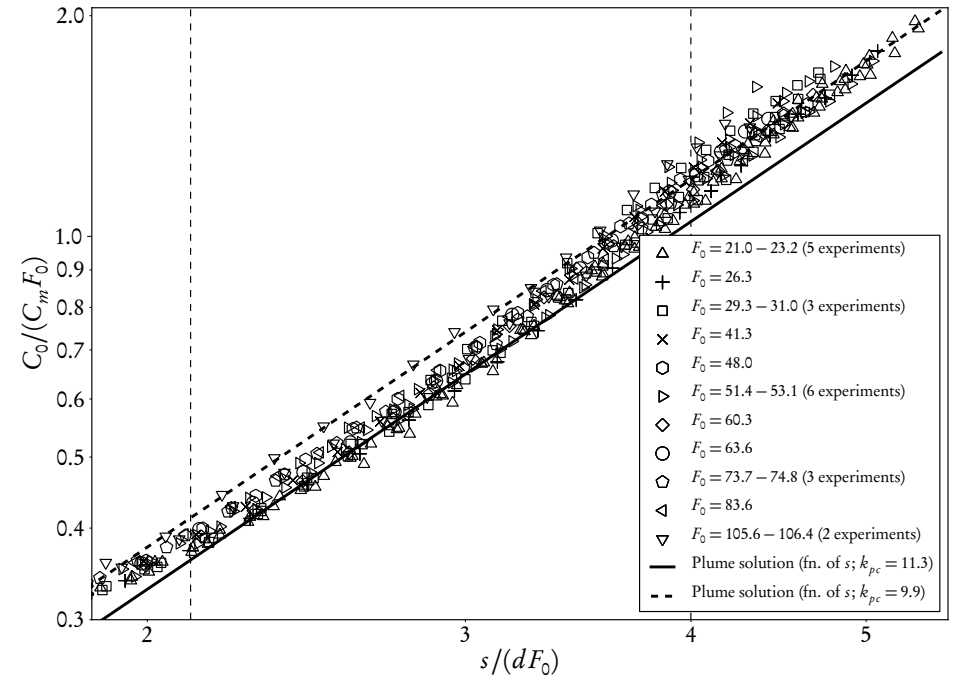

Figure 5.20: Same as Figure 5.19 but focused on plume region

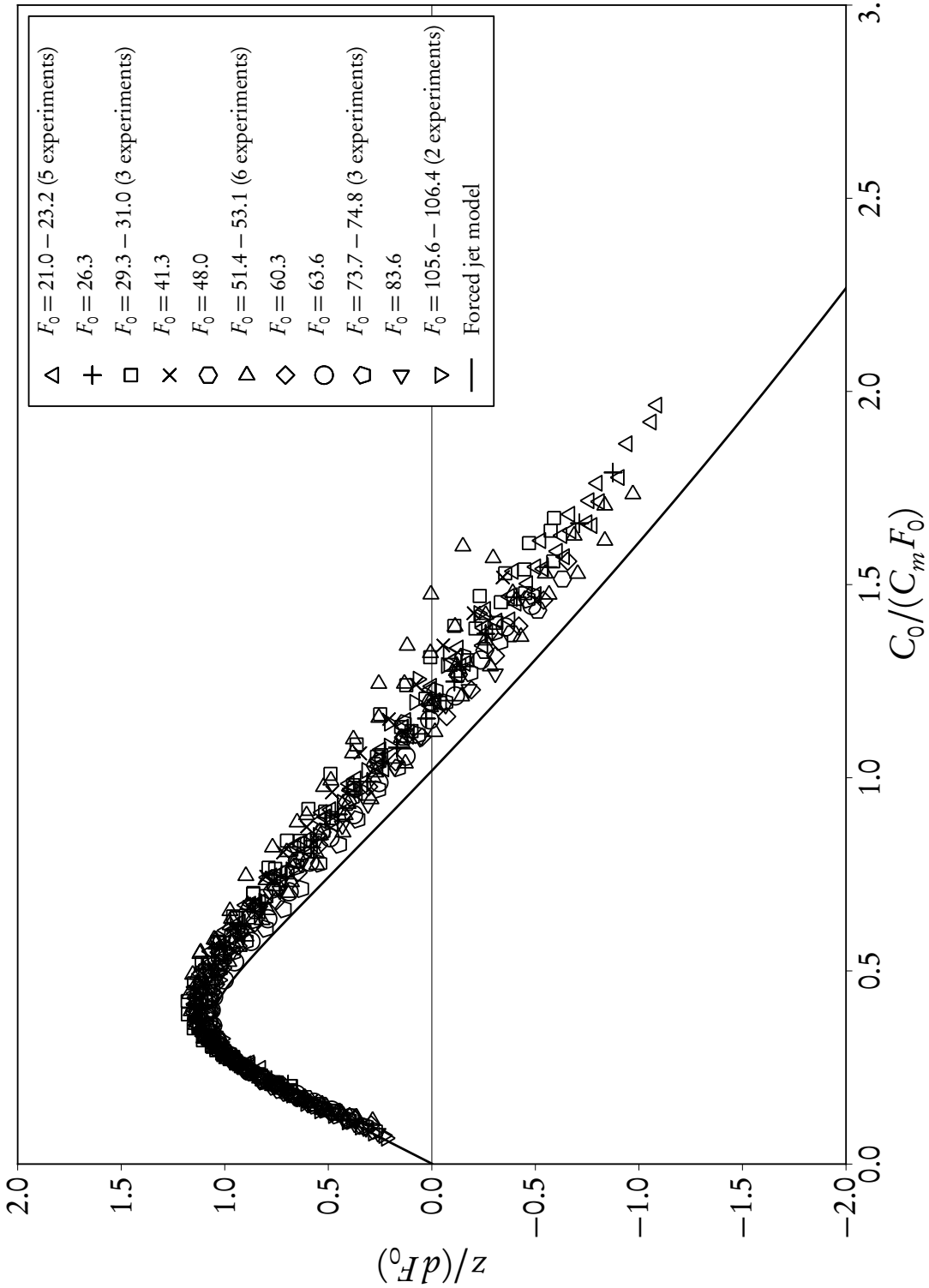

Figure 5.21: Normalised dilution against vertical height for 45° negatively buoyant jet

experimental data scatter.

Nevertheless, in order to employ Equation 5.2 (in terms of z), or in fact to plot a log-graph of dilution against vertical height, some definition of a "virtual source location" must be made. Kikkert *et al.* (2007) developed an analytical model that used a deflected jet solution up to and past the centreline maximum, and a plume solution from where the buoyancy generated momentum flux was equal to the initial momentum flux. They calculated a virtual source location above the centreline maximum for this purpose, such that bulk parameters at the transition point would be matched. Figure 5.22 plots the present experimental results in terms of z', the distance from the virtual source defined by Kikkert *et al.* From approximately the return point location ($z'/(dF_0) = 3.53$) experimental dilution results fall upon a 5/3 slope (corresponding to Equation 5.2 with $z = z'$ and $k_{pc} = 8.0$). Consequently, we may deduce that at least on the outer side, the flow for a 45° negatively buoyant jet is fully plume-like from the return point onwards[12].

As with trajectory and spread data, dilution at maximum height and return point scale closely with initial Froude number (Figure 5.23). However, when these coefficients are each divided by their respective F_0 value and plotted against F_0 (such as was done in Figure 5.14 for k_{xm} and k_{zm}), no additional relationship is seen.

5.4 Coefficients For All Inclinations

Thus far trajectory, spread and dilution data have been presented for the 45° negatively-buoyant jet only. From here, attention will turn to the relationship between non-dimensional coefficients that are characteristic of the flow and the initial inclination angle. The k-notation introduced in Section 5.3.1 will be used for the spatial scales depicted in Figure 1.1; the experimental configuration plot. Likewise, dilution at maximum height (S_m) and at return point (S_r) will be normalised by F_0. For the sake of convenience, the configuration plot (Figure 1.1) is repeated here in Figure 5.24.

Experimental coefficients are tabulated in Table 5.2, and are plotted graphically against data from other workers (given earlier in Tables 2.1 to 2.5) in a series of figures that will be discussed in the following sections. Underlying per-experiment data may be found in Appendix B. No dilution data are presented for the 70° inclination, as the calibration upon which these experiments were based was clearly unreliable. Yet before discussing these figures in detail, it is helpful to develop a conceptual framework within which to evaluate qualitative trends.

5.4.1 Estimation of shape

Whilst it has been shown that the trajectory of a negatively buoyant jet is not parabolic, it bears similarities to the trajectory of a simple projectile, such as a ball thrown through the air. Like a

[12] It is helpful to point out that the definition of the virtual source location affects the slope. That the Kikkert *et al.* (2007) definition generates a 5/3 slope indicates that it is at or very close to the 'correct' location; that is, the location where plume solutions match jet solutions accurately at the transition point.

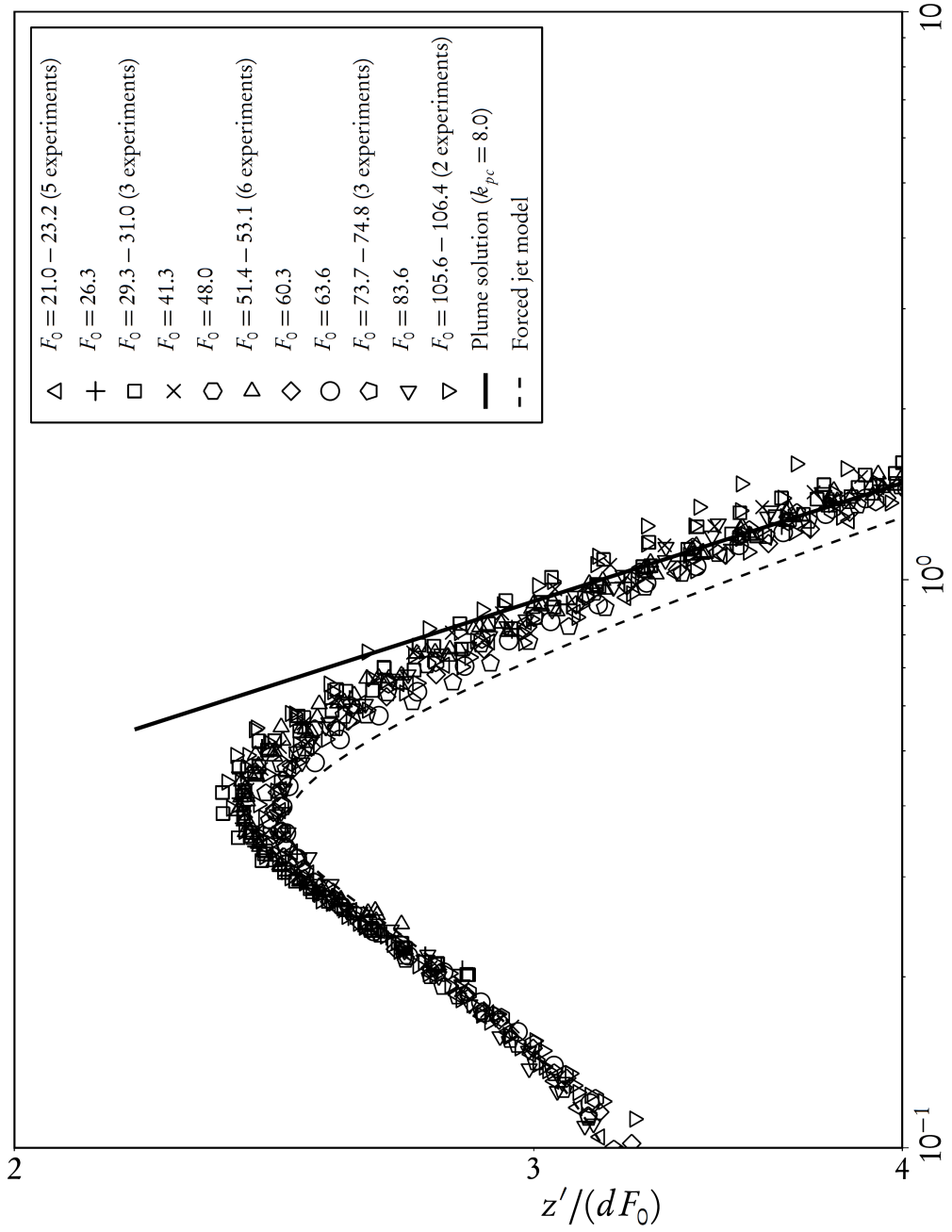

Figure 5.22: Normalised dilution against vertical distance from virtual source, z', for 45° negatively buoyant jet. At this location the virtual source is at $z = 3.53(dF_0)$

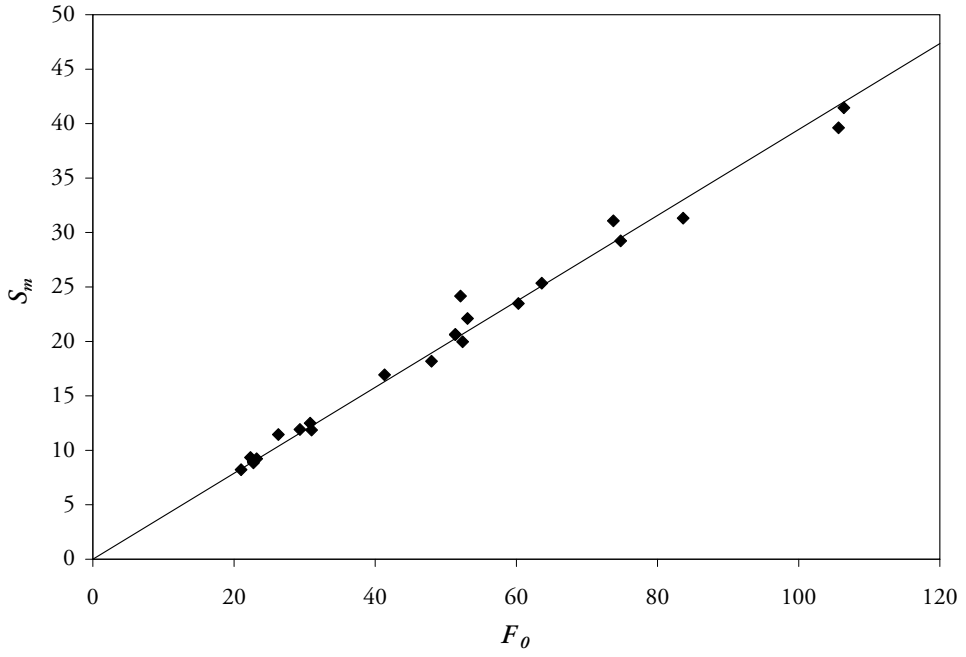

(**a**) Minimum dilution at maximum centreline height

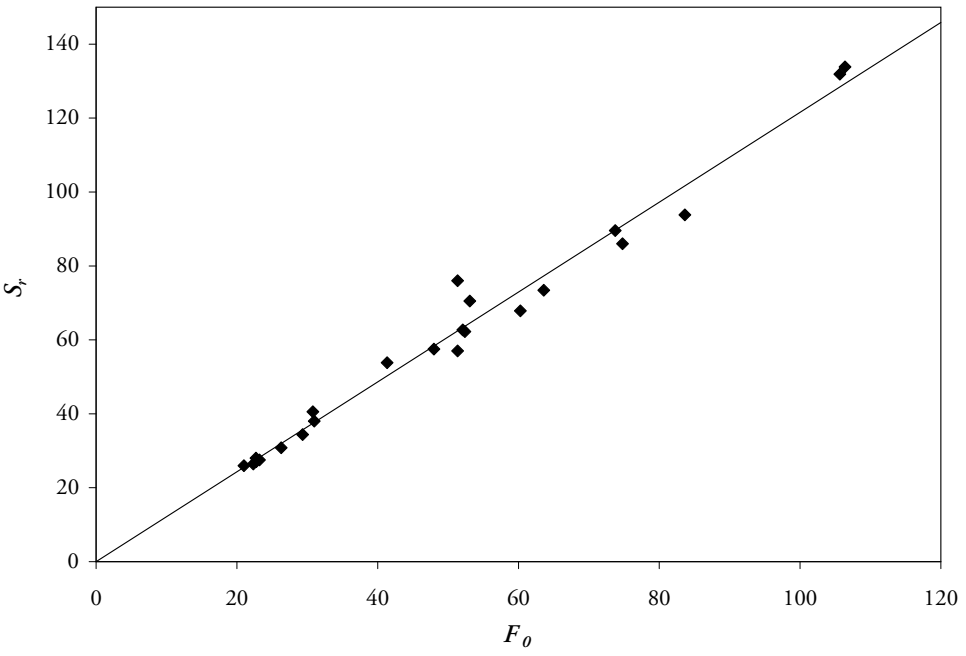

(**b**) Minimum dilution at return point

Figure 5.23: Minimum dilution at maximum centreline height and return point for a source inclination of 45°, as a function of F_0. Linear best-fit line passing through origin also plotted

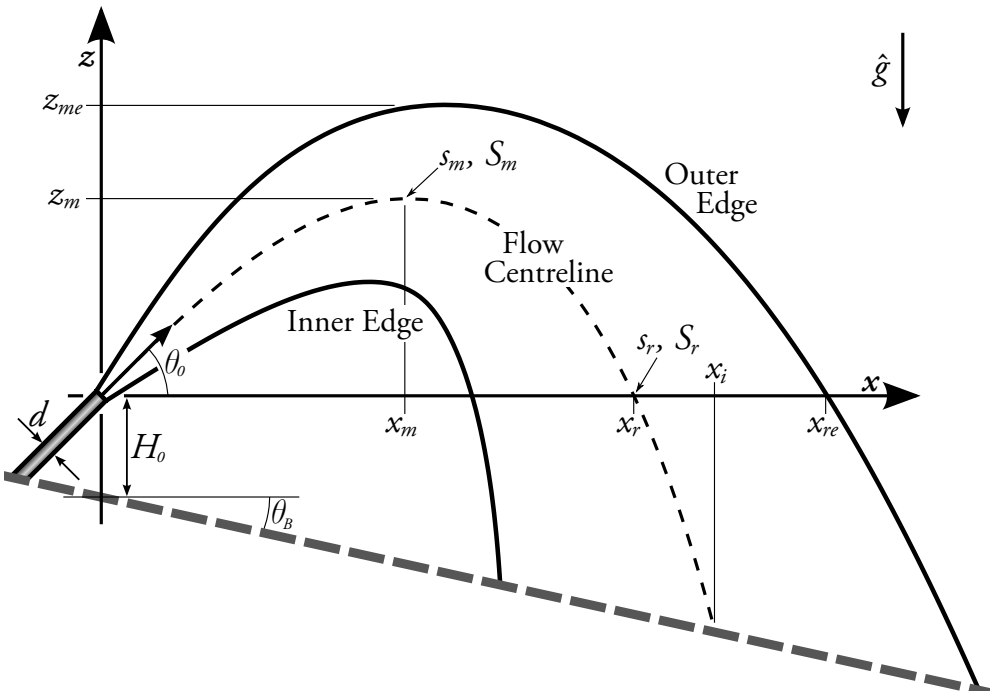

Figure 5.24: Configuration and notation plot for an inclined negatively-buoyant jet. Vertical and horizontal coordinates are both measured from the discharge nozzle

Table 5.2: Experimental coefficients

Inclination	k_{xm}	k_{zm}	k_{sm}	k_{zme}	k_{xr}	k_{sr}	S_m/F_0	S_r/F_0	k_{xre}
15°	1.37	0.24	1.39	0.63	2.39	2.45	0.25	0.48	3.68
30°	1.75	0.66	1.90	1.15	3.08	3.45	0.34	0.84	4.34
45°	1.75	1.09	2.11	1.65	3.13	4.00	0.39	1.22	4.29
60°	1.53	1.61	2.31	2.21	2.76	4.48	0.42	1.55	3.96
70°	1.13	1.84	2.25	2.44	2.00	4.44	—	—	3.29
75°	0.97	1.89	2.23	2.53	1.67	4.39	0.39	1.53	2.93

projectile, a negatively buoyant jet is thrust upwards by some initial source of momentum. Both begin slowing due to gravitational acceleration, and after some maximum height is reached, fall back downwards. As such, projectile motion can form a simple conceptual framework in which to estimate and evaluate the form of experimental results, particularly with respect to inclination angle.

Nevertheless, it must be emphasised that significant differences do exist between projectile motion and negatively buoyant jets. While frictional effects are exerted on most projectiles, projectiles do not interact with their environment as negatively buoyant jets do; entraining and mixing with the environment. Projectiles are not turbulent bodies themselves, and thus do not exhibit turbulent characteristics such as unsteadiness and irregularity. Therefore, while as a conceptual model projectile motion has relevant value for the first-order qualitative prediction of results, it cannot make accurate quantitative estimations.

An ideal projectile—*i.e.* with no frictional effects, such as a ball in a vacuum—thrust upwards

at an angle has the parabolic coordinates

$$x = v_{0x}\, t \tag{5.3}$$

$$z = v_{0y}\, t - \frac{1}{2} g\, t^2 \tag{5.4}$$

where $[v_{0x}, v_{0z}]$ is initial velocity in the x and z directions, g is acceleration due to gravity and t is time. Figure 5.25 plots non-dimensional coefficients at maximum rise height for an ideal projectile at various initial inclinations. Horizontal distance to this location is a simple parabola, with a maxima at 45°. Vertical location however is S-shaped, rising slowly near 0° and 90°, and rapidly at moderate inclinations. Path length is roughly the combination of horizontal and vertical heights; rising to a peak at approximately 56° and falling down to be equal to vertical height at 90°. It should be noted that for a projectile, horizontal location of the return point is twice the horizontal location of the maximum height, and path length to the return point is twice the path length to the maximum height.

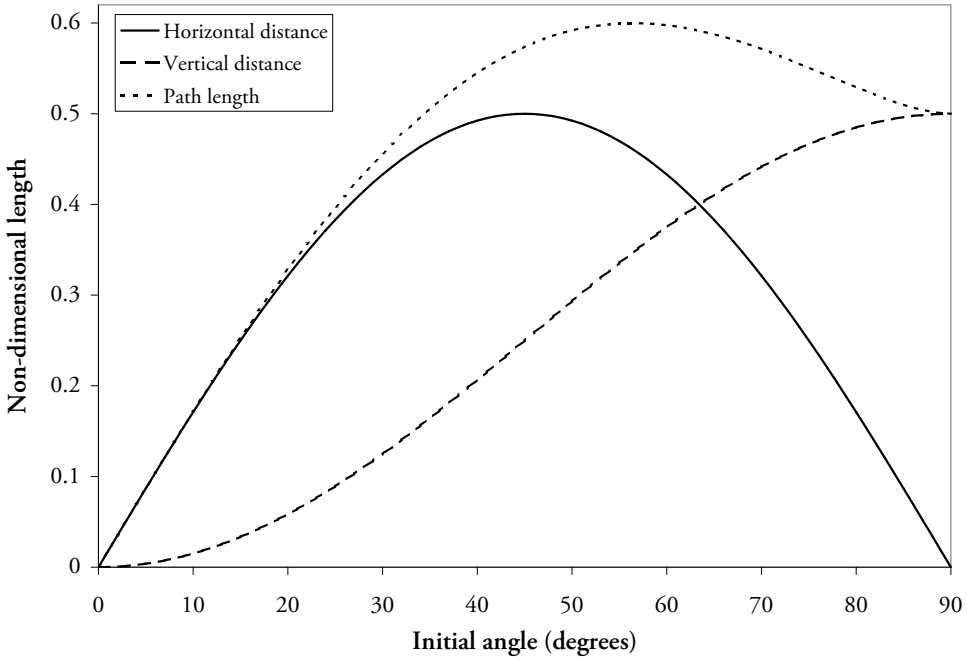

Figure 5.25: Centreline-maximum spatial scales (x_m, z_m and s_m) for an ideal projectile (*i.e.* Equations 5.3 and 5.4), normalised by v_0^2/g. Return-point scales are equal to twice the corresponding centreline-maximum scales: $x_r = 2x_m$ and $s_r = 2s_m$

Projectiles by definition do not "dilute" in any way, so no direct comparison may be made for concentration statistics. However, as a general rule, dilution in a turbulent jet increases with increasing path length. Therefore we may assume that a dilution plot would be similar to that of the projectile path-length plot.

A coarse comparison with the experimental data to be discussed in this section (Table 5.2) may be conducted by fitting polynomial curves through measured coefficients and identifying the

discharge angle where these curves are at their maximum values. Table 5.3 provides the results of such a procedure. It is important to note that these results are effectively an interpolation and/or extrapolation of the *trends* seen in experimental data.

Table 5.3: Discharge inclination of maximum value, as determined by third-order best fit polynomial line through 15–75° experimental data

Coefficient	Polynomial-fit maximum	Inclination of maximum
k_{zm}	1.971	84.3°
k_{zme}	2.610	85.1°
k_{xm}	1.798	38.8°
k_{xr}	3.196	40.4°
k_{xre}	4.391	39.3°
k_{sm}	2.281	63.4°
k_{sr}	4.462	66.4°
S_m/F_0	0.415	59.1°
S_r/F_0	1.583	67.9°

Vertical distances (k_{zm} and k_{zme}) are found to reach their maximum at approximately 85°; contrasted with a maximum at 90° for projectile vertical distances. Severe fountain-like re-entrainment was not observed in the present experiments, but this result suggests the effect on rise height begins to become apparent as low as the 75° inclination. Horizontal distances (k_{xm}, k_{xr} and k_{xre}) are found to reach their maximum at approximately 40°; marginally shallower than projectile horizontal distances which reach their maximum at 45° inclinations.

Path lengths (k_{sm} and k_{sr}) are found to reach their maximum at approximately 65°; slightly steeper than for projectile path lengths which are maximised at approximately 56°. Experimental dilutions at maximum centreline height (S_m/F_0) reach their maximum at 60°; yet dilutions at return point (S_r/F_0) reach their maximum at 67°. Therefore it appears that dilution rate—at least at maximum centreline height—is not a direct function of path length.

Zeitoun *et al.* (1970) recommended the use of negatively buoyant jets at a source inclination of 60° based on an estimation of path length to the return point, which was found to be maximised at an angle of 63°. They argued that "the 60° angle nozzles will produce a maximum path and therefore maximum dilution of the effluent under the same conditions of initial flow." Return-point path length and dilution in the current data are both maximised at approximately the same inclination; yet this inclination is somewhat steeper than 60°. Although the polynomial fit line for return point dilution at 60° is just 3.1% less than its maximum value (at 67°), it is only 0.2% less than this value at a 70° inclination. Therefore, based on the current dataset, it appears that a 70° source inclination would be a more appropriate recommendation.

5.4.2 Vertical distances

Figures 5.26 and 5.27 plot maximum centreline height and maximum edge height respectively against initial discharge inclination. Model predictions from Visjet, CorJet, the analytical model by Kikkert *et al.* (2007) and the present 'forced jet' model are plotted alongside experimental results for comparison.

5.4.2.1 Shape of experimental data

Like the vertical distance line in Figure 5.25, experimental data for k_{zm} in Figure 5.26 follows an "S-shape", with steep gradients at moderate angles and shallow gradients at low and high angles. Yet, consistent with previously-discussed polynomial fit results, it appears that a gradient of zero will be reached *before* 90°. Following the scope defined for the present study, no k_{zm} data are plotted on this graph at 90°. However, a cursory survey of turbulent fountain literature reveals k_{zme} (maximum edge height coefficient) values in the order of 1.7–1.9[13]. That is, *outer edge* heights at 90° are equal to or smaller than centreline heights at 75°. This of course is due to re-entrainment. Fluid in a turbulent fountain rises through the centre then falls down around itself, and in falling, is partially re-entrained into the rising fluid. Therefore rising fluid cannot be mixed as well as in an equivalent flow where buoyancy is in (essentially) the same direction as flow movement, and it does not rise as high. While turbulent fountains are obvious examples of re-entrainment, similar effects occur at inclinations close to 90°. As will be demonstrated in Section 5.2.1.1, 75° experiments showed evidence of re-entrainment near the maximum centreline height.

k_{zme} is plotted against inclination in Figure 5.27. Very similar patterns are seen for this coefficient. Here however, values are larger than k_{zm} by approximately $2b_c/(d\,F_0)$: not always *exactly* equal to this due the fact that centreline and edge maximums occur at slightly different horizontal locations.

5.4.2.2 Possible reasons for discrepancies

Major experimental discrepancies in these vertical distance figures are likely due to the following factors:

- The Bosanquet *et al.* (1961) k_{zm} data point at 45° is around 150% greater than other data points at this inclination. This data point is based upon only one experiment, and it is unclear whether the flow in this experiment was allowed adequate time to become fully established. Centreline trajectory was assumed to be midway between visually determined flow edges; a coarse approximation in the context of the inner-side instabilities that have been discussed herein. As k_{zm} was not directly provided by the authors, it was calculated here by simply assuming the source diameter for this experiment was the same as that

[13] Abraham (1967) gave 1.94; Fan & Brooks (1966) gave 1.9; Zeitoun *et al.* (1970) gave 1.72; Turner (1966) and Baines *et al.* (1990) gave 1.74.

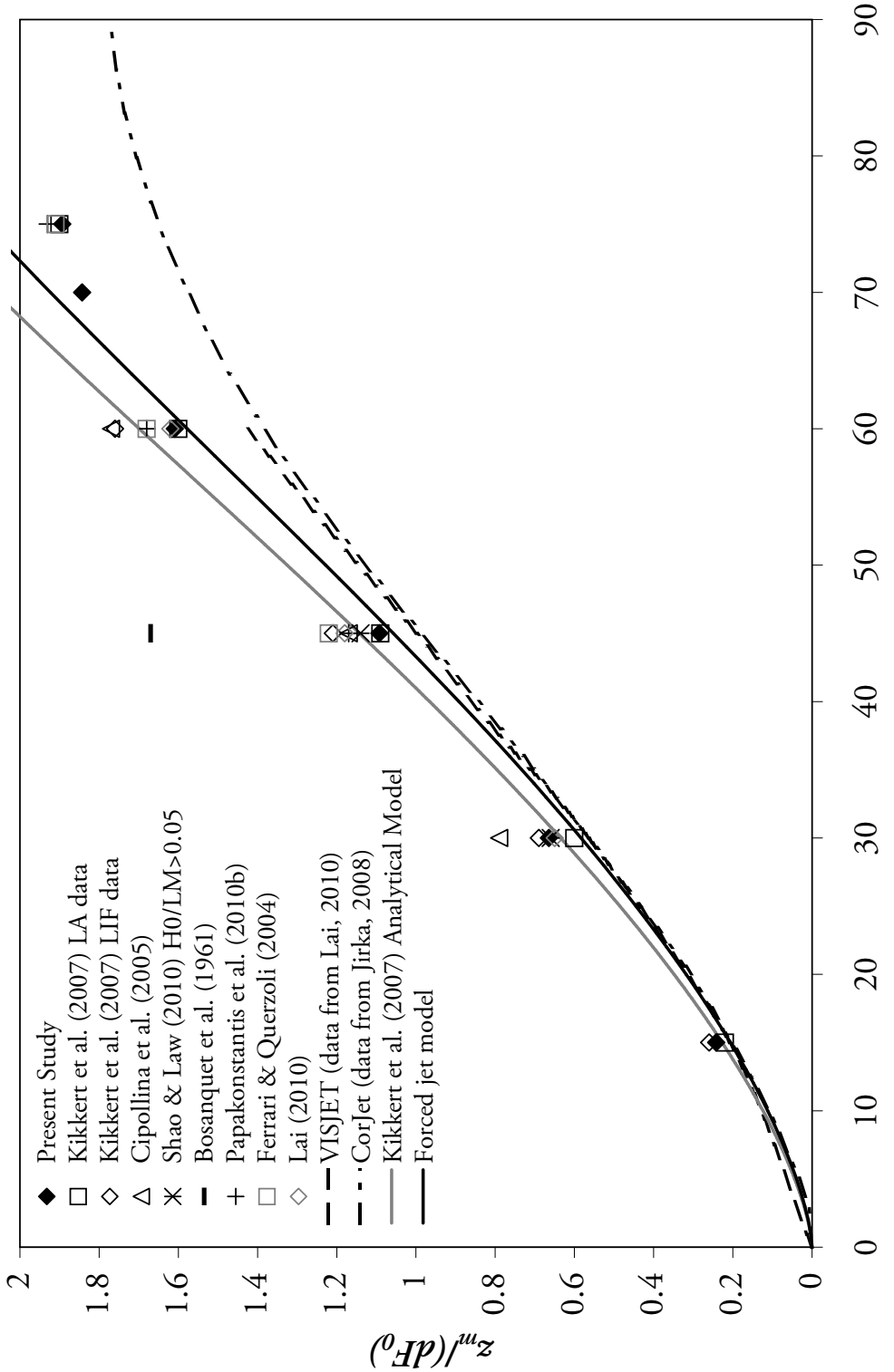

Figure 5.26: Dimensionless coefficient for maximum centreline height as a function of source inclination

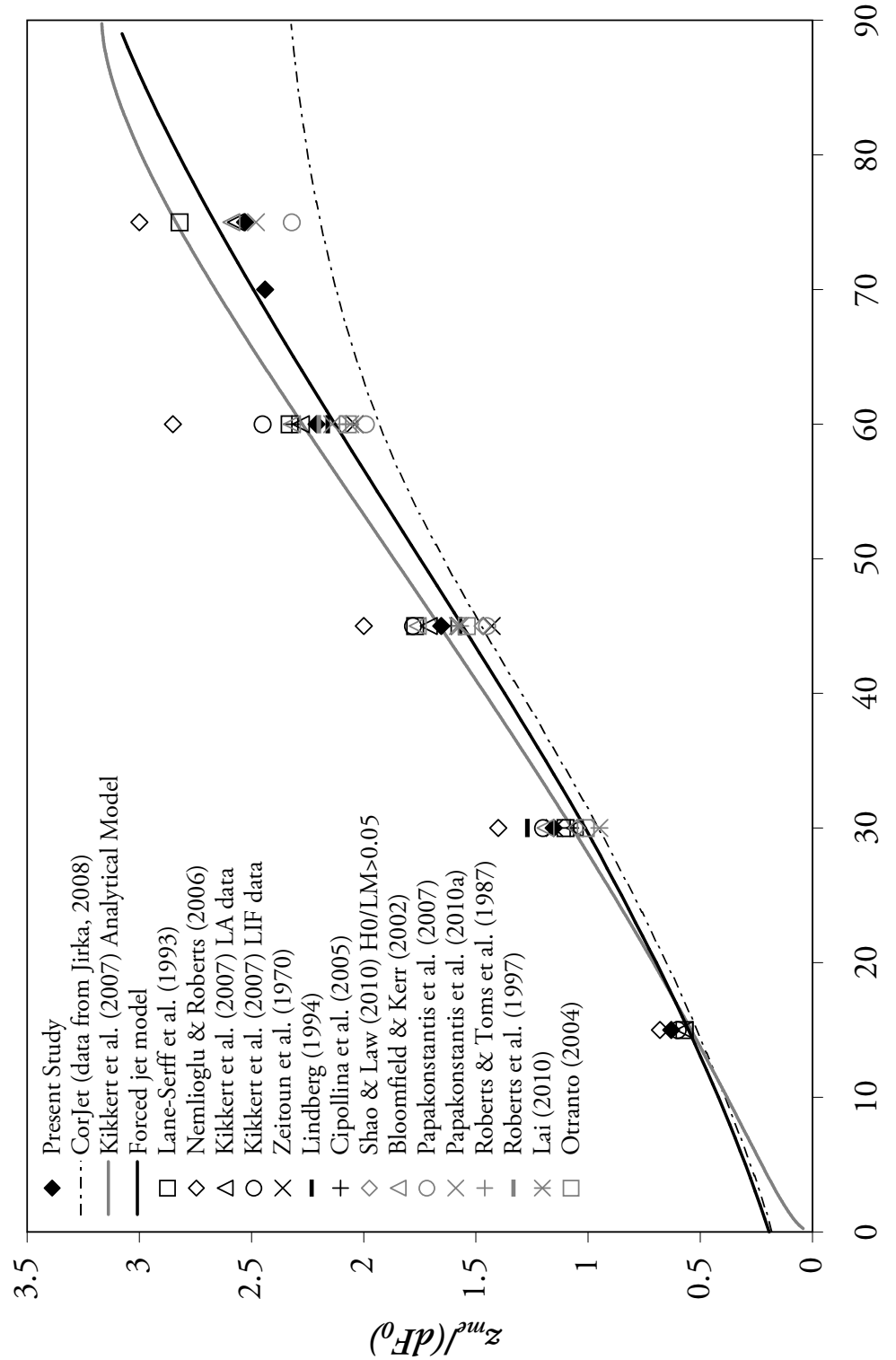

Figure 5.27: Dimensionless coefficient for maximum edge height as a function of source inclination

used for horizontal jets. The discrepancy observed is likely to be primarily due to this assumption. Note that 45° was the only inclination at which Bosanquet *et al.* performed negatively buoyant jet experiments.

- The Cipollina *et al.* (2005) k_{zm} data point at 30° inclination is slightly higher than other data at the same inclination. Few details were provided on their experimental system—a simple form of LA—but it is stated that images were recorded over a period of only 30 s, at 1 Hz. It appears that their experimental analysis was also reasonably crude, as spatial dimensions were recorded to only the nearest 10 mm. Tabulated experimental data are presented in their Table 1, and coefficients calculated from this data are up to 18.3% different from the coefficients presented in the text (it is the latter that are plotted here).
- Nemlioglu & Roberts (2006) k_{zme} data are consistently high. Only one experiment was conducted at each inclination; with the exception of the 60° inclination, at which two experiments were conducted. All F_0 values were very similar (in the range 21.2–24.1). It is unclear how long their experiments were conducted for. Very little information is provided on the experimental system employed. The k_{zme} coefficients presented for the 60° inclination experiments differ by 19%; demonstrating a lack of experimental reproducibility.
- Papakonstantis *et al.* (2007) k_{zme} values are consistently on the lower end of k_{zme} data ranges; a fact which becomes particularly apparent at 75°. While their data were derived from (a small number of) LA images, the only information regarding how this was done is the opaque statement, "an algorithm was developed using the image processing pack of Mathcad software to measure distances." It is difficult to assess the overall accuracy of the experimental systems employed by these authors.

5.4.2.3 Model performance

Analytical and forced jet model predictions for centreline maximum height (z_m) are within experimental scatter for 15–60°. It is worth reiterating that the forced jet model is not expected to be applicable for $\theta_0 \gtrsim 60°$. On average, forced-jet predictions for k_{zm} are 7.5% smaller than analytical predictions; a result largely due to differences in integral constants employed. CorJet and VISJET predictions are consistent with forced jet predictions until approximately 40°, and significantly under-predict experimental data at 60° and steeper.

Analytical and forced jet model predictions for maximum edge height (z_{me}) are within experimental scatter for 15–75°. However, curve gradients remain approximately constant in the region between 60° and 75° where a significant flattening in slope is seen in the present experimental data. In fact no model predictions plotted for either k_{zm} or k_{zme} reach their maximum before 90°.

CorJet model data for k_{zme} somewhat under-predicts experimental data at 75°, although not as significantly as is the case for the k_{zm} coefficient at this inclination. The CorJet curve gradient

for k_{zme} between 70° and 75° inclinations matches the gradient seen in the present experimental data. It is important to note that CorJet data for k_{zme} is the $C/C_m = 0.03$ contour, while analytical and forced jet model data as well as present experimental data for this parameter are based on the $C/C_m = e^{-(2^2)} \approx 0.018$ contour.

Forced jet and CorJet predictions of k_{zme} do not go to zero as $\theta_0 \to 0°$. In the case of the forced jet model, this is due to the fact that z_{me} is not simply $z_m + 2b_c$ but rather the outer edge ($2b_c$ from the centreline) is tracked independently of the centreline and its maximum defined accordingly. That is, the horizontal distance to the location of maximum *edge* height may be different to (usually greater than) the horizontal distance to the location of maximum *centreline* height. It is assumed that CorJet follows the same approach.

5.4.3 Horizontal distances

5.4.3.1 Shape of experimental data

Consistent with the projectile horizontal-distance line in Figure 5.25, experimental data for k_{xm}, k_{xr} and k_{xre} against inclination (Figures 5.28 to 5.30) follow an almost-parabolic shape. However, all experimental data appears to reach a maximum at a slightly shallower angle than 45°. This effect is a byproduct of the spreading and diluting behaviour of buoyant flows generally, and is not a direct function of inner-side instabilities. Predictions from Visjet and CorJet—models which do not take account of inner-side instabilities—also reach a maximum below the 45° inclination; confirming this argument.

Data for all horizontal coefficients is more scattered than vertical coefficient data. This is due to the inherent difficulty in recording the exact zero-gradient trajectory location with precision.

It is important to note that few workers have conducted experiments in such a manner that return point flow is completely unaffected by the bottom boundary in their experimental vessel. Some, such as Roberts *et al.* (1997) and Shao & Law (2010), have intentionally used small riser heights (H_0) in order to replicate typical field configurations. Others such as Cipollina *et al.* (2005) have positioned the source near the boundary but also employed a continuous washing system to prevent buildup of dense fluid in the experimental tank. Others have simply ensured that their riser height is greater than the observed bottom layer thickness. As discussed in Section 2.1.4, coefficients measured at these impact points have been assumed here to be equivalent to return point coefficients; *i.e.* $x_i = x_r$ and $S_i = S_r$. Nevertheless, where data are presented at the return point itself, the presence of boundaries near this location will at the least mean that eddies are constricted. Additionally, there is a possibility that the flow may have been deflected horizontally. Contrary to the assertion of Shao & Law (2010), these results are not "generally applicable" as they remain a function of riser height (and/or bed slope).

Figure 5.31 plots the relationship between x_r and x_m values. Here the data being considered are not absolute distances but *relative distances*: that is, the distance to the return point as a fraction of (horizontal) distance to the maximum centreline height. While it was discussed in

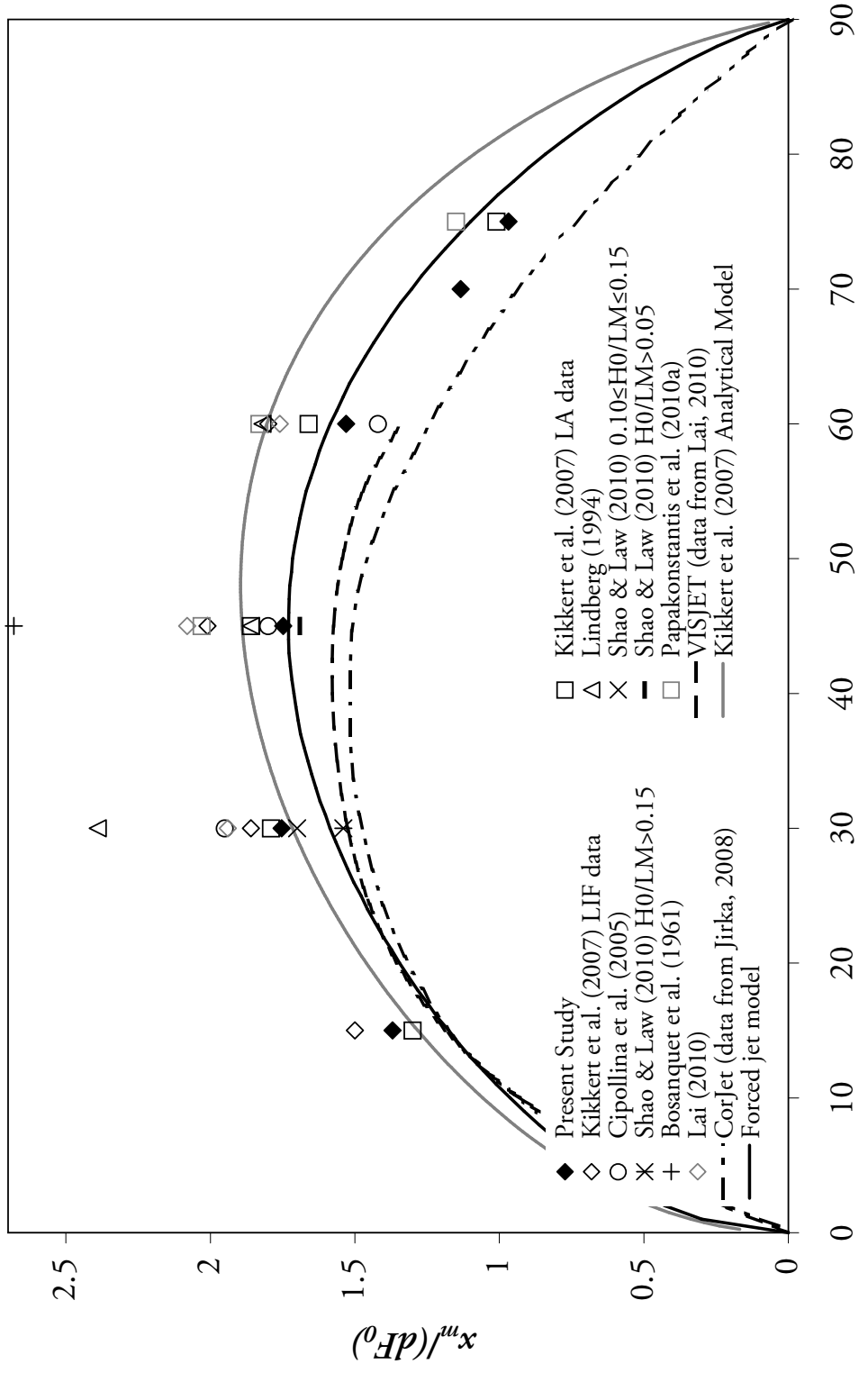

Figure 5.28: Dimensionless coefficient for horizontal distance to location of maximum centreline height as a function of source inclination

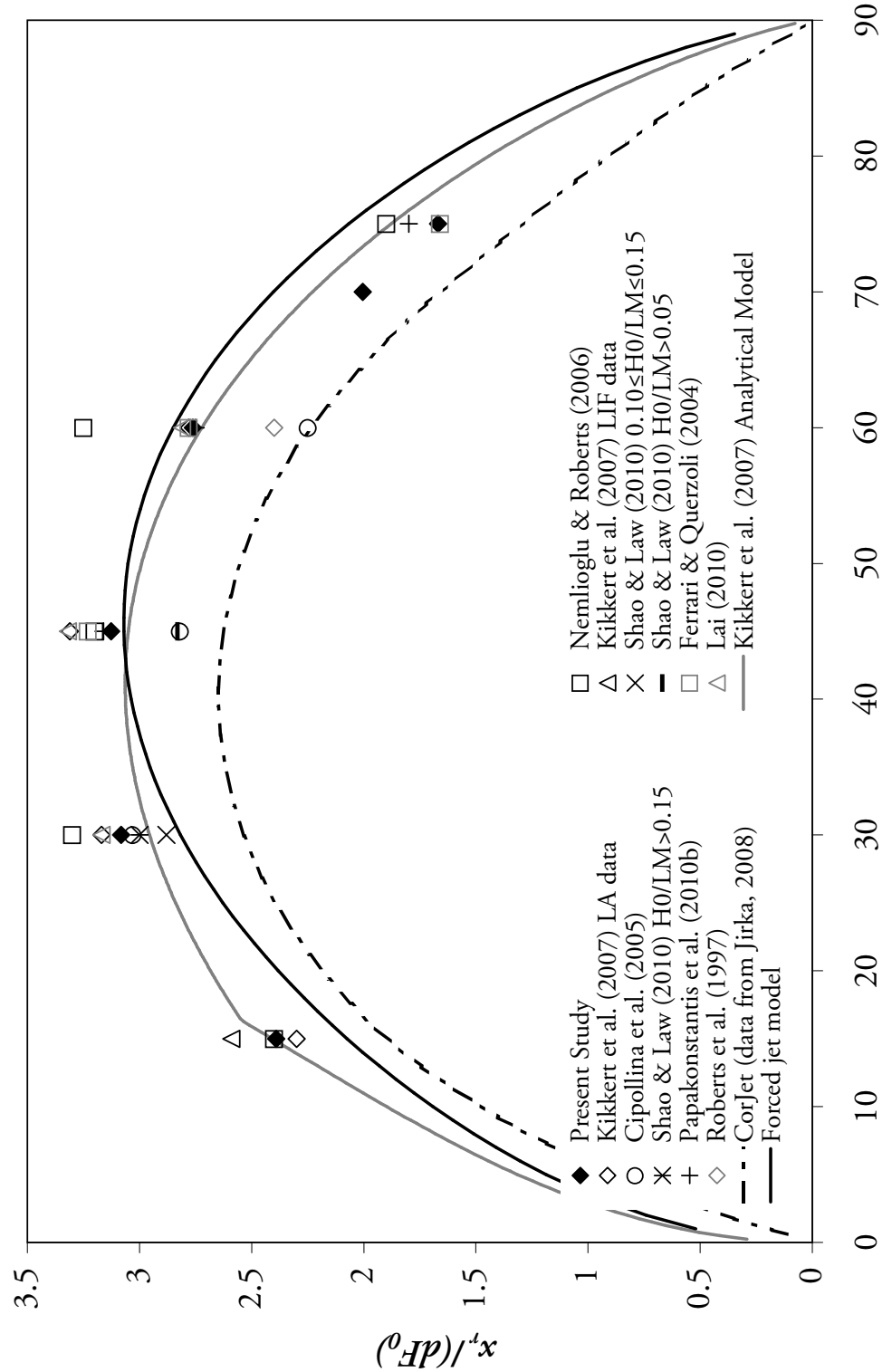

Figure 5.29: Dimensionless coefficient for horizontal distance to centreline at return point as a function of source inclination

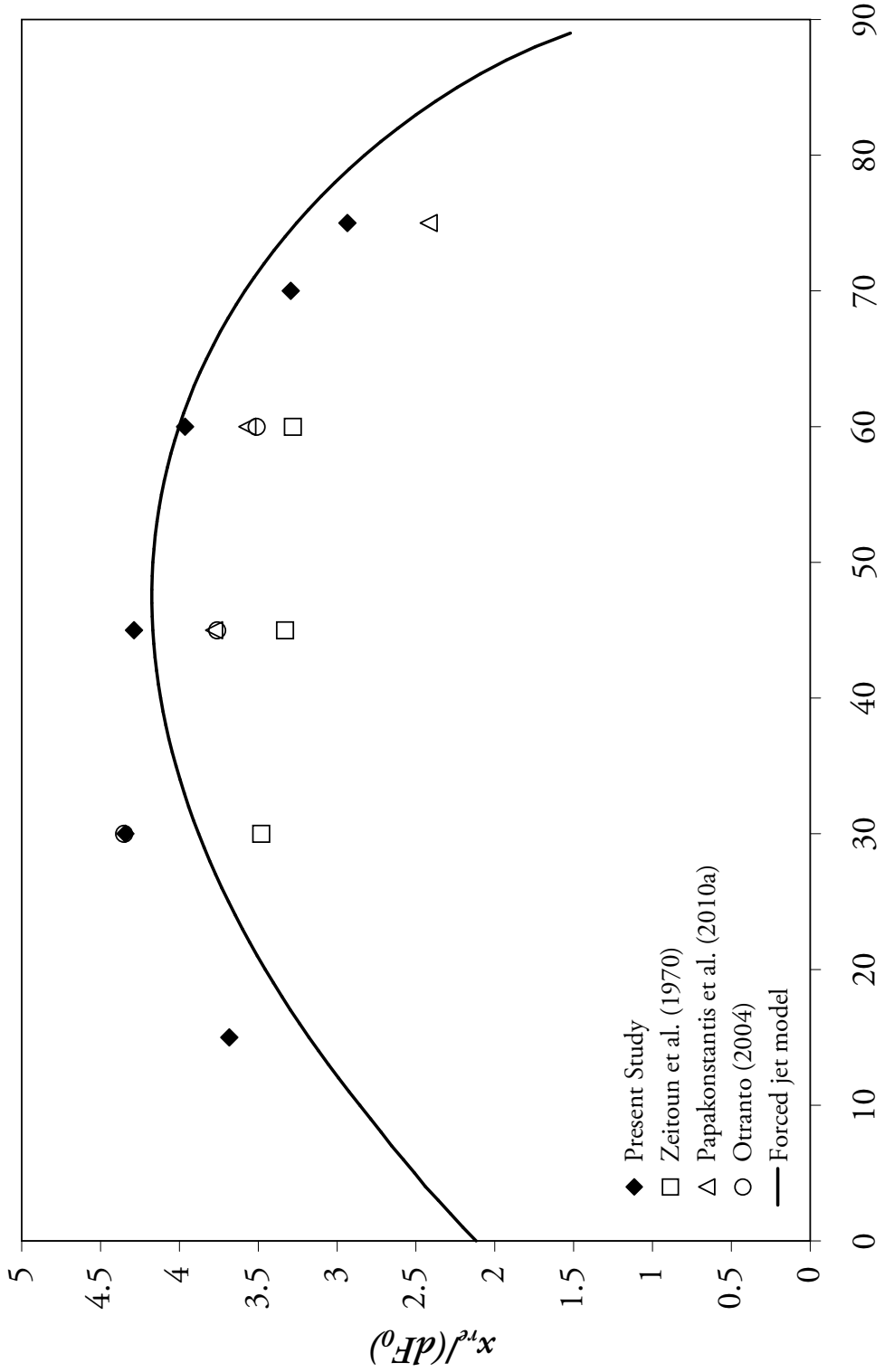

Figure 5.30: Dimensionless coefficient for horizontal distance to outer edge of flow at source height as a function of source inclination

Section 5.3.1 that $x_r/x_m < 2.0$, we see in this figure that such a relationship holds true for $15° \leqslant \theta_0 \leqslant 75°$. Therefore, with respect to horizontal distance we may state that the negatively buoyant jet falls "more quickly" than it rises. It is worth noting that this is a direct consequence of the fact that buoyancy-induced momentum increases with distance travelled while initial momentum is essentially conserved. We may expect that even if no instabilities occurred at all on the lower side of a negatively buoyant jet, x_r/x_m would still be less than 2.0.

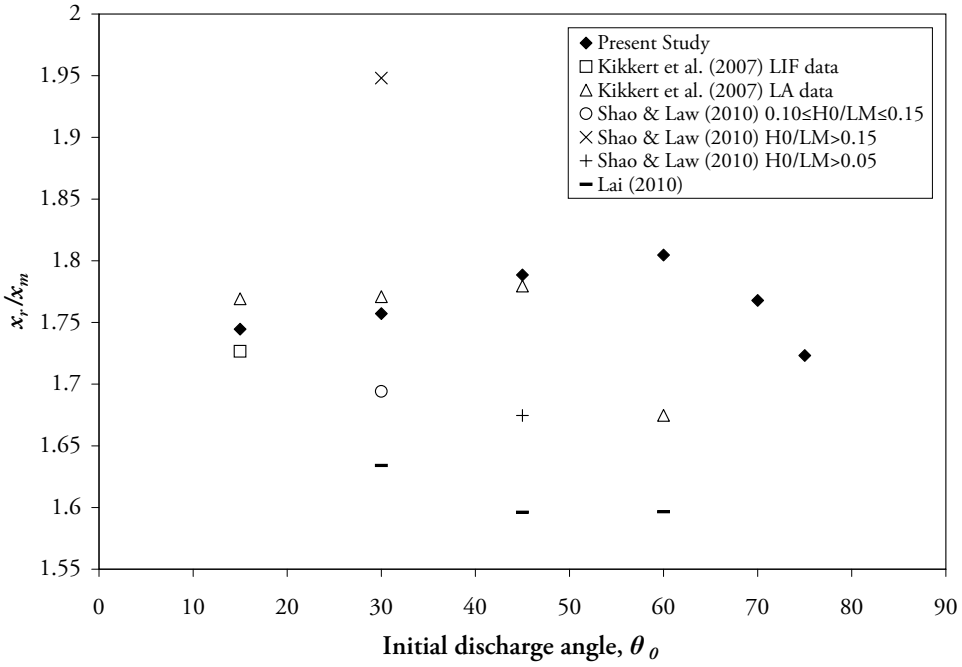

Figure 5.31: Horizontal distance to outer edge of flow at source height divided by horizontal distance to location of maximum centreline height, as a function of source inclination

x_r/x_m values in Figure 5.31 from the present study remain largely the same magnitude over the range of experimental inclinations; the largest being only 4.7% greater than the smallest. It is difficult to determine whether their trend is real or simply an artifact of experimental error. Data from other workers is scattered and provides little support to this trend. The average of all present-study values is $x_r/x_m = 1.76$.

Figure 5.32 plots trajectories from all experiments, normalised by their return point distance and maximum centreline height (in the horizontal and vertical directions respectively). Trajectories follow a consistent shape across all inclination angles. Falling-side trajectory gradients are steeper than on the rising-side, confirming the deductions made from x_r/x_m data. It appears that the influence of buoyancy on centreline trajectories is consistent for all inclination angles, regardless of whether the transition to "plume-like" flow is made near maximum height (as for steep inclinations) or beyond the return point (as for shallow inclinations).

5.4.3.2 Possible reasons for discrepancies

In Figures 5.28 to 5.30, major experimental discrepancies are likely due to the following factors:

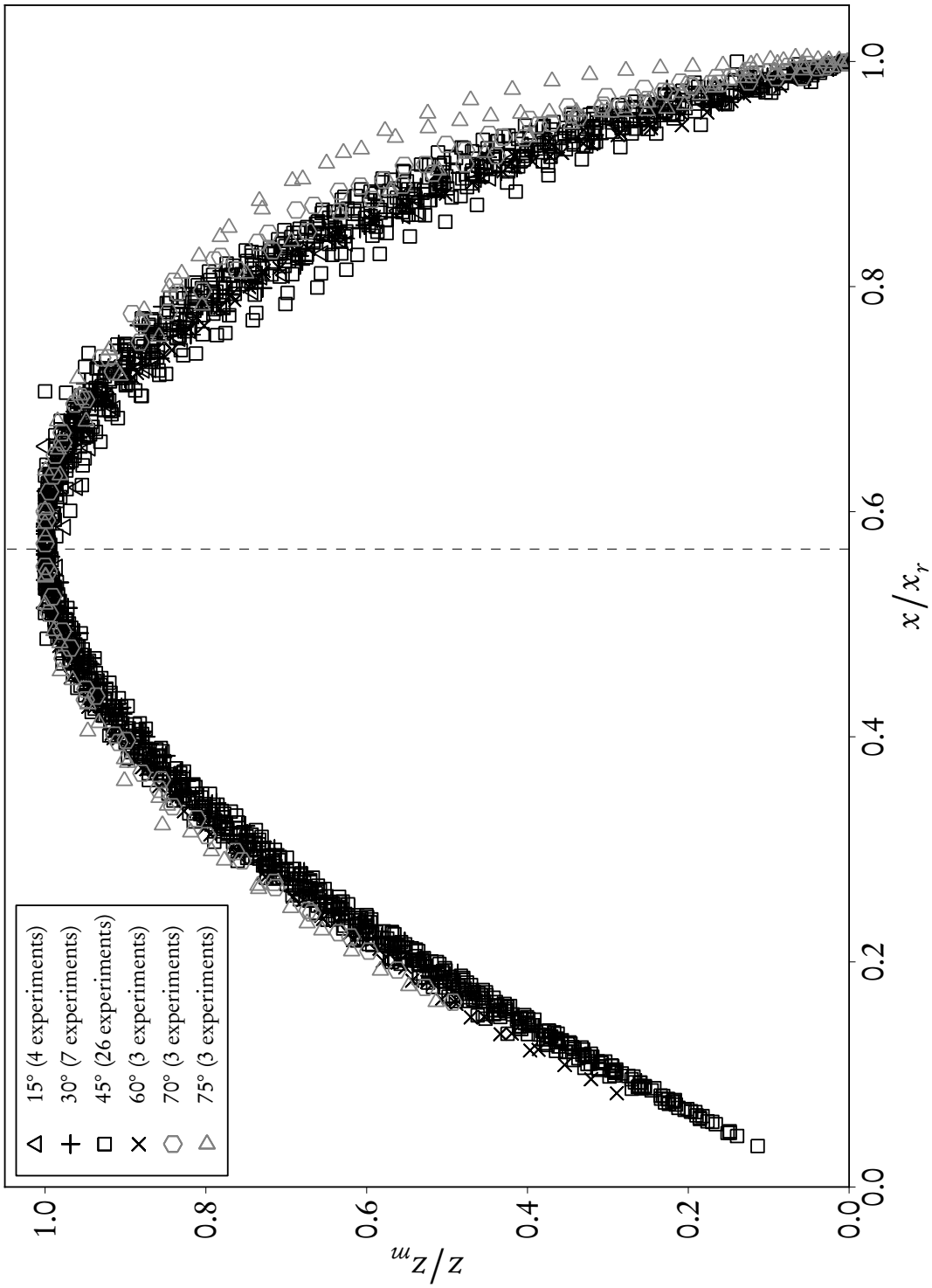

Figure 5.32: Trajectories of all experiments from the the current study; normalised by return point distance and maximum centreline height respectively. Dashed vertical line drawn at average x_m/x_r location

- The Lindberg (1994) k_{xm} data point at 30° is significantly higher than that of other workers. In addition, k_{xm} data the author presents across 30°, 45° and 60° inclinations follows a distinctly non-intuitive trend. While 45° and 60° horizontal distances are almost identical, the 30° horizontal distance is 30% greater. It is difficult to justify such a marked decrease in k_{xm} between 30° and 45° with respect to flow features while simultaneously expecting 45° and 60° values to stay constant. Intriguingly, the k_{zme} data that Lindberg presents fall within the scatter of other workers' data (Figure 5.27). Lindberg does not discuss k_{xm} or k_{zme} parameters directly; focusing instead on the scenario where an ambient cross-flow is present. Lindberg employed a shadowgraph technique, but very little information is given regarding his experimental methods or how his data were derived.

- The Bosanquet *et al.* (1961) k_{xm} value (at 45°) is very high. The experimental issues associated with this dataset have already been discussed.

- The far-boundary 30° k_{xm} value presented by Shao & Law (2010) was somewhat lower than most experimental coefficients at this inclination. They argue that a near boundary led to "an elongated x_m". Yet as the data presented in Figure 5.28 is derived from a combination of both near and far boundary experiments, it appears that this discrepancy is more likely due to experimental technique. In particular, the approach taken by Shao & Law to derive the centreline trajectory is questionable. As discussed in Section 2.1.2, Shao & Law defined the centreline of the flow to be the streamline (in the averaged velocity field) starting from the centre of the nozzle. This approach was afforded by the simultaneous velocity field measurements taken, but did not necessarily guarantee that the centreline trajectory coincided with either maximum axial velocity locations or the maximum concentration locations. It is not difficult to envisage small errors in each discrete velocity measurement accumulating to divert the streamline off-course. In addition, the extent of inner-side discharge fluid seen in profiles taken from the current experiments—such as seen in Figure 5.3a—indicates that a (radial) transfer of fluid may be occuring across the location of maximum concentration. Shao & Law argue that forming the trajectory by determining local-maximum concentration or velocity locations is an iterative procedure and thus a time-consuming procedure. Yet when conducted using appropriate software algorithms, the time consumption of such an approach is negligible, and provides much more rigorous results.

- The 45° inclination k_{xr} data point presented by Shao & Law (2010) is low. Noting a difference between their streamline trajectory and the concentration centreline near the impingement region, they chose to determine return point position—and dilution—by identifying the location of minimum dilution along a horizontal cut at the source height. Relevant plots are presented, and it is evident that dilution gradients in this region are shallow. In combination with the significant fluctuations present in this data, the chosen locations appear somewhat arbitrary. In some cases it appears that positions 10% greater

or less than these locations would be equally appropriate.

- The Nemlioglu & Roberts (2006) k_{xr} data point at 60° inclination is high, while the Cipollina *et al.* (2005) 45° and 60° k_{xr} values are low. The experimental issues associated with these datasets have already been discussed. It may be added that experiments by both workers were conducted with small riser heights and significant boundary interaction, as evidenced by the configuration and instantaneous images presented. In fact, neither workers state the exact riser height that was employed.
- Roberts *et al.* (1997) presented only one horizontal distance coefficient; k_{xr} at 60°. This data point was approximately 13% lower than corresponding coefficients from the present study and four other studies, which were almost equal in value. Roberts *et al.* focused on the transition to horizontal flow after the impact point of a near bottom boundary. Because of this, the discharge was subject to significant boundary effects. It is not clear whether the bottom layer itself may have impacted upon (and subsequently reflected off) either lateral or longitudinal boundaries, but at least the former appears likely. As such, their results are in large part specific to the particular tank size and experimental system that were employed. Roberts *et al.* determined impact point locations from microconductivity probe measurements near the boundary; visually identifying the point of lowest dilution.

Return point edge data (Figure 5.30) is significantly more sparse than for other horizontal coefficients, and for this reason it is difficult to determine which data are accurate and which are not. While acknowledging that it is impossible to know the exact or complete causes of experimental error, the following comments can be made:

- Otranto (2004) measured length scales visually by using a grid "superimposed" over ten light attenuation images, each spaced five seconds apart. Although k_{zme} data presented was closely consistent with that of other workers (see Figure 5.27), k_{xre} data here does not appear to follow the correct trend.
- Zeitoun *et al.* (1970) calculated spatial coefficients by averaging visually-determined edge locations from five successive images taken at 2 Hz. As it was determined that steady state was reached within 10 seconds "from the time of turning on the jet fluid", images began at a time of 15 seconds. Riser heights were 152 mm; sufficient to allow discharge fluid to settle without directly interfering with the recorded flow. Regarding their k_{xre} data, Zeitoun *et al.* remarked that "the horizontal spread seems to be the same" at 30°, 45° and 60°. It is unclear whether the limited number of measurements used to derive these data were sufficient to capture characteristic flow behaviour.
- Papakonstantis *et al.* (2011a) conducted numerous LA experiments at each inclination, but it appears that spatial coefficients have been determined visually. As discussed in Section 2.1.2, their spatial resolution was low (2.5 mm/pixel) and measurements were averaged only over "several" frames per experiment.

5.4.3.3 Model performance

Forced jet model predictions for horizontal distance to location of maximum centreline height, k_{xm}, under-predict most experimental data at 15° and 30° but fall within experimental scatter at steeper angles. Maximum k_{xm} for the forced jet model is at 45°. Analytical model predictions fall within experimental scatter for 15–60° but over-predict k_{xm} at 75°. This model predicts a maximum k_{xm} at 48°, in contrast to experimental data observations (Section 5.4.3.1).

At the return point, analytical and forced jet model spatial predictions somewhat diverge in form. This is due to the difference in implementation of falling-side predictions. In this region, the analytical model switches to pure-plume predictions after some transition point; whereas the forced jet model simply continues with a fixed $B_\star$ value that invariably is less than one. Because the jet-to-plume transition point is lower than $z = 0$ for low discharge inclinations, in some cases analytical predictions at the return point are still based on jet solutions. For this reason a distinct discontinuity is seen in analytical predictions for k_{xr} at 16.5°. On the whole, analytical predictions for k_{xr} are superior to forced jet predictions for this parameter. Nevertheless, the forced jet model provides reasonably good results also.

CorJet and VISJET results for k_{xm} largely under-predict experimental distances, at all inclinations. Their maximums however are found at $\theta_0 < 45°$, consistent with the aforementioned experimental observations. CorJet results for k_{xr} likewise under-predict most experimental data, although follow the correct form.

Forced jet predictions for k_{xre} fall within experimental scatter for $\theta_0 \leq 60°$; the same range for which the model was expected to be applicable for. As for other horizontal coefficients, the form of the plotted curve does not match the general trend of experimental data closely. However predictions are good overall.

5.4.4 Path lengths

Figure 5.33 plots path length to the maximum centreline height location and the return point. No data by other workers was found for comparison. Both datasets plotted follow very consistent trends, and these trends are very similar to the path length curve plotted in Figure 5.25. Nevertheless, k_{sr} is not simply twice the value of k_{sm}. Figure 5.34 plots s_r/s_m, and it may be seen that although this ratio approaches 2.0 as $\theta_0 \to 90°$ (an intuitive result), it is significantly lower for shallower source inclinations. Earlier the normalised trajectory plot (Figure 5.32) demonstrated that trajectories for 15–75° follow the same basic form; simply being stretched to different horizontal (x_r) and vertical (z_m) proportions. Thus for instance, one may envisage that in the limit as $z_m \to 0$, s_r/s_m would equal x_r/x_m. Figure 5.34 also plots a second-order polynomial curve fitted to the experimental data, while constrained to pass through $s_r/s_m = 2.0$ at 90°. This curve suggest that the limit of s_r/s_m as $\theta_0 \to 0°$ is 1.67; a ratio not dissimilar to the average x_r/x_m value found here (1.76).

It has been discussed already that spread in a negatively buoyant jet is linear (or nearly linear)

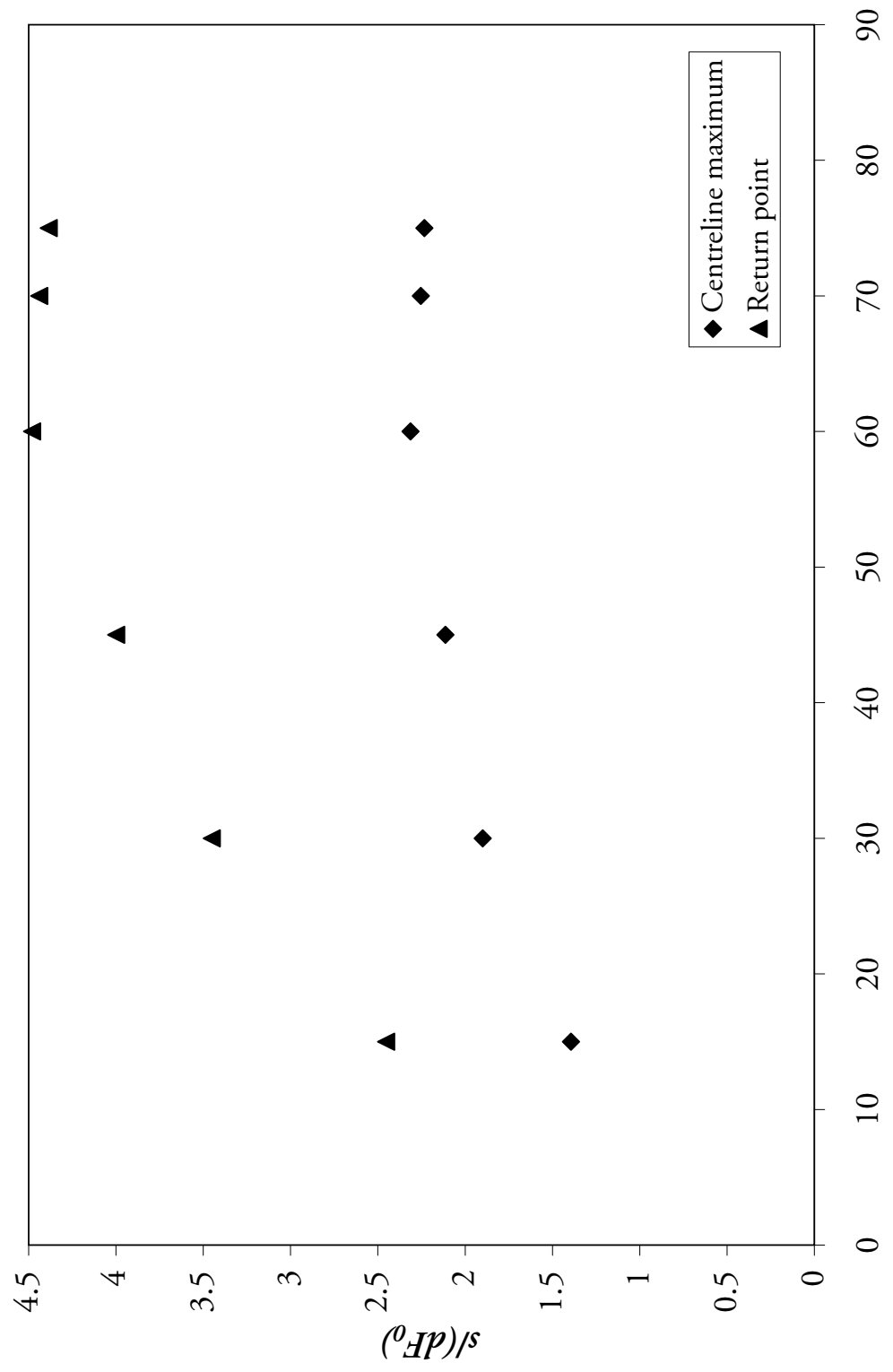

Figure 5.33: Dimensionless coefficient for path length to maximum centreline height and return point as a function of source inclination

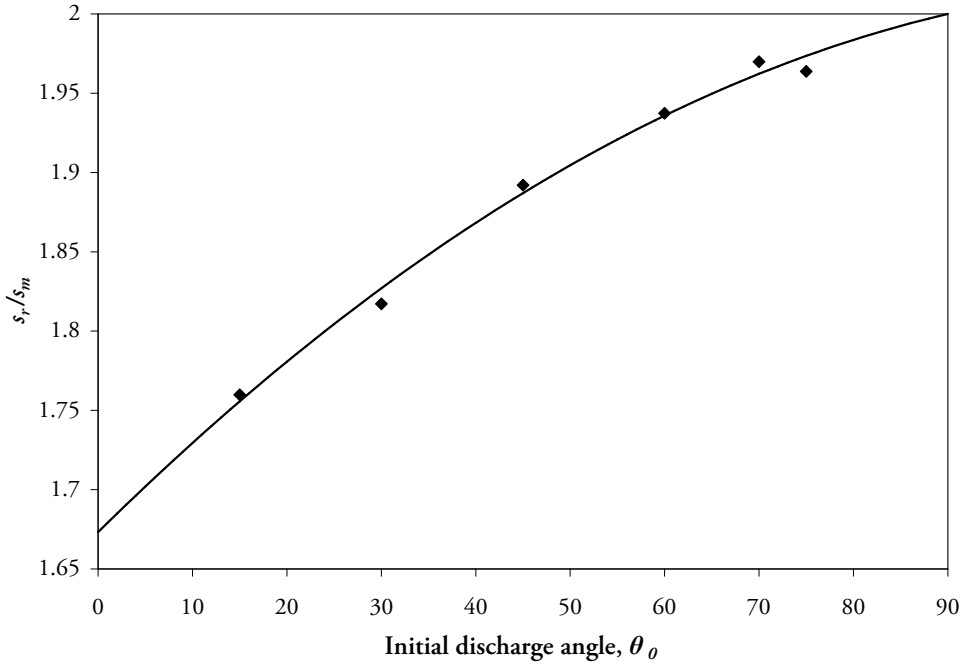

Figure 5.34: Coefficient for path length to return point divided by coefficient for path length to maximum centreline height, as a function of source inclination. Best-fit second order polynomial curve constrained to pass through $s_r/s_m = 2.0$ at 90° plotted as solid line

with path length. It has also been discussed that the difference $k_{zme} - k_{zm}$ is approximately equal to twice the spread rate; *i.e.* $2b_c/(d\,F_0)$. Figure 5.35 plots $k_{zme} - k_{zm}$ against inclination, and as expected, the trend is very similar to the trends seen in Figure 5.33.

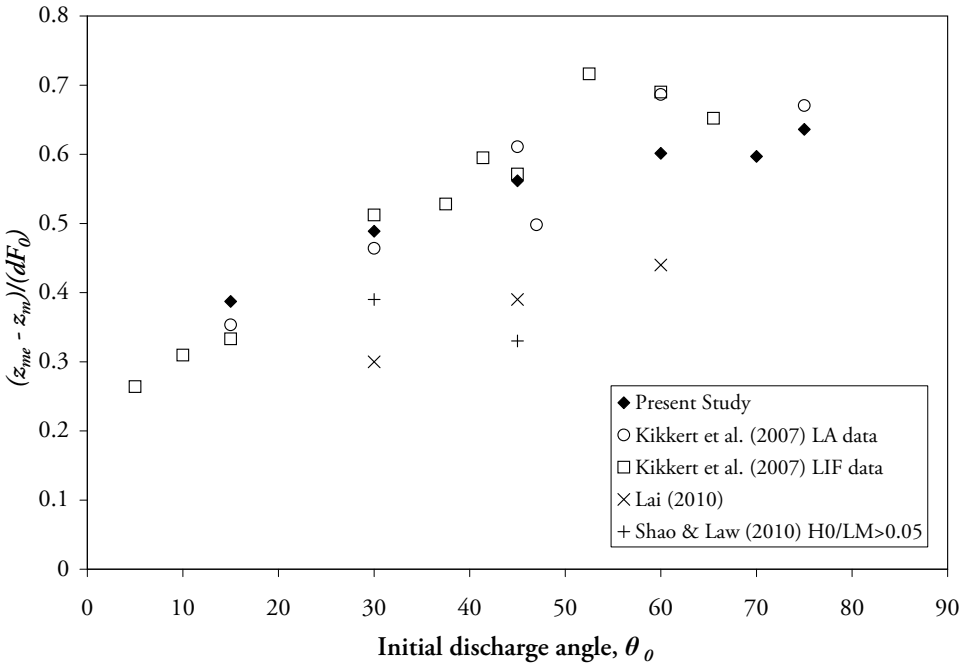

Figure 5.35: Difference between dimensionless coefficients for maximum edge height and maximum centreline height as a function of source inclination

5.4.5 Dilution rates

5.4.5.1 Shape of experimental data

Figures 5.36 and 5.37 plot minimum dilution rates at the maximum centreline height and return points, respectively. Trends in experimental data are much more difficult to discern than for the spatial coefficients already presented due to a substantial increase in scatter. However, data from the current study follows smooth patterns. Certainly maximum centreline height dilution (S_m) trends from the current study are consistent with the path-length shape given for the projectile in Figure 5.25. It is likely that while lower-side entrainment is hindered at high source inclinations, this effect has not significantly altered centreline dilution rates at this location; at least until 75°.

Return point dilution (S_r) data from other workers is particularly scattered. This reflects the difficulty of measuring accurate dilution rates in a region where eddy timescales are considerable. The dataset of Nemlioglu & Roberts (2006) is particularly striking in that it follows a completely different pattern to that of the projectile path length. This pattern is also very difficult to argue for in a conceptual sense, as 45° and 60° dilutions are in fact *less* than those at both 30° and 75°.

Return point dilution data from the current study is linear between 15° and 60°, showing a distinct trend that is not clearly evident in previous datasets. The current data is maximised at 60°, supporting the "maximum dilution" argument of Zeitoun *et al.* (1970). However, dilution rates at 75° are very similar to those at 60° (a 1.2% difference) and therefore with respect to this parameter alone 60° and 75° source inclinations may both be recommended. Of course, as centreline concentration levels at the return point have been significantly affected by lower-side instabilities, it is reasonable to expect somewhat different trends than were seen at maximum centreline height.

It is an interesting exercise to consider what values S_r/F_0 might take as source inclination tended further towards 90°. Yet a value at a 90° inclination itself makes no sense, as the falling flow is penetrated through its centre by rising flow. As a result, there is no distinct definition of "centreline concentration" here.

Figure 5.38 plots dilution at return point as a fraction of dilution at maximum centreline height. Some experimental scatter is evident, but as a whole this ratio appears to increase linearly between 15° and 75° inclinations.

It is peculiar that there is not more experimental data available for return point dilution. This data are the most crucial information for evaluating model performance, and ultimately, for field discharge design. It is imperative that further carefully-performed studies are undertaken to confirm the return point dilution data presented by the current study.

5.4.5.2 Experimental data

While it is difficult to identify clear trends in the dilution data presented in Figures 5.36 and 5.37, it is worthwhile discussing the experimental systems employed by various workers.

As outlined in Section 2.1.2, Shao & Law (2010) conducted experiments at riser heights

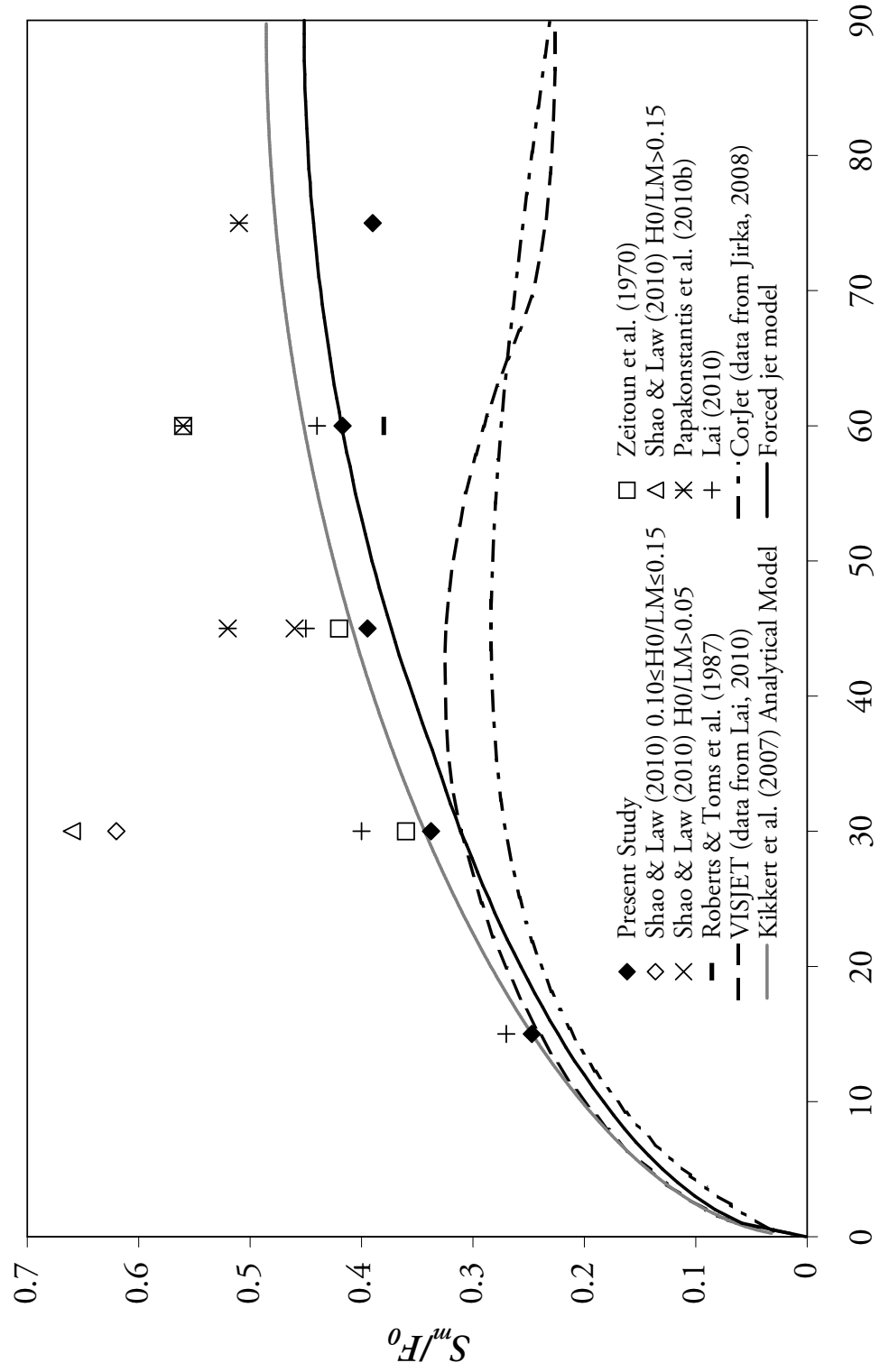

Figure 5.36: Dimensionless coefficient for minimum dilution at maximum centreline height as a function of source inclination

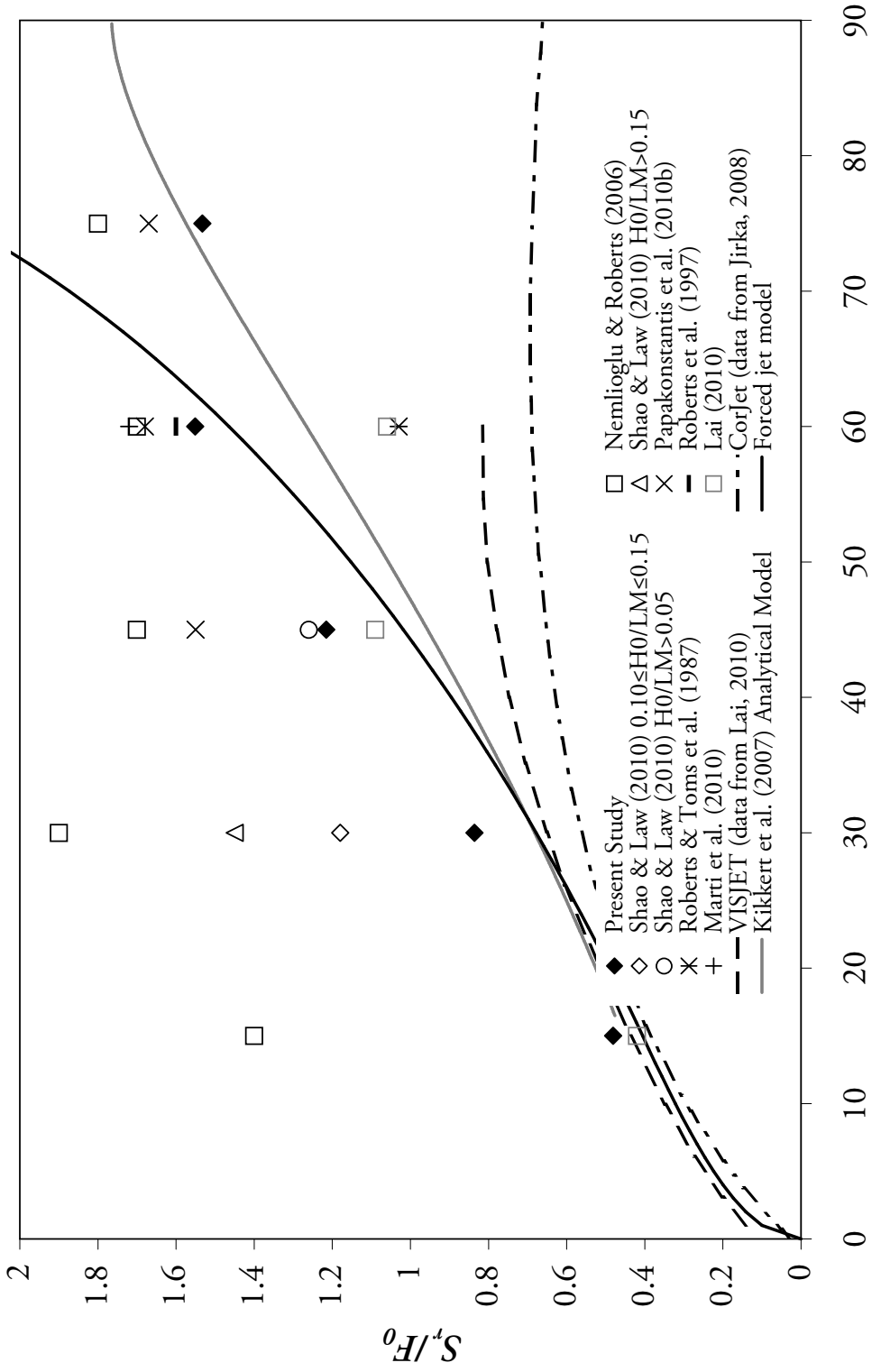

Figure 5.37: Dimensionless coefficient for minimum dilution at return point as a function of source inclination

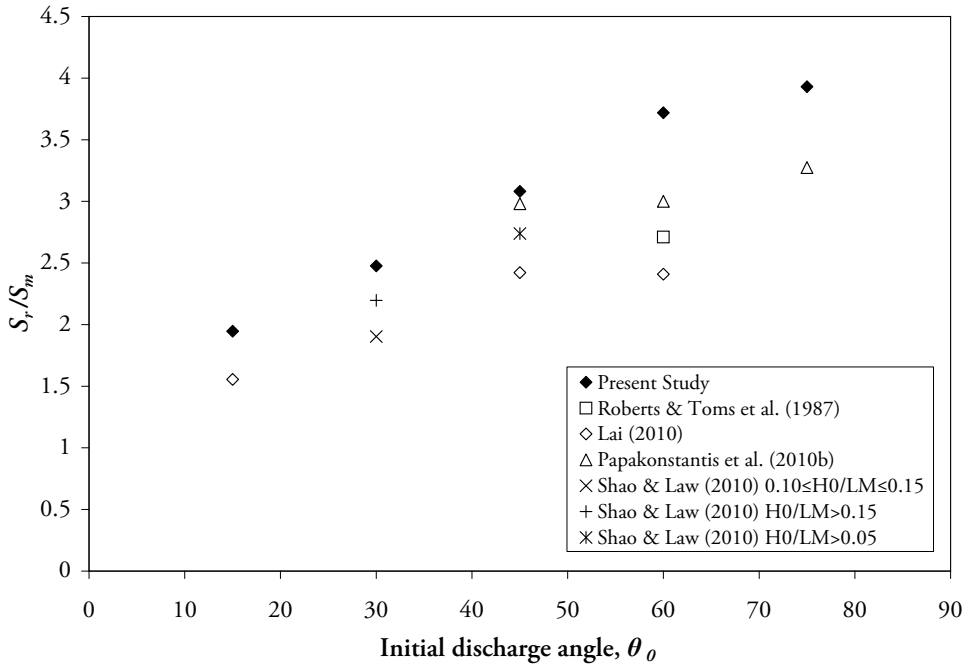

Figure 5.38: Coefficient for dilution at return point divided by coefficient for dilution at maximum centreline height, as a function of source inclination

between $0.05\,dF_0$ and $0.41\,dF_0$ and then examined the relationship between riser height and derived coefficients. Shao & Law found no significant variation at the 45° inclination, but a distinction at the 30° inclination between experiments with $H_0/(d\,F_0)$ below and above 0.141. As may be expected, experiments with small rise heights had smaller dilution rates than those with larger rise heights. Yet this was the case not only at the return point but at the maximum centreline height.

It has already been discussed that the method used by Shao & Law (2010) to determine the flow centreline did not guarantee that this centreline was always at the location of maximum cross-sectional concentration. If this were not the case, dilutions based upon concentrations found along that centreline—of which S_m here is one—would be artificially amplified. This may explain the relative magnitude of Shao & Law 30° inclination S_m/F_0 coefficients. However, their 45° coefficient is approximately 25% smaller, and is similar in magnitude to data from other workers. Such a significant drop is itself unexpected: it is difficult to imagine re-entrainment or other buoyancy induced effects reducing dilution so dramatically around these moderate angles.

Shao & Law (2010) are careful to present data for return point dilution rather than impact point dilution (*i.e.* dilution from along the bottom boundary itself). Therefore the difference in 30° S_r/F_0 coefficients at high and low riser heights is not due simply to a difference in travel distance. The authors clearly state that high riser height experiments are those "without boundary effect", and present results in such a way that assumes experiments employing any riser heights greater than $0.141\,dF_0$ will not achieve greater return point dilution. However, as dilution or spatial coefficients are not plotted as a function of riser height, it is difficult to assess the reliability

of such an assertion.

When a negatively buoyant jet approaches a bottom boundary, its large-scale eddies become constricted and cannot readily entrain further fluid. Fluid is forced to move outwards; forming a gravity-driven layer that travels along the boundary. This vertical deceleration is associated with an increased pressure near the boundary. In addition, discharge fluid which has not been expelled from around the impact point reduces the buoyancy force upon falling fluid, further slowing its travel.

Cavalletti & Davies (2003) found that velocity and concentration fields in a vertical buoyant jet impacting upon a rigid boundary were affected well above the bottom layer that was formed; up to a height of approximately $0.4dF_0^{4/3}$. It may be assumed that a similar effect occurs in a negatively buoyant jet that is impacting upon a boundary. A simple order-of-magnitude estimate of the extent to which the boundary has an effect may be conducted by analysing return point spread. Where the largest flow eddies would be expected to have a radius greater than the distance to the boundary, they will be constricted and not able to dilute at the same rate.

Figure 5.39 plots concentration spread at the return point from the present study (b_{cr}), in which $H_0/(dF_0)$ was much larger. At 30°, $b_{cr}/(dF_0) = 0.43$. The critical rise height given by Shao & Law (2010) for the 30° inclination—$0.141\ dF_0$—is only 33% of this value. This suggests that all 30° experiments conducted by Shao & Law were affected by the bottom boundary in some way.

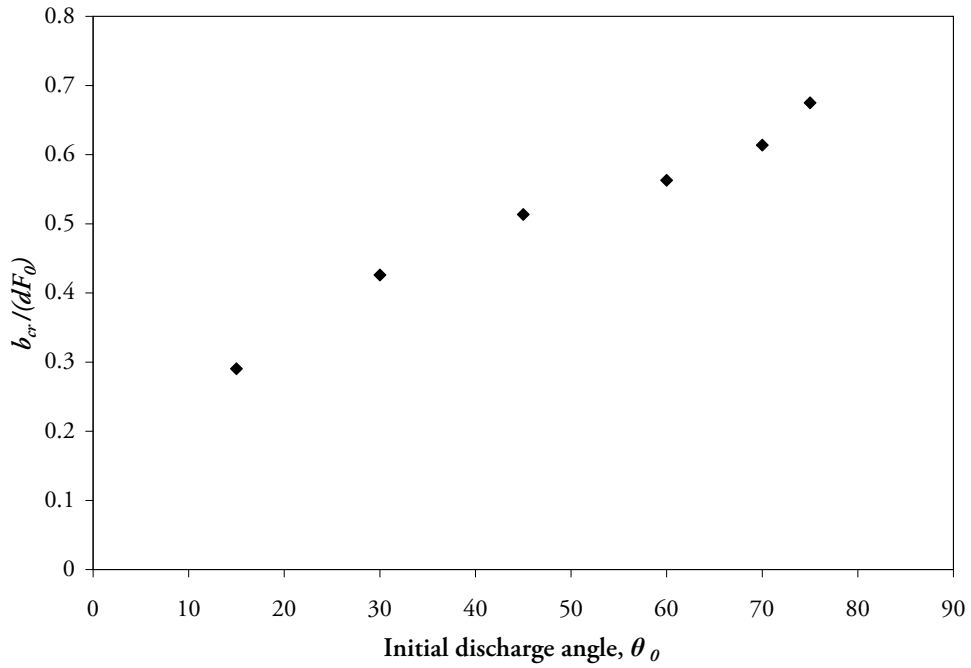

Figure 5.39: Concentration spread (b_c) at return point as a function of source inclination

Nevertheless, it is striking that no boundary effects are found by Shao & Law in return point dilution coefficients at the 45° inclination. In the present study, $b_{cr}/(dF_0) = 0.51$ for this inclination; significantly greater than the highest riser height used by Shao & Law. As with

the 30° inclination, it is likely that all experiments conducted by Shao & Law (2010) at this inclination were affected by the bottom boundary in some way.

At first examination, the difference between their 30° dilution coefficients at maximum centreline height (S_m/F_0) for high and low riser heights is an intriguing result. While it is easily understood that return point behaviour may be affected by the presence of a bottom boundary, the flow at maximum centreline height has not (on the average) begun moving down towards this boundary. Nevertheless, the key consideration here is the return point eddy sizes. In the present (unconstricted) study, return point concentration spread (b_{cr}) was 64.1% of the maximum centreline height (z_m) distance. As this discharge was shallow, the flow did not rise far with respect to the eddy sizes present in the flow. Therefore it is likely that return point conditions would have some measurable effect at the maximum rise height. With a 45° inclination this effect is expected to be less significant, as confirmed by the ratio $b_{cr}/z_m = 0.47$ in the present study.

Dilution rates measured by Zeitoun *et al.* (1970) at maximum centreline height are consistent with the present study at 30° and 45° inclinations, but are much higher at the 60° inclination (consistent instead with data from Papakonstantis *et al.*, 2011b). They measured dilution by extracting samples by vacuum from the flow and measuring their specific gravity. With respect to these measurements they state,

> "Measurements of dye concentrations in the jet stream of dense jets injected at an angle yielded erratic results that were difficult to correlate, due to the instability of the flow pattern with respect to time and a lack of knowledge of the exact position of the axis of an inclined jet."

Because of this, Zeitoun *et al.* estimated dilution levels based on (inferred) path length, and used these estimations to determine which source inclination would produce the maximum dilution at the return point.

S_m measurements by Papakonstantis *et al.* (2011b) were made using a conductivity probe that was moved vertically through the flow at the estimated horizontal location of the maximum edge height (z_{me}). S_m/F_0 coefficients measured by Papakonstantis *et al.* were approximately 30% higher than those from the present study; following the same trend. It is unclear how return point dilution coefficients were measured, but per-experiment values were much more scattered.

Roberts & Toms (1987) measured dilutions by extracting samples from the flow at fixed heights (minimum spacing of $2.3d$) and visually-identified horizontal locations. However, their data are similar in magnitude to that of other workers; both at maximum centreline height and return point.

Results of a field study were presented by Marti *et al.* (2010), and as such the return point dilution results they provide are only estimates based on concentrated CTD profiling near the source.

Dilution rates measured by Lai (2010) at maximum centreline height are similar in magnitude

to results from the present study. At the return point, 15° and 45° results are also similar to those from the present study, but their 60° coefficient is 32% smaller. It is difficult to determine the cause of this discrepancy. As mentioned in Section 2.1.2, per experiment dilution coefficients at maximum centreline height correlated poorly with initial Froude number. One contributing factor may be the short recording length (1 minute) used for experiments.

5.4.5.3 Model performance

Forced jet predictions for S_m/F_0 are smaller in magnitude than experimental data of the same for $15° \leq \theta_0 \leq 45°$. However, the correct trend is predicted. At 60°, forced jet model predictions fall well within experimental data.

Analytical predictions are excellent for $\theta_0 < 60°$. While at 75° forced jet and analytical model predictions both fall between two experimental data points, accuracy of these respective models is unclear. As may be expected, analytical and forced jet model predictions follow the same trend across all inclinations. It appears the difference in their magnitude is largely due to choice of integral constants.

CorJet model predictions are much lower than all experimental data across the full range of inclinations. VISJET provides excellent predictions at 15°, but rapidly begins to under-predict dilution rates for $\theta_0 > 30°$. Indeed, in the range $45° \leq \theta_0 \leq 60°$ VISJET predictions for S_m/F_0 decrease where experimental dilution rates can still be seen to increase. CorJet and VISJET model predictions are approximately 40% less than experimental data at the 75° inclination.

It is difficult to asses the accuracy of model predictions for dilution at the return point. At inclinations steeper than 15°, CorJet and VISJET predictions are significantly smaller in magnitude than all experimental data. Analytical model predictions appear to follow the same form as the present experimental data; indeed multiplying its predictions by a factor of 1.25 provides excellent correlations with present data for 30°, 45° and 60° inclinations. Forced jet model predictions for return point dilution are low in all cases except the 75° inclination, and also do not appear to predict the experimental data trends accurately. As discussed in Section 3.3, the forced jet model is not expected to perform well for inclinations greater than 60° as dilution rates at this return point go to infinity as $\theta_0 \to 90°$.

5.4.6 Overall model performance

Both analytical solutions of Kikkert *et al.* (2007) and the 'forced jet' model developed in Section 3.3 generate spatial predictions for negatively buoyant jets that match experimental data reasonably well. Dilution predictions are harder to assess, but it is evident that the forced jet model does not generate good dilution predictions above 60°. It appears also that the trend of dilution at the return point with respect to source inclination is not accurately predicted. Based on the current experimental data it is estimated that the analytical solutions of Kikkert *et al.* underpredict return point dilution by approximately 20% at 30°, 45° and 60° inclinations. It is

also likely that the analytical model overpredicts maximum centreline height dilution rate at 75°.

Nevertheless, these model results are significantly better than those generated by the CorJet and VISJET integral modelling packages; particularly with respect to dilution rates at moderate to steep inclinations. Consequently it may be seen that enforcing jet-like behaviour at least until maximum centreline height is on the whole an improved technique over that of standard modelling approaches. In addition, it is concluded that the forced jet model predictions are reasonable in the range $0° \leq \theta_0 \leq 60°$.

5.5 Temporal Signal Characteristics

Attention will now be turned to the temporal characteristics of negatively buoyant jet concentration fields. First of all, time series from various locations in the flow will be qualitatively described, and corresponding cumulative averages will be presented. Secondly, time series over spatially-wide vertical and horizontal cut lines will be discussed. Following this, frequency spectra and correlation data will be presented.

Various flow timescales will be calculated in this section from two negatively buoyant jet experiment datasets. This analysis is not intended to be a comprehensive treatment of negatively buoyant jet timescales. Rather, the goal is to investigate the broad temporal parameters of typical discharges and provide experimentalists a coarse estimation of necessary minimum measurement durations.

In discussing the following data, it is helpful to formulate a systematic method of comparing the current temporal results with those from other experimental studies.

The turnover time of the largest eddies centered around a given point in the flow trajectory, which we shall denote t_{LE}, may be calculated by dividing their length scale (ℓ_{LE}) by their velocity scale (u_{LE}). Although neither were calculated directly from the current experimental data, we may hypothesise that

$$\ell_{LE} = c_1 b_c \tag{5.5}$$

$$u_{LE} = c_2 u_{\text{℄}} \tag{5.6}$$

where c_1 and c_2 are constants. At this point along the flow trajectory, for a fixed source inclination, we hypothesise that

$$\frac{b}{dF_0} = c_4 \tag{5.7}$$

$$\frac{U_0}{u_{\text{℄}} F_0} = c_3 \tag{5.8}$$

where c_3 and c_4 are likewise constants. Equation 5.7 is supported by experimental data in the current study such as Figure 5.15. Equation 5.8 is assumed by integral models applied to negatively

buoyant jets (see Chapter 3) and is seen in experimental results from studies on positively-buoyant jets, such as Wang & Law (2002).

Therefore, the large-eddy turnover time t_{LE} is

$$t_{LE} = c_5 \frac{dF_0^2}{U_0} \tag{5.9}$$

As this local expression is a function only of initial variables, its coefficient (c_5) may be assumed to be a function of both path distance and source inclination.

Although t_{LE} will not be determined explicitly in the following discussion, the parameter $\frac{dF_0^2}{U_0}$ (with its units of time) will be stated along with source inclination and trajectory-location information in order to facilitate comparisons between experiments. For different experimental datasets at the same source inclination and trajectory location, this parameter provides a ratio upon which large-eddy turnover times may be expected to scale.

5.5.1 General observations

Figure 5.40 shows temporal intensity plots for three pixel locations along the centreline trajectory of the same experimental recording as considered in Section 5.1. For this experiment, source inclination was 60° and dF_0^2/U_0 was 2.83 s. Because intensity varied linearly with concentration, these plots are effectively plots of relative concentration over time. However, it is expected that camera noise has a visually discernible effect upon the precision of these plots as no spatial or temporal averaging was carried out on the signal.

The first location (Figure 5.40a) was at $s = 0.5s_m$: half way between the source and the maximum centreline height location; well within the jet-region. Here, intensities typically fluctuated symmetrically by approximately ±20% of the mean, reaching a minimum value of 42.2% and maximum value of 139.6%. Fluctuations were rapid. It is important to note that the image exposure time (due to the camera frame rate) of 1/16 s provided a minimum temporal resolution for the data presented. As recorded peaks and troughs were sharp, true intensity extrema may well have been greater than depicted. Additionally, in this part of the jet, intensity fluctuations due to refraction of the light sheet (described in Section 4.3.3.5) were more significant. Nevertheless, fluctuations are relatively small and the signal could not be described as intermittent; consistent with previous observations.

The second location (Figure 5.40b) was at the maximum centreline location. Here intensity fluctuations were much more marked, and although *most* fluctuations occurred symmetrically around the mean (by approximately ±30%), on a number of occasions intensities dropped close to the black-level (0%) for brief periods. Instantaneous images centred around the maximum centreline location are plotted in Figure 5.41 for three of these periods. Significant intermittency events intruding through to x_m, z_m are cleary seen[14]. Image sequences spanning these time peri-

[14]These events were not driven by flowrate fluctuations. Discharge flowrate remained steady throughout the

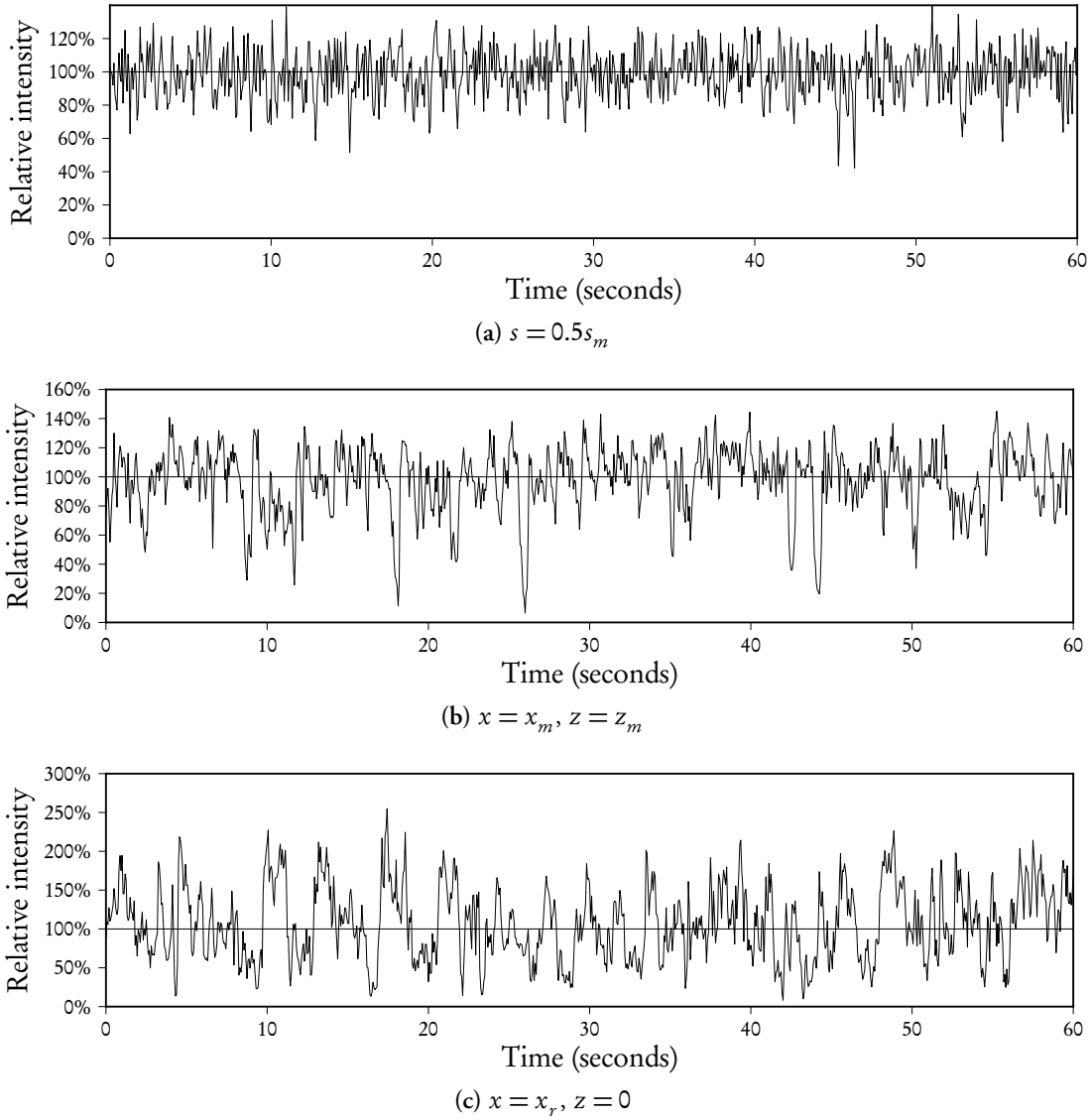

(a) $s = 0.5s_m$

(b) $x = x_m$, $z = z_m$

(c) $x = x_r$, $z = 0$

Figure 5.40: Pixel intensity values as percentage of average value for complete experiment, where 0% is black-level. Horizontal lines drawn at 100%

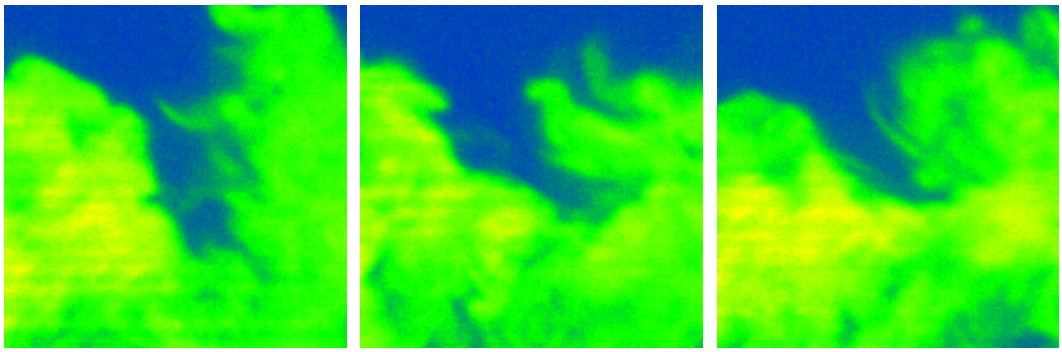

(a) t =18.1 s (b) t =26.0 s (c) t =44.3 s

Figure 5.41: False-colour instantaneous images centred on x_m, z_m location, at different time periods during experimental recording plotted in Figure 5.40b

ods (plotted in Figure A.5) suggest that entrained ambient fluid originates from the outer edge and also lateral edges. While this signal overall could not categorically be described as "intermittent", there are clearly a number of intermittent events occurring. Thus, based on intermittency arguments, it is evident that the maximum centreline location in a 60° negatively buoyant jet is in the *transition* between jet and plume dominated regions. Fluctuation periods in Figure 5.40b are much longer than those in Figure 5.40a, indicating dominant eddies with longer timescales.

The final location (Figure 5.40c) was the return point location. Here the average intensity was only two-fifths of the maximum intensity. There are significant periods of low signal, and clearly an increase in intermittency.

Figure 5.42 plots cumulative averages of intensities at each of these locations, across the complete experiment length (8 minutes & 57.5 seconds). It is important to note that vertical scales on each subplot are different. As may be expected, the cumulative average at location $s = 0.5s_m$ took much less time to come within some selected percentage of the long-term average value than did cumulative averages at the other two locations. Although changes can be seen in each plot across the entire experiment length, these changes are small after approximately 180 s. Consequently, in order to derive high quality centreline dilution data it is recommended that a 60° negatively-buoyant jet experiment of $dF_0^2/U_0 = 2.83s$ should be recorded for at least 180 s.

Nonetheless, while time-averaged minimum dilution—tracked by the flow centreline—is of greatest interest to industry practitioners, in order to build a complete picture of the negatively buoyant flow field, time-averaged cross-sectional concentration profiles must also be described accurately. High quality centreline dilution data does not necessarily imply high quality inner- or outer-side dilution data, and these data are essential for profile fitting; as has been performed in this study. Invariably profile fitting influences the determination of centreline dilution values as well, and hence it is inadvisable for experiment recording times to be chosen with respect only to convergence of centreline point-average values.

Figure 5.43 plots the cumulative average of intensity over a twenty-by-twenty pixel block centred at source height ($z = 0$) for three horizontal locations: $x = x_r + 0.5b_c$, $x = x_r + 1.0b_c$ and $x = x_r + 1.5b_c$. Spatial averaging has been performed here in addition to temporal averaging so as to reduce system noise and focus only on flow features.

The latter of these plots—Figure 5.43c—strongly indicates the effect of large and distinct events occurring. It is only at 300 s that the average value begins to properly stabilise. Figure 5.44 plots the time series used to generate Figure 5.43c, and as may be expected, tracer patches of large intensity relative to the average intensity move through at irregular intervals. These patches are remarkably intermittent. It may be seen that the average concentration in this region is as much a function of the time between patches as it is of the concentration of each patch.

Although separate events are harder to discern in the cumulative average plot at $x_r + 1.0b_c$ (Figure 5.43b), the average value does not appear to stabilise until approximately 400 s. Therefore, accounting for behaviour seen in Figures 5.43 & 5.42 and allowing for statistical variability,

duration of this experiment; the flowmeter data for this period is plotted Figure A.6.

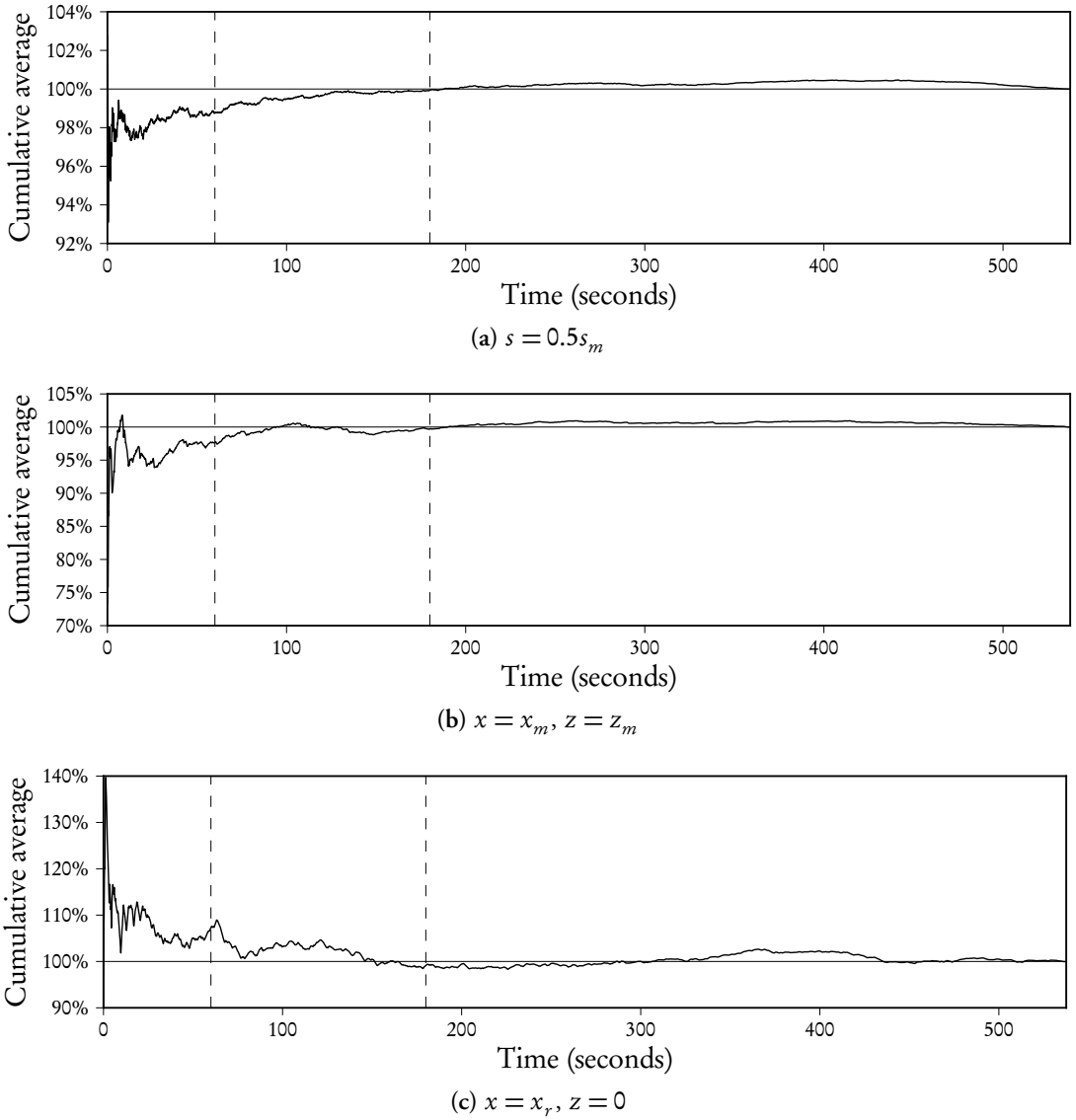

Figure 5.42: Centreline pixel cumulative intensity averages as percentage of average value for complete experiment, where 0% is black-level. Solid horizontal line drawn at 100%, and dashed vertical lines drawn at 60 s and 180 s

it is recommended that a 60° negatively-buoyant jet experiment with $dF_0^2/U_0 = 2.83s$ should be recorded for 300 s or more wherever possible.

5.5.2 Temporal cuts

Figure 5.45 plots an image of intensity over time along a pixel-thin vertical cut line through the centreline-maximum (x_m) of a 45° inclination experiment ($F_0 = 22.7$, Re $= 3382$, $dF_0^2/U_0 = 2.77s$). Each successive line of pixels displayed horizontally on this plot (*i.e.* along the $z/(dF_0)$ axis) is taken from the same vertical line of pixels in successive frames. Because time increases from bottom to top, an object (detectable by the camera) that fell slowly down this line of pixels would appear as a diagonal line, beginning in the bottom left corner of the plot and heading upwards towards the right-hand side. Data shown here are uncalibrated greyscale intensities, meaning that

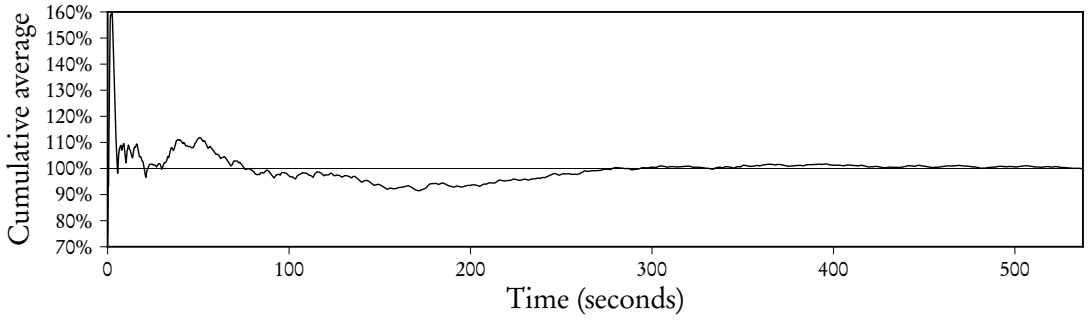

(**a**) $x = x_r + 0.5b_c$, $z = 0$ ($C/C_m = 0.779$ on fitted Gaussian curve)

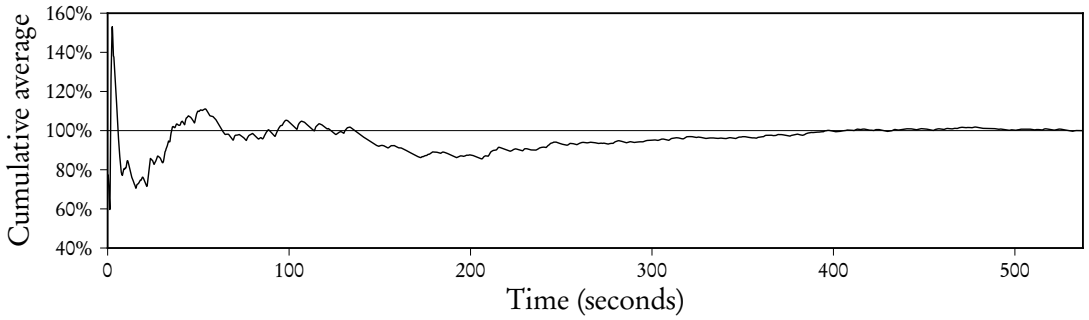

(**b**) $x = x_r + 1.0b_c$, $z = 0$ ($C/C_m = 0.368$ on fitted Gaussian curve)

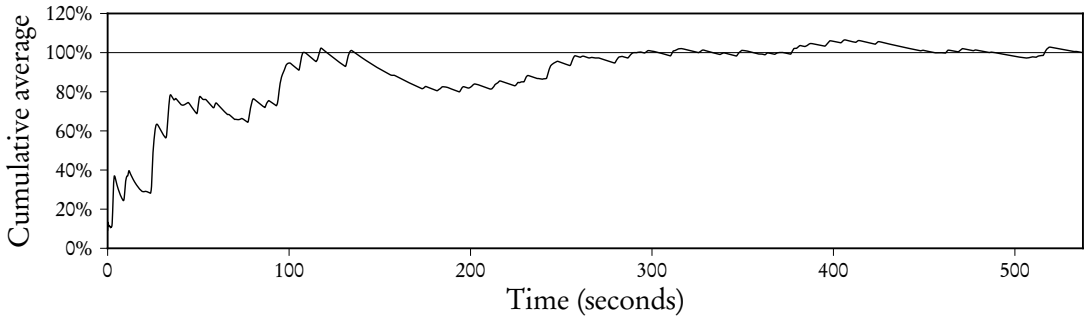

(**c**) $x = x_r + 1.5b_c$, $z = 0$ ($C/C_m = 0.105$ on fitted Gaussian curve). Same data series as plotted in Figure 5.44

Figure 5.43: Cumulative intensity averages of 20-by-20 pixel blocks centred at various locations on outer edge of centreline at source height

while qualitative trends are faithfully represented, concentrations may not be directly derived. These intensities are plotted using a high-contrast colour scheme.

A solid line is drawn in Figure 5.45 through the maximum centreline height (z_m). Around this location flow velocity is high, so discharge fluid passing through this cut line appears as thin 'strips' stacked beside each other. These strips do not appear to lie on an angle; consistent with the expectation that the flow here is travelling almost horizontally. Nevertheless, it must be pointed out that sloped strips are not necessarily proof of vertical movement; they may also be created due to the inherent shape of a tracer patch.

At z_m there is very little evidence of intermittency; consistent with Figure 5.40b. It appears discharge fluid travels past this point continuously: some times less concentrated than other times, but always present. As discussed earlier, this is consistent with a jet-dominated region. Yet as time series lines at increasing heights (that is, at increasing $z/(d\,F_0)$ levels above the $z_m/(d\,F_0)$

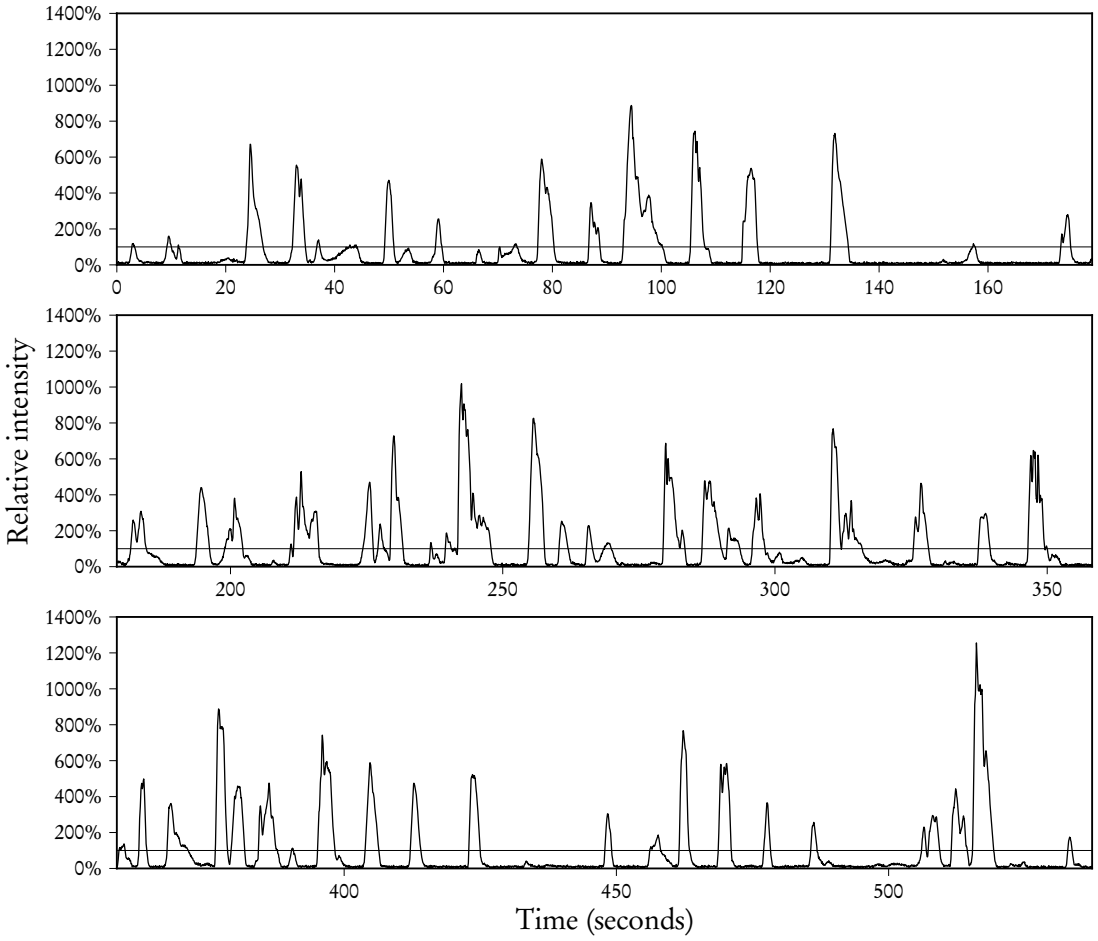

Figure 5.44: Average relative intensity in 20-by-20 pixel block centred $1.5b_c$ from return point (*i.e.* $x = x_r + 1.5b_c$, $z = 0$), where 0% is black-level. Solid horizontal line drawn at 100%

location) are examined, large gaps may quickly be found.

Tracer patches extending to the outer edge vary substantially in size; where 'size' refers to their observed spatial-width, but correlates also with time taken for patches to pass through the vertical cut-line under examination. As these patches increase in size, their frequency of occurrence decreases. Therefore, intermittency increases on this edge as typical patch size increases.

A time-averaged intensity distribution calculated from a longer portion of the same experimental data are displayed in the upper subplot of Figure 5.45. As the centreline trajectory at z_m was almost horizontal, this distribution is effectively an uncalibrated version of the data which the *scalar traverse* algorithm (Section 4.5.4.1) employed here for Gaussian-fitting purposes; deriving a spread of $b_c/(d\,F_0) = 0.305$. It is worth noting the location of outer edge patches with respect to their corresponding location on this distribution. It is apparent that below $C/C_m \approx 0.5$, intermittency between outer-edge patches plays a large part in the reduction of temporally-averaged concentrations. Where patches occur they appear to remain relatively concentrated; it is instead their frequency of occurrence that dictates average concentration. Yet although patches here seem to remain "concentrated", significant gaps between patches are at least in part a reflection of strong entrainment and mixing that is taking place in this area.

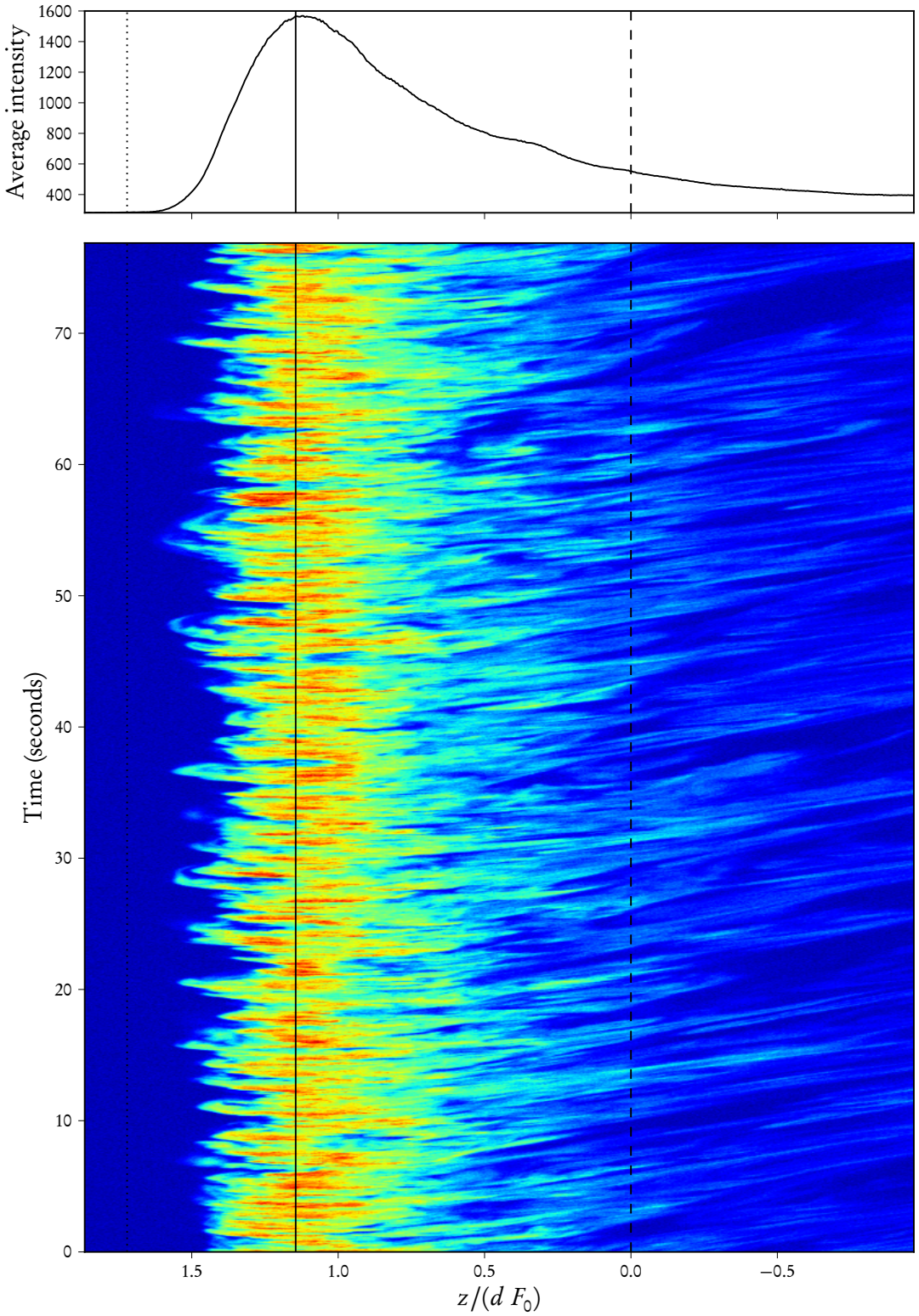

Figure 5.45: Upper subplot is uncalibrated temporally-averaged intensity along vertical cut at centreline maximum (x_m) of 45° inclination experiment ($F_0 = 22.72$, Re = 3382). Average carried out over 6052 consecutive frames (6 minutes and 18 seconds). Lower subplot is false-colour temporal plot of a portion (1 minute and 16.9 seconds) of the same data. That is, each successive line of pixels in this subplot image is taken from the same location in successive frames. Solid vertical line drawn at z_m; dashed vertical line drawn at source height ($z = 0$); short-dash vertical line drawn at outer edge (z_{me}, defined in Section 5.3.2)

In a number of cases, patches that extend from the z_m location across to the outer edge appear to be slightly 'tilted', with portions near z_m crossing the vertical cut-line slightly before portions further out. This tilting effect is accentuated as $z/(d\,F_0)$ increases above the centreline and shear stresses against slow ambient fluid increasingly act to slow down eddy movement. In fact, fluid can often be seen to drag behind the far boundary of the largest patches; having being slowed and stretched by the same shear forces. This fluid frequently is drawn back towards the main flow by entrainment and buoyancy forces; as is evident near 47 seconds and 54 seconds for example. Such behaviour is consistent with the outer-side interfaces being inherently stable.

On the inner side ($z < z_m$), patches initially appear to be travelling horizontally in the same manner as at the centreline-maximum location. Vertical motion is detectable below approximately $z/(d\,F_0) = 0.9$, and quickly becomes significant. A range of 'interface slopes' are apparent on this plot, yet their consistency is also striking. Inner side patches at a given height appear to move with a fairly constant vertical velocity, suggesting similar scales and buoyancy levels. As many interfaces remain distinct across a long vertical distance, inner side patches along this cut line may be assumed to have little horizontal velocity. Quantitative timescales will be derived from this data in sections 5.5.3 and 5.5.4.

Intermittency likewise increases with distance below the maximum centreline height. For example, a particularly large gap can be seen at around $z/(d\,F_0) = -0.5$ after 70 seconds. Intermittency can occur due to tracer fluid moving transversely or horizontally into other parts of the flow; as evident from the apparent disappearance of tracer fluid above the largest intermittency events. As in standard experimental images, discharge fluid is not necessarily conserved within the spatiotemporal area under consideration. It must also be noted that inner side fluid continues to spread and mix as it travels downwards.

Figure 5.46 plots in the same fashion intensities along a horizontal cut-line at the source height ($z = 0$). A solid line is drawn at the horizontal distance to maximum centreline height (x_m) and a dash-dot line is drawn at the return point (x_r). It must be noted that the trajectory here is not vertical[15], meaning that structures moving parallel to the trajectory will appear 'tilted' on this plot.

It is immediately apparent that intermittency is well developed in all parts of this flow segment. Ambient fluid may be seen extending through to the flow centreline (x_r) in numerous places. Indeed, because patch concentrations appear to remain high in most parts of the flow, it is difficult to visually identify the location of peak time-averaged concentration. Significant activity appears to occur between approximately x_m and $1.1x_r$; an observation that is confirmed by high temporally-averaged intensities in the upper subplot.

Outer edge patches in Figure 5.46 appear similar in structure to the outer edge patches seen in Figure 5.45. Here however, these patches are 'wider' and take longer to pass through the cut line. This is expected, as flow spread has increased and typical velocities have decreased from their values at the maximum centreline height. Tracer patches are periodic and remain reasonably

[15] This was demonstrated in Figure 5.10.

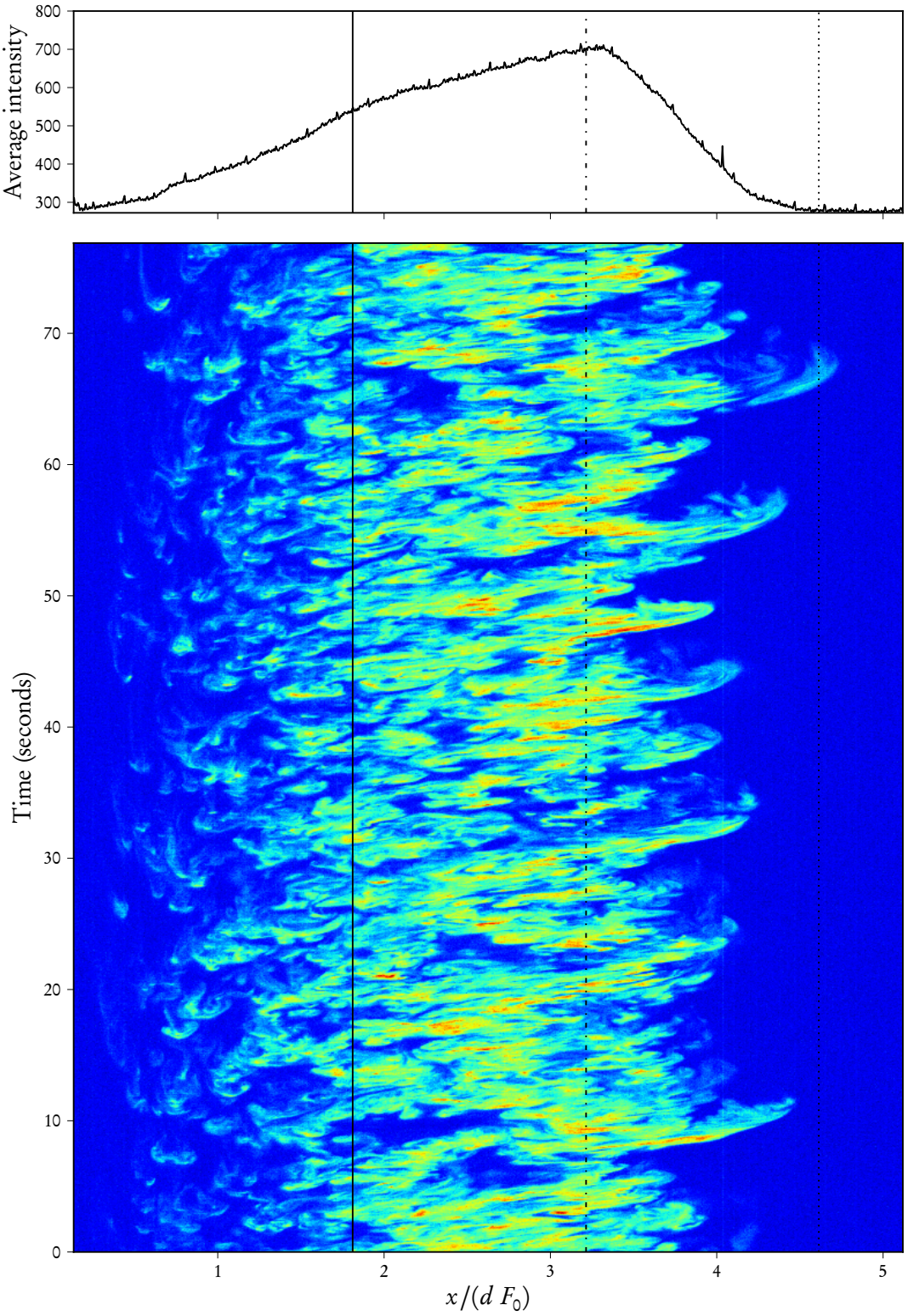

Figure 5.46: Upper subplot is uncalibrated temporally-averaged intensity along horizontal cut at source height ($z = 0$) of 6052 consecutive frames from same experiment as in Figure 5.45. Lower subplot is false-colour temporal plot of a portion of the same data (*i.e.* each successive line of pixels in this subplot image is taken from the same location in successive frames). Solid vertical line drawn at x_m; dash-dot vertical line drawn at x_r; short-dash vertical line drawn at outer edge (x_{re}, defined in Section 5.3.2)

concentrated, consistent with the temporal intensity plot of Figure 5.44 discussed earlier for the location $[x = x_r + 1.5b_c, z = 0]$ on a 60° inclination experiment.

Unlike the outer edge, the near-source region ($x/(d F_0) \lesssim 1.2$) is much less distinct. Many small and discrete patches can be seen here. These patches tend to trail discharge fluid behind themselves[16]; creating a "wispy" or "woolly" appearance. As such patches were surrounded by clear ambient fluid, rapid mixing is expected. Patch size and frequency decreased towards the source.

Figures 5.45 and 5.46 do not of themselves provide quantitative information regarding length or timescales present in the flow. Data of this type will be calculated in the following two sections (Spectra and Correlation; sections 5.5.3 and 5.5.4). However, these figures visually illustrate something of the flow structure present in two portions of the negatively buoyant jet, providing a useful complement to quantitative insights.

Similar figures were plotted by Papantoniou & List (1989, p. 184) along the centreline axis of a pure jet and pure plume; reproduced here in Figure 5.47. Each pixel value in their data was divided through by the temporally-averaged value for that pixel: a method that was found to create less robust images for the current data, due to the effect of noise in areas of low concentration. They observed that, consistent with earlier observations in jets by Dimotakis *et al.* (1983), the scaling required on dimensional grounds, $t \sim x^2$ for a jet and $t \sim x^{4/3}$ for a plume, is obeyed "only in an average sense for a particular concentration pattern".

5.5.3 Spectra

While all experimental data were recorded in the time domain—that is, by making measurements over a period of time—to understand the characteristics of negatively buoyant jet behaviour, it is instructive to assess their *frequency spectra*. The frequency spectrum of a data series is a representation of that signal in the "frequency domain", where the signal is described by its frequency, amplitude and phase. The conversion of a time-domain signal to the frequency-domain is achieved by way of the Fourier Transform, which is typically implemented using the Fast Fourier Transform (FFT) technique (see for example, Rao *et al.*, 2008).

Simmons *et al.* (1938) showed that the time variation of velocity at a point in a turbulent stream could be analysed with a frequency spectrum, and subsequently frequency spectra of turbulent velocity signals have been computed by many workers. Gibson (1963) found the streamwise and cross-stream velocity spectrum functions to be well fitted by the $-5/3$ power decay law predicted by the Kolmogorov theory for an inertial subrange (Kolmogorov, 1941). Papanicolaou & List (1988) conducted LIF experiments upon turbulent jets and plumes, and found the power spectra for *concentration* fluctuations along the axis of a jet also approximately followed a $-5/3$ power decay, and along the axis of a plume followed a $-1/3$ power decay at high frequencies (above 20 Hz) and a $-5/3$ power decay for lower frequencies.

[16]Note that this behaviour was more evident in low-contrast representations of intensity data.

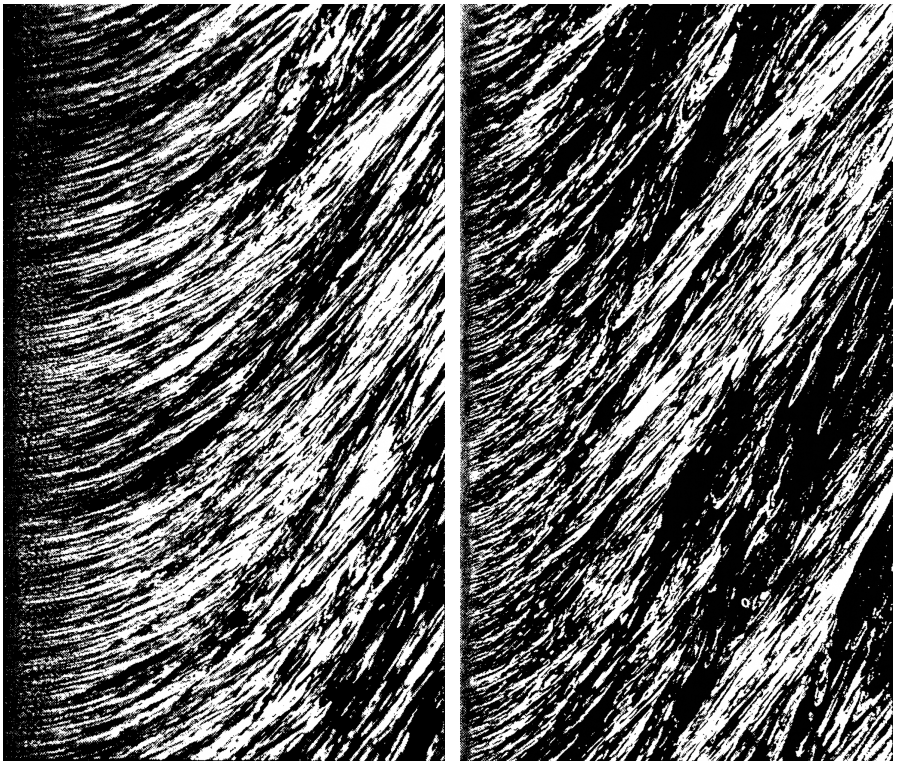

(**a**) Jet (**b**) Plume

Figure 5.47: Time sequence of concentration profiles along centreline axis, from Papantoniou & List (1989). Path direction along horizontal axis (left to right); time along vertical axis (bottom to top). Instantaneous values of concentration have been divided by local time-averaged values; white corresponds to high concentration and black corresponds to clear ambient fluid

Figure 5.48 plots concentration frequency spectra at various vertical locations at $x = x_m$, derived from the data plotted in Figure 5.45. Prior to calculating spectra, any linear trending was removed[17], a Blackman windowing function was applied to reduce spectral leakage and the data (of 6052 samples in length; *i.e.* 6 minutes and 18 seconds duration) was zero-padded to 2^{15} samples long in order to obtain more spectrum sample points. A small number of adjacent spectra have been averaged together in each case, in order to create clearer plots. Visual investigation confirmed that spectrum behaviour did not vary in any significant manner across averaged sets. A similar effect could be achieved by further increasing sampling duration, but this was difficult with the present experimental equipment.

Figure 5.48a displays a typical noise spectrum plot. Spectral power does not exceed 5×10^1. As with all frequency spectra plots, no information is plotted above half of the sampling frequency (Nyquist, 1928); here equal to 8 Hz. As low-frequency data are less reliable and somewhat sensitive to the particular windowing function chosen, the horizontal axis is truncated at the one-minute period length.

Figure 5.48b plots the spectrum mid-way between z_m and z_{me}. Spectral power peaks in the 0.1–0.5 Hz range, corresponding to periods of 2–10 seconds. Timescales such as these corres-

[17] In practice, this simply meant the removal of the signal mean.

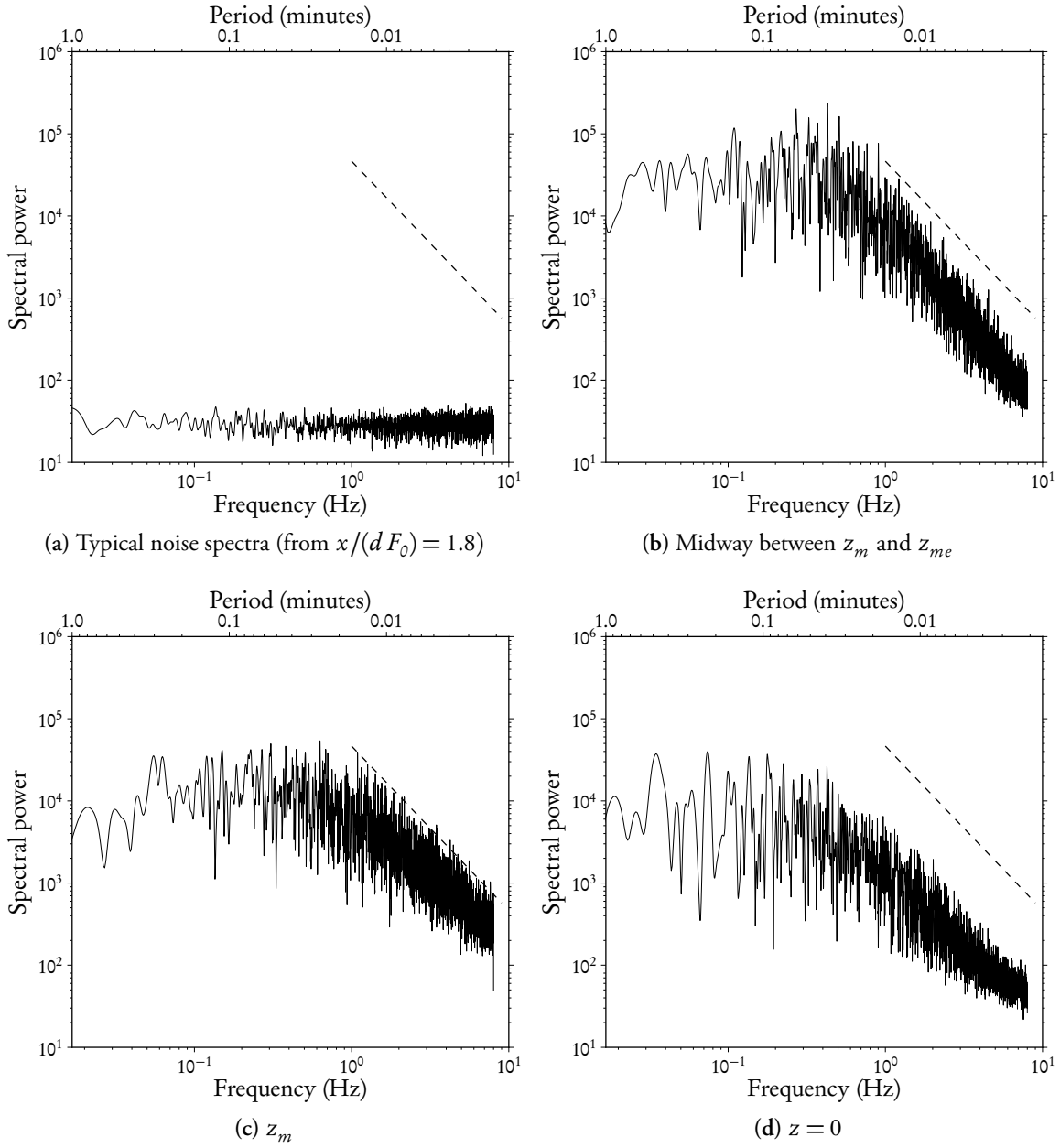

(a) Typical noise spectra (from $x/(d\,F_0) = 1.8$)

(b) Midway between z_m and z_{me}

(c) z_m

(d) $z = 0$

Figure 5.48: Average of 29 spectra (corresponding to width of 0.155 along the $z/(d\,F_0)$ axis) centred around various locations in vertical cut at x_m; calculated from same data as plotted in Figure 5.45. Dashed line indicates $-5/3$ power slope

pond to eddy production scales: the scale of large eddy formation due to shear effects. This eddy formation extracts energy from the mean flow, converting it to turbulent energy which in turn is transferred to smaller eddies. Spectral power in Figure 5.48b—and in other plots—does not roll-off clearly or abruptly at lower frequencies, suggesting a wide range of eddy production timescales. For instance, a high spectral power peak can be seen at an approximately 40-second period.

The frequency spectrum at z_m is plotted in Figure 5.48c. Here, decay at high frequencies (*i.e.* above 1 Hz) appears to closely resemble a $-5/3$ power decay, as found by Papanicolaou & List (1988) in jets and plumes. It is remarkable that such a spectra plot, based on a two-dimensional concentration field, is so similar to turbulent velocity spectra plots, based on a three-dimensional field. A wider range of similar-magnitude peaks is observed; spanning between 1.5 second and 15 second periods.

At $z = 0$ the frequency spectrum (Figure 5.48d) is similar, though lower in power at frequencies above 0.6 Hz. Above 6 Hz the spectrum plot appears to flatten, possibly tending towards the noise spectrum seen in Figure 5.48a.

Equivalent plots at various horizontal locations along $z = 0$ are given in Figure 5.49. Comparable features are observed. Spectral power generally peaks at longer periods; in the order of 5–12 seconds. This spectrum decays at a rate shallower than $-5/3$, and appears to become dominated by noise fluctuations above 3 Hz.

In a number of the spectral plots presented here within the flow, high spectral power is seen at periods approaching the one-minute range. If the spectral data from this particular experiment (45° inclination, $dF_0^2/U_0 = 2.77s$) can be seen as representative of typical negatively buoyant jet experiments, this would indicate that the recommendation made in Section 5.5.1 for five-minute minimum recording durations of 60° negatively buoyant jets may be applicable for all moderate inclinations.

5.5.4 Correlation

A further analysis tool that may be employed to investigate temporal behaviour along a given line is the correlation function.

If $C'(x,t)$ is the time series of concentration fluctuations at spatial position x that begins at time t and spans a fixed period of time (T_{series}), then the normalised correlation function R with the like time series beginning at $x + \Delta x$, $t + \tau$ is

$$R(\Delta x, \tau) = \frac{\overline{C'(x,t)C'(x+\Delta x, t+\tau)}}{\sqrt{\overline{C'(x,t)^2}} \cdot \sqrt{\overline{C'(x+\Delta x, t+\tau)^2}}} \tag{5.10}$$

A variety of information may be derived from this data; including a direct measure of the average velocity along the direction of the line under consideration. Here however, attention will

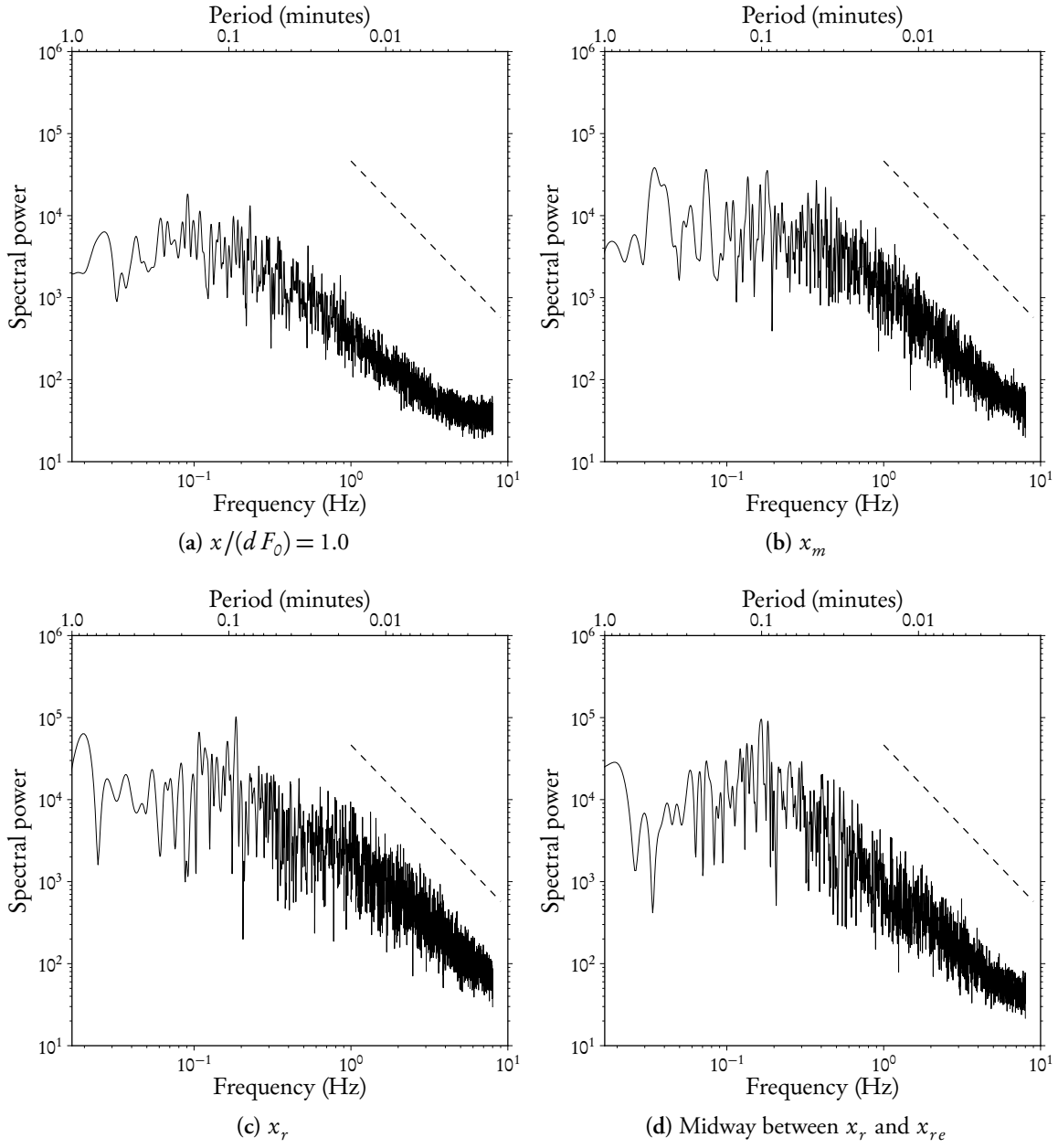

(a) $x/(dF_0) = 1.0$ (b) x_m

(c) x_r (d) Midway between x_r and x_{re}

Figure 5.49: Average of 29 spectra (corresponding to a width of 0.160 along the $x/(dF_0)$ axis) centred around various points on horizontal cut at $z = 0$; calculated from same data as plotted in Figure 5.46. Dashed line indicates $-5/3$ power slope

be restricted to integral length and timescales calculated by integrating $R(\Delta x, \tau)$ in the Δx and τ directions respectively (see for example, Papantoniou & List, 1989).

The integral length scale is defined as

$$L_{\text{int}} = \int_0^\infty R(\Delta x, \tau = 0)\, d\Delta x \tag{5.11}$$

This parameter is the average decorrelation distance in the spatial direction considered, and corresponds to the average scale of the largest turbulent structures in this direction.

Likewise the integral timescale of concentration fluctuations is

$$T_{\text{int}} = \int_0^\infty R(\Delta x = 0, \tau)\, d\tau \tag{5.12}$$

This parameter is the average signal decorrelation time at a fixed point. If Taylor's "frozen turbulence" hypothesis (Taylor, 1938) may be invoked[18], this is a measure of the average eddy timescales present in the flow. However, the frozen turbulence hypothesis can be justified in turbulent discharges only if (Wygnanski & Fiedler, 1969):

$$\left| \overline{u} \frac{\partial u'}{\partial s} \right| \gg \left| v' \frac{\partial \overline{u}}{\partial y_n} \right| \quad \text{and} \quad \frac{\overline{u'^2}}{\overline{u}^2} \ll 1.0 \tag{5.13}$$

where u is velocity in the axial direction (s), y_n is the lateral direction (perpendicular to s) and v is velocity in that direction. While the present study has not measured velocity data, concentration fluctuations observed (see for example, Figure 5.40) strongly indicate that the second condition will be violated in large portions of the flow.

Decorrelations in time are in fact associated with flow mixing processes as well as transportation effects. In this context, T_{int} does not directly correspond to the period of eddy events; instead it is simply the average time duration at which eddies appear correlated. This is a timescale nonetheless, and will decrease and increase approximately as flow velocities do the same.

Both integral length and timescale parameters are particularly sensitive to T_{series} duration; becoming stable and meaningful only after long durations.

Figure 5.50 plots integral length and timescales calculated from the vertical cut data plotted previously in Figure 5.45, with $T_{\text{series}} = 376.4s$. Length scales are remarkably consistent across the entire region plotted[19]. Timescales however are variable. Near the centreline maximum height (z_m, marked with a solid vertical line through Figure 5.50) timescales are short: an intuitive result as fluid here is travelling quickly in a predominantly horizontal direction. Above this location timescales increase, as discharge fluid becomes increasingly more affected by the

[18] Taylor's frozen turbulence hypothesis assumes that advection contributed by turbulent circulations themselves is small, and therefore the advection of a field of turbulence past a fixed point can be taken to be primarily a result of the mean flow.

[19] For calculation consistency, values have not been calculated in areas within 99 pixels of the data edge.

surrounding ambient fluid and travels slower. Timescales drop to zero beyond $z/(d\,F_0) = 1.57$ as tracer patches become significantly more sparse. Below the centreline maximum height, timescales increase steadily as the tracer falls from the flow.

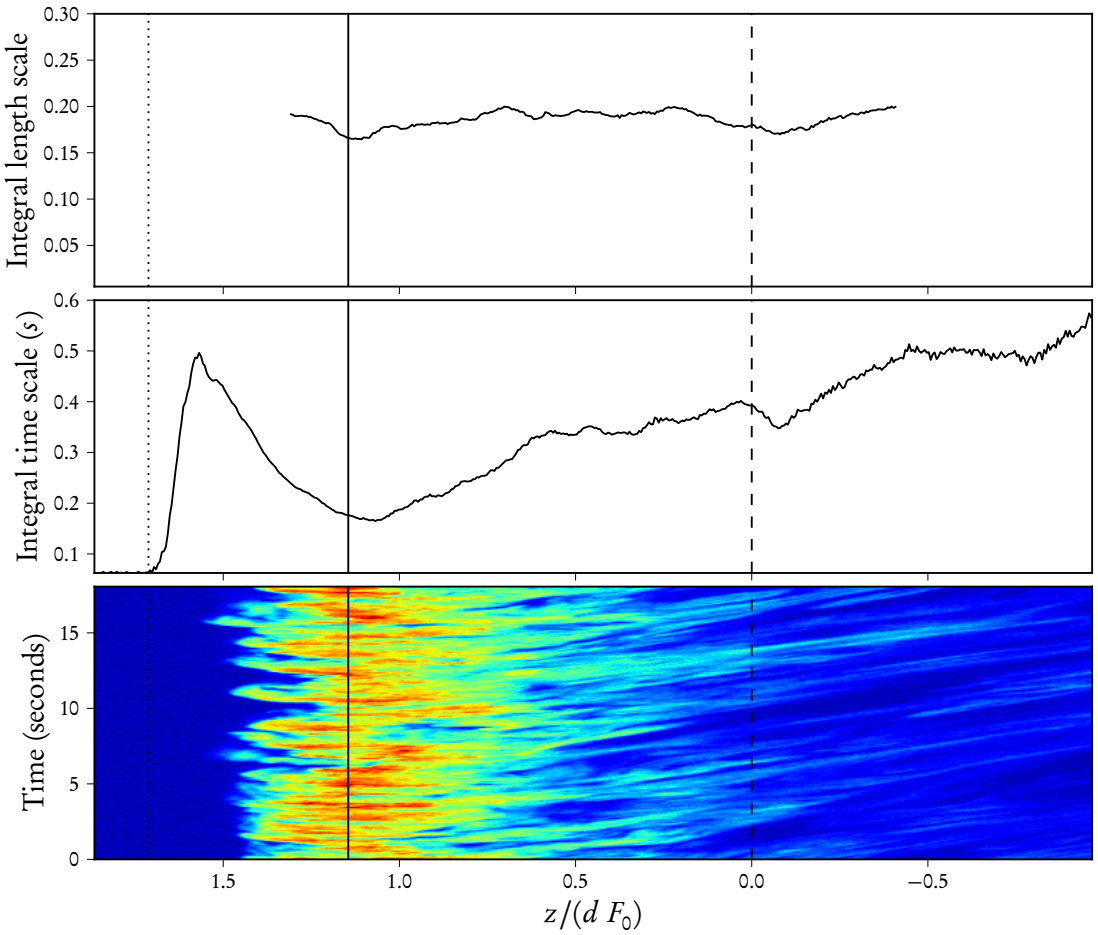

Figure 5.50: Integral length scale (L_{int}; Equation 5.11) and integral timescale (T_{int}; Equation 5.12) calculated from time series of intensity data (6 minute 18.25 second duration) along vertical line at x_m through 45° inclination experiment shown in part in lower subplot and identical to that plotted in Figure 5.45. Correlations calculated over time average length of $T_{\text{series}} = 376.4s$ (6022 frames), to a limit of $\Delta x = 1.10$ and $\tau = 1.81s$. Length scales normalised in same manner as z-axis is normalised

Figure 5.51 plots the equivalent scales from horizontal cut data shown earlier in Figure 5.46. Length scales are consistent over a large portion of the spatial distance considered; decreasing on the outer edge and also towards the inner edge. This latter region of fluid is in addition characterised by long timescales, as eddies move more slowly and hence the tracer fluid stretches out over a greater time period. Timescales on the outer edge of the flow become large as eddies in this region likewise move more slowly than at the return point (x_r) and are more influenced by surrounding stagnant ambient fluid.

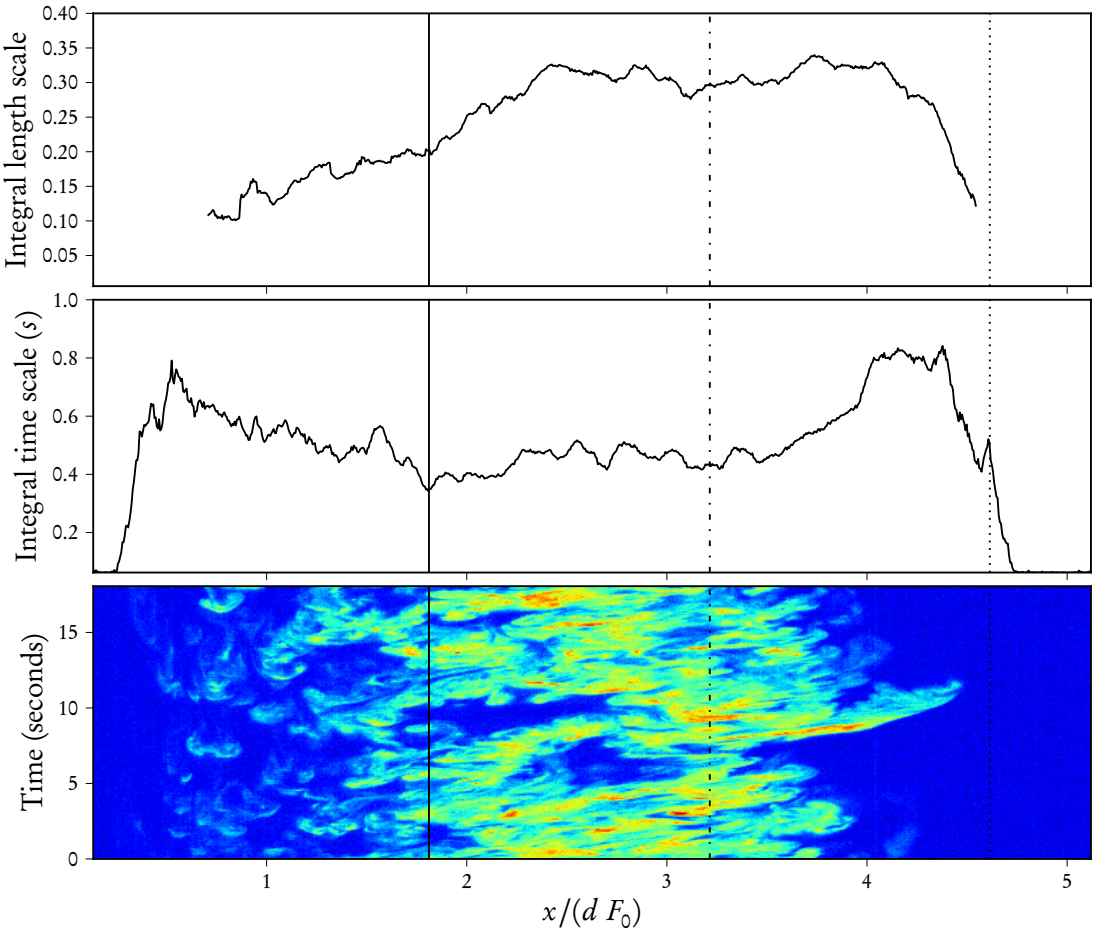

Figure 5.51: Integral length scale (L_{int}; Equation 5.11) and integral timescale (T_{int}; Equation 5.12) calculated from time series of intensity data (6 minute 18.25 second duration) along horizontal line at $z = 0$ through 45° inclination experiment shown in part in lower subplot and identical to that plotted in Figure 5.46. Correlations calculated over time average length of $T_{\text{series}} = 376.4s$ (6022 frames), to a limit of $\Delta x = 1.13$ and $\tau = 1.81s$. Length scales normalised in same manner as x-axis is normalised

5.5.5 Summary of temporal signal characteristics

For a 60° inclination negatively buoyant jet with $dF_0^2/U_0 = 2.83s$, recording durations of at least 180 s were required in order to derive accurate time-average centreline data. Likewise, recording durations of at least 300 s were required in order to derive accurate time-average outer edge data necessary for profile fitting. Therefore, in order to characterise time-average spatial and concentration flow behaviour, recording durations of 300 s or greater should be employed wherever possible.

Spectral power plots of concentration fluctuations at various locations from a 45° inclination negatively buoyant jet ($dF_0^2/U_0 = 2.77s$) were found to peak at periods of 2–12 seconds. Significant spectral activity was also seen approaching one-minute periods. In most plots the high frequency energy cascade followed a $-5/3$ power decay. Low frequency spectral power roll-off was not clear or abrupt in many plots, indicating a wide range of eddy production timescales. This reinforces cumulative time-average results discussed.

Integral timescales of up to 0.6 s were found in $x = x_m$ vertical cut data extracted from this same experiment, and up to 0.8 s in the $z = 0$ horizontal direction. These timescales are the average time duration at which eddies appear correlated, associated with a combination of transportation effects and flow mixing processes. While plots of such data (as plotted in Figures 5.51 and 5.50) provide valuable qualitative trend information, in the current context they do not provide specific information about maximum timescales in the flow as the data is a function of both mixing processes and transportation effects.

It is important to note that while there are many means of assessing the minimum recording duration necessary to derive reliable experimental data of these turbulent flows, ultimately it is only those means determined *a posteriori* which are reliable. That is, one cannot determine without reference to previous negatively buoyant jet experiments the recording duration that will be necessary. It is strongly recommended that experimentalists conduct five-minute duration experiments or longer wherever possible, and subsequently assess their data to ensure that it adequately captures all timescales present in the flow.

5.6 Summary

Key spatial and concentration characteristics of negatively buoyant jets have been analysed in this chapter. Parameters from the present study have been compared with those in the literature. In some cases parameters are reasonably consistent and trends are readily discerned. In other cases considerable scatter is apparent. It has been shown here that experimental conditions, analysis techniques and sampling times varied considerably between available datasets, and this in turn was responsible for the variation in data quality.

Data from the present study has been shown to be self-consistent. This demonstrates the importance of rigorous attention to measurement quality (Section 4.3) and extended recording times.

In addition, predictions from a variety of integral and analytical models have been compared with experimental data. The popular integral models VISJET and CorJet generate good predictions for some parameters but largely fail to predict the extent of dilution seen experimentally at maximum centreline height and return point. Analytical solutions presented by Kikkert *et al.* (2007) and the new 'forced jet' model generate reasonable predictions with respect to spatial parameters. Dilution predictions are significantly improved; however forced jet results are seen to be invalid for source inclinations greater than 60°.

Chapter 6

CFD Simulations

"Fiction reveals truths that reality obscures"
Jessamyn West (1957, p. 39)

This chapter discusses work that was conducted prior to the present experimental study (Chapters 4 and 5), so comparisons were only made to data available at that time. Where possible, current results have been added for comparison. Due to time constraints, other more directly applicable results were not able to be extracted from the simulation datasets. Note this work has been published (Oliver *et al.*, 2008) and this chapter presents an updated version of that paper.

Continued advances in computing power have made simulation of fluid flows by numerically modelling—or solving—the Navier-Stokes equations feasible for many applications. Such Computational Fluid Dynamics (CFD) simulations are appealing as they provide detailed three-dimensional flow-field information at much less cost and much greater speed than possible with laboratory experimentation. Section 2.2.2 discussed research by two authors conducting CFD simulations of negatively buoyant jets: Vafeiadou *et al.* (2005) using the SST turbulence model, and Seil & Zhang (2010) using the SST and RNG turbulence models. Both models are strongly related to the k-ε model. Despite concerns raised by workers such as McGuirk & Rodi (1977) on the applicability of k-ε and similar RANS-based turbulence models to turbulent jets, these studies are evidence that such simulations continue to be employed. In at least the case of Seil & Zhang (2010), research was driven by commercial application needs; highlighting the need to conduct formal validation of such models against comprehensive experimental datasets.

In this chapter, k-ε CFD predictions are compared with experimental data from Kikkert *et al.* (2007) and others. The k-ε model is implemented using standard parameter settings (following Vafeiadou *et al.*, 2005) and in a calibrated form, where the turbulent Schmidt number in the tracer transport equation is modified to provide reasonable predictions of a vertically discharged positively buoyant jet, before it is applied to inclined negatively buoyant jet discharges.

6.1 Model Setup & Calibration

Conditions typical of laboratory experiments were simulated; where a pipe of 5 mm diameter delivered fluid of density 1026.91 kg/m^3 and velocity (uniform) 1.867 m/s into a quiescent receiving water, with a density of 997 kg/m^3. This gave the flow an initial Reynolds number $Re = 10{,}458$ and an initial densimetric Froude number $F_0 = 48.66$, matching experimental data collected by Kikkert *et al.* (2007). For these simulations *ANSYS CFX*, a three-dimensional finite volume package, was employed with an irregular tetrahedral mesh of 2.2–2.6 million nodes (12–15 million elements), and refinements in the regions of jet flow.

As indicated above, the *k-ε* turbulence model was used to close the RANS equations, with standard values for its five parameters ($c_\mu = 0.09$, $c_1 = 1.44$, $c_2 = 1.92$, $\sigma_k = 1.0$, $\sigma_\varepsilon = 1.3$). An initial assessment of the applicability of this model to buoyant discharges was conducted by simulating a vertical buoyant jet and comparing the predicted behaviour with available experimental data. These comparisons focused on the bulk parameters of the flow, because these are of primary practical interest and necessarily precede any more detailed comparisons. Figure 6.1 shows comparisons of the predicted centreline velocity decay and velocity spread of vertical buoyant jets with experimental data. While there is a slight tendency for the simulations to over-predict the velocity spread, the velocity decay compares favourably with the experimental data and the predictions are reasonable. However, predictions of the decay and spread of the tracer concentration field, shown in Figure 6.2, are less satisfactory.

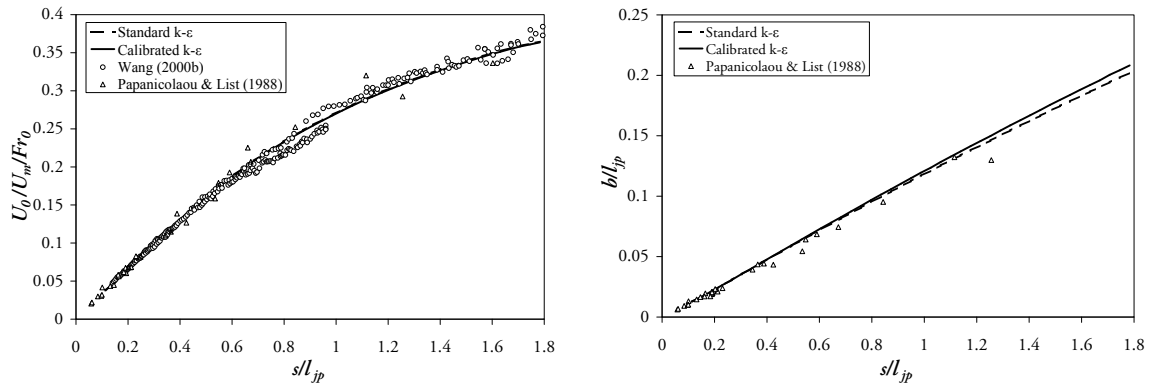

(**a**) Velocity decay (**b**) Velocity spread

Figure 6.1: Velocity decay and velocity spread for vertical buoyant jets. U_m is the centreline mean velocity, b is velocity spread defined by the standard Gaussian form (Equation 1.4), s the centreline path length and l_{jp} is the length scale for the transition from the jet region to plume region ($= 2.3(\pi/4)^{0.25} F_0 d$, after Kikkert, 2006)

In two-component *k-ε* simulations, the rate of diffusion of the secondary component (the tracer) is controlled by the turbulent Schmidt number, Sc_t, in the tracer transport equation. The standard value adopted by CFX for this parameter is 0.9. Previous work on non-buoyant jets has suggested a value of approximately 0.7 for the same parameter (*e.g.* Yimer *et al.*, 2002), although this result is not directly relevant to the simulation of buoyant jets. To address the

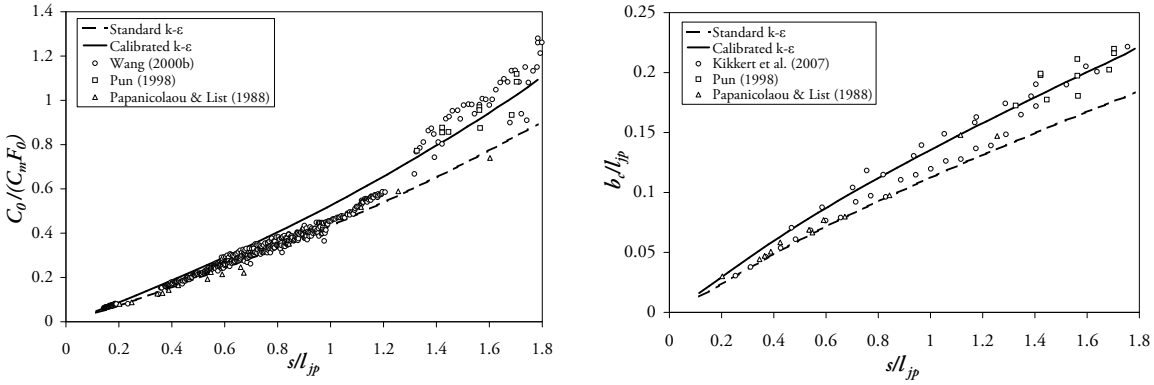

(**a**) Concentration decay (**b**) Concentration spread

Figure 6.2: Dilution and concentration spread for vertical buoyant jet. C_m is the centreline mean concentration and b_c is the concentration spread defined by the standard Gaussian form (Equation 1.4)

relatively poor tracer field predictions, simulations of vertical buoyant jets were carried out for a range of turbulent Schmidt numbers and it was found that a value of 0.6 matched experimental data reasonably well. Predictions from the calibrated simulations, $Sc_t = 0.6$, are also shown in Figures 6.1 and 6.2, where evidence of improvements in the predicted tracer field can be seen. It is worth noting that modifications to the turbulent Schmidt number in the production term for the buoyancy generated turbulence were also explored, but the predictions were insensitive to these changes. In addition the predictions were slightly sensitive to the turbulence level set at the source, but this sensitivity was well within the scatter of the experimental data. A "medium" level of source turbulence, 5% intensity, was adopted for the subsequent simulations.

Standard ($Sc_t = 0.9$) and calibrated ($Sc_t = 0.6$) forms of the *k-ε* model were then employed to simulate negatively buoyant jets with source inclinations of 15°, 30°, 45° and 60° to the horizontal. Although based on vertical buoyant jet predictions the standard form of the model was not expected to perform well, its predictions provide a basis for comparison with the calibrated form of the model. In addition it is consistent with the earlier work of Vafeiadou *et al.* (2005). Tracer mass fraction results from each simulation were interpolated onto a regular grid (with 2 mm spacing in each direction) and then integrated horizontally, perpendicular to the central flow plane, for direct comparison with the laboratory data of Kikkert *et al.*

6.2 Results & Discussion

6.2.1 Cross-sectional profiles

Mean centreline concentration profiles, perpendicular to the flow path, are shown in Figure 6.3 along with those from Kikkert *et al.* Predictions from standard and calibrated forms of the model are qualitatively similar to the experimental data. Both display essentially self-similar Gaussian behaviour on the outer side of the flow (negative r/b_c in Figure 6.3) and a distinctive trend

of rising inner-side concentrations (relative to the centreline maximum) with distance from the source, which is consistent with the experimental data. While neither form of the model is able to accurately predict the evolution of the mean centreline concentration profiles, profiles from the standard form of the model are more consistent with the experimental data.

6.2.2 Dilution

Dilution of the integrated centreline tracer concentration at the maximum rise height is presented in Figure 6.4 as a function of densimetric Froude number. Comparisons are made between the standard and calibrated *k-ε* forms of the model, Kikkert *et al.*'s data, analytical solutions and integral model predictions (CorJet and VISJET). While the *k-ε* model predictions are superior to those from the integral models; they also underestimate the integrated dilution and show a weak dependence on initial discharge angle that is not evident in the data. However, the latter is less evident when compared to the integral model predictions; particularly for the calibrated simulations. Predictions from both forms of the *k-ε* model are therefore conservative, with those from the calibrated simulations being slightly less so than those from the standard simulations. The calibrated predictions are reasonably consistent with predictions from the analytical solutions.

6.2.3 Trajectory and spread

Predictions of the spatial extent of the flow are of considerable practical importance. Here we will continue to focus on the location of, and conditions at, the maximum height, because accurate predictions of these is essential if conditions at the return point are to be estimated with reasonable accuracy. Figure 6.5 shows the dimensionless coefficients for determining the horizontal (k_{xm}) and vertical (k_{zm}) coordinates of the centreline maximum height, relative to the source. Uncalibrated *k-ε* predictions lie within the bounds of experimental scatter for $15° \leq \theta_0 \leq 45°$, and do not diverge significantly at 60°. Calibrated predictions for both k_{xm} and k_{zm} are lower than their uncalibrated counterparts, but differences are small. Calibrated and uncalibrated CFD simulations are no better than the analytical model solutions developed by Kikkert *et al.* (2007) or the forced jet model developed herein at predicting spatial distances to the maximum centreline height. These models are both based on a significantly simplified flow where asymmetries in the mean velocity and concentration profiles are not directly incorporated. CFD predictions are only marginally better than those generated by the CorJet and VISJET integral modelling packages.

Figure 6.6 shows the dimensionless coefficient for determining the maximum edge height of the flow (k_{zme}), which is also linearly dependent on the source Froude number. Again, correlation with experimental data is reasonable. Here however both forms of the *k-ε* model generate almost identical predictions.

The difference between the maximum edge height and maximum centreline height is a measure of the extent of the flow at this location. While the comparisons in Figures 6.5 and 6.6 suggest that the spread of the flow is well predicted by both forms of the *k-ε* model, it is important to

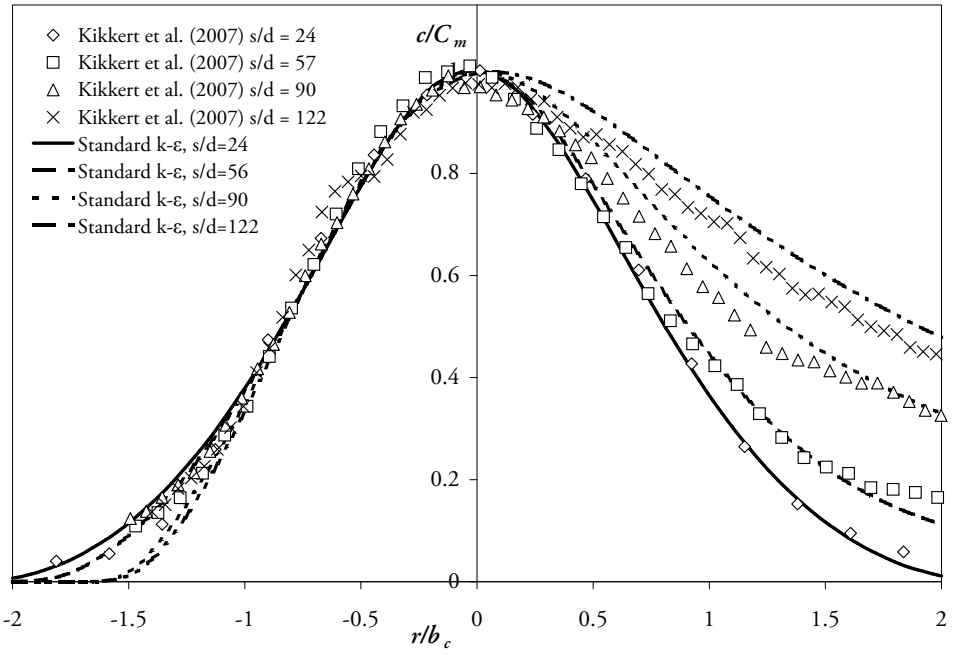

(**a**) Standard predictions

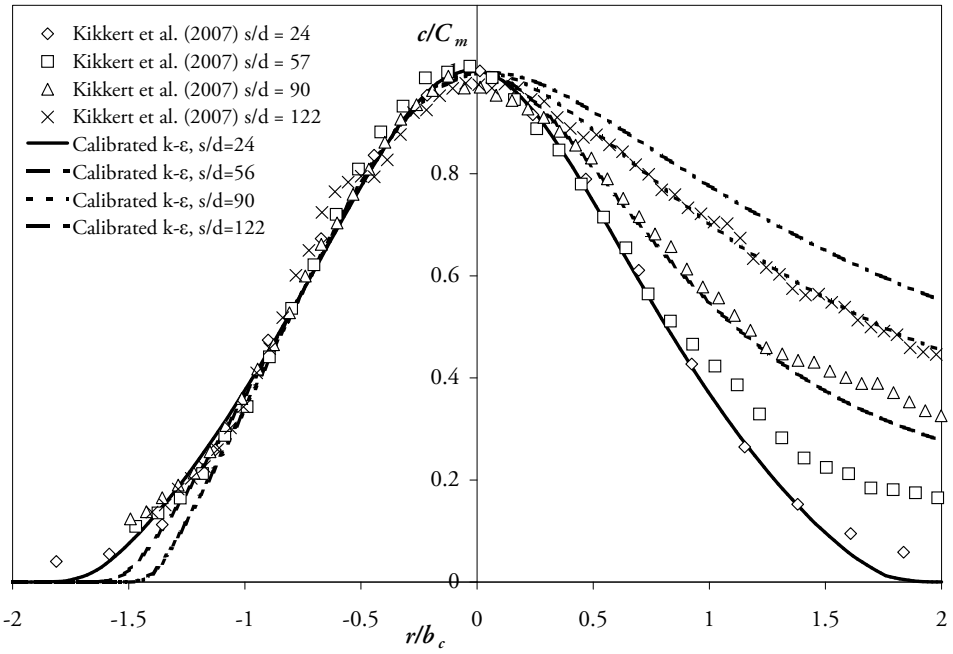

(**b**) Calibrated predictions

Figure 6.3: Centre plane concentration profiles from LIF data of Kikkert *et al.* (2007) with standard and calibrated *k-ε* predictions superimposed. The initial densimetric Froude number and discharge angle were 48.66 and 45° respectively. Note: s is the path length, c is the local concentration, r is the radial coordinate, and b_c is determined based on data on the outer side of the profile (negative r)

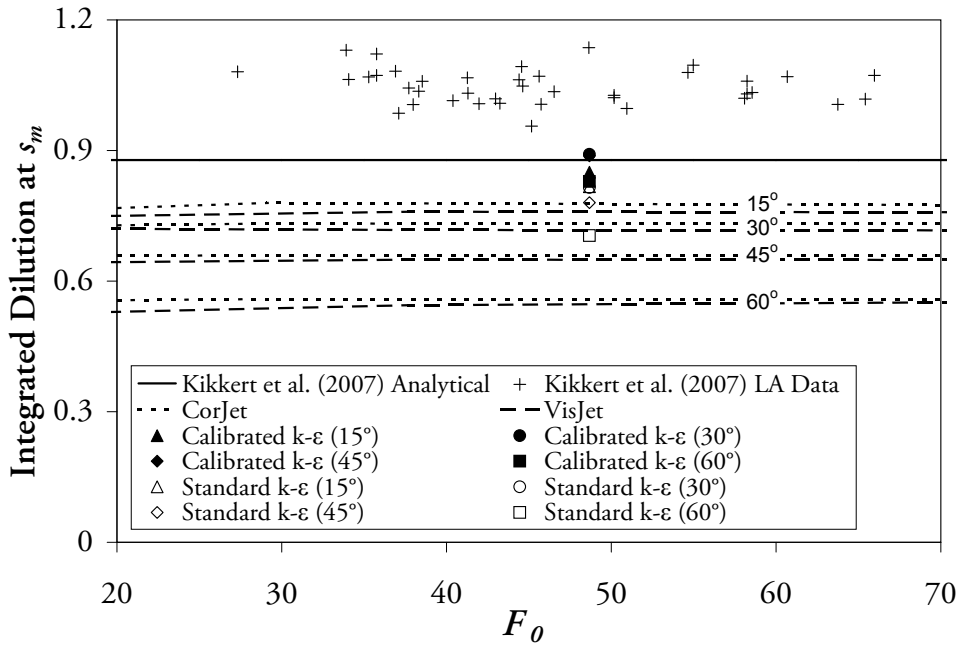

Figure 6.4: Centreline integrated dilution at maximum height as a function of Froude number. Note: The LA data from Kikkert *et al.* (2007) was measured for initial discharge angles of 15°, 30°, 45° and 60°

note that the flow spread is a relatively small portion of the maximum edge height. As a result, errors in spread predictions are not obvious in Figure 6.6. Indeed, comparisons of flow spread on the outer side of the flow reveal significant discrepancies between the predicted and measured behaviour. This can be seen in Figure 6.7, where the concentration spread is plotted against path length. While predictions from the calibrated form of the model are more consistent with the experimental data in the region where these flows reach maximum height, both sets of predictions show a decline in spreading rate in this region. This decline is not evident in the experimental data and suggests both forms of the model are overestimating the stabilising influence of the density gradients.

Further evidence of this can be seen in Figure 6.8 where comparisons of concentration contours, perpendicular to the flow path, at maximum height are shown. While the comparisons are rather crude, it is evident that the cross-sectional shapes of the predicted and actual flows are quite different. The *k-ε* cross-sections show evidence of suppressed spread on the outer side of the flow (here appearing as the upper side), although less so for the calibrated simulations; and while there is evidence of increased mixing on the inner side of the flow, this is not as significant as that shown in the uncalibrated LIF contours from Kikkert (2006).

6.3 Conclusions

Two sets of *k-ε* simulations, one based on standard parameter settings and the other on calibration of the turbulent Schmidt number, have been compared to prior and current experimental data

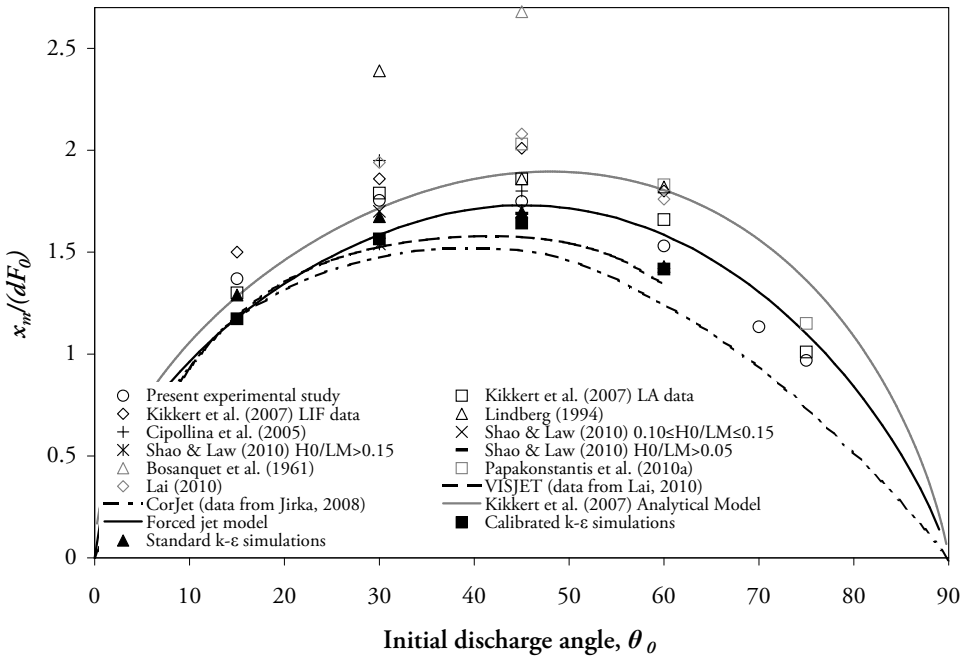

(**a**) Horizontal location of centreline maximum

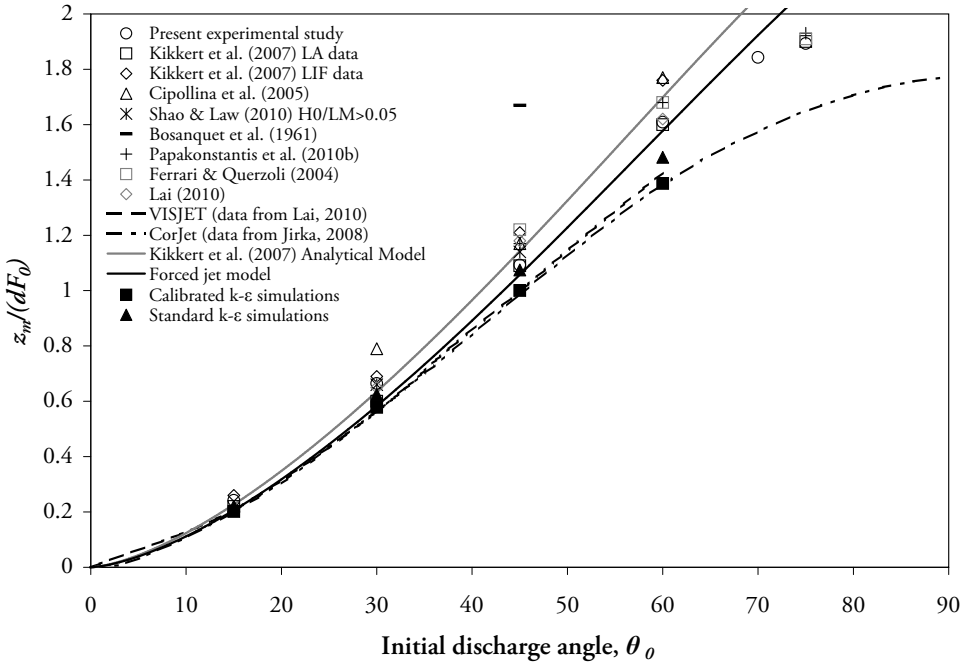

(**b**) Vertical location of centreline maximum

Figure 6.5: Coefficients for horizontal and vertical location of centreline at maximum height, as a function of initial discharge angle. Note that in 6.5a the 60° data point from the present study sits directly on top of a Cipollina *et al.* (2005) data point

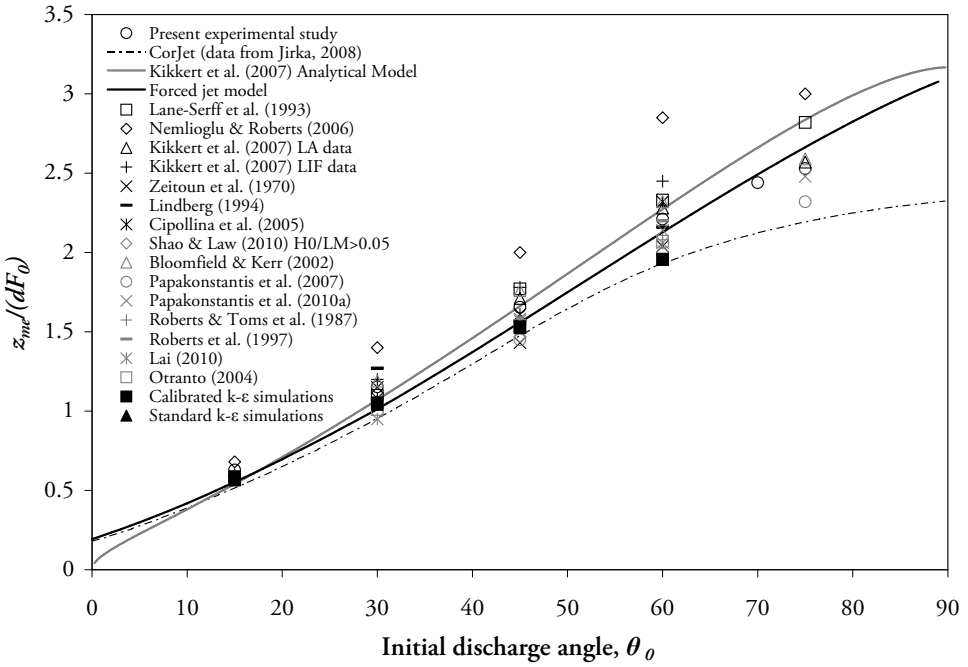

Figure 6.6: Coefficient for maximum elevation of the flow edge as a function of initial discharge angle

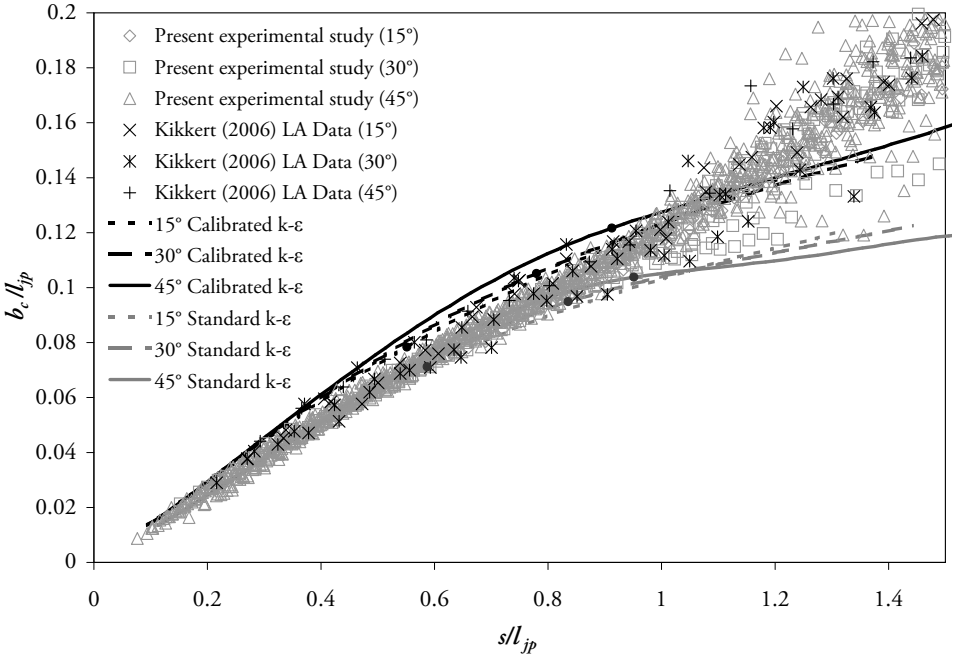

Figure 6.7: Tracer spread data compared with predictions from both standard and calibrated implementations of the *k-ε* model, where solid circles denote the location of maximum rise height for each simulation

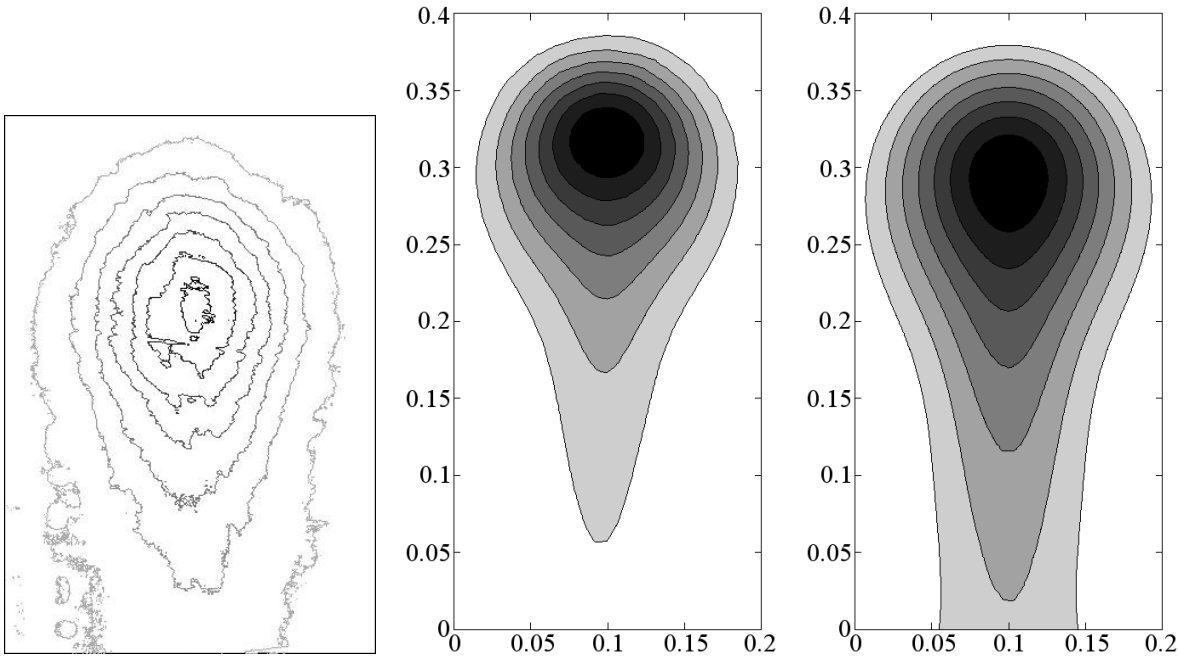

(a) Uncalibrated LIF image from Kikkert (2006)

(b) Standard k-ε image, with co-ordinates in meters

(c) Calibrated k-ε image, with co-ordinates in meters

Figure 6.8: Cross-section planes at maximum trajectory height for 45° discharge at $F_0 = 48.66$

from inclined negatively buoyant discharges. Both implementations of the k-ε model provide a more accurate representation of the physical processes present in inclined negatively buoyant discharges when compared to integral model predictions and analytical solutions. The influence of the buoyancy-induced instabilities, observed in numerous experimental studies, is clearly evident on the lower (inner) side of the flow. However, the k-ε simulations (both standard and calibrated) overestimate the influence of the stabilising density gradients, and hence they tend to under-predict the flow spread and the integrated centreline dilution at the maximum elevation. Despite the sophistication of these models, the quality of spatial and dilution bulk flow predictions at the centreline maximum height are no better than those obtained from analytical solutions, which are based on a simplified flow. Spatial k-ε predictions are also no better than the 'forced jet' integral model which is likewise based on a significant set of simplifying assumptions.

Chapter 7

Conclusions

"For now we see in a mirror dimly, but then face to face. Now I know in part; then I shall know fully, even as I have been fully known."
1 Corinthians 13:12, ESV

Negatively buoyant jets are turbulent flows that are frequently employed by the rapidly expanding desalination industry to disperse reject brines into oceanic environments. Although such brines are largely characterised by elevated concentrations of the same elemental components as the discharge environment contains, there is significant potential for marine ecosystem damage if this waste is not diluted properly. In addition, reject brines typically contain increased heavy metal loads, added chemicals and reduced levels of dissolved oxygen; all of which have important potential environmental effects.

Numerous workers have analysed the dilution and spatial characteristics of negatively buoyant jets, but few have presented minimum dilution rates in stagnant ambient conditions at the location where the discharge returns to the source height. This information forms an essential "base case" for evaluating the performance of models used to predict the behaviour of negatively buoyant jets. Of the experimental data that is available, large discrepancies are evident and clear trends with respect to source inclination are difficult to discern. An important reason for this inconsistency is the variety of bottom-boundary conditions employed. Much so-called "return point" data coincides with the point at which these discharges impact upon the bottom boundary, or is not far above this point.

In the present study, near field experimental dilution data has been collected from single component negatively buoyant jets under still ambient conditions, for the source inclinations of 15–75°, where the bottom boundary distances were sufficiently large to avoid any influence at the return point. The Laser Induced Fluorescence (LIF) experimental technique has been used. In the current implementation, light from a 2 W Nd:YAG laser frequency-doubled to a 532 nm wavelength was directed into a scanning mirror and parabolic mirror unit designed to produce a narrow sheet of laser light (approximately 6 mm thick and 700 mm tall). This sheet of light was in turn directed through the centre of the primary experimental tank (1.78 m high by 2.30 m wide

by 1.23 m deep) and the negatively buoyant jet discharge was configured such that its centreline would fall along the light plane. The Rhodamine 6G fluorescent dye was mixed with a brine solution in the header tank used to feed the experimental discharge.

Considerable attention has been paid to issues of experimental data quality, such as light sheet stability, light attenuation, camera noise and fluctuations resulting from fluid refractive index variations. All relevant aspects have been discussed and mitigated where possible. In general the initial source concentration (C_0) was determined based on analysis of dilution behaviour in the jet region as this was considered to be the most reliable method; reducing the possibility of accumulated error. Experiments have been conducted over long recording durations, ranging from 100 to 688 seconds. *A posteriori* analysis of temporal data indicated that for typical negatively buoyant jets, recording durations of at least 300 s should be employed in order to accurately characterise time-average spatial and concentration flow behaviour.

As noted above, previous experimental data has largely been collected in the presence of significant boundary influence. Indeed, few authors have explicitly stated boundary proximity in appropriate non-dimensional terms, and therefore data tabulated in the current literature review was generally calculated from information provided in each respective article. In order to ensure the boundary had no influence, source heights in the present experimental study ranged between $2.33\,d\ F_0$ and $8.07\,d\ F_0$. At the minimum, these source heights were 1.68 times the largest boundary proximity given in previous literature (Papakonstantis *et al.*, 2011b). These source heights were significantly higher than the steady-state thickness of the bottom layer extending from negatively buoyant jets (measured by Roberts *et al.* (1997) to be $0.7\,dF_0$ for a 60° source inclination and by Lai (2010) to be $0.4\,dF_0$ for 15° to 60° source inclinations). While the present experimental apparatus dictated that the bottom layer would build up steadily over time, grey-scale intensity along the lowest portion of experimental images was analysed and data was not considered past the point at which bottom layer intrusion was detected.

A variety of time-averaged and temporal statistics were calculated from experimental data recorded. These statistics have been compared against published experimental data and predictions by integral models such as VISJET and CorJet. Many inconsistencies can be seen in available dilution and spatial relationship data. The attention to signal quality and the self-consistency of derived experimental results in the present study suggest a high level of accuracy, and large distances to the bottom boundary ensured that results were not confused by boundary interaction. Dilution and trajectory data from experiments at each source inclination were found to collapse well with appropriate non-dimensional scaling. Dilution plotted against vertical height demonstrated a remarkably constant rate of change on the falling side of the flow. Trajectories from all source inclinations were also plotted together with horizontal and vertical distances normalised with respect to return point distance and maximum centreline height, and this data was found to follow a consistent shape; indicating that the influence of buoyancy on centreline trajectories was consistent for all inclination angles, regardless of where the transition to "plume-like" flow was made.

Data for dilution rate against source inclination where the discharge returns to its source height followed a significantly clearer trend than seen in previous datasets, supporting the use of higher source inclinations (60° and 75°) to maximise dilution capability. It is imperative however that further carefully-performed studies are undertaken to independently confirm the results presented in the current study.

Integral models presented by Jirka (2004) and Papanicolaou *et al.* (2008) have been outlined and discussed. The spread at the maximum rise height tends to infinity in both of these models as $\theta_0 \rightarrow 90°$. Fundamentally, this is a result of applying conservation of mass in a time-averaged system of equations: as time-averaged velocity in this location goes to zero, concentration, spread or both must go to infinity. It has been argued that it is precisely the ability of an integral model to produce finite and reasonable results for a fountain that predicts its ability to more broadly model the behaviour of negatively buoyant jets at moderate inclinations.

Kikkert *et al.* (2007) presented an analytical model for negatively buoyant jets based on jet solutions that was found to generate reasonably accurate predictions at the maximum centreline height. Building on the success of this model, a new 'forced jet' model has been developed that incorporates the concept of a reducing buoyancy flux as the flow rises to maximum height. While this new model is unable to accurately predict dilution rates at source inclinations greater than 60°, predictions at other inclinations are reasonable; particularly in the case of spatial parameters. Dilution predictions are notably improved when compared to those from existing integral models.

Finally, Computational Fluid Dynamics (CFD) simulations of negatively buoyant jets have been conducted using the k-ε turbulence model. Results from two sets of simulations, one based on standard parameter settings and the other on calibration of the turbulent Schmidt number, were compared with available experimental data. Both implementations of the k-ε model provided a more accurate representation of negatively buoyant jet bulk behaviour when compared to integral model predictions or analytical solutions. However, all k-ε simulations overestimated the influence of the stabilising density gradients, and hence tended to under-predict the flow spread and the integrated centreline dilution at the maximum elevation. Despite the sophistication of these models, the quality of spatial and dilution bulk flow predictions at the centreline maximum height are no better than those obtained from the forced jet model or analytical solutions of Kikkert *et al.* (2007).

7.1 Future Work

It is recommended that further experimental work is performed under still and unstratified ambient conditions, without boundary influence at the return point, to confirm the results presented in this current study. In addition, a systematic experimental study should be undertaken to investigate and accurately characterise the effect of bottom-boundary interaction.

New integral models should be developed that further improve predictions of negatively

buoyant jet spatial and dilution bulk parameters. These models should be applicable for a wide range of inclinations, and account for re-entrainment effects seen at steep inclinations. Time-dependant CFD simulations—for example, employing the Large Eddy Simulation (LES) approach— should also be carried out to investigate where accurate and economical numerical simulations are possible for this turbulent discharge. Successful implementation of such models provides an important opportunity to further explore the flow physics.

Appendix A

Additional Figures

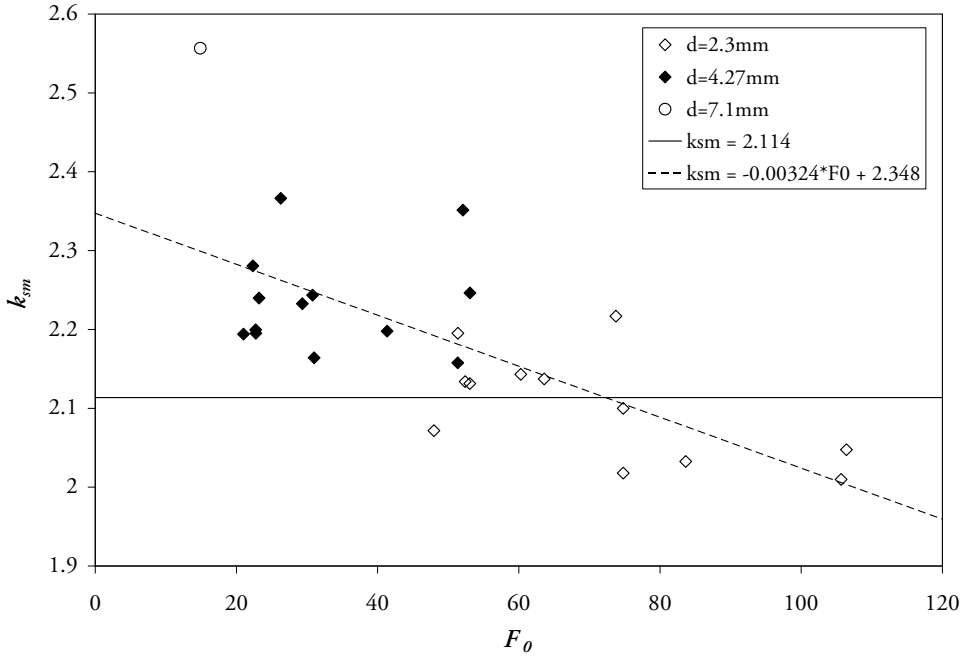

(**a**) Coefficient for distance to maximum centreline height

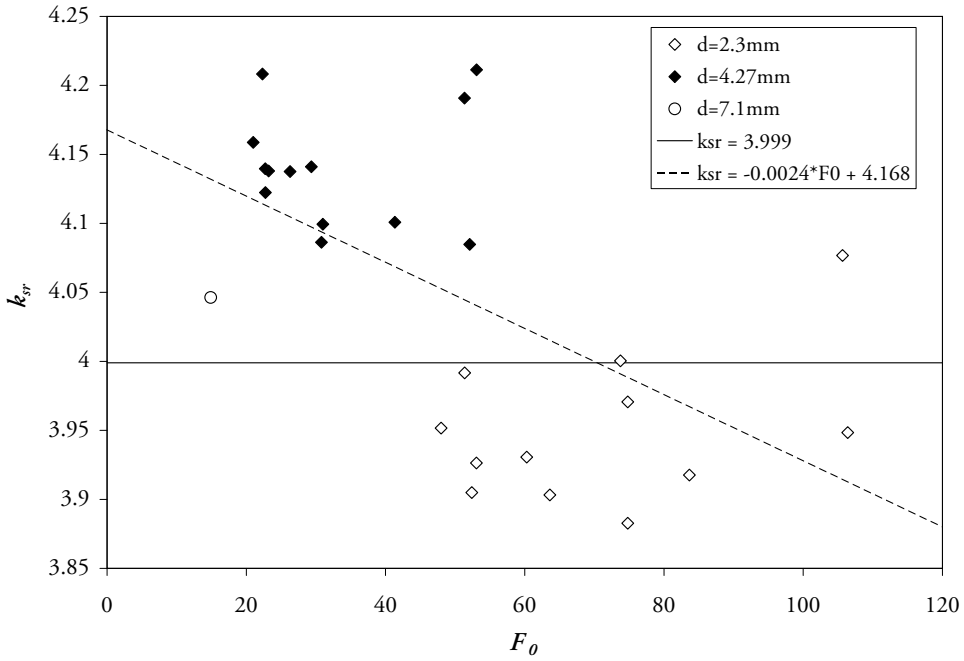

(**b**) Coefficient for distance to return point

Figure A.1: k-coefficients for path length to location of maximum centreline height and the return point for a source inclination of 45°, as a function of densimetric Froude number. Slope of lines plotted in Figure 5.13 plotted (here as horizontal lines), along with linear best-fit lines between the data plotted

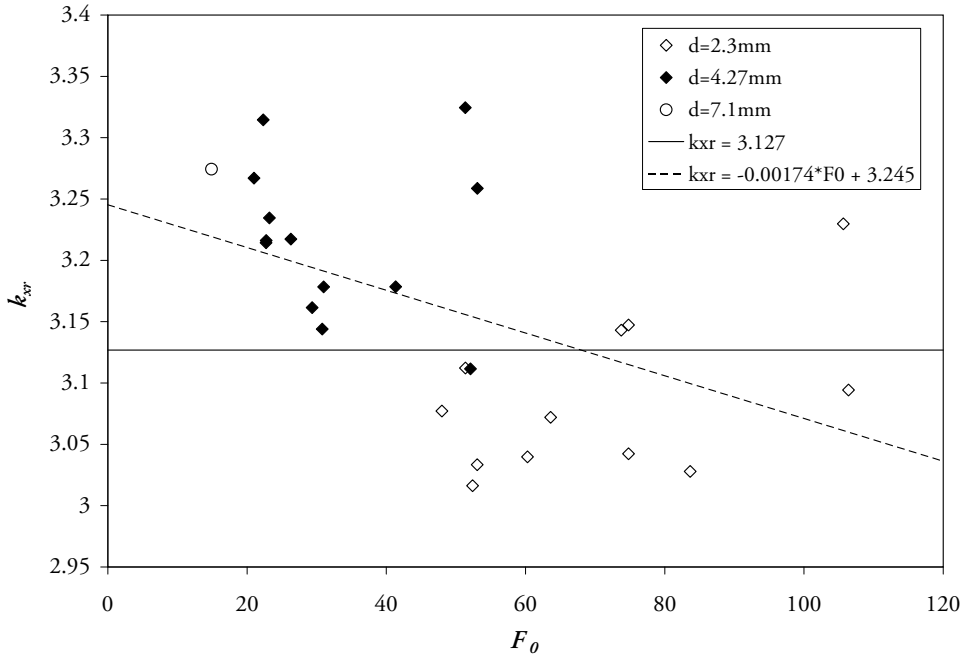

(**a**) Coefficient for distance to return point

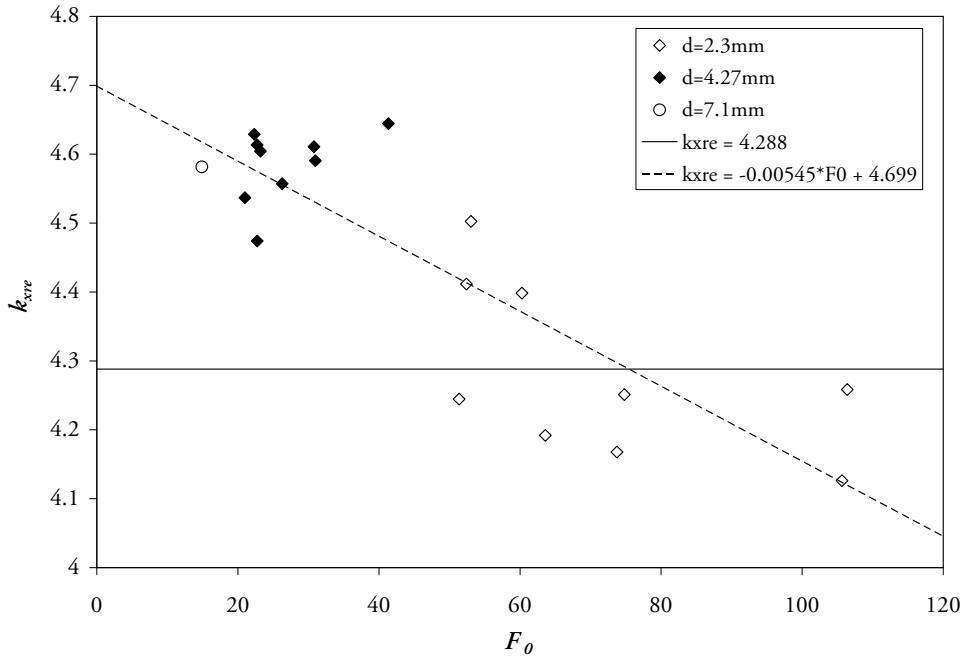

(**b**) Coefficient for distance to return point outer edge

Figure A.2: k-coefficients for distance to return point and outer edge at source height for an inclination of 45°, as a function of densimetric Froude number. Slope of lines plotted in Figure 5.12 plotted (here as horizontal line), along with linear best-fit lines between the data plotted

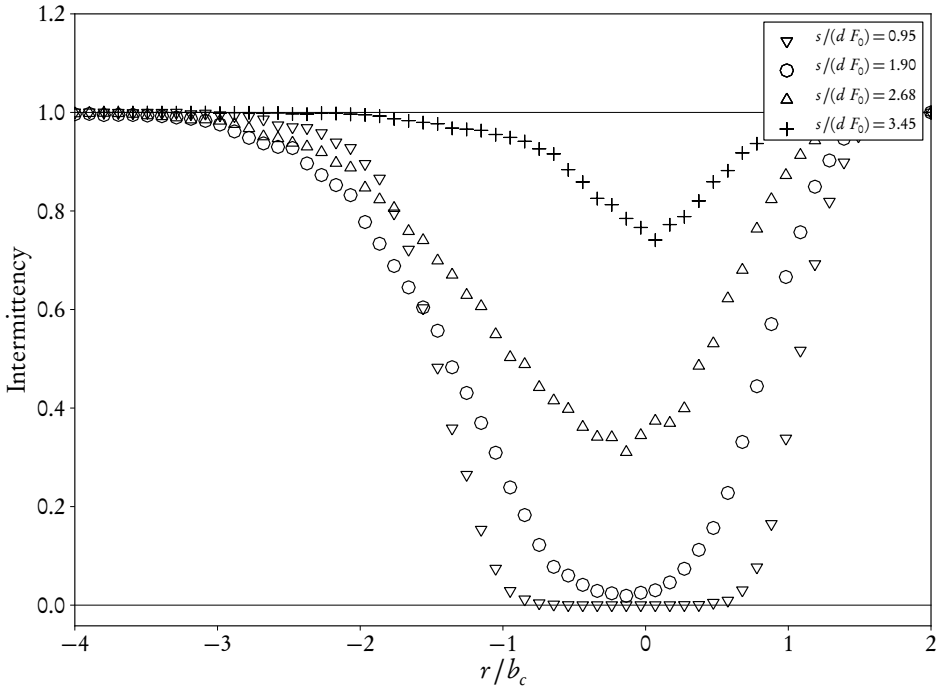

(**a**) Intermittency profile; threshold of 0.020 C_0

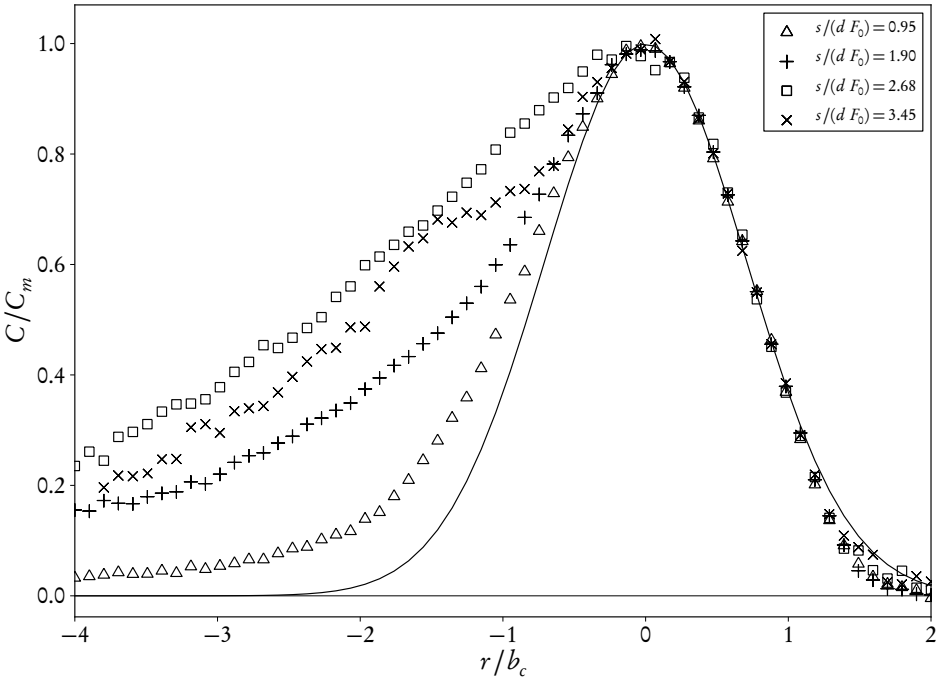

(**b**) Temporally-averaged concentration profile

Figure A.3: Intermittency and average concentration profiles taken at same locations from experiment at 30° inclination. $s/(d\,F_0) = 1.90$ is centreline maximum height location; $s/(d\,F_0) = 3.45$ is return point location. $F_0 = 75.17$ and $\mathrm{Re} = 4429$

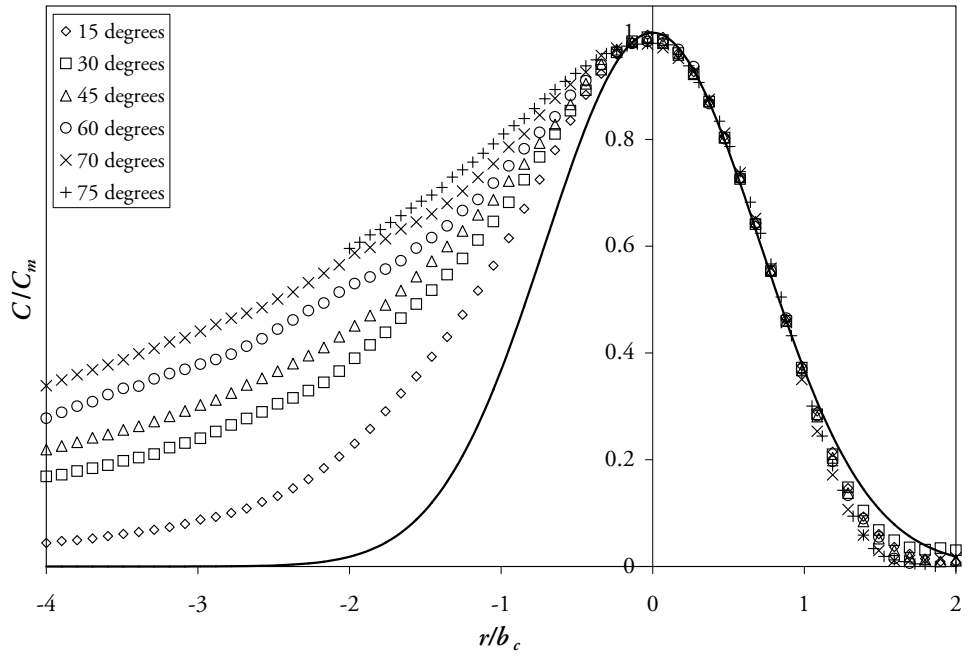

(**a**) Temporally averaged concentration. Solid line is Gaussian distribution ($C/C_m = e^{-(r/b)^2}$)

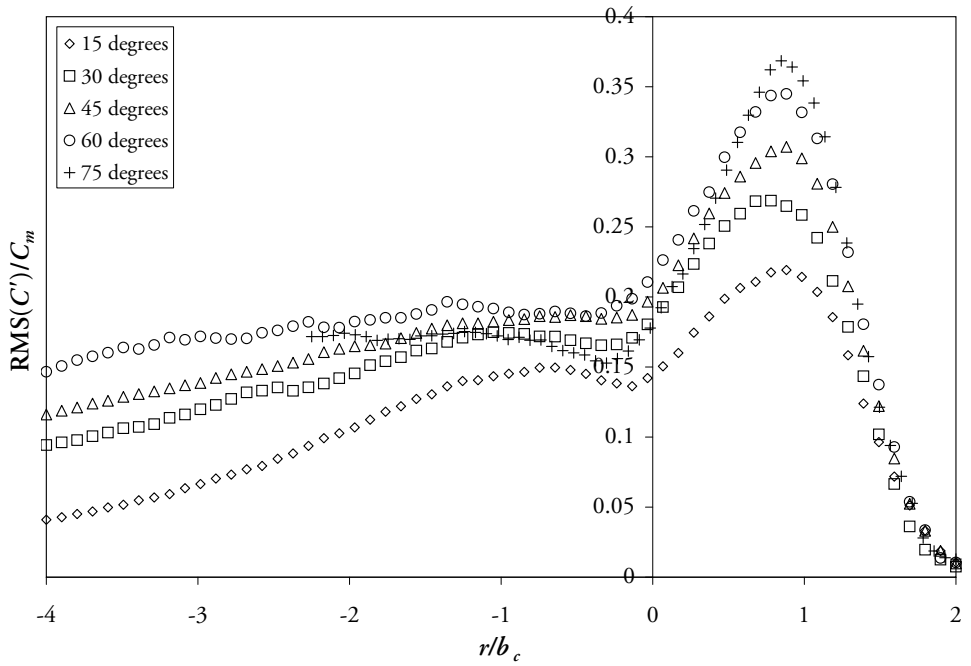

(**b**) RMS of concentration fluctuations

Figure A.4: Profiles of temporally-averaged concentration and RMS of concentration fluctuations at centreline maximum location (s_m), averaged across experimental data at each source inclination

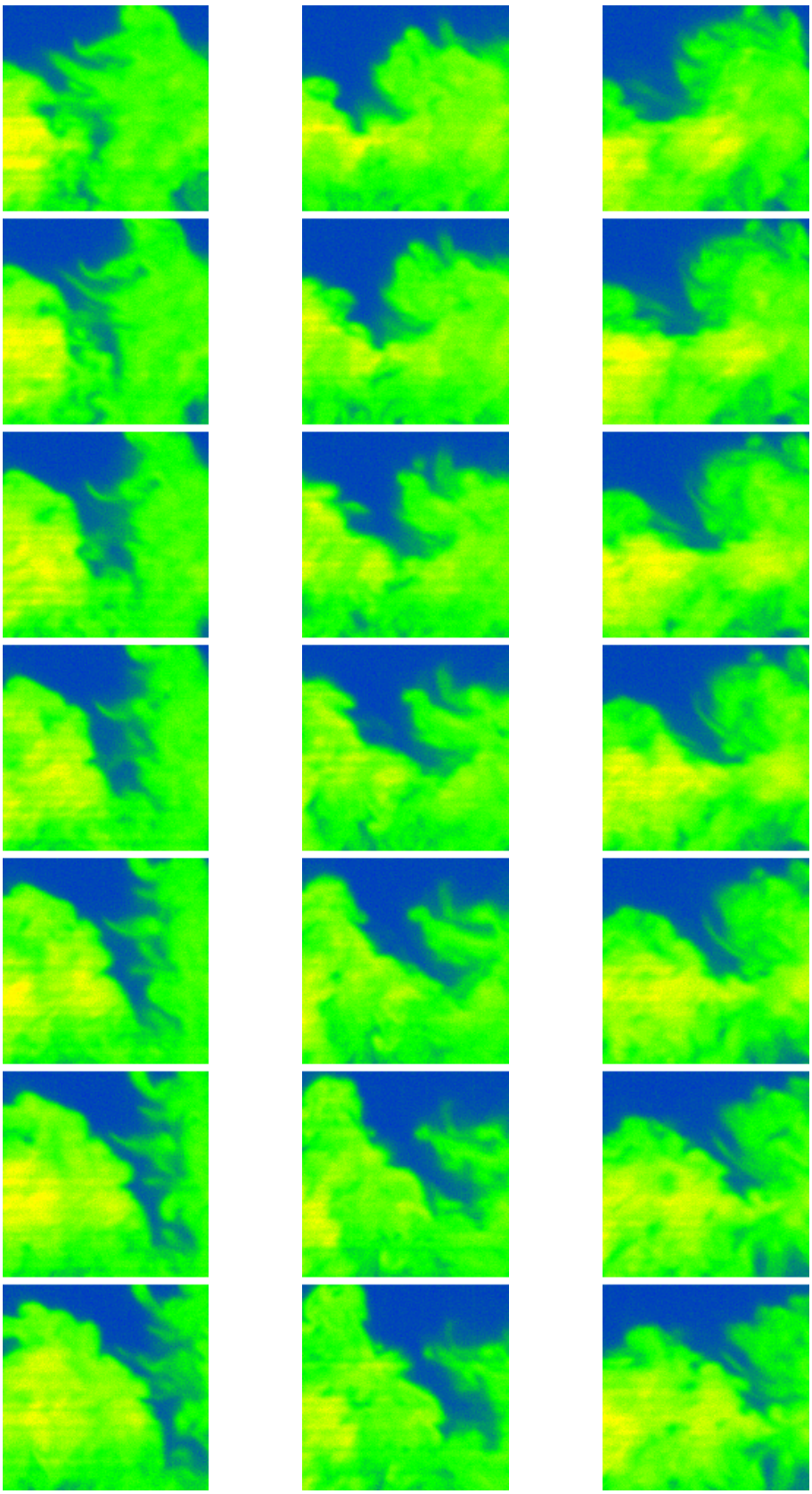

(a) $t = 17.75$–18.50 s (b) $t = 25.63$–26.38 s (c) $t = 43.88$–44.63 s

Figure A.5: Sequences of false-colour images centred on x_m, z_m location, at different time periods during experimental recording plotted in Figure 5.40b. Every second frame shown. Central frames in each sequence are identical to those plotted in Figure 5.41

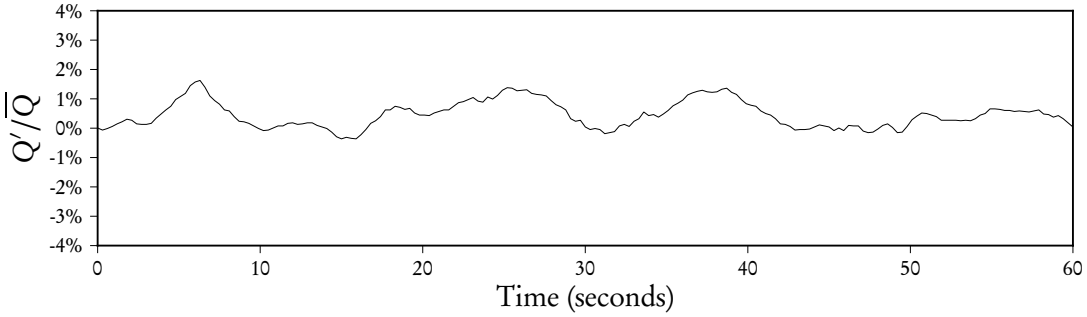

Figure A.6: Fluctuations of flowrate Q, from same experiment and period as data plotted in Figure 5.40

Appendix B

Experimental Coefficients

Table B.1: Experimental coefficients from present study. *Note:* Duration refers to recording duration

Angle	F_0	d (mm)	Duration (s)	dF_0^2/U_0 (s)	$H_0/(dF_0)$	x_m/d	z_m/d	s_m/d	z_{me}/d	x_r/d	s_r/d	S_m	S_r	x_{re}/d	b_c/d at x_r
15°	22.4	4.27	428.3	2.74	8.07	35.55	5.26	35.94	14.38	54.03	55.26	6.38	10.41	83.08	6.56
15°	30.6	4.27	343.8	3.73	5.92	40.75	7.43	41.49	19.31	72.50	74.49	7.47	14.40	113.94	9.09
15°	30.8	4.27	400.0	3.75	5.88	37.95	7.57	38.70	19.34	73.78	75.71	7.02	14.99	112.02	8.90
15°	41.4	4.27	271.9	5.05	4.38	58.03	10.00	59.07	25.87	98.90	101.54	10.26	20.21	152.22	11.86
30°	22.3	4.27	233.3	2.72	7.68	39.98	14.59	43.00	25.70	68.53	76.53	7.66	17.80	100.53	10.14
30°	30.8	4.27	275.0	3.75	5.57	55.21	20.26	59.55	35.68	93.66	104.93	10.50	25.62	136.46	14.86
30°	40.9	4.27	150.0	4.99	4.18	75.66	28.30	81.69	48.15	129.84	144.97	14.71	35.65	187.65	18.10
30°	41.2	4.27	131.3	5.02	4.16	75.62	27.97	81.61	48.48	130.33	145.37	14.90	34.69	186.41	18.45
30°	51.0	2.3	493.8	4.57	6.40	86.33	33.93	93.77	59.20	152.75	171.33	16.51	40.69	220.55	24.36
30°	75.2	2.3	193.8	6.72	3.76	135.53	49.34	146.58	85.72	230.07	257.89	—	—	312.27	31.01
30°	75.7	2.3	143.8	6.78	4.31	126.34	50.07	137.41	86.81	234.25	262.78	24.92	63.94	331.37	29.68
45°	14.9	7.1	212.5	2.34	7.71	34.47	16.17	38.08	24.43	48.77	60.26	—	—	68.23	8.16
45°	21.0	4.27	688.1	2.57	6.20	37.80	24.14	46.07	36.12	68.60	87.32	8.23	25.98	95.26	10.73
45°	22.3	4.27	167.6	2.74	5.84	42.34	25.62	50.93	38.56	74.01	93.97	9.34	26.42	103.37	11.20
45°	22.7	4.27	465.6	2.77	5.60	41.15	26.02	49.97	38.90	73.03	94.05	8.97	28.00	104.82	13.13
45°	22.7	4.27	480.8	2.77	5.59	41.08	25.79	49.92	39.00	73.14	93.74	8.85	27.08	101.74	11.79
45°	23.2	4.27	283.9	2.83	5.48	43.02	26.37	51.98	39.71	75.07	96.04	9.22	27.53	106.86	12.85
45°	26.3	4.27	193.8	3.22	4.96	52.00	30.14	62.20	45.13	84.57	108.76	11.45	30.81	119.79	13.84
45°	29.3	4.27	173.8	3.60	4.45	53.76	34.62	65.52	51.31	92.77	121.51	11.92	34.37	—	17.39
45°	30.8	4.27	362.4	3.76	4.13	57.18	35.15	69.08	53.21	96.81	125.83	12.50	40.56	141.99	17.39
45°	31.0	4.27	349.9	3.78	4.10	55.08	35.34	67.07	53.07	98.51	127.06	11.87	38.02	142.28	17.43
45°	41.3	4.27	187.5	5.04	3.08	75.06	46.98	90.86	71.05	131.40	169.53	16.93	53.83	192.00	24.80
45°	48.0	2.3	168.8	4.31	4.91	82.40	51.43	99.40	78.32	147.64	189.60	18.18	57.50	—	30.70
45°	51.4	4.27	187.5	6.27	2.48	90.81	58.88	110.80	89.03	170.72	215.20	20.63	76.00	—	23.63
45°	51.4	2.3	166.3	4.62	4.83	93.88	57.11	112.74	83.52	159.85	205.01	20.64	57.00	218.01	26.26

Table B.1: Experimental coefficients from present study (continued)

Angle	F_0	d (mm)	Duration (s)	dF_0^2/U_0 (s)	$H_0/(d\,F_0)$	x_m/d	z_m/d	s_m/d	z_{me}/d	x_r/d	s_r/d	S_m	S_r	x_{re}/d	b_c/d at x_r
45°	52.1	4.27	112.4	6.35	2.44	102.44	59.71	122.46	89.55	162.06	212.75	24.16	62.71	—	31.58
45°	52.4	2.3	364.1	4.69	4.74	92.49	57.75	111.80	87.28	158.03	204.59	19.97	62.24	231.14	31.71
45°	53.1	2.3	170.0	4.77	4.44	93.81	58.10	113.08	85.20	160.94	208.32	—	—	238.88	34.99
45°	53.1	4.27	168.8	6.50	2.46	98.25	62.23	119.24	93.12	172.98	223.55	22.10	70.52	—	33.10
45°	60.3	2.3	262.5	5.40	4.12	107.04	65.33	129.19	98.94	183.23	236.93	23.48	67.86	265.13	34.38
45°	63.6	2.3	250.0	5.72	3.71	113.29	67.77	135.92	102.34	195.36	248.23	25.35	73.41	266.59	29.19
45°	73.7	2.3	248.8	6.63	3.36	136.52	80.97	163.48	121.52	231.78	295.01	31.07	89.56	307.36	35.72
45°	74.8	2.3	100.0	6.72	3.15	130.10	80.89	157.05	122.10	235.38	296.95	29.24	85.99	317.93	37.66
45°	74.8	2.3	106.3	6.72	3.15	124.84	78.98	150.91	120.48	227.52	290.37	—	—	—	33.79
45°	83.6	2.3	160.6	7.52	2.82	140.16	89.76	170.00	135.95	253.26	327.68	31.32	93.81	—	50.84
45°	105.6	2.3	125.0	9.50	2.35	174.01	113.84	212.32	173.22	341.20	430.68	39.62	131.86	435.92	36.72
45°	106.4	2.3	137.5	9.57	2.33	179.77	113.69	217.85	176.30	329.22	420.09	41.46	133.86	453.07	54.68
60°	23.2	4.27	537.5	2.83	6.10	35.87	38.02	54.39	51.75	64.99	105.44	9.59	32.88	93.88	13.46
60°	30.9	4.27	312.5	3.78	4.57	49.48	49.73	73.69	68.85	84.44	138.16	13.47	48.22	122.89	17.86
60°	41.1	4.27	218.8	5.01	3.44	61.07	65.77	93.04	90.24	113.73	183.66	16.76	65.30	161.63	22.57
70°	22.8	4.27	362.5	2.77	6.03	26.80	41.86	52.23	55.88	44.66	100.47	—	—	78.64	16.66
70°	31.2	4.27	262.5	3.80	4.40	35.22	57.59	70.17	76.32	61.61	138.02	—	—	101.34	19.67
70°	39.9	4.27	143.8	4.86	3.44	44.76	73.47	89.47	96.94	81.18	177.79	—	—	130.32	22.53
75°	23.3	4.27	615.2	2.85	5.59	21.11	44.55	50.82	60.11	40.77	102.93	8.78	38.00	70.36	14.50
75°	30.8	4.27	537.5	3.76	4.24	30.80	58.52	69.85	78.48	51.20	135.21	12.54	47.84	92.99	20.58
75°	41.3	4.27	193.8	5.04	3.16	40.16	77.88	92.28	103.50	68.13	180.88	15.92	61.65	118.32	28.77

Appendix C

Software Code

Forced Jet Model

Implementation written in Python 2.6, using Numpy 1.2.1 and Scipy 0.7.0.

```
from math import atan, pi, log, atan
from scipy import integrate, linspace, logspace, optimize
from numpy import empty, array, sin, cos, isinf, choose
import os, csv

kT = 0.15

def forced_jet(V,s,kT,Fr0,M0,theta0,bc_b_estimate):
    """
    Calculate derivatives of parameters in forced jet model (buoyant
    jet forced to have pure-jet dilution decay up to centreline maximum height)
    """
    b = V[0]; x = V[1]; z = V[2]; M_v = V[3]; M = V[4]; Q = V[5]; B = V[6];

    M_h = M0 * cos(theta0)
    theta = atan(M_v/M_h);
    if M_h < 0:
        theta = theta + pi;
    elif M_v < 0:
        theta = theta + 2*pi;

    g = B/Q
    u = M/Q
    Fl = u/(g*b)**0.5
    lambda_j = 1.217; lambda_p = 1.038; k_jH = 1.076; k_pH = 1.15
    bc_b = optimize.fmin(bc_b_func, bc_b_estimate.bc_b,
                         args=(Fl, Fr0, lambda_j, lambda_p, k_jH, k_pH),
                         disp=0, xtol=0.01)[0]
    bc_b_estimate.bc_b = bc_b
```

```
    dx_ds = M_h/M;
    dz_ds = M_v/M;
    dM_v_ds = -(4. * g * b**2 * bc_b**2)/(Fr0**2)
    dM_ds = M_v/M*dM_v_ds
    db_ds = kT
    dQ_ds = (b/M**0.5)*dM_ds  +  2*M**0.5*db_ds

    if dz_ds < 0:
        dB_ds = 0.0
    else:
        #Fixing dilution rate to that of a jet
        dB_ds = (B/Q)*dQ_ds - 2*Q*kT*g**2

    return (db_ds, dx_ds, dz_ds, dM_v_ds, dM_ds, dQ_ds, dB_ds)

def bc_b_func(bc_b, Fl, Fr0, lambda_j, lambda_p, k_jH, k_pH):
    """ In which badgers crave blueberries. i.e., function used to iteratively
    calculate bc/b """
    Flp = ((5./4)*bc_b**2)**0.5*2 / Fr0
    if Fl < Flp: Flp = Fl
    lambda_ = lambda_j - (lambda_j - lambda_p)*(Flp/Fl)**1.5
    k_H = k_jH - (k_jH - k_pH)*(Flp/Fl)**2
    I_Q = pi
    I_M = 1.1 * pi/2
    I_QC = k_H*pi/(1+1/lambda_**2)
    I_C = lambda_**2 * pi
    return abs(bc_b-(I_C*I_M/(I_Q*I_QC))**0.5)

def run_forced_jet_model(theta0_degrees,Fr0,s_dFr_max=None):
    """
    Function that runs forced jet model, converts results to corresponding
    Gaussian parameters, and returns these values
    """
    #== Set up variables ==
    theta0 = theta0_degrees*pi/180

    #Initial Conditions
    b_star0 = 0.05
    x_star0 = 0.
    z_star0 = 0.
    B_star0 = 1.
    M_star0 = 1.
    M_v_star0 = M_star0 * sin(theta0)
    M_h_star0 = M_star0 * cos(theta0)
    U_star0 = (M_star0/(4.*b_star0**2))**0.5
    Q_star0 = 4. * U_star0 * b_star0**2
```

```
#Distance to solve up to
if isinf(Fr0):
    s_star_max = 2000
elif s_dFr_max == None:
    s_star_max = 10 * Fr0
else:
    s_star_max = s_dFr_max * Fr0
s_star = linspace(0, s_star_max, 3000)

#== Perform numerical integration ==
V, infodict = integrate.odeint(forced_jet, [b_star0, x_star0, z_star0, M_v_star0,
                                            M_star0, Q_star0, B_star0], s_star,
                               args=(kT,Fr0,M_star0,theta0,Bcb_object(1.07)),
                               full_output=True)

#== Post Process ==
delta_t_star = V[:,6] / V[:,5]  #B_star/Q_star
U_t_star = V[:,4] / V[:,5]  #M_star/Q_star

#Calculate appropriate lambda value for each step
Fl = U_t_star/(delta_t_star*V[:,0])**0.5 #Fl = u/(g*b)**0.5
lambda_j = 1.217; lambda_p = 1.038; k_jH = 1.076; k_pH = 1.15
lambda_ = empty(Fl.shape)
Flp = empty(Fl.shape)
bc_b = empty(Fl.shape)
bc_b[-1] = 1.07 #Initial bc_b estimate
for i, ff in enumerate(Fl):
    bc_b[i] = optimize.fmin(bc_b_func, bc_b[i-1],
                            args=(Fl[i], Fr0, lambda_j, lambda_p, k_jH, k_pH),
                            disp=0, xtol=0.01, maxfun=4)[0]
Flp = ((5./4)*bc_b**2)**0.5*2 / Fr0
take = 1*(Flp>Fl)
Flp = choose(take,[Flp,Fl]) #Equivalent to if Fl[i] < Flp[i]: Flp[i] = Fl[i]
k_H = k_jH - (k_jH - k_pH)*(Flp/Fl)**2
lambda_ = lambda_j - (lambda_j - lambda_p)*(Flp/Fl)**1.5
I_QC = k_H*pi/(1+1/lambda_**2)
I_Q = pi
I_M = 1.1 * pi/2

U_m_star = (I_Q/I_M) * U_t_star
b_star = (pi*I_M/I_Q**2)**0.5 * V[:,0]
bc_star = lambda_ * b_star
C_m_star = I_Q / I_QC * delta_t_star

s_dFr0 = s_star / Fr0
bc_dFr0 = bc_star / Fr0
```

```
    C0_CmFr0 = (1/C_m_star) / Fr0
    U0_UmFr0 = (1/U_m_star) / Fr0
    x_dFr0 = V[:,1]/Fr0
    z_dFr0 = V[:,2]/Fr0

    M_h = cos(theta0)
    theta = array([atan(M_v/M_h) for M_v in V[:,3]])
    if M_h < 0:
        theta = theta + pi
    else:
        for i, M_v in enumerate(V[:,3]):
            if M_v<0:
                theta[i] = theta[i] + 2*pi;

    return (s_dFr0, bc_dFr0, C0_CmFr0, U0_UmFr0, x_dFr0, z_dFr0, theta)


class Bcb_object:
    def __init__(self,bc_b):
        self.bc_b = bc_b
```

Bibliography

Abraham, G. 1967. Jets with negative buoyancy in homogeneous fluid. *Journal of Hydraulic Research*, **5**(4), 235–248.

Allison, P. (ed). 2006. *The 2006 Global Water Awards*. Media Analytics Ltd.

Amiji, M. M., & Sandmann, B. J. 2002. *Applied physical pharmacy*. McGraw-Hill Professional.

Anderson, J. L., Parker, F. L., & Benedict, B. A. 1973. *Negatively buoyant jets in a cross flow*. Environmental Protection Agency. Report Number EPA-660/2-73-012.

Andrews, W. T., & Laker, D. S. 2001. A twelve-year history of large scale application of work-exchanger energy recovery technology. *Desalination*, **138**, 201–206.

Aristotle. c. 350 BC. *Meteorology II*. Translated by E. W. Webster, 2007.

Association of American Railroads. 1924. *Proceedings of the Regular Meeting, Car Service Division*.

Baalousha, H. 2006. Desalination status in the Gaza Strip and its environmental impact. *Desalination*, **196**, 1–12.

Baines, W. D., Turner, J. S., & Campbell, I. H. 1990. Turbulent fountains in an open chamber. *Journal of Fluid Mechanics*, **212**, 557–592.

Baker, R. W. 2004. *Membrane technology and applications*. 2nd edn. John Wiley and Sons.

Bloomfield, L. J., & Kerr, R. C. 2002. Inclined turbulent fountains. *Journal of Fluid Mechanics*, **451**, 283–294.

Bosanquet, C. H., Horn, G., & Thring, M. W. 1961. The effect of density differences on the path of jets. *Proceedings of the Royal Society of London, Series A.*, **263**(1314), 340–352.

Boussinesq, J. 1903. *Théorie analytique de la chaleur*. Vol. 2. Gauthier-Villars.

Brewster, Sir David. 1855. *Memoirs of the life, writings, and discoveries of Sir Isaac Newton, Volume 1*. Edinburgh: Thomas Constable and Co.

Brzoska, M. A., Hickmott, S., Stock, D. E., Rabbit, M., Smith, R. M., & Romero, E. 2000. Numerical simulation of flow from a negatively bouyant jet. *In: Proceedings of FEDSM'00: Fluids Engineering Division Annual Summer Meeting & Exhibition*.

Carazzo, G., Kaminski, E., & Tait, S. 2010. The rise and fall of turbulent fountains: a new model for improved quantitative predictions. *Journal of Fluid Mechanics*, **657**, 265–284.

Cavalletti, A., & Davies, P. A. 2003. Impact of Vertical, Turbulent, Planar, Negatively Buoyant Jet With Rigid Horizontal Bottom Boundary. *Journal of Hydraulic Engineering*, **129**, 54–62.

Cipollina, A., Brucato, A., Grisafi, F., & Nicosia, S. 2005. Bench-Scale Investigation of Inclined Dense Jets. *Journal of Hydraulic Engineering*, **131**(11), 1017–1022.

Comprehensive Assessment of Water Management in Agriculture (CA). 2007. *Water for Food, Water for Life: A Comprehensive Assessment of Water Management in Agriculture*. London: Earthscan, and Colombo: International Water Management Institute.

Cresswell, R.W., & Szczepura, R.T. 1993. Experimental investigation into a turbulent jet with negative buoyancy. *Physics of Fluids A*, **5**(11), 2865–2878.

Crimaldi, J. P. 2008. Planar laser induced fluorescence in aqueous flows. *Experiments in Fluids*, **44**(6), 851–863.

Crisp, G. 2008. Seawater desalination in Australia and the Perth experience—a sustainable solution. *In: 2nd International Salinity Forum*.

Davidson, M. J., & Pun, K. L. 1999. Weakly advected jets in cross-flow. *Journal of Hydraulic Engineering*, **125**(1), 47–58.

Daviero, G. J., Roberts, P. J. W., & Maile, K. 2006. Refractive index matching in large-scale stratified experiments. *Experiments in Fluids*, **31**, 119–126.

Del Bene, J.V., Jirka, G., & Largier, J. 1994. Ocean Brine Disposal. *Desalination*, **97**(1–3), 365–372.

Devine, M. 2008. Thumbs down to city's daft desalination plant. *Sydney Morning Herald*, April 27.

Dimotakis, P. E., Miake-Lye, R. C., & Papantoniou, D. A. 1983. Structure and dynamics of round turbulent jets. *Physics of Fluids*, **26**, 3185–3192.

Doneker, R. L., & Jirka, G. H. 1999. Discussion of "Mixing in Inclined Dense Jets". *Journal of Hydraulic Engineering*, **125**, 317–318.

Du, H., Fuh, R. A., Li, J., Corkan, A., & Lindsey, J. S. 1998. PhotochemCAD: A computer-aided design and research tool in photochemistry. *Photochemistry and Photobiology*, **68**(2), 141–142.

Eggeling, C., Volkmer, A., & Seidel, C. 2005. Molecular photobleaching kinetics of Rhodamine 6G by one-and two-photon induced confocal fluorescence microscopy. *ChemPhysChem*, **6**(5), 791–804.

Einav, R., & Lokiec, F. 2003. Environmental aspects of a desalination plant in Ashkelon. *Desalination*, **156**, 79–85.

Fan, L. N., & Brooks, N. H. 1966. Discussion of horizontal jets in a stratified fluid of other density. *Journal of Hydraulics Division, ASCE*, **HY2**, 423–429.

Fernández-Torquemada, Y., & Sáanchez-Lizaso, J. L. 2005. Effects of salinity on leaf growth and survival of the Mediterranean seagrass *Posidonia oceanica* (L.) Delile. *Journal of Experimental Marine Biology and Ecology*, **320**, 57–63.

Fernández-Torquemada, Y., Sáanchez-Lizaso, J. L., & González-Correa, J. M. 2005. Preliminary results of the monitoring of the brine discharge produced by the SWRO desalination plant of Alicante (SE Spain). *Desalination*, **182**, 395–402.

Ferrari, S., & Querzoli, G. 2004. Sea discharge of brine from desalination plants: a laboratory model of negatively buoyant jets. *In: Proceedings of 3rd International Conference on Marine Waste Water Disposal and Marine Environment*.

Ferrari, S., & Querzoli, G. 2010. Mixing and re-entrainment in a negatively buoyant jet. *Journal of Hydraulic Research*, **48**(5), 632–640.

Ferrier, A. J., Funk, D. R., & Roberts, P. J. W. 1993. Application of optical techniques to the study of plumes in stratified fluids. *Dynamics of Atmospheres and Oceans*, **20**, 155–183.

Fischer, H. B., List, E. J., Koh, R. C. Y., Imberger, J., & Brooks, N. H. 1979. *Mixing in Inland and Coastal Waters*. Academic Press, New York.

García-Rodríguez, L. 2003. Renewable energy applications in desalination: state of the art. *Solar Energy*, **75**.

Gibson, M. M. 1963. Spectra of turbulence in a round jet. *Journal of Fluid Mechanics*, **15**, 161–173.

Gille, D. 2003. Seawater intakes for desalination plants. *Desalination*, **156**, 249–256.

Glater, J. 1998. The early history of reverse osmosis membrane development. *Desalination*, **117**, 297–309.

Gleick, P. H. 2000. *The World's Water 2000-2001: The Biennial Report on Freshwater Resources*. Island Press.

Gleick, P. H., Cooley, H., Katz, D., Lee, E., Morrison, J., Palaniappan, M., Samulon, A., & Wolff, G. H. 2006. *The World's Water 2006-2007: The Biennial Report on Freshwater Resources*. Island Press.

Greenlee, L. F., Lawler, D. F., Freeman, B. D., Marrot, B., & Moulin, P. 2009. Reverse osmosis desalination: Water sources, technology, and today's challenges. *Water Research*, **43**(9).

Gungor, E., & Roberts, P. J. W. 2009. Experimental Studies on Vertical Dense Jets in a Flowing Current. *Journal of Hydraulic Engineering*, **135**(11), 935–948.

Hannoun, I. A. 1985. *Matching the refractive index in density stratified flows*. Tech. Memo. 85-1. WM Keck Laboratory of Hydraulics and Water Resources, California Institute of Technology.

Hashmin, A., & Hajjaj, M. 2005. Impact of desalination plants fluid effluents on the integrity of seawater, with the Arabian Gulf in perspective. *Desalination*, **182**, 373–393.

Haub, C. 2010. *2010 World Population Data Sheet*. Population Reference Bureau.

Hinze, J.O. 1975. *Turbulence*. McGraw-Hill.

Holly, F. M., & Grace, J. H. 1972. Model study of dense jet in flowing fluid. *Journal of the Hydraulics Division*, **98**(11), 1921–1933.

Höpner, T., & Windelberg, J. 1996. Elements of environmental impact studies on coastal desalination plants. *Desalination*, **108**, 11–18.

Hussein, H. J., Capp, S. P., & K., George W. 1994. Velocity measurements in a high-Reynolds-number, momentum-conserving, axisymmetric, turbulent jet. *Journal of Fluid Mechanics*, **258**, 31–75.

International Desalination Association. 2009. *IDA Desalination Yearbook 2008–2009*.

Irie, K., McKinnon, A. E., Unsworth, K., & Woodhead, I. M. 2008. A Technique for Evaluation of CCD Video-Camera Noise. *IEEE Transactions on Circuits and Systems for Video Technology*, **18**(2), 280–284.

James, W. P., Vergara, I., & Kim, K. 1983. Dilution of a Dense Vertical Jet. *Journal of Environmental Engineering*, **109**(6), 1273–1283.

Jirka, G. H. 2004. Integral Model for Turbulent Buoyant Jets in Unbounded Stratified Flows. Part I: Single Round Jet. *Environmental Fluid Mechanics*, **4**(1), 1–56.

Jirka, G. H. 2008. Improved Discharge Configurations for Brine Effluents from Desalination Plants. *Journal of Hydraulic Engineering*, **134**(1), 116–120.

Johnson, S. 1766. *A dictionary of the English language: in which the words are deduced from their originals, explained in their different meanings and authorized by the names of the writers in whose works they are found*. Vol. 2. London: Printed for A. Millar.

Karleskint, G., Turner, R., & Small, J. 2009. *Introduction to Marine Biology*. 3rd edn. Cengage Learning.

Kaye, N.B., & Hunt, G.R. 2006. Weak fountains. *Journal of Fluid Mechanics*, **558**, 319–328.

Kikkert, G. A. 2006. *Buoyant Jets with Two- and Three-dimensional Trajectories*. Ph.D. thesis, University of Canterbury, Christchurch, New Zealand.

Kikkert, G. A., Davidson, M. J., & Nokes, R. I. 2007. Inclined Negatively Buoyant Discharges. *Journal of Hydraulic Engineering (ASCE)*, **133**(5), 545–554.

Kolmogorov, A. N. 1941. The local structure of turbulence in incompressible viscous fluid for very large Reynolds numbers. *Doklady Akademii Nauk SSSR*, **30**(4).

Lai, C. C. K. 2010. *Mixing of Inclined Dense Jets*. M.Phil. thesis, The University of Hong Kong.

Lane-Serff, G. F., Linden, P. F., & Hillel, M. 1993. Forced, angled plumes. *Journal of Hazardous Materials*, **33**, 75–99.

Lattemann, S., & Höpner, T. 2008. Environmental impact and impact assessment of seawater desalination. *Desalination*, **220**, 1–15.

Law, A. W.-K., & Wang, H. 2000. Measurement of mixing processes with combined digital particle image velocimetry and planar laser induced fluorescence. *Experimental Thermal and Fluid Science*, **22**, 213–229.

Law, A. W.-K., Ho, W. F., & Monismith, S. G. 2004. Double Diffusive Effect on Desalination Discharges. *Journal of Hydraulic Engineering*, **130**(5), 450–457.

Lee, J. H. W., & Chu, V. 2003. *Turbulent jets and plumes: a Lagrangian approach*. Kluwer Academic Publishers.

Lee, J. H. W., Cheung, V., Wang, W. P., & Cheung, S. K. B. 2000. Lagrangian modeling and visualization of rosette outfall plumes. *In: Proceedings of the Hydroinformatics 2000, University of Iowa, July 2000*.

Lide, D. R. (ed). 2004. *CRC Handbook of Chemistry and Physics: A Ready-reference Book of Chemical and Physical Data*. 85th edn. CRC Press.

Lindberg, W. R. 1994. Experiments on negatively buoyant jets, with and without cross-flow. *Pages 131–145 of: Recent Research Advances in the Fluid Mechanics of Turbulent Jets and Plumes*. Kluwer Academic Publishers.

List, E. J. 1982. Mechanics of turbulent buoyant jets and plumes. *Pages 1–68 of: Turbulent Buoyant Jets and Plumes*. Pergamon.

Litman, T. 2001. Generated Traffic: Implications for Transport Planning. *Institute of Transportation Engineers Journal*, **71**(4), 38–47.

Magde, D., Wong, R., & Seybold, P. G. 2002. Fluorescence quantum yields and their relation to lifetime of rhodamine 6G and fluorescein in nine solvents: Improved absolute standards for quantum yields. *Photochemistry and Photobiology.*, **75**, 327–334.

Mankiw, N. G. 2002. *Macroeconomics*. 5th edn. Worth Publishers.

Marti, C. L., Antenucci, J. P., Luketina, D., Okely, P., & Imberger, J. 2010. Near field dilution characteristics of a negatively buoyant hypersaline jet generated by a desalination plant. *Journal of Hydraulic Engineering*, **137**, 57–65.

Martínez Beltrán, J., & Koo-Oshima, S. (eds). 2006. *Water desalination for agricultural applications*. Rome: Food and Agriculture Organisation of the United Nations.

McDougall, T. J. 1979. On the elimination of refractive-index variations in turbulent density-stratified liquid flows. *Journal of Fluid Mechanics*, **93**, 83–96.

McDougall, T. J. 1983. Double-diffusive plumes in unconfined and confined environments. *Journal of Fluid Mechanics*, **133**, 321–343.

McGuirk, J. J., & Rodi, W. 1977. The calculation of three-dimensional turbulent free jets. *Pages 1.29–1.36 of: Symposium on Turbulent Shear Flows, University Park, Pennsylvania*.

Meerganz von Medeazza, G. L. 2005. "Direct" and socially-induced environmental impacts of desalination. *Desalination*, **185**, 57–70.

Mill, J. 1808. *Commerce Defended. An Answer to the Arguments by which Mr. Spence, Mr. Cobbett, and Others, have attempted to Prove that Commerce is not a source of National Wealth*. C. and R. Baldwin, London. Accessed from http://oll.libertyfund.org/title/1668/, April 27, 2009.

Morris, R. M. 1993. The development of the multi-stage flash distillation process: A designer's viewpoint. *Desalination*, **93**, 57–68.

Morton, A. J., Callister, I. K., & Wade, N. M. 1996. Environmental impacts of seawater distillation and reverse osmosis processes. *Desalination*, **108**, 1–10.

Morton, B. R., Taylor, G., & Turner, J. S. 1956. Turbulent Gravitational Convection from Maintained and Instantaneous Sources. *Proceedings of the Royal Society of London, Series A*, **234**, 1–23.

Naredo, J. M. 2003. La encrucijada de la gestión del agua en España. *Archipiélago: Cuadernos de crítica de la cultura*, **57**, 17–33.

Nemlioglu, S., & Roberts, P. J. W. 2006. Experiments on Dense Jets Using Three-Dimensional Laser-Induced Fluorescence (3DLIF). *In: 4th International Conference on Marine Waste Water Disposal and Marine Environment*.

Nyquist, H. 1928. Certain topics in telegraph transmission theory. *Transactions of the American Institute of Electrical Engineers*, **47**, 617–644.

Ojanen, H. 1999. *Automatic Correction of Lens Distortion by Using Digital Image Processing*. Rutgers University Department of Mathematics technical report.

Oliver, C. J., Davidson, M. J., & Nokes, R. I. 2008. k-ε predictions of the initial mixing of desalination discharges. *Environmental Fluid Mechanics*, **8**, 617–625.

Otranto, F. 2004. *Laboratory modelling of sea-brine discharges*. Undergraduate Report. The University of Western Australia.

Pankratz, T. 2004. An Overview of Seawater Intake Facilities for Seawater Desalination. *In: The Future of Desalination in Texas, Volume II: Technical Papers, Case Studies and Desalination Technology Resources*. Texas Water Development Board.

Pantokratoras, A. 1999. Vertical Penetration of Inclined Heated Water Jets Discharged Downward. *Journal of Environmental Engineering*, **125**(4), 389–393.

Pantzlaff, L., & Lueptow, R. M. 1999. Transient positively and negatively buoyant turbulent round jets. *Experiments in Fluids*, **27**, 117–125.

Papakonstantis, I., Kampourelli, M., & Christodoulou, G. 2007. Height of rise of inclined and vertical negatively buoyant jets. *In:* Di Silvio, G., & Lanzoni, S. (eds), *Proceedings of the 32nd IAHR Congress: Harmonizing the Demands of Art and Nature in Hydraulics; Fluid Mechanics and Hydraulics Theme*.

Papakonstantis, I. G., Christodoulou, G. C., & Papanicolaou, P. N. 2011a. Inclined negatively buoyant jets 1: geometrical characteristics. *Journal of Hydraulic Research*, **49**(1), 3–12.

Papakonstantis, I. G., Christodoulou, G. C., & Papanicolaou, P. N. 2011b. Inclined negatively buoyant jets 2: concentration measurements. *Journal of Hydraulic Research*, **49**(1), 13–22.

Papanicolaou, P. N. 1984. *Mass and momentum transport in a turbulent buoyant vertical axisymmetric jet*. Ph.D. thesis, W. M. Keck Laboratory of Hydraulic and Water Resources, California Institute of Technology.

Papanicolaou, P. N., & List, E. J. 1988. Investigations of round vertical turbulent buoyant jets. *Journal of Fluid Mechanics*, **195**, 341–391.

Papanicolaou, P. N., Papakonstantis, I. G., & Christodoulou, G. C. 2008. On the entrainment coefficient in negatively buoyant jets. *Journal of Fluid Mechanics*, **614**, 447–470.

Papantoniou, D., & List, E. J. 1989. Large-scale structure in the far field of buoyant jets. *Journal of Fluid Mechanics*, **209**, 151–190.

Parry, M. L., Canziani, O. F., Palutikof, J. P., van der Linden, P. J., & Hanson, C. E. (eds). 2007. *Climate Change 2007: Impacts, Adaptation and Vulnerability. Contribution of Working Group II to the Fourth Assessment Report of the Intergovernmental Panel on Climate Change*. Cambridge University Press, Cambridge, UK.

Petersen, O., & Larsen, T. 1998. Dilution in a dense bottom jet in cross currents. *Water Science and Technology*, **38**(10), 331–336.

Planck, M. 1901. Ueber das Gesetz der Energieverteilung im Normalspectrum. *Annalen der Physik*, **309**.

Pope, S. B. 2000. *Turbulent flows*. Cambridge University Press.

Priestley, C. H., & Ball, F. K. 1955. Continuous convection from an isolated source of heat. *Quarterly Journal of the Royal Meteorological Society*, **81**, 144–157.

Pun, K. L. 1998. *Hybrid models for jets and plumes in a flowing ambient fluid*. Ph.D. thesis, Department of Civil Engineering, The Hong Kong University of Science and Technology, Hong Kong.

Purnama, A., & Al-Barwani, H. H. 2006. Spreading of brine waste discharges into the Gulf of Oman. *Desalination*, **195**, 26–31.

Randall, R. E. 1981. Measurement of a negatively buoyant plume in the coastal waters off Freeport, Texas. *Ocean engineering*, **8**(4), 407–419.

Rao, K., Kim, D.N., & Hwang, J.J. 2008. *Fast Fourier Transform*. Springer.

Raventos, N., Macpherson, E., & García-Rubiés, A. 2006. Effect of brine discharge from a desalination plant on macrobenthic communities in the NW Mediterranean. *Marine Environmental Research*, **62**, 1–14.

Roberts, P. J. W. 1979. Line Plume and Ocean Outfall Dispersion. *Journal of the Hydraulics Division*, **105**(4), 313–331.

Roberts, P. J. W., & Toms, G. 1987. Inclined dense jets in flowing current. *Journal of Hydraulic Engineering*, **113**(3), 323–341.

Roberts, P. J. W., & Toms, G. 1988. Ocean outfall system for dense and buoyant effluents. *Journal of Environmental Engineering*, **114**(5), 1175–1199.

Roberts, P. J. W., Ferrier, A., & Daviero, G. 1997. Mixing in inclined dense jets. *Journal of Hydraulic Engineering*, **123**(8), 693–699.

Roberts, P. J. W., Ferrier, A., & Daviero, G. 1999. Closure of "Mixing in Inclined Dense Jets". *Journal of Hydraulic Engineering*, **125**, 318–319.

Sadhwani, J. J., Verza, J. M., & Santana, C. 2005. Case studies on environmental impact of seawater desalination. *Desalination*, **185**, 1–8.

Sáanchez-Lizaso, J. L., Romero, J., Ruiz, J., Gacia, E., Buceta, J. L., Invers, O., Fernández-Torquemada, Y. F., Mas, J., Ruiz-Mateo, A., & Manzanera, M. 2008. Salinity tolerance of the Mediterranean seagrass *Posidonia oceanica*: recommendations to minimize the impact of brine discharges from desalination plants. *Desalination*, **221**, 602–607.

Seil, G., & Zhang, Q. 2010. CFD modelling of desalination plant brine discharge systems. *Water: Journal of the Australian Water Association*, **37**(6).

Shao, D. D., & Law, A. W.-K. 2009. Salinity Build-Up due to Brine Discharges Into Shallow Coastal Waters. *Modern Physics Letters B*, **23**, 541–544.

Shao, D. D., & Law, A. W.-K. 2010. Mixing and boundary interactions of 30° and 45° inclined dense jets. *Environmental Fluid Mechanics*, **10**(5), 521–553.

Simmons, L. F. G., Salter, C., & Taylor, G. I. 1938. An Experimental Determination of the Spectrum of Turbulence. *Proceedings of the Royal Society of London. Series A, Mathematical and Physical Sciences*, **165**(920), 73–89.

Smits, A. J., & Lim, T. T. (eds). 2000. *Flow visualization: Techniques and examples*. Imperial College Press.

Stokes, G. G. 1852. On the Change of Refrangibility of Light. *Philosophical Transactions of the Royal Society of London*, **142**, 463–562.

Stratfor. 1999. *Singapore attempts to assert pressure on Malaysia*. Internet: http://www.stratfor.com/node/968. Accessed 10 April 2009.

Streeter, V. L. (ed). 1961. *Handbook of Fluid Dynamics*. McGraw-Hill Book Company.

Sydney Water. 2007. *Contract signed for Sydney's desalination project*. Internet: http://www.sydneywater.com.au/WhoWeAre/MediaCentre/MediaView.cfm?ID=386. Accessed 26 April 2009.

Taylor, G. I. 1938. The Spectrum of Turbulence. *Proceedings of the Royal Society of London. Series A, Mathematical and Physical Sciences*, **164**(919), 476–490.

Taylor, J. R., & Veronis, G. 1996. Experiments on double-diffusive sugar-salt fingers at high stability ratio. *Journal of Fluid Mechanics*, **321**, 315–333.

Tennekes, H., & Lumley, J. L. 1972. *A first course in turbulence*. MIT Press.

Thomas Fuller. 1732. *Gnomologia: adagies and proverbs; wise sentences and witty sayings, ancient and modern, foreign and British*. B. Barker and A. Bettesworth & C. Hitch, London.

Tomasko, D. A., Blake, N. J., Dye, C. W., & Hammond, M. A. 2000. Effects of the Disposal of Reverse Osmosis Seawater Desalination Discharges on a Seagrass Meadow (*Thalassia testudinum*) Offshore of Antigua, West Indies. *Pages 99–112 of:* Bortone, S. A. (ed), *Seagrasses: Monitoring, Ecology, Physiology and Management*. CRC Press.

Tong, S. S., & Stolzenbach, K. D. 1979. *Submerged discharges of dense effluent*. Tech. rept. Report No. 243. Ralph M. Parsons Laboratory for Water Resources and Hydrodynamics.

Townsend, A. A. 1976. *The structure of turbulent shear flow*. 2nd edn. Cambridge University Press.

Truesdall, J., Mickley, M., & Hamilton, R. 1995. Survey of membrane drinking water plant disposal methods. *Desalination*, **102**, 93–105.

Turner, J. S. 1966. Jets and plumes with negative or reversing buoyancy. *Journal of Fluid Mechanics*, **26**, 779–792.

Turner, J. S. 1995. Laboratory models of double-diffusive processes. *Pages 11–29 of: Double-Diffisive Convection (Geophysical Monograph 94)*. American Geophysical Union.

Turner, J. S. 2003. Vertical transports produced by double-diffusive plumes in a confined homogeneous environment. *Journal of Fluid Mechanics*, **493**, 131–149.

UN Water. 2007. *Coping with water scarcity: challenge of the twenty-first century*. Prepared for World Water Day 2007. Internet: http://www.unwater.org/wwd07/downloads/documents/escarcity.pdf. Accessed 1 March 2010.

United Nations (UN). 2009. *The Millennium Development Goals Report*. United Nations Department of Economic and Social Affairs.

Vafeiadou, P., Papakonstantis, I., & Christodoulou, G. 2005. Numerical simulation of inclined negatively buoyant jets. *Pages A–1537–A–1542 of: Proceedings of the 9th International Conference on Environmental Science and Technology*.

Wada, A., Katano, N., & Coto, T. 1977. Prediction of the diffusion of discharged brine by a simulation analytical method. *Desalination*, **22**, 91–100.

Wang, H., & Law, A. W.-K. 2002. Second-order integral model for a round turbulent buoyant jet. *Journal of Fluid Mechanics*, **459**, 397–428.

Wang, Haijing. 2000a. *Jet interaction in a still or co-flowing environment*. Ph.D. thesis, Department of Civil Engineering, Hong Kong University of Science and Technology.

Wang, Hongwei. 2000b. *Investigations of buoyant jet discharges using digital particle image velocimetry (DPIV) and planar laser induced fluorescence (PLIF)*. Ph.D. thesis, School of Civil and Environmental Engineering, Nanyang Technological University, Singapore.

West, J. 1957. *To See the Dream*. Harcourt, Brace.

Winters, H., Isquith, I. R., & Bakish, R. 1979. Influence of Desalination Effluents on Marine Ecosystems. *Desalination*, **30**, 403–410.

Wood, I. R., Bell, R. G., & Wilkinson, D. L. 1993. *Ocean Disposal of Wastewater*. World Scientific.

Wygnanski, I., & Fiedler, H. 1969. Some measurements in the self-preserving jet. *Journal of Fluid Mechanics*, **38**, 577–612.

Yimer, I., Campbell, I., & L.-Y., Jiang. 2002. Estimation of the turbulent Schmidt number from experimental profiles of axial velocity and concentration for high-Reynolds-number jet flows. *Canadian Aeronautics and Space Journal*, **48**(3), 195–200.

Zeitoun, M. A., Mcllhenny, W. F., & Reid, R. O. 1970. *Conceptual Designs of Outfall Systems for Desalting Plants*. Washington, D.C., 1139.: U.S. Dept of the Interior.

Zhang, H., & Baddour, R. E. 1998. Maximum penetration of vertical round dense jets at small and large Froude numbers. *Journal of Hydraulic Engineering*, **124**(5), 550–552.